University of Sussex

Ultrafast Terahertz Characterisation of Surface Free Carrier Dynamics

Jacob Tunesi

Submitted for the degree of Doctor of Philosophy

University of Sussex

21^{st} December 2020

Declaration

I hereby declare that this thesis has not been and will not be submitted in whole or in part to another University for the award of any other degree.

Signature:

Jacob Tunesi

UNIVERSITY OF SUSSEX

Jacob Tunesi, Doctor of Philosophy

Ultrafast Terahertz Characterisation of Surface Free Carrier Dynamics

Summary

The invention of ultrafast pulsed laser sources, operating with pulse durations shorter than 10^{-12}s, has enabled researchers to fully exploit and observe dynamic systems operating on these timescales. Furthermore, the successful amplification of such short pulses then provided the next leap towards observing such fast processes when under much more extreme nonlinear regimes. The amplification of ultrafast sources was considered such a significant impact that Strickland and Mourou were awarded the Nobel prize in Physics for 2018. One such consequence of the ultrafast laser is the birth of time-resolved pump-probe experimental methodologies, where a weak probe pulse is exploited to observe a sample under investigation, while a strong pump pulse modifies the sample via its nonlinear-optical response at ultrafast timescales. It is then trivial to vary the delay between the pump and probe pulses in order to directly measure the dynamical properties of the sample as it relaxes back to equilibrium. This thesis contains the results obtained in the Emergent Photonics research lab, where I have been developing several embodiments of these pump-probe schemes. Understanding of a system's response to extreme excitation is pivotal to my investigation into the generation and manipulation of Terahertz waves, another field born thanks to the invention of the ultrafast laser. One promising approach to the development of Terahertz technologies is through the nonlinear interaction of ultrashort pulses with matter. Therefore, by developing pump-probe approaches which are able to observe specifically the region where such a nonlinear interaction occurs, I am able to reveal and study the complex processes underpinning the Terahertz generation. This thesis is structured as follows. First, in the introduction I will provide an outline of the physical processes relevant to my work and publications, including a full and critical literature review of the fields impacted by my work. Each chapter will then focus on one of my publications, summarising and describing how it relates to my previous work, and explaining how it was received after publication. I will then finish by outlining how my work could be continued in the future and making any concluding remarks.

Acknowledgements

The decision to do a PhD was not an easy one, I mean who chooses to risk their relationships to be underpaid and stressed to high hell for 4 years? But without a doubt, from the high highs to the low lows, this experience has been one that I will cherish forever as a defining moment in my life and I have come out of it as a better human as a result. I have loved, hated, embraced and feared my work all in varying degrees throughout the past 4 years, and this only names but a few of the emotions I have felt in this time. Every single one will be valued and entirely worth it in the end.

My first acknowledgement of course goes to my main supervisor Professor Marco Peccianti. It was you who took me on all those years ago as a naive undergrad and introduced me to this world of nonlinear optics. Then it was you who offered me the opportunity to continue and to join this incredible PhD world. And towards the end it was you who stood by me in my lowest moments, a gesture that I don't know how I can repay. Lastly I can now tell you that you are wrong about British food and produce, maybe one day you will learn the joys of our cooking!

To my second supervisor, Dr Alessia Pasquazi, you are a rock of this group. Both guiding and lifting me up over these years, it has truly been a pleasure and I thank you.

To Dr Luke Peters, you inducted me into this laboratory and provided me with an excellent foundation for this crazy journey. Thanks for everything.

To Dr Juan Sebastian Totero Gongora, you are amazing. Without you I don't know where I'd be, probably still bashing my head against a wall trying to figure out what an FDTD is. Thank you.

Lastly, to my office friends who I had many a laugh with and risked many a computer with due to the addition of the rugby ball and football. Pedro Burdett, Vittorio Cecconi, Antonio Cutrona, Vivek Kumar, Luana Olivieri, Maxwell Rowley and Robyn Tucker, thanks for everything.

My second set of acknowledgements go to my family, who have all supported me relentlessly from the very second I was born. I owe you all so much for providing me with the greatest start to life that any child can hope for.

To my Mother, who has always been near and who allowed me to squat in her precious home for so long, I truly put that house through its paces, sorry... I love you and I am eternally grateful.

To my Father, who taught me so much and spent many an hour taking me to rugby, football, camping etc. Without you I'd live a very boring life! I love you and thank you for being a questionable role model.

To the rest, the Grans, Aunties, Uncles and Cousins, I love you and thanks for all the laughs.

On top of all these it would be remiss to leave out my group of amazing friends, you have always been there to pummel me back down to Earth and keep me grounded, usually by taking the piss in the only way friends can. Adam Holt, Will Kisby, Daniel Mounce, George Pretlove, Cameron Robertson and Stephen Welch, thank you for the endless entertainment and I love you all.

This then leads me to my beautiful girlfriend Helen Roberts. I've not known you very long but every minute is an absolute joy and I am so excited to see what the future holds for us. You have truly made these final months of the PhD so amazing, I love you and I look forward to seeing you grow into a wonderful and successful paramedic.

Lastly, to my incredible Husky Shadow, you truly are man's best friend and you came to me in my time of darkness to drag me right out of it. I love you buddy.

And with this thesis I am done. Jacob. Out.

Contents

List of Tables

List of Figures

Introduction

This thesis represents a thorough investigation into the fields of THz Photonics and its application to the direct observation of surface free-carrier dynamics. Throughout this work I have observed several novel phenomena and developed new techniques for understanding them. Initially I will introduce the relevant physics required for the understanding of the works which I am presenting, via an in-depth literature review. I will discuss the standard methodologies in THz Photonics and some of the remarkable results associated with the development of THz technologies and spectroscopy. Then, I will introduce the specific framework of nonlinear THz processes from semiconducting surfaces. I will then progress into a discussion on pump-probe techniques, both in the optical and THz ranges, for the determination of how an injection of hot free carriers and their subsequent motion can be directly observed in the time-resolved modulation on a probing field. This discussion will be concluded with a brief commentary on how some of these ideas can be applied to media whose dielectric function varies rapidly in time.

Moving forward, I will present a series of articles, both published and in submission, to which I have contributed throughout the project. Firstly, a novel pump-probe based technique in the THz range is shown. I will then present how this was used to study the nonlinear limits of optical-to-THz surface conversion processes. Following this, I present a journal article where such limits have been overcome by circumventing the contribution of the surface electric field entirely. The final chapter then provides a focal point of this thesis where many of the previous ideas converged to the investigation of time-dependent processes within these THz emitting surfaces. Lastly, I will make some concluding remarks while considering how this work will be taken forward and continued in the future.

Additionally, I have attached as appendices several articles where my work has been applied to other investigations into free-electron dynamics and THz imaging. Starting with a discussion as to how my expertise in pump-probe methodologies contributed to the design of an all-optical benchmark for the characterisation of novel organic polymers for LED applications. The second appendix contains articles presenting a remarkable demonstration of THz nonlinear imaging, where the potential application of such an imaging system relies on the integration of the nonlinear surfaces discussed throughout this thesis in order to improve its performance even further.

Chapter 1

Literature Review

In this chapter I will provide an overview of the several areas of physics I have drawn from throughout the course of this work. Starting with Terahertz Photonics before branching into photoexcitation dynamics and time-dependent metamaterials. The primary enabling factor for which is the invention of ultrafast laser sources.

Pulsed laser sources capable of achieving high peak powers within ultrashort durations enabled the observation of a wide spectrum of nonlinear phenomena and their temporal dynamics [2, 3, 4]. Historically speaking, driven by the desire to investigate physical phenomena occurring on specific timescales, experimentation always converged onto the need of having optical sampling probes of comparable duration (or shorter). For instance, the famous Muybridge's demonstration that a horse running has all feet off the ground for brief periods was realised by developing cameras capable of shutter times orders of magnitude shorter than the state-of-the-art in the early 1870s [5]. Shutter time in high-speed cameras has improved tremendously in the proceeding one and a half centuries, reaching the technological limits imposed by electronic technologies, the limiting factor being reactive effects in electron transport (typically on nanosecond and sub-nanosecond scales). A large kernel of physical processes occurring in picoseconds is still therefore out of reach for this approach and remained largely a mystery until the second half of the 20^{th} century. This forms the modern definition of ultrafast phenomena. Ultrafast optics involves the use of laser pulses with picosecond and sub-picosecond durations to observe and manipulate such physical dynamics. The remarkably short duration of these pulses has several other highly sought features beyond the access to high temporal resolution. Firstly, the *mode-locking* (the basic operating principle of pulsed lasers) temporally redistributes the output laser power, confining the finite amount of optical energy into very short temporal windows. This implies a brief instant where the peak power can be several orders of magnitude larger than the laser's average power. Because the relative importance of

electromagnetic nonlinear polarisation terms (compared to the linear ones) increases with the field strength, pulses provide access to a large constellation of nonlinear phenomena, including frequency mixing between photons [6]. Lastly, a short pulse inherently has a wide optical spectrum, i.e. it allows for forms of single-pulse spectroscopy techniques.

Although nonlinear optical processes were observed shortly after the invention of the laser, optical frequency products were significantly weak. It was marked in history in the case where the editorial board of Physical Review Letters erased the faint trace of the optical second-harmonic signal from quartz observed by Franken *et al* in 1961, assuming it a photographic imperfection [7], In fact, optical nonlinear responses of many systems (with notable exceptions) are vanishingly low for continuous wave excitations, and the widespread availability of pulsed sources has been pivotal in enabling access to nonlinear dynamics.

In a very basic definition, we define the "nonlinear regime" to be the condition in which the result when the optical propagation in the medium cannot be described in terms of a linear combination of the optical excitations. Said differently, the spectral transfer function of a linear optical system changes with its inputs. A large class of nonlinear effects can be modelled via a perturbation approach, i.e. the expanded polarisation of the medium in response to an applied electric field $\mathbf{E}$ is given by

$$\mathbf{P}_{\text{Tot}} = \epsilon_0[\chi^{(1)}\mathbf{E} + \chi^{(2)}\mathbf{E}^2 + \chi^{(3)}\mathbf{E}^3 + ...], \tag{1.1}$$

where ϵ_0 is the permittivity of free space and $\chi^{(n)}$ is the n^{th} order susceptibility of the medium. In contrast, in the traditional linear regime $\mathbf{E}$ is small and thus the higher order terms become negligible. As the total polarisation acts as a source term in the wave equation,

$$\nabla^2\mathbf{E} - \frac{n^2}{c^2}\frac{\partial^2\mathbf{E}}{\partial t^2} = \frac{1}{\epsilon_0 c^2}\frac{\partial^2\mathbf{P}_{\text{Tot}}}{\partial t^2}, \tag{1.2}$$

the nonlinear field products in (1.1) become the source of polarisation components oscillating at new frequencies. As $\chi^{(n)}$ generally becomes exponentially smaller as n increases, their associated terms tend to be relevant only at or above certain electric field magnitudes such as that characteristic of ultrashort pulses [8].

1.1 Terahertz Photonics

The use of photonics to investigate physical processes relies on the wide availability of laser sources operating at a broad range of wavelengths covering the optical electromagnetic spectrum. After more than 60 years of development a large selection of natural and artificial media, with the inclusion of different nonlinear devices, enable laser emission from the Mid-IR to the

UV frequency regions. On the lower end of the electromagnetic spectrum, electronic oscillators and antenna devices are able to produce bright electromagnetic radiation from the long-wave (kHz) to the microwave (hundreds of GHz) bands. In between these two different technological platforms however there lies the so-called Terahertz band (or far-infrared range in the photonics denomination). For many years this portion of the electromagnetic spectrum has been known as the THz "gap" due to a lack of efficient or cheap and accessible sources [9]. In fact, the typical range of frequencies ($0.3 \rightarrow 30$ THz) did not allow for any agile electronic implementations. Conversely, the typically low photon energy makes THz lasing via photonic quantum transitions quite challenging [10]. Approaches from either side have been attempted in the form of electronic multiplexing of microwave signals and nonlinear multiplying chains, or in the manufacture of multi-quantum well structures enabling lasing at THz frequencies [11, 12]. In addition, for similar reasons the lack of efficient detection methods has also limited the growth of THz technologies. Early approaches required the use of bolometers and cryogenic cooling to gain sensitivity against thermal noise from black body radiation [13]. The proliferation of ultrafast laser sources has brought a completely different methodological pathway via the exploitation of several nonlinear optical processes.

The pursuit towards bright THz sources and efficient detectors has been fuelled by some highly promising application scenarios. Many rotational and vibrational resonances of many materials fall within the THz region, including many forms of biological matter [14]. Furthermore, modern forms of Time-Domain THz spectroscopy reconstruct the temporal dynamics of the scattered THz field, hence enabling the retrieval of the full complex refractive index and absorption of the sample under study [15]. Lastly, imaging using THz waves has many attractive potential applications ranging from security to medical [16]. In security, many common plastics and fabrics are transparent to THz waves, therefore scanners are able to assess potential metallic and non-metallic threats contained in enclosures or hidden under clothing [17]. In medicine, the highly absorbing nature of water in the THz range results in a high contrast when skin tumours are imaged [18].

1.1.1 Optical Rectification

Perhaps the most ubiquitous approach for nonlinear optical-to-THz conversion exploit the process known as optical rectification (OR). OR is an example of difference frequency generation (DFG) occurring between different frequency components of an ultrashort optical pulse. This mixing produces near-DC (in relative terms) components within the THz band [19]. An important aspect in any nonlinear effect involving waves at multiple frequencies is that the conversion

(and the direction in which energy is transferred) depends on the relative delay (or phase) between the fields. The condition in which the velocity of waves matches is known as phase matching and it can be practically difficult to satisfy in many cases. For example, an interaction between waves propagating in the same direction would require that the refractive index of the material be the same at all frequencies [20]. It can be demonstrated that for the OR case (where the frequency product is closer to DC), this condition translates to having the group velocity of the optical pulse matching the phase velocity of the generated THz waveform. Zinc Telluride (ZnTe) is a commonly used crystal for collinear OR when Ti:Sapphire ultrafast sources are used as the group velocity at 800nm is approximately matched to the phase velocity between $0.1 \rightarrow 3$ THz [21]. Yet, because of the relatively broad spectrum generated (i.e. the ratio between bandwidth and central frequency), the velocity matching condition cannot be accurately kept for all the generated frequency components. As the phase error accumulates, those frequencies disappear. The "coherence length" quantifies the propagation distance at which an interaction between wavelengths is still efficient in transferring the pump energy to the generated product. As a rule of thumb, to preserve the full output bandwidth the interaction length in a nonlinear crystal should be kept small enough not to exceed the coherence length for all the frequency components generated. Hence, in general, the ZnTe output bandwidth can be increased by decreasing the thickness of the crystal used. However, there is still a fundamental limitation due to a large transverse optical phonon absorption band at 5.3THz [22]. Other bulk crystals used for OR at other fundamental wavelengths include semiconductors such as GaP or GaAs, each with their own trade-off between bandwidth and peak field emission. A huge kernel of work has also been conducted to find novel organic materials such as dimethyl amino $4-N-$methylstilbazolium tosylate (DAST) with exceptionally high nonlinear coefficients which are able to realise phase matching across a wide THz frequency range [23, 24]. In cases where longitudinal phase matching cannot be achieved, such as in Lithium Niobate ($LiNbO_3$), complex illumination geometries have been developed exploiting a diffraction grating to apply a spatial tilt to the pulse prior to non-collinear THz generation in a $LiNbO_3$ prism [25, 26].

Here I will present a brief description of the OR nonlinear process in terms of the second-order polarisation term shown in (1.1), by imagining the nonlinear frequency mixing of two electric fields with frequencies ω_1 and ω_2. Such that the total electric field within the crystal is given by

$$\mathbf{E}(t) = \mathbf{E}_1(t)e^{-i\omega_1 t} + \mathbf{E}_2(t)e^{-i\omega_2 t} + c.c. \tag{1.3}$$

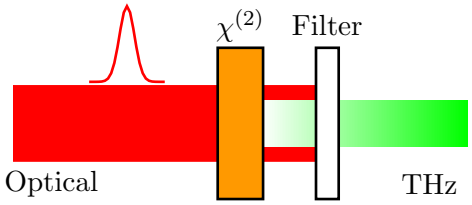

Figure 1.1: The excitation scheme for Optical Rectification of ultrashort pulses in a $\chi^{(2)}$ nonlinear medium.

Which, when substituted into the second term in equation (1.1), the full second-order polarisation becomes

$$\begin{aligned}\mathbf{P}^{(2)} = \epsilon_0\chi^{(2)}[\mathbf{E}_1^2 e^{-i2\omega_1 t} + \mathbf{E}_2^2 e^{-i2\omega_2 t} + 2\mathbf{E}_1\mathbf{E}_2 e^{-i(\omega_1+\omega_2)t} \\ +2\mathbf{E}_1^*\mathbf{E}_2 e^{-i(\omega_1-\omega_2)t} + c.c.] + 2\epsilon_0\chi^{(2)}[\mathbf{E}_1\mathbf{E}_1^* + \mathbf{E}_2\mathbf{E}_2^*].\end{aligned} \tag{1.4}$$

This polarisation then acts as a driving term in the wave equation resulting in the emission of electromagnetic radiation at the various frequency components in (1.4) provided that phase matching is achieved [27].

OR is namely the zero frequency term in (1.4). In terms of THz generation however, because the ultrashort optical pulse isn't monochromatic it is more intuitive to consider the term arising as the difference between fundamental frequencies contained within that pulse

$$\mathbf{P}_{\mathrm{DFG}}^{(2)} = 2\epsilon_0\chi^{(2)}\mathbf{E}_1^*\mathbf{E}_2[e^{-i(\omega_1-\omega_2)t} + c.c.]. \tag{1.5}$$

Describing the emission of radiation with a frequency equal to the difference $\omega_{\mathrm{DFG}} = \omega_1 - \omega_2$. Therefore by defining $\omega_1 = \omega$ and $\omega_2 = \omega+\Omega$ (with Ω lying within the THz range), such that the difference radiates low-frequency THz components [28]. Such collinear OR schemes are often the simplest means by which broadband THz pulses may be generated due to their operation in transmission, as shown in figure 1.1

1.1.2 Electro-Optic Sampling

Electro-optic sampling (EOS) is the most popular methodology to detect ultrafast THz fields [29, 30]. It relies on a THz field-induced birefringence within a second order $\chi^{(2)}$ nonlinear medium. Analogous to the reverse process of OR, EOS enables the complete field-sensitive detection of THz waves by inducing a rotation of the polarisation of an ultrashort optical pulse. EOS is implemented by co-propagating a linearly polarised ultrashort optical pulse with a THz pulse inside an EO crystal such as ZnTe, as shown in figure 1.2. When an electric field is applied to an EO crystal, its refractive index along a particular crystallographic axis is shifted [31]. The effect of this is to encode a phase delay onto the two polarisation axes of the co-propagating

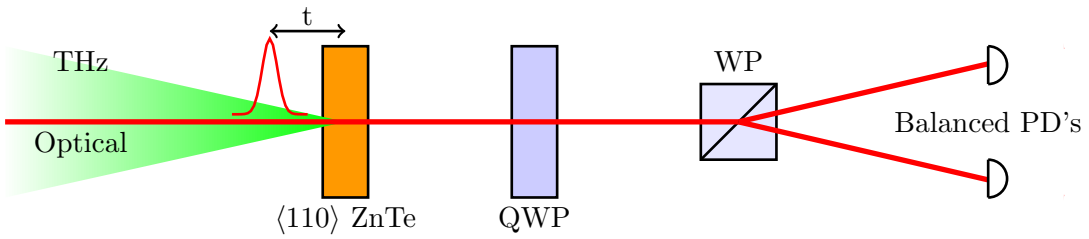

Figure 1.2: The experimental set up for electro-optic sampling of a THz (green) pulse. The input optical (red) pulse is linearly polarised before the ZnTe, after which is a quarter wave plate (QWP), Wollaston prism (WP) and a pair of balanced photodiodes (PD)

optical pulse, resulting in a polarisation rotation of the probing pulse. In EOS, the applied electric field is given by the THz waveform, for a ⟨110⟩ zincblende EO crystal such as ZnTe therefore, this phase shift Γ is given by [9]

$$\Gamma = E_{\mathrm{THz}} \frac{\pi d n_0^3 \gamma_{41}}{\lambda} \sqrt{1 + \sin^2 \phi}, \tag{1.6}$$

where E_{THz} is the applied THz electric field, d is the thickness of the crystal, n_0 is the refractive index with no external field, γ_{41} is the EO coefficient, λ is the central wavelength of the probe pulse and ϕ is the angle between the optical polarisation and the refractive index ellipsoid's long axis.

The polarisation rotation of the optical probe can then be detected by the combination of a quarter wave plate (QWP), a Wollaston prism (WP) and a pair of balanced photodiodes. The QWP acts to transform the slightly elliptically polarised pulse back into a superposition of horizontal and vertical polarisations. These are then separated by the WP, with each component detected separately by the pair of balanced photodiodes. The difference signal obtained from the two photodiode responses is then directly proportional to the phase shift given in (1.6), with the signal S being given by

$$S = I_0 \sin\Gamma \sin 2\phi \approx I_0 \Gamma \sin 2\phi, \tag{1.7}$$

where I_0 is the optical pulse intensity and I have made the assumption that Γ is small. Therefore the signal S is directly proportional to the THz field, which can be recreated in time by delaying the optical probe with respect to the THz waveform.

1.1.3 Photoconductive Switch

A methodology worth noting in the development of THz sources and detectors is the photoconductive (PC) switch [32, 33]. Its working mechanism is based on the drift of photocarriers

between two electrodes inside a semiconductor excited by an ultrashort pulse, shown in figure 1.3. The PC switch involves a patterning of a semiconducting substrate with metallic electrodes acting as the antenna, leaving a gap between the anode and cathode where THz generation or detection can occur. These devices have quickly become a popular solution for commercial THz technologies due to their compact nature, their compatibility with common ultrafast fiber oscillators and their high signal-to-noise ratio.

When generating THz radiation from such a device, a large potential voltage is applied across the semiconducting gap, thus creating a static electric bias field $\mathbf{E}_{\text{bias}}$ between the electrodes. An ultrashort optical pulse with photon energies above the band gap of the semiconductor is then exploited to photo-excite hot electrons into the conduction band (low-mobility holes can be considered negligible), as shown in figure 1.3a. These conducting free electrons are then accelerated by the applied bias field, with a photocurrent density described as

$$\mathbf{J}(t) = N(t)e\mu\mathbf{E}_{\text{bias}}, \tag{1.8}$$

where $N(t)$ is the free-electron density with an explicit time-dependence given by the convolution of the pulse intensity with the semiconductor's photoexcitation response, e the electron charge and μ the electron mobility [34, 9]. The resulting THz field radiated from the PC antenna by this time-varying photocurrent is then be given by its time-derivative

$$\mathbf{E}_{\text{THz}} \propto \frac{\partial \mathbf{J}(t)}{\partial t} \propto \frac{\partial N(t)}{\partial t}\mathbf{E}_{\text{bias}}. \tag{1.9}$$

When detecting THz radiation from PC antenna, the electric bias potential is removed and replaced with an electrical current detection, as shown in figure 1.3b, effectively establishing an electro-optic sampling setup. In this scheme, the ultrashort optical pulse is still exploited to generate a free-carrier density within the electrode gap. The drift of the electrons however is supported by the THz field itself as opposed to any external field. This THz-field induced photocurrent density is given by

$$\mathbf{J}(t) \propto \bar{N}\mathbf{E}_{\text{THz}}(t), \tag{1.10}$$

where $\bar{N}$ is the average electron density in this case [35].

1.1.4 Time-Domain Spectroscopy

The peculiarity of the electro-optical sampling is in its ability to fully reveal the THz field waveform generated by ultrafast devices. The synchronisation between those two processes is the key enabling element of THz Time Domain Spectroscopy (TDS). In THz-TDS, the same ultrashort pulse is exploited for generation and detection. As this pulse is much shorter than the

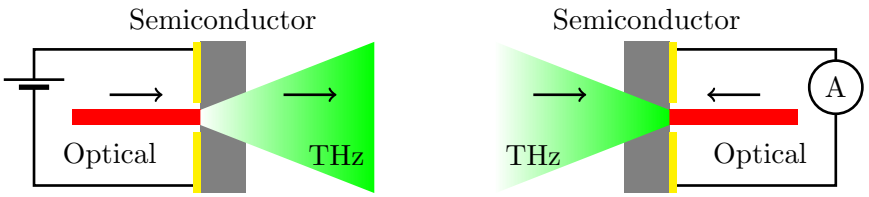

(a) Photoconductive THz Emission (b) Photoconductive THz Detection

Figure 1.3: The concept of photoconductive emission and detection, the black arrows indicate the propagation direction of the pulse.

shortest wavelength component in the THz transient (a common occurrence as the THz pulse bandwidth is significantly smaller than the probe pulse bandwidth), it enables the reconstruction of the THz waveform (Shannon theorem). The pulse probes a specific section of the THz field depending on their mutual temporal overlap. By delaying the optical probe with respect to the THz waveform, the instantaneous value of the THz electric field is encoded into a property of the optical pulse that can be detected. In doing so, comes the remarkable nature of THz-TDS, both the temporal envelope and phase $E_{\mathrm{THz}}(t) = \sqrt{I(t)}e^{i\Omega t}e^{i\phi(t)}$ are known, a condition quite complex to achieve in photonics. More than that, the knowledge of the "delay" translates directly into the knowledge of the phase at any frequency, which removes a classical ambiguity on coherent optical measurements.

It is trivial to then apply the Fourier transform in order to also retrieve the full spectral amplitude and phase $E_{\mathrm{THz}}(\omega - \Omega) = \sqrt{I(\omega - \Omega)}e^{-i\phi(\omega-\Omega)}$. Unlike conventional spectroscopy, access to the spectral phase as well as amplitude means that it is possible to extract the full complex refractive index and absorption $\tilde{n} = n + i\alpha$ from any sample the field has passed through. To do so in transmission, a reference spectrum is taken as well as the signal spectrum which is taken after a propagation d through the sample. With these two measurements, the absorption coefficient is then given by

$$\alpha(\omega) = \frac{1}{d}\ln\left(\frac{E_{\mathrm{ref}}(\omega)}{E_{\mathrm{sig}}(\omega)}\right), \tag{1.11}$$

and the refractive index is

$$n(\omega) = 1 + \frac{c}{d\omega}(\phi_{\mathrm{sig}}(\omega) - \phi_{\mathrm{ref}}(\omega)), \tag{1.12}$$

with c the speed of light in vacuum, $E_{\mathrm{ref,sig}}(\omega)$ the reference and signal THz spectra respectively and $\phi_{\mathrm{ref,sig}}(\omega)$ the reference and signal spectral phases respectively. We can understand the fundamental relevance of this framework, observing that the refractive index is usually not a direct measurable in optical measurements and its knowledge normally requires relative measurements

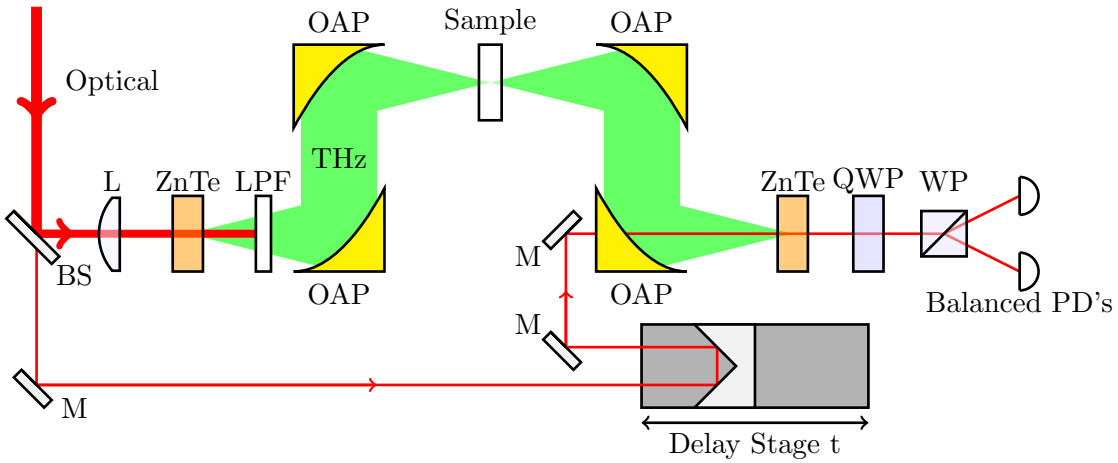

Figure 1.4: The experimental setup for a typical THz Time Domain Spectrometer exploiting OR and EOS from ZnTe crystals for generation and detection respectively. BS: Beam Splitter, L: Lens, M: Mirror, LPF: Low-Pass Filter, OAP: 90° Off-Axis Parabolic Mirror, QWP: Quarter Waveplate, WP: Wollaston Prism, PD: Photodiode.

of the phase, mapped onto intensity variations.

The full setup for THz spectroscopy is shown in figure 1.4, where a motorised delay stage has been used to provide the temporal delay between the detected THz field and the optical probing pulse in EOS. An example of the measured THz waveform using such a setup is shown in figure 1.5a, where the single-cycle THz pulse is retrieved followed by a coherent ringing due to the resonant excitation of water molecules in the air. The fast-Fourier transform of the electric field waveform is shown in figure 1.5b. It provides the spectral components of the pulse, where

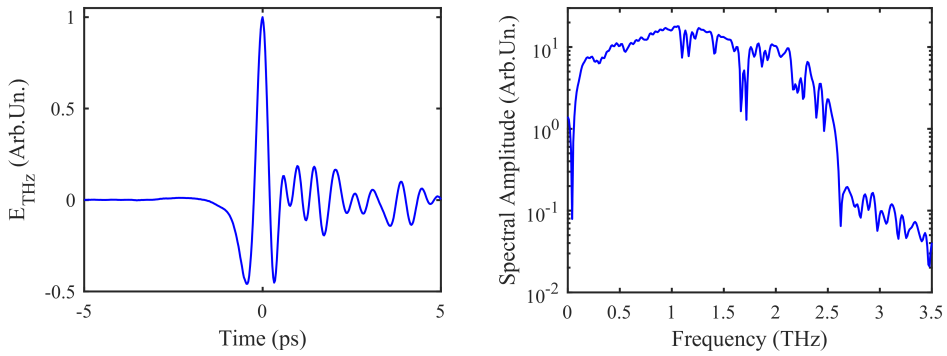

(a) THz time-domain electric field.

(b) THz spectral amplitude.

Figure 1.5: The experimental THz electric field (a) and spectrum (b) as measured with the THz TDS shown in figure 1.4.

it can be seen that the spectrum extends from $0.1 \rightarrow 2.7$THz with several sharp absorption lines characteristic of rotational and vibrational excitation modes in atmospheric water vapour [36]. These very sharp spectral fingerprints within the THz range, corresponding to the rotational and vibrational energy levels of molecules, make THz spectroscopy such a powerful tool. In fact, chiral compounds of the same molecule (usually offering very similar optical properties) such as Thalidomide can even be distinguished due to their very different rotational modes, clearly valuable when the different chiral configurations can have drastically different effects on the human body [37].

As with any evolving technology, there are future challenges to be addressed before its widespread adoption. One being the time to acquire the full THz waveform, with solutions including single-shot TDS embodiments which encodes the THz electric field onto an optical spectrum [38]. It is also worth mentioning that it is desirable to extend the usable THz bandwidth beyond that provided by the most common THz emitters such as ZnTe. A potential solution to this involves reducing the interaction length for broader phase matching and is explored in chapter 4.

1.2 Free-Carrier Dynamics

Charge carriers clearly play a fundamental role in THz photonics, where their dynamic motion can be either beneficial or detrimental for sought applications. Because of the low-energy of the THz photons, the field-matter interaction is mostly governed by the classical acceleration of quasi-free charges. In photocarrier-driven nonlinear mechanisms, the ultrafast injection of photocarriers (i.e. absorption) is obviously required. On the other hand however, the increased conductivity due this process (either via one or multi-photon absorption) screens the propagating THz field saturating the THz output [39]. Means of directly observing the dynamics of free carriers following photoexcitation are therefore essential in gaining an understanding of the complex interplay between the various scattering and recombination processes governing their motion [40, 41]. Each of these processes have their own timescales associated with them, which can vary from anywhere between hundreds of femtoseconds to nanoseconds [42]. It's therefore in the observation of these ultrafast dynamics where femtosecond pulses may be exploited as our ultrashort stroboscopic flash to freeze the dynamics as the events unfold. Pump-probe type experiments have been designed for this specific purpose, where a weak probe pulse is either transmitted or reflected by the sample in question with minimal interaction. A strong pump pulse is then overlapped spatially with the probe and used to photoexcite hot carriers in the same region, thus modulating the absorption, the reflection and the transmission of the probe [43, 44, 45]. Then by delaying the pump and probe pulses with respect to each other, the

excitation and recovery dynamics corresponding to the transient motion of the photocarriers can be directly observed.

Research groups have been very prolific in devising several embodiments of these pump-probe methods, with pump and probe wavelengths ranging across the entire electromagnetic spectrum, with various pulse bandwidths [46, 47, 48]. Furthermore, nonlinearities can be probed by observing modifications to the higher order responses experienced by the probe due to the pump excitation [49]. When THz is involved however, in addition to observing the interesting physical processes on such timescales associated with their generation and manipulation, we also gain information on the fully time-dependent complex refractive index thanks to THz-TDS.

1.2.1 Transient-Carrier Spectroscopy

In its simplest embodiment, the dynamics of charge carriers following photo-excitation can be monitored using the Transient-Carrier (TC) Spectroscopy setup shown in figure 1.6. Early experiments involved the investigation of the bandstructure in metals, specifically probing interband excitations, where thermal effects as well as band structure collapse modifies the reflectivity of the metal [44, 50, 51]. The high energy pump pulse excites a localised region of hot carriers, thus increasing the electron temperature and modifying their population distribution. The change in such a distribution thus has a knock-on effect on the dielectric function and complex refractive index, modifying the Fresnel coefficients and therefore the transmissivity / reflectivity [52]. Following excitation, the thermalization decay time back to equilibrium is

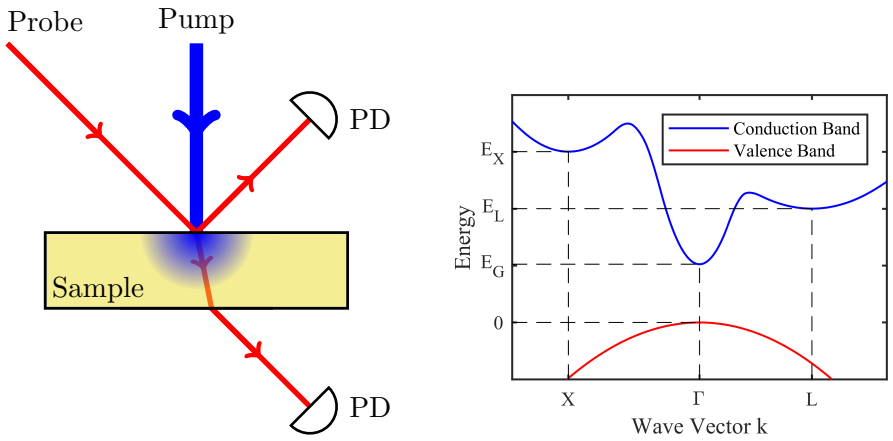

(a) Experimental Setup. (b) Semiconductor Bandstructure.

Figure 1.6: (a) The experimental set up for Transient Carrier Spectroscopy, where a high energy pump pulse modifies the sample and hence modulates the reflection, absorption and transmission of the probe, observed via two photodiodes (PD). (b) Direct semiconductor bandstructure.

then determined via electron-electron and electron-phonon scattering as shown in figure 1.7a, wherein an 800nm pump pulse excites a gold surface prior to probing by a 400nm pulse. It can be seen that the entire dynamics is contained within a few picoseconds, thus the thermal relaxation time is on this timescale.

A somewhat more relevant scheme for this thesis arises when the strong pump pulse excites a semiconductor sample with photon energies above the band gap, as exploited by the THz generation from surfaces discussed in chapter 2.1. Where the dynamics of the Fresnel coefficients can be rather different [41]. An example of the simplified bandstructure for a direct semiconductor such as InAs is shown in figure 1.6b. In these cases, we are transitioning from a regime of very low conductivity (typical of a semiconductor) to a regime of much higher conductivity, via a freeing of bonded carriers. When considering a Gaussian beam profile of spot-size w, the photo-carrier density n can be assumed to be governed by the linear single-photon absorption coefficient α and given by

$$n(x,y,z) = t_F \frac{W_{\text{Pump}}}{\hbar\omega} \frac{\alpha}{\pi w^2} e^{-\frac{x^2+y^2}{w^2}} e^{-\alpha z}, \tag{1.13}$$

where t_F is the Fresnel coefficient of transmission at the air-semiconductor interface, ω is the photon frequency, $\hbar$ is the reduced Planck's constant and W_{Pump} is the incident optical pulse energy. Such an injection of free carriers naturally increases the conductivity of the surface, and again subsequently modifies the dielectric function observed by the probe. It is worth noting that equation (1.13) assumes that the pump penetration (i.e. t_F) is not significantly altered by the photo-carrier density. This assumption typically holds until the free-carrier absorption becomes significant compared to the single-photon absorption process (i.e. the semiconductor surface conductivity approaches that typical of metals). The decay of the conductivity is gov-

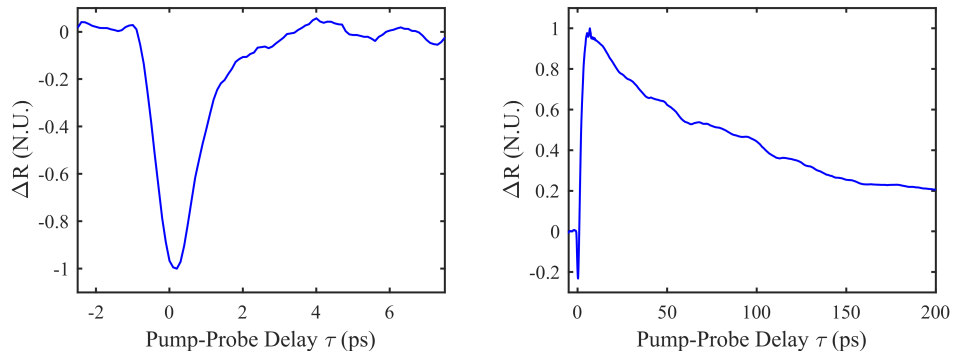

(a) Gold.

(b) InAs.

Figure 1.7: Transient Carrier dynamics measured for Gold and InAs by observing the probe reflectivity as a function of the pump delay time τ

erned by the carrier recombination, as well as their diffusion, the presence of long-lifetime trap states due to impurities or inter-facial materials [53, 54]. As the optical pulse energy increases, saturation of the Γ-valley increases the probability of inter-valley scattering, where additional carriers will be excited into side-valleys with lower mobilities, these valleys therefore contribute less to the TC signal [55]. In usual settings, the slowest of the observable dynamics is attributed to the spontaneous recombination of carriers back into the valence band [56]. An example of the dynamics for InAs surfaces is shown in figure 1.7b, where an additional process contributes to a dip in the reflectivity at $\tau = 0$ps, such a sharp peak is characteristic of a nonlinear product of the pump and probe pulses. This is then followed by a initial transient on the order of 50ps compatible with diffusion and a somewhat slower decay after that due to spontaneous recombination.

In it's most basic form, TC spectroscopy enables the inference of a significant amount of information on the free-carrier dynamics and the timescales associated with the various processes. More complicated schemes have been developed exploiting a white light supercontinuum as the probe pulse [57], where by spectrally resolving the modulated signal it is possible to probe across a huge bandwidth covering the entire optical range and thus each frequency will probe a different electronic transition [58]. TC spectroscopy has had far-reaching impact within the field of ultrafast optics, with applicability in the study of surface science [55], nanomaterial development [59, 60], and chemistry [42]. As such, the use and further development of these schemes provides a central role in this thesis.

1.2.2 Optical Pump Terahertz Probe

A natural progression to these pump-probe ideas is to extend the frequency range of interest out of the optical and into other electromagnetic domains. Remarkable works have extended the probing fields into the X-ray range, where the electronic and structural dynamics of molecular systems is studied [47]. Further extensions have enabled the probing with electron beams, where the perturbation of the e-beam diffraction can be measured with the pump delay to monitor the modification to the crystal lattice [61]. Relevant to this thesis, exploiting a THz pulse as the probing field has become a prolific technique with a high impact due to the power of THz time domain spectroscopy, as discussed in 1.1. Optical Pump Terahertz Probe (OPTP) therefore has gained a large amount of interest since the wide-spread establishment of the field of THz Photonics, early experiments focused on the measurement of carrier mobility in semiconductors [62] or on the recombination lifetime in semiconducting quantum wells [63]. Worth noting again, is that, unlike with other regions of the electromagnetic spectrum, the THz field detec-

tion enables the full retrieval of the amplitude and phase of the probing pulse. In such a way, the direct measurement of the sample's refractive index and power absorption is easily achievable [64], without the need to carry out the significantly challenging Kramers-Kronig analysis to extract the refractive index from incoherent transmission measurements.

Similarly to TC spectroscopy, the timescales associated with the change in absorption of the sample can be related to the photocarrier dynamics such as intervalley scattering, thermalization, and carrier recombination [65]. The exploitation of OPTP to study surfaces can however be challenging due to a limited terahertz sensitivity in many experimental settings [66]. Furthermore, an intrinsic complication in the use of OPTP in reflection is due to the often very different properties of the sample between optical and THz frequencies. In fact, the low-energy THz photons often results in a long penetration depth as opposed to the high-energy optical pump photons which purposefully excites photocarriers above the bandgap within a much thinner region. Therefore the actual overlap between the interacting fields with the region of hot carriers is often limited. This limiting factor is one of the main focuses of this thesis to be discussed in chapter 2. Finally, another scheme worth mentioning briefly is in the works on THz pump THz probe spectroscopy, where rotational energy levels are excited and the coherent motion of electrons can be controlled, this scheme has been used to observe separately intervalley scattering [67] and impact ionization [68] dynamics.

1.2.3 Time-Dependent Metamaterials

One rather unexpected outcome of investigating these pump-probe methodologies, specific to OPTP, is in that optical pulses can easily trigger transitions on timescales smaller than the THz wave period. The regime where media vary rapidly with respect to the electromagnetic field has spawned the relatively new field of time-dependent materials [69, 70, 71, 72]. In these cases, a transition in the dielectric function of the material over time creates a temporal boundary which can be analogously related to a spatial boundary. Such a boundary, with initial and final refractive indices n_i and n_f even brings with it its own version of Snell's law given by [73]

$$n_i\omega_i = n_f\omega_f. \tag{1.14}$$

As can be appreciated, one result of this regime is a frequency shift in the electric field impinging on such a boundary (which in someway recalls the Doppler shift mechanism). A more rigorous approach to these time-dependent media has given rise to the theoretical study of highly exotic nonlinear processes such as time refraction and photon acceleration [74, 75, 76]. Further work has been conducted in the context of flash ionization of gases in optical cavities, where these novel and complex nonlinearities have been demonstrated due to the instantaneous plasma

formation [77]. These ideas are yet to be truly understood however due to a lack of experimental frameworks where they can be studied. This is simply due to the fact that the optical period is very fast from a technological point of view and so a sub-period refractive index transition is far too difficult to achieve reliably. Ultrafast THz photonics, with picosecond periods, therefore represents an ideal and rather unexplored scenario where these effects can be studied. Recently, the excitation of a highly sub-period transition has shown a frequency shifting in the form of THz shockwaves in a traditional OPTP context [78].

These conditions are of further interest to the metasurfaces community where the engineering of the nonlinear surface can enable a wide range of interesting optical responses via the coupling to highly localised plasmonic modes [79, 80, 81]. The net effect of such structures have demonstrated complete control over the amplitude and phase of the reflected or transmitted electromagnetic field [82, 83, 84, 85]. These surfaces are typically metallic in nature and fixed at the design phase, therefore they demonstrate highly limited tunability. Recent advances in semiconducting metasurfaces however have enabled such tunability based on the application of electrical bias or via optical photoexcitation [86, 87, 88]. Another natural progression of these ideas therefore lies in these time-dependent media where the semiconducting metasurface can be excited with a sub-period excitation. This has been demonstrated in the context of the so-called bound states in the continuum (BIC), where a all-dielectric THz metasurface exhibits an active time-dependent response due to such a ultrashort sub-period excitation [89]. This highly exciting and fertile research area is rapidly growing and these ideas will also be exploited in chapter 5 of this thesis.

Chapter 2

Published Paper: Optical Pump Rectification Emission: Route to Terahertz Free-Standing Surface Potential Diagnostics

Driven by the remarkable Terahertz generation efficiencies afforded by semiconductor surfaces, my first publication [90] on this topic was on the development of a novel technique for measuring the surface potential seeding the nonlinearity. In order to understand specifically how the nonlinear conversion occurs it is obviously a requirement to have a means of probing the surface. It soon became clear however, that standard approaches from the literature such as OPTP [62, 91, 65] would not be suitable for investigating surfaces in reflection. This is due to the huge mismatch between the skin depths at the pump and probe wavelengths. Several embodiments exploiting the emitted THz as the probe had been developed [92, 93, 94], however the actual relation between the measured THz field and the surface field is not direct as these approaches exploited the free-carrier nonlinearity instead of surface optical rectification. Therefore, before investigation into the properties of the THz generation, it was necessary to invent a method which is both specific to the surface of the semiconductor while also providing a direct measurement of the potential.

In this work my role was initially to assist in the experiments studying the surface optical rectification phenomenon. I then worked on the physical understanding of the results, developing the model of the surface field screening mechanism, relating the free-carrier dynamics to the pinning of the fermi level at the surface shown in figure 2.2 of the article. Lastly I made signi-

ficant contributions to the writing of the text prior to submission. The article was submitted to Scientific Reports on the 27^{th} February 2017 and published online on the 29^{th} August 2017.

2.1 Surface Terahertz Emitters

Prior to introducing the article itself it is important to introduce the various physical processes converging to generate THz pulses at semiconductor surfaces when photoexcited by ultrashort optical pulses. These processes may be categorised into two main categories, photocarrier-driven current transients and perturbative ($\chi^{(n)}$) frequency mixing.

In photocarrier-driven mechanisms, the generation of photocurrents is driven by the thermoelectric drift-diffusion equation as

$$\mathbf{J}_{e,h} = qn\mu_{e,h}\mathbf{E} + qD_{e,h}\nabla n + qnP_T\nabla T, \tag{2.1}$$

where q, n, $\mu_{e,h}$, $D_{e,h}$ and P_T are the carrier electric charge, volume density, mobility, diffusion constant and thermoelectric power respectively [95, 96, 97].

The first term in (2.1) represents the charge carrier drift induced by electric fields, and as discussed previously in chapter 1.1.3, is responsible for the emission and detection of THz waves in photoconductive antennae. At surfaces, although there is no externally applied electric field, there is however a static surface field established at the symmetry-breaking semiconductor-air interface [98, 99]. Its establishment is due to the Schottky barrier formed between the vacuum and the bulk semiconductor, driven by the 2 dimensional surface density of charged states, which pins the Fermi level at the interface. The Fermi-level equalisation with the bulk results in a carrier accumulation region close to the surface and in the formation of a depletion field [100], as depicted in figure 2.1a. Taking InAs as our example (because the sign of the effect depends on the bulk material) and assuming a volume density N_A of ionised acceptors, a depletion region with depth $(Z_0 + L)$, and a 2-dimensional surface density N_S of accumulated electrons, this surface field at the semiconductor-air interface is then given by [99]

$$E_z^{\text{surf}}(z = 0) = \frac{e}{\epsilon}[N_A(Z_0 + L) + N_S]. \tag{2.2}$$

When an ultrashort pulse excites photocarriers within this surface field region, these carriers will be immediately accelerated by this surface field, creating an ultrafast current dipole which radiates a THz field as

$$\mathbf{E}_{\text{THz}}(t) = \frac{\partial \mathbf{J}}{\partial t}, \tag{2.3}$$

with $\mathbf{J}$ being given by the substitution of (2.2) into the first term in (2.1). This nonlinear mechanism is depicted in figure 2.1b and is known as the generation of THz by ultrafast surge

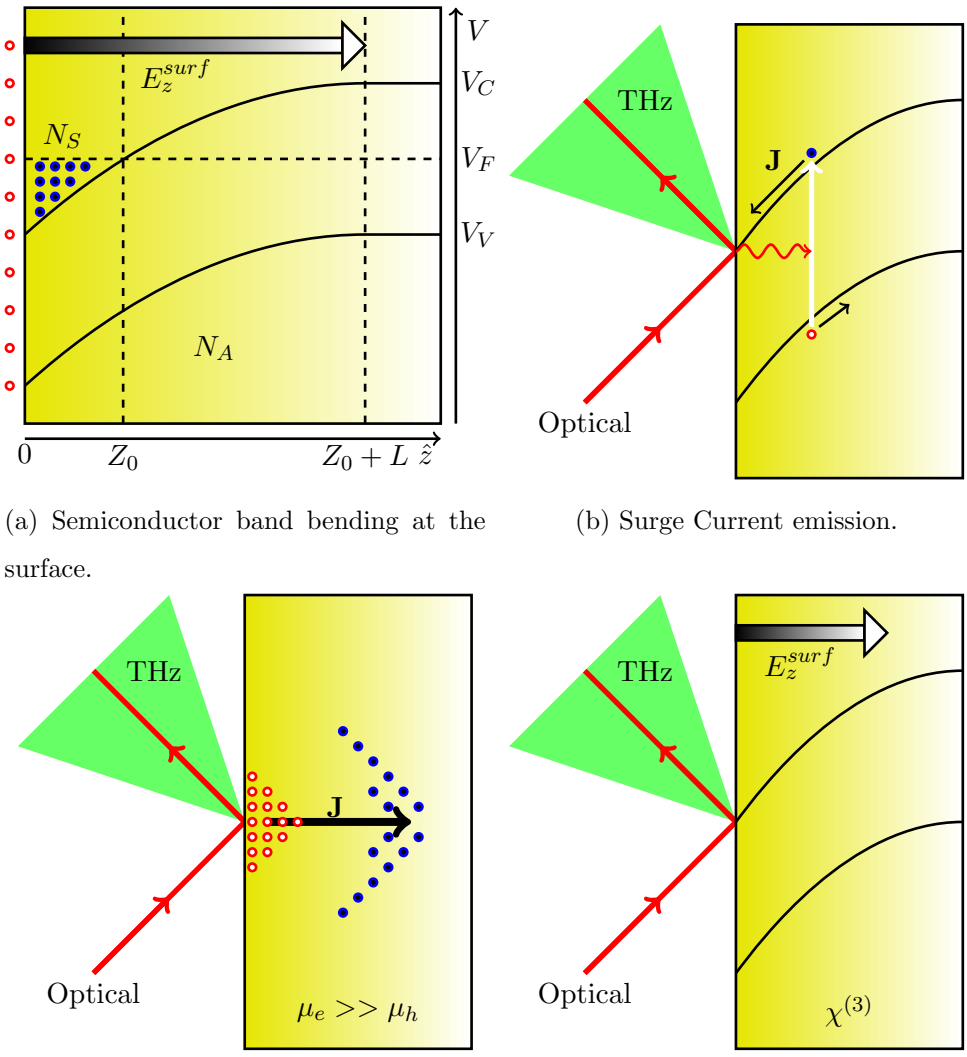

(a) Semiconductor band bending at the surface.

(b) Surge Current emission.

(c) Photo Dember effect.

(d) Surface Optical Rectification.

Figure 2.1: The physical mechanisms governing surface THz emission when semiconductor surfaces are excited by ultrashort optical pulses. Depicting the positively charged holes (white and red) and negatively charged electrons (black and blue).

currents (SC) and has been used as a valuable diagnostic tool in the measurement of surface potentials in semiconductor-based devices [101, 102] and solar cells [94].

The second term of (2.1), is associated to a very relevant second THz generation mechanism, known as the photo-Dember (p-D) effect. In this case, the THz emission can be induced in highly absorptive conditions, when a thin sheet of photocarriers is generated in proximity of the interface. When a significant difference in mobility between electrons and holes exists, the faster carrier will diffuse into the bulk of the material more quickly, this process therefore results in an ultrafast current transient [103, 104], as depicted in figure 2.1c. At low-energy excitation, the p-D effect represents a major benchmark in surface THz emitters, with a further boost in

the emitted THz energy possible via the application of an external magnetic field [105] or the introduction of an asymmetric excitation profile known as the lateral p-D effect [106]. These schemes enhance the emission by rotating the nonlinear dipole such that there is a stronger coupling between the radiation cone and free space.

An important distinction to make when considering the surface THz emission due to SC or p-D photocarrier-migration-based effects is in the symmetry of the generated photocurrent. Where in both cases the ultrafast current dipole is established perpendicular to the semiconductor-air interface. For SC mechanisms this is due to the surface field itself which by definition is directed along the surface normal direction $\hat{\mathbf{z}}$ and hence accelerates photocarriers in the same direction. For p-D mechanisms the diffusion term has equal preference in the $\hat{\mathbf{x}}$ and $\hat{\mathbf{y}}$ directions, resulting in a homogeneous distribution which cancels the photocurrent in all but the depth coordinate $\hat{\mathbf{z}}$. The critical consequence of this is that the THz field radiating from the dipole is emitted exclusively p-polarised and independent of the impinging optical field polarisation and semiconductor orientation, so therefore it can be distinguished from other perturbative nonlinearities such as optical rectification [107, 104].

As the impinging optical pulse energy increases, photocarrier driven mechanisms saturate due to scattering to other lower-mobility valleys in the conduction band as well as THz screening induced by the higher photocarrier driven conductivity [97]. Conversely, perturbative nonlinearities increase their relative importance as they are usually associated with more superficial regions of the medium. Although OR is usually connected to the bulk second-order nonlineariy, as discussed in chapter 1.1.1, where the radiated THz field is governed by (1.5), it has been shown however that for narrow-bandgap, direct semiconductors, there is a dominant contribution due to a third-order process [108, 109]. This is because of the large resonant $\chi^{(3)}$ induced by the absorption and the small penetration depth. This mechanism is shown in figure 2.1d, known as Surface Optical Rectification (SOR), it is seeded by the same semiconductor surface field required in SC emission and results in an effective second order response [110]

$$\chi^{(2)}_{\text{eff}} = \chi^{(3)} E_z^{\text{surf}}. \tag{2.4}$$

Said differently, SOR is the result of the frequency mixing between the optical pulse and a DC field in the form $\Omega_{THz} = \omega_{\text{opt}} - \omega_{\text{opt}} + 0_{DC}$.

A key difference in distinguishing SOR (from photocarrier driven mechanisms) is the introduction of the $\chi^{(3)}$ material response, whose components map the incident optical field onto the various output polarisation components of the emitted THz field. For $\bar{4}3m$ symmetry crystals

such as InAs, with a $\langle 100 \rangle$ surface facet, radiates p-polarised fields as

$$E_{\mathrm{THz}}^{\text{p-Pol}} \propto \alpha_p \left(E_G^{\text{p-Pol}} \right)^2 + \alpha_s \left(E_G^{\text{s-Pol}} \right)^2, \tag{2.5}$$

where $\alpha_{p,s}$ are linear coefficients determined via a rigorous analytical treatment of the nonlinear susceptibility and $E_G^{\text{p,s-Pol}}$ are the polarisation components of the impinging optical field [111]. Then similarly for s-polarised fields

$$E_{\mathrm{THz}}^{\text{s-Pol}} \propto E_G^{\text{p-Pol}} E_G^{\text{s-Pol}}, \tag{2.6}$$

therefore the dependence on the optical polarisation of SOR can be used not only to distinguish between different regimes but also to exclude any photocarrier-based mechanisms which would be detrimental to investigations into the dynamics of SOR.

This phenomena is confirmed in this way to be very much the dominant THz conversion process at very high optical excitation regimes, however it has been shown to saturate as the fluence increases [109]. The physics of this saturation process however remains quite unstudied as it is a complex interaction between the nonlinearity, absorption and the neutralisation of the surface-field by the photocarriers. This study has a central role in this thesis along with the investigation of dynamical screening of the interacting fields following photoexcitation.

2.2 Summary

The article introduces the technique of Optical Pump Rectification Emission (OPRE), where instead of generating the THz probe pulse externally as in OPTP, an optical probe generates the THz field directly on the surface. This third order nonlinear process relies on a symmetry breaking static electric field, which is able to mix with the optical field in order to generate the rectified THz waveform

$$\mathbf{P}_{\mathrm{THz}} = \chi^{(3)}(\omega_{\mathrm{THz}} : -\omega; \omega; 0) : \mathbf{E}_G(-\omega) : \mathbf{E}_G(\omega) : E_z^{\mathrm{surf}} \hat{\mathbf{z}} \tag{2.7}$$

where $\chi^{(3)}$ is the third order nonlinear susceptibility tensor, $\mathbf{E}_G$ is the generating optical field and E_z^{surf} is this static surface field which seeds the rectification [110]. Importantly here are two points, firstly the direct linear relation between the THz polarisation and the surface field, and secondly the source is confined to the spatial overlap between the optical and the static surface fields. Therefore the detected THz electric field is a direct measurement of the surface potential, confined specifically to the surface field region. For direct low-bandgap semiconductors such as InAs, the skin depth at 800nm is in fact on the order of the surface field region ($\sim$ 140nm) [112]. When the screening pump is introduced, also at 800nm, the injection of photocarriers is also

confined to precisely the same region as the THz source, so any free-carrier dynamics are related to the surface and any bulk contributions are removed. This was observed by the presence of two decay timescales after pumping in OPRE, as opposed to one in the OPTP case. Furthermore, by calculating the efficiency of the screened pulse for various pumping energies, it is possible to quantitatively estimate the value of the surface field.

2.3 Impact

This publication targeted the Nature publishing group journal Scientific Reports, which has a 5-year impact factor of 4.525. The journal has a very broad scope covering many disciplines including surface science and Terahertz photonics. Furthermore, the iterative nature of the work meets the journal's requirements for novelty. Lastly, the longer report style of the article obviously fitted well with the journal.

Since publication, the article has been cited 19 times according to Scopus and has been presented at two highly prestigious conferences, CLEO Europe and the Advanced Photonics Congress.

2.4 Journal Article

2.4.1 Abstract

We introduce a method for diagnosing the electric surface potential of a semiconductor based on THz surface generation. In our scheme, that we name Optical Pump Rectification Emission, a THz field is generated directly on the surface via surface optical rectification of an ultrashort pulse after which the DC surface potential is screened with a second optical pump pulse. As the THz generation directly relates to the surface potential arising from the surface states, we can then observe the temporal dynamics of the static surface field induced by the screening effect of the photo-carriers. Such an approach is potentially insensitive to bulk carrier dynamics and does not require special illumination geometries.

2.4.2 Introduction

The diagnosis of electric surface potentials in semiconductors, arising as a result of the charged states at the surface of the material, together with the measurement of the dynamics of the surface carriers, has been at the heart of the development of many modern technologies [113]. In particular, in semiconductor technology, the map of surface carrier dynamics is of paramount importance in a number of industrial steps; for example, it is well established that the surface

states strongly influence the potential of Schottky junctions [114]. Many rising technologies, such as photovoltaics and tuneable metamaterials, rely on thin-layer semiconductors and surface engineering [115, 116], requiring fast and in-situ monitoring of the surface properties, capable of evaluating the dynamics of carriers and static potentials at the surface.

There are several ways (e.g. surface-tunnelling microscopy [117, 118]) to investigate the nature of surface potentials. Optical approaches have been largely investigated as effective, non-invasive alternatives, particularly suitable when ultrafast carrier dynamics need to be reconstructed. In these scenarios, the Terahertz (THz) electromagnetic radiation, lying in the electromagnetic spectrum between infrared and microwaves [119], has been shown to be an important tool.

Optical Pump THz Probe (OPTP) is a well-established spectroscopy technique [62, 120, 121, 122] to monitor bulk photo-excited carrier dynamics. An ultrashort optical pulse is exploited to generate free electron-hole pairs, whereas a THz pulse is exploited to probe the excited semiconductor. The photo-carriers effectively screen the THz field, increasing the absorption of the sample: the measurement of the THz field hence provides a direct measurement of the photo-induced free electrons. By changing the relative delay between the exciting pulse and the measured THz probe, the dynamical response of the free-charges can be reconstructed. Such a technique is very popular to map the photo-carrier dynamics in bulk semiconductors, providing relevant information about their mobility and recombination time. OPTP can be used to reveal a vast array of information, such as the ultrafast carrier trapping in semiconductors [91] and the electronic properties of nanowires [123].

The OPTP technique can in principle be extended to measure surface photo-carrier dynamics, with an embodiment operating in reflection: a change in reflectivity of the sample can be related to the density of photo-generated electron-hole pairs, as is generally done in transmission. The optical penetration depth, when illuminating with photon energies largely exceeding the semiconductor bandgap, can be within the order of a few hundred atomic layers or lower [112]. This short depth results in the excitation of carriers in proximity of the surface. However, OPTP is in overall an approach weakly sensitive to surface dynamics. The most important limitation is that, in all practical scenarios, the THz penetration depth is usually very large, on the order of some tens of microns. This situation implies that the actual overlap between the THz decaying field and the photo-excited layer is always quite weak and very weakly dependent on the carrier dynamics in the surface field region. Most importantly, OPTP is not directly sensitive to the surface potential.

Better approaches have been proposed in literature to analyse photo-excited surface carriers.

The Dynamic Terahertz Emission Microscope (DTEM) is an extension of the Laser Terahertz Emission Microscope (LTEM) [101, 93]. In these techniques a pump laser is used to excite photo-carriers. The surface current generated by such photo-carriers is the source of a THz field, which is directly generated in the photo-excited region of the sample, in striking contrast with the OPTP. The DTEM has been applied to phenomenologically describe the THz generated by surge currents in a polycrystalline silicon solar cell [94].

Moreover, LTEM based approaches allow information on the surface potential to be extracted. Very recently, it has been demonstrated that electrically induced changes in the surface potential of materials such as gallium nitride, where the generation mechanism is dominated by surge current effects, directly affects the THz generation. Here LTEM has been used to map changes in the THz spectrum induced by the surface potential [101]. Furthermore, LTEM has since been used to probe the surface potential of electrically biased silicon [102]. Mag-Usara et al. proposed the "double optical pump" THz time-domain emission spectroscopy, which maps the carrier lifetimes by observing variation in the surge-current generated THz electric field when varying the delay between a THz generating pump and a second optical screening pump [92].

A potential complexity of LTEM based approaches is that the relationship between the surface potential and the THz field is not direct: the surface field accelerates the surface photo-carriers, while the emitted THz is connected to their motional dynamics. Most importantly, in low bandgap semiconductors, THz generation mechanisms related to carrier dynamics (surge current generation and photo-Dember emission) are known to saturate quickly as the excitation increases. A recent study [124] modelling photo-Dember carrier dynamics has attributed its saturation to the coulomb attraction. For excitation fluences of about tens of μJ/cm^2, the THz emission is ruled by surface optical rectification.

In such regimes, the THz generation is directly related to a symmetry-breaking, static surface field which seeds optical rectification [110]. It is well established that the THz surface optical generation arises from a third order nonlinear effect involving the optical, THz and static surface field itself. The resulting THz field is then directly proportional to the surface field, with an important fallout in surface field monitoring that we will exploit in this paper. Very interestingly, in most semiconductor surfaces, such surface fields arise directly from the pinning of the Fermi Level induced by the surface states [98]. Thanks to this mechanism, the optical nonlinearity has been proposed for probing surface states in topological insulators [125].

In this paper, we investigate the use of optical rectification to probe the surface static potential dynamics of a semiconductor by inducing a population of photo-carriers in the surface

field region. An ultrashort optical pulse interacts with the surface and, thanks to the presence of the electrostatic surface field, THz radiation is emitted via a third-order nonlinearity, while a second optical 'screening pump' is used to generate surface photo-carriers. Differently from OPTP, where the photo-carriers screen a THz field, here the photo-carriers screen the static field directly and hence inhibits the generated THz. We will assume a screening pump with typical penetration depth on the scale of the surface field region thickness. This translates to wavelengths of 800nm or shorter in our case of study (InAs). We name our technique Optical Pump Rectification Emission (OPRE). It is worth noting that the screening of the propagating fields has a negligible role in the OPRE.

Similar to LTEM, our approach has the benefit of directly generating the THz field on the surface of the semiconductor, with the advantage of the THz emission being directly proportional to the surface potential. Moreover, OPRE can also be efficiently applied to low-bandgap semiconductors, where the nonlinear generation is the dominating mechanism. As such, we could measure a clear linear relation between the photo-excited charges and the screening optical energy.

This approach may then open up the possibility of using THz spectroscopy for quantitative analysis of the surface potential distribution in semiconductors and, eventually, of the surface states. Moreover, our results demonstrate that it provides an efficient alternative to OPTP and LTEM for the detection of the photo-induced surface carrier dynamics.

2.4.3 Optical Pump Rectification Emission

Before entering into the experimental details, it is useful to describe the general principle of the OPRE, together with a brief summary of the OPTP technique, which we will use in a reflection configuration as a benchmark for probing photo-induced surface carrier dynamics. Figure 2.2 sketches the interaction geometry in the two approaches, OPTP and OPRE in (a) and (b) respectively.

In the OPTP technique (Fig. 2.2(a)) a THz beam is used in reflection geometry to probe the surface carriers generated by a powerful screening pump. The pump has photon energies far exceeding the semiconductor bandgap and induces electron-hole free carrier pairs. The optical penetration depth depends on the strong single photon absorption process and, for a wavelength of 800nm as used in this experiment is on the order of 140nm [112]. Note that, in general, such penetration depths are not affected by the generated free-carriers until very high injections. The absorption process of the THz wave, conversely, is ruled solely by the contribution of free-carriers. Hence, the photo-induced charges screen the reflected THz wave.

The absorption by free-carriers is weaker than the single photon absorption process therefore the THz penetration depth (on the order of 50μm in undoped InAs [126]) is much larger than the penetration of the optical screening pump. We experimentally observe that this results in a small change in the reflectivity of the THz probe. In general, other important limitations arise from the fact that semiconductors usually exhibit a very high refractive index at THz frequencies [15], hence the signal under investigation is normally superimposed with a large contribution originating from the Fresnel reflection. This aspect translates in the need of specific

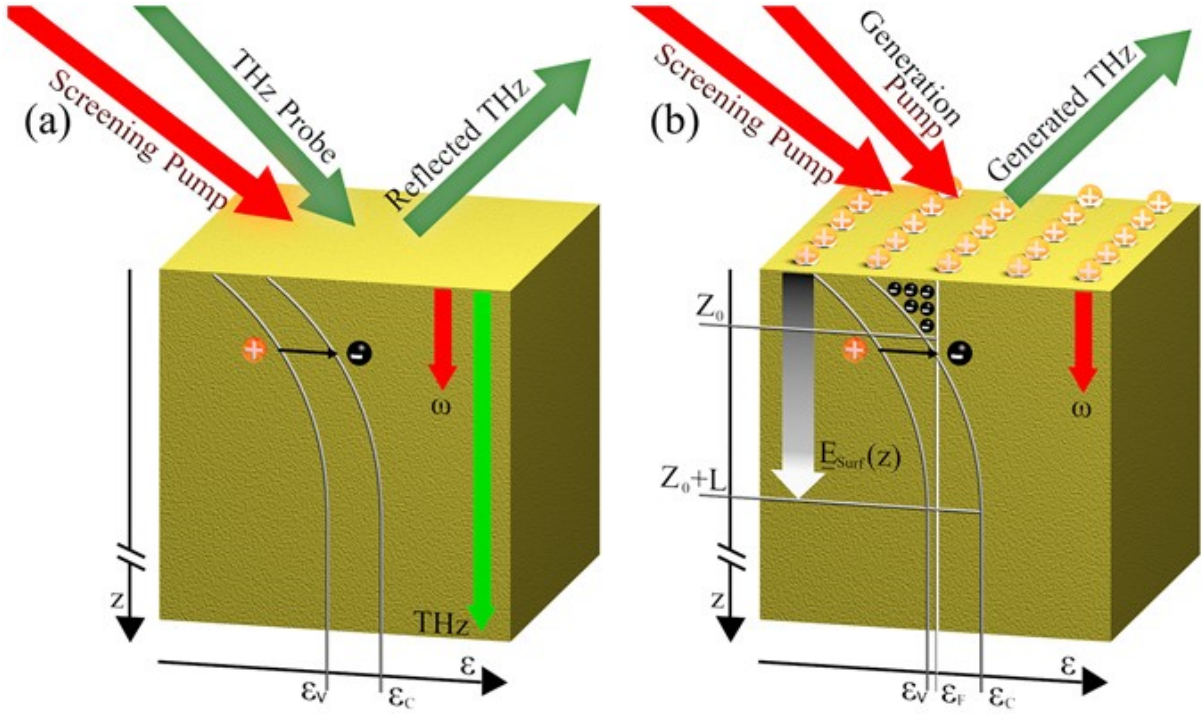

Figure 2.2: A schematic of the excitation geometry of the InAs surface, depicting the relevant physical interactions, for OPTP (a) and OPRE (b) Band diagrams along the depth direction z, with the valence and conducting energies ϵ_V and ϵ_C are indicated in both cases. (a) A screening pump induces free electron-hole pairs, such free-carriers are generated mostly within the skin depth of the pump, indicated with the red arrow. The concentration of free-carriers changes the reflectivity of a THz probe. The skin depth of the THz is indicated in green. (b) The surface field $\mathbf{E}_z^{\text{surf}}$ is indicated by the gradated arrow, resulting from the balancing of the surface charges (plus signs on the top) and localised free-electrons in the surface accumulation region ($0 < z < Z_0$) and the spatial charge in the depleted ($Z_0 < z < Z_0 + L$) region. Free-electrons in the conduction band are indicated by black dots with minus signs, while ϵ_F indicates the Fermi level. The THz is generated by the interaction of the generation pump with the surface field, while the screening pump also generates free-carriers in this case, effectively screening the surface field $\mathbf{E}_z^{\text{surf}}$.

reflection geometries to suppress the strong linear reflection (e.g. the usage of a p-polarised field at the Brewster angle). Moreover, the optical pump can in principle produce an additional change in the THz reflection coefficient through other nonlinear mechanisms, e.g. Kerr-cross phase modulation [127] unrelated to the surface free carrier concentration.

In the OPRE technique the THz wave is generated directly in the sample surface field region. It is important to stress that the underlying principle of surface optical rectification relies on a symmetry-breaking static (DC) surface depletion field $E = E_z^{surf}\hat{\mathbf{z}}$ [128]. The DC surface field is directed along the normal of the surface $\hat{\mathbf{z}}$, as depicted in Fig. 2.2(b); together with the optical generating field ($E_G(\omega)$ in the frequency domain) it contributes to the nonlinear surface polarization P_{THz} that acts as a source for the emission of a quasi-static THz field with frequency $\omega_{THz} << \omega$ where

$$P_{\mathrm{THz}} = \chi^{(3)}(\omega_{\mathrm{THz}} : -\omega; \omega; 0) : \mathbf{E}_G(-\omega) : \mathbf{E}_G(\omega) : E_z^{\mathrm{surf}}\hat{\mathbf{z}}, \tag{2.8}$$

with $\chi^{(3)}$ the third order nonlinear susceptibility tensor. The surface then behaves as an effective second-order material [129]. The elements of the resulting nonlinear susceptibility tensor $\chi^{(2)}$ are:

$$\chi^{(2)}_{ijk}(\omega_{\mathrm{THz}} : -\omega; \omega) = E_z^{\mathrm{surf}}(0)\chi^{(3)}_{ijkz}(\omega_{\mathrm{THz}} : -\omega; \omega; 0). \tag{2.9}$$

The effective nonlinear coefficient is thus directly proportional to the DC surface field of the material. It is important to stress that this quadratic contribution is not related to the quadratic nonlinearity of the medium. The THz wave is then generated by an equivalent second order optical rectification of the ultrashort pulse [130]. From Eq. (2.8), we shall expect a trend of the THz peak field of the form $E_{THz} \propto W_G E_z^{\mathrm{surf}}$, where W_G is the energy of the THz generating pulse, i.e. the generation efficiency is:

$$\eta = \frac{E_{\mathrm{THz}}}{W_G} \propto E_z^{\mathrm{surf}}. \tag{2.10}$$

There are two important considerations that need to be addressed. The first is that, following Eq. (2.8), the THz source is entirely confined within the penetration depth of the optical field (140nm at $\lambda = 800$nm). With the generating volume decreasing as the wavelength decreases and can be as low as 16nm at $\lambda = 400$nm [112]. The second, following Eq. (2.10), is that the efficiency η directly reveals the DC surface field E_z^{surf}.

Before describing the role of the screening pump, it is important to clarify the nature of the DC surface field, which is directly related to the electric surface states of the semiconductor. To formalise the problem and, specifically, the band bending, we consider the general case of a p-type semiconductor (i.e. with Fermi-level approaching the valence band) and a band

bending enriching of a negative charge region in proximity of the surface. It is important to note, however, that in many materials (e.g. InAs, which will be used in the experiments) a significant band bending also occurs in the undoped case, due to the significant charge of the surface states.

The electron/hole surface states of a semiconductor represent a perturbation to the charge balance. The total charge Q_{surf}, hosted by such surface states, needs to balance (and hence neutralise) the charge in the semiconductor. Such a charge is mostly confined in the band-bending region close to the material surface [100], comprising the negative accumulation and Schottky depletion regions, represented in Fig. 2.2(b) for $0 < z < Z_0$ and $Z_0 < z < Z_0 + L$ respectively.

The Schottky depletion region L is characterised by a constant density of space charge, resulting in a total charge Q_{Sc}:

$$Q_{Sc} = -eN_A L, \tag{2.11}$$

with N_A the density of ionised acceptors. Close to the surface, the bending of the bands increases and the Fermi level approaches the conduction band minimum. Here the semiconductor has a narrow accumulation region rich of free-electrons with 2-dimensional concentration N_s [131, 132], the total charge is:

$$Q_{Z_0} = -e(N_s + N_A Z_0). \tag{2.12}$$

The total charge balancing the surface charge Q_{surf} in the band-bending region is then $Q_{Z_0}+Q_{Sc}$. In Fig. 2.2(b) we reported the energy level diagram in the surface accumulation and Schottky depletion regions. The surface charge Q_{surf} is represented on the top surface of the material. The free-electron charges are sketched behind the surface. They represent a large fraction of the total charge when the Fermi level is pinned well above the conduction band minimum. The biasing potential induced by the charge of the surface states gives rise to the DC surface electric field that seeds the four wave-mixing process in Eq. (2.8). The DC field immediately at the surface [99] is then

$$E_z^{\text{surf}}(z=0) = -\frac{Q_{Z_0} + Q_{Sc}}{\epsilon} = \frac{e}{\epsilon}\left[N_A(Z_0 + L) + N_s\right]. \tag{2.13}$$

The DC surface field monotonically decreases with z in the Schottky region until it completely neutralises. In surface optical rectification, however, we can assume that a significant fraction of the generated THz can be attributed to the region between the surface and the electron accumulation layer (where the surface field is maximum and approximately constant) and is proportional to the electric field given by Eq. (2.13). This is also true in low-doped or intrinsic materials, as in those cases the DC surface field is only strong for $z < Z_0$.

We can now take into account the role of the screening optical pump. When photoexcitation is included, hot carriers are induced in proximity of the surface, similarly to the case of OPTP. We will assume that, immediately after excitation, most of the photo-excited electrons are localised in the potential well and drift (because of the high mobility) towards the surface, screening the surface charges and hence the DC surface field E_z^{surf}. By assuming that the saturation dynamics is effective within the typical THz timescales (our screening time resolution is within the order of 3ps) the density of photo-electrons close to the surface layer can be approximated as a surface density n_{Ph}, which directly modifies Eq. (2.13):

$$E_z^{\text{surf}}(z=0) = \frac{e}{\epsilon}\left[N_A(Z_0+L) + N_s - n_{Ph}\right]. \tag{2.14}$$

The carriers inhibit the DC surface field E_z^{surf}, effectively reducing the THz generation efficiency in proximity of the accumulation region (where the nonlinear conversion is stronger because of the high field). Relevantly, at low injections, the density of screening photo-electrons is proportional to the impinging optical energy. Neglecting the very small impinging angle difference between screening pump and THz generating pump, we expect a dependence of the type:

$$n_{Ph}(z) \propto (W_G + W_S), \tag{2.15}$$

where W_S is the energy of the screening pulse. For low energy, the modulation of the surface potential is the sole source of change, as the THz emission is not significantly related to the screening of any of the propagating fields, in stark contrast to OPTP where the photo-carriers screen the THz field directly by increasing its reflection.

Before closing this section, it is worth briefly discussing the expected dynamics of the photo-carriers. The total electromotive field for electrons is [96]

$$E(z) = E_z^{\text{surf}}(z) + P_T\frac{dT}{dz} + \frac{eD_N}{\sigma}\frac{dN_{Ph}}{dz}, \tag{2.16}$$

with P_T the thermoelectric power, T the temperature, D_N the electron diffusion coefficient, N_{Ph} the volume density of photo-generated carriers and σ the conductivity. At high screening injections, we expect $E_z^{\text{surf}}(z)$ to be comparable or smaller than the thermoelectric and diffusion terms in Eq. (2.16), hence other dynamics may become relevant. It is outside the scope of this paper to discuss high-injection dynamics, but we can argue that, as the excitation increases, the depletion layer contracts because the band-bending is reduced by the accumulation of photo-electrons close to the surface. This means that we expect a saturation of the screening effect because most of the carriers will then be generated near or outside the surface field region. The motion of those carriers is then dominated by diffusion and thermal dynamics, only marginally contributing to further screening of $E_z^{\text{surf}}(z)$.

2.4.4 Experimental Setup

Figure 2.3(a) and (b) show the experimental setup for OPTP (used as reference) and OPRE respectively. The excitation pulses are supplied by a 5mJ-class Ti:Sa regenerative amplifier (Coherent Libra-He) generating 100fs pulses centred at $\lambda = 800$nm, with a 1kHz repetition rate. The beam diameter (intensity at $1/e^2$) $d = 9$mm was determined via knife-edge technique. The setup comprises of three separate beam lines, the THz excitation pump (~ 1.5mJ), the screening pump (~ 2.5mJ) and the optical sampling probe ($\sim 1\mu$J) for the detection. A THz electro-optic detection is implemented by co-propagating the THz field and the optical sampling probe in a standard 1mm thick $\langle 110 \rangle$ ZnTe crystal [1]. For the OPTP, the detection crystal and the probe polarisation are set to detect the p-polarised THz field. For the OPRE a s-detection is preferred as it is in principle unaffected by any carrier-mediated generation phenomena. As in standard TDS schemes, the time-domain traces are reconstructed by changing the delay t_d between the THz and the optical probe. The TDS signal is measured with a balanced photo-detection unit feeding a lock-in amplifier.

The main emitter consists of a standard 1mm thick $\langle 110 \rangle$ ZnTe crystal for the OPTP case that generates the THz probe. The sample under investigation is an undoped 0.5mm-thick $\langle 100 \rangle$ InAs crystal, which is also used for generating the THz in the OPRE case. The typical semiconductor bandgap is on the order of 0.35eV, much lower than the photon energy of 1.55eV used for both the generating and screening pumps, translating to a skin depth for normal illumination on the order of 140nm [112]. This value needs to be considered as an upper boundary, and it has been found that the skin depth decreases with the impinging angle [133] of the optical beam on the surface. The angle between the screening pump and THz probe and between the screening pump and generating pump is fixed at 11.9° for both OPTP and OPRE respectively. This results in a temporal smearing and thus a resolution of the pump delay within the order of 3ps.

A system of delay lines allows for the independent control of the group delay in the screening pump and optical probe lines.

For the OPRE case in Fig. 2.3(b), the generation mechanism of the s-polarised THz emission in InAs was confirmed to be optical rectification by rotating the polarisation of the generation pump: we observed a two-fold symmetry typical of optical rectification emission from surfaces [128]. This also allowed us to exclude any relevant contribution of the photo-Dember effect, which is unaffected by a change of polarisation [128] and was not detectable for angles of minimum generation by optical rectification. In contrast to [124], where the sample was rotated to suppress the surface optical rectification, we oriented the surface and the generating pump

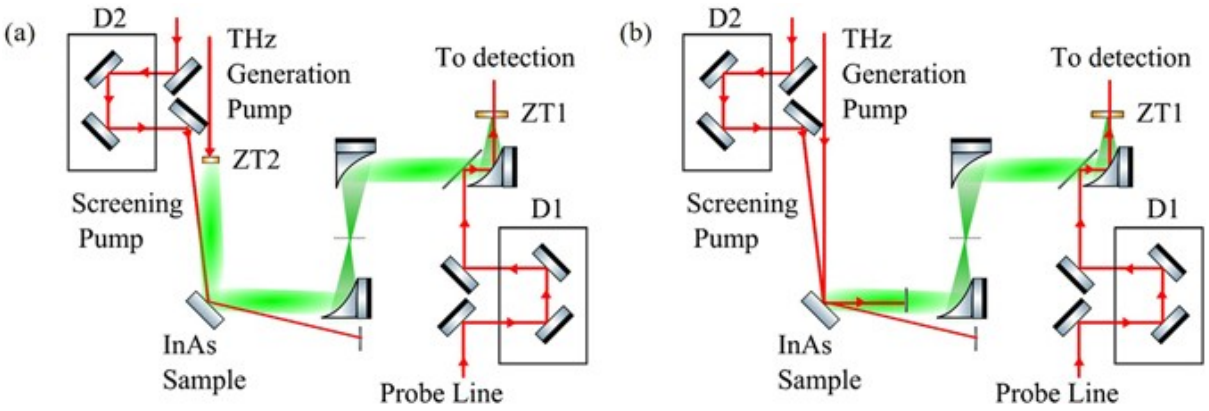

Figure 2.3: Experimental setup for OPTP (a) and OPRE (b) diagnostics. The red and green beam paths denote the 800nm optical and THz beam paths respectively. For both setups, the THz field is measured with a standard electro-optic detection [1], which retrieves the change of polarisation of an optical probe of energy ($\sim 1\mu$J) inside a ZnTe detection crystal (ZT1) due to the THz field. A delay line D1 controls the delay t_d between the THz and the optical probe and allows for the reconstruction of the THz waveform. (a) The THz is generated by a ZnTe crystal (ZT2) converting a generation pump with a pulse energy of 1mJ. (b) The THz is directly generated on the sample under investigation (InAs sample) converting a generating pump with energy 0.1mJ. In both configurations, the relative angle between the screening pump beam and the THz probe beam (a) or optical generating pump (b) is 11.9°. The p-polarised screening pump energy was 1mJ and 0.1mJ for (a) and (b) respectively. The delay between the screening optical pulse and the generating optical pulse τ_s is controlled with the delay line D2 in both cases.

polarisation to maximise the nonlinear conversion efficiency.

2.4.5 Results and Discussion

As a benchmark of our technique, we measured the photo-carrier dynamics with a reflective OPTP trace for an undoped InAs substrate. In this experiment, the THz was generated by bulk optical rectification of 1mJ optical pulses in a ZnTe crystal. Figure 2.4(a) reports a typical THz wave generated in the system, reconstructed in time against the delay t_d between the THz pulse and the optical probe pulse in the detection scheme (Fig. 2.3). The reflectivity of the sample for the THz probe was increased when a screening pump of 1mJ was overlapped in the sample. This is visible in Fig. 2.4(b) where we report the evolution of the THz waveform with the delay τ_s between the optical screening pump and the THz. The change of reflectivity is visible in a weak modulation of the THz wave that fades away for large delays. Reflective OPTP

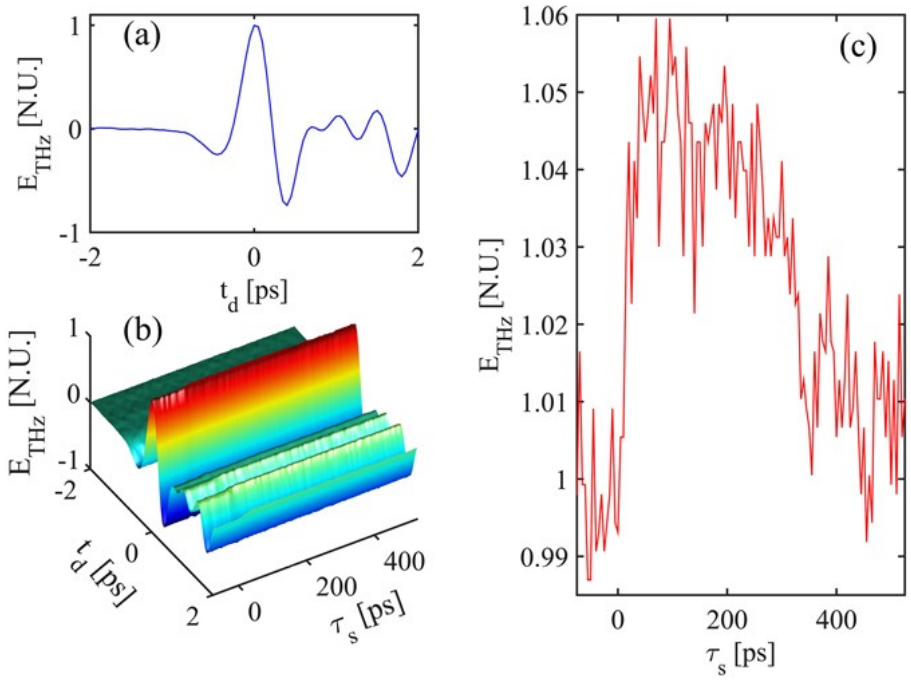

Figure 2.4: Reflective OPTP trace for an undoped ⟨100⟩ InAs substrate. (a) A typical THz waveform reflected by the InAs sample, for a generating pump energy of 1mJ, as a function of the TDS delay t_d. (b) Measured THz field as reflected from the InAs substrate as a function of the TDS delay t_d and screening pump delay τ_s, for a THz pump energy and screening pump energy of 1mJ. The delay $\tau_s = 0$ represents the perfect temporal matching between the screening pump and the peak of the impinging THz wave. (c) Detail of the recovery of the peak THz field ($t_d = 0$) vs the screening pump delay τ_s.

indeed allows for the carrier relaxation dynamics to be inferred from the change in reflectivity of the sample. The increase in reflectivity is related to the increased conductivity due to the photo-carriers generated by the screening pump.

As stated above, the interpretation of the time-resolved or frequency resolved traces is quite complex because in many practical scenarios the penetration depth of THz and optical fields are rather different. Hence, the distribution of photo-carriers along z is very inhomogeneous on the scale of the THz penetration depth. This makes the modelling of the reflection using the standard Leontovich approach difficult [134].

Most importantly, the key drawback of this technique is that the signal variation (and therefore the change in the THz signal) is very small when compared to the total signal received, as visible in Fig. 2.4(b). A better visualisation of the reflectivity change is obtained by plotting the THz peak field (measured for a fixed delay $t_d = 0$), as reported in Fig. 2.4(c). This is the measurement with the best contrast and the relative change in THz field is approximately

5×10^{-2}. The RMS noise of this measurement was 8.2×10^{-3}, resulting in a signal-to-noise ratio (SNR) lower than 8.6dB.

Widening our comparison to the reflective electro-optic sampling approach [135] (that estimates the carrier density from the optical reflectivity) we also experimentally observed a very faint relative change of the power of the reflected THz generating optical pump, which is on the order of 4×10^{-5}.

Summarising, the OPTP approach leads to signal contrast on the order of 5×10^{-2}, with a low SNR of 8.6dB, in measuring the photo-carriers effect on the reflectivity. In addition, the observed carrier dynamics show a decay on the order of ns, as visible in Fig. 2.4(c). Such a decay time is compatible with the carriers' recombination time and appears mostly unrelated to the dynamics of the surface potential, which are expected to occur at lower time scales.

More importantly, we observe here rather different temporal dynamics. This is visible in Fig. 2.5(b), where we observe the change in the THz field with the delay τ_s for the whole temporal scale, and in Fig. 2.5(c), where we observe the recovery of the THz peak measured at $t_d = 0$.

Differently from the OPTP trace in Fig. 2.4(c), that shows a slow recovery in the ns range, the OPRE reveals a fast recovery immediately after the screening time $\tau_s = 0$. We argue that OPRE perceives the modulation of the DC surface potential (which is established in a thin region), where the diffusion of photo-electrons (described in Eq. (2.16)) is a relevant process in InAs on the ps scale [97], making it the source of these fast dynamics. This migration reduces the effective concentration of charges screening the DC surface electric field. A second, slower, dynamic is instead related to the recombination time, similarly to what we observed with the OPTP diagnostics. In sharp difference with the OPTP, however, the OPRE technique explicitly reveals the dynamics of carriers interacting with the DC surface field region.

For the data in Fig. 2.5, we found that the decaying curve can be fit by a combination of two exponential decays (reported in dashed black) with different time constants: a fast recovery time constant on the order of 50ps, that we can associate to the diffusion of the photo-carriers away from the surface-field region, and the much slower recombination time, above 1ns (the fit of the fast recovery is quite sensitive to the estimation of the screening time). This description potentially provides another physical mechanism consistent with the need in literature to fit surface charge decay rates with two different time constants in experiments based on THz emission spectroscopy [136], e.g. when emitted by surge currents [92]. In fact, such an experiment could face a similar decay trend as in our OPRE case.

To further analyse the capability of the OPRE experiments, we studied the effect of the

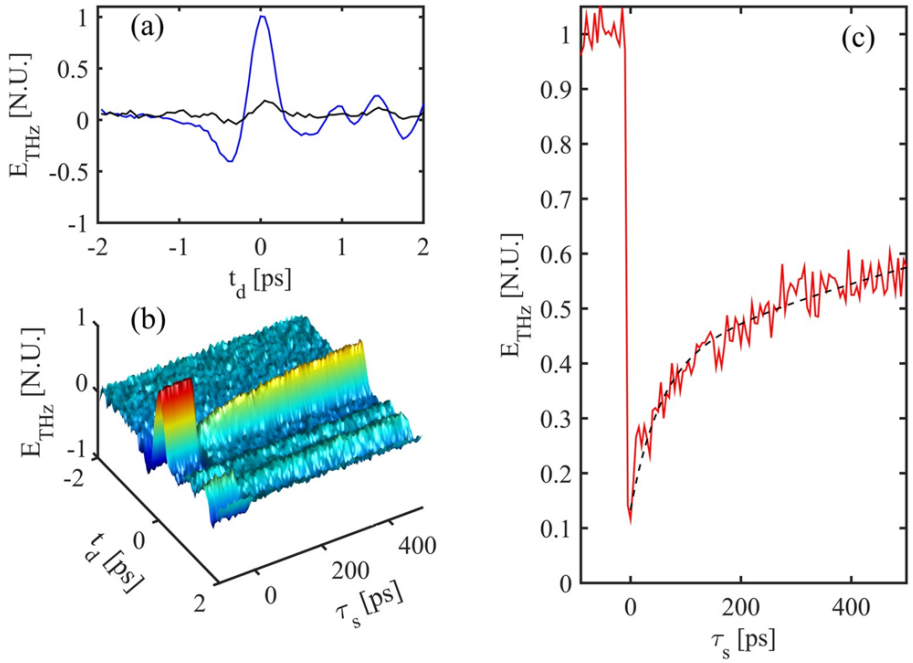

Figure 2.5: OPRE trace for an undoped ⟨100⟩ InAs substrate. (a) A typical THz waveform generated by the InAs sample, by a pump energy of 0.1mJ, as a function of the TDS delay t_d. The blue plot is the TDS trace for no screening pump, the black plot is for a perfectly overlapped ($\tau_s = 0$) screening pump of 0.1mJ (b) Measured THz field as generated from the InAs substrate as a function of the TDS delay t_d and screening pump delay τ_s, for a THz pump energy and screening pump energy of 0.1mJ. The delay $\tau_s = 0$ represents the perfect temporal matching between the screening pump and the peak of the impinging THz wave. (c) Detail of the recovery of the peak THz field ($t_d = 0$) vs the screening pump delay τ_s. The dashed-plot represents the best fit with a double-exponential trend. Under measuring conditions, the laser source stability introduces noise with RMS relative to the peak field estimated to be lower than 3.5%.

screening pump energy on the THz generation efficiency η defined by Eq. (2.10).

Specifically, we considered the reduced efficiency resulting from the screening pump by measuring the THz peak field, that occurs at $\tau_s = 0$ and $t_d = 0$ (black plot in Fig. 2.5(a)). In Fig. 5 we report such a minimum for the efficiency at various screening pulse energies obtained from OPRE scans.

In line with Eqs (2.15, 2.16), as discussed previously, such a measurement is mapping the screening of the DC surface field. As visible in Fig. 2.6(a), the THz field initially decreases linearly with the screening pump at low energy injection (better highlighted in Fig. 2.6(b)) for values below 2μJ, whereas the dependence becomes more complex at high screening energies. This result is consistent with the prediction of the linear dependence between DC surface field

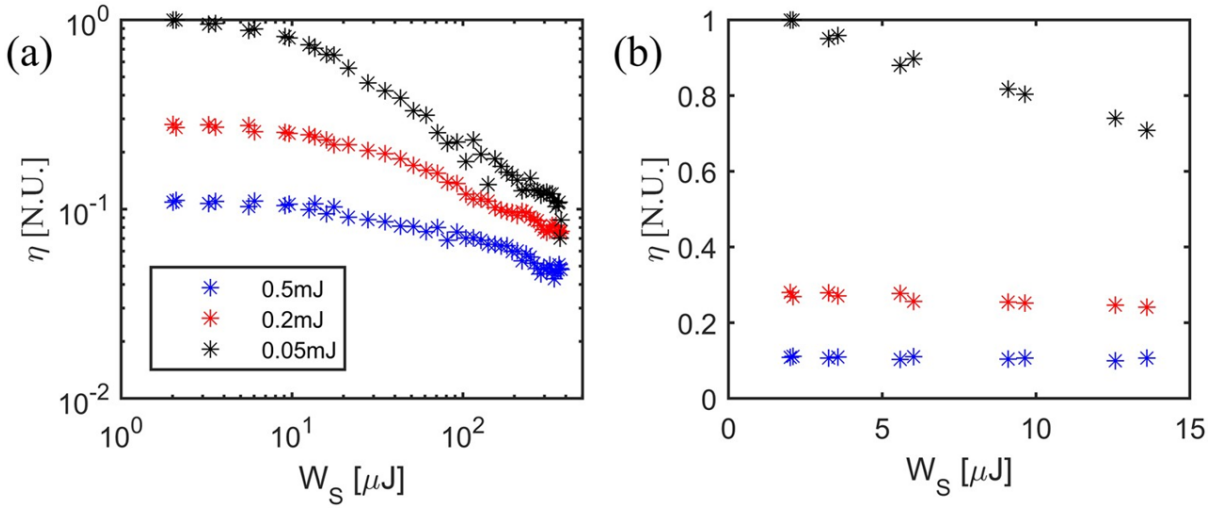

Figure 2.6: (a) Generation efficiency $\eta = E_{\mathrm{THz}}/W_G$ vs. screening pump energy W_S for three different THz generation pump energies W_G. (b) Detail of the generation efficiency at low screening energies, showing the linear trend with the screening energy W_S.

and screening pulse energy (i.e. a quadratic dependence between the THz pulse energy and the screening energy). Such a linear dependence also occurs with the energy of the generating pump W_G. From Fig. 2.6(b), we can appreciate that, in the case where $W_G = 0.5$mJ, the efficiency η for $W_S \approx 0$ is approximately 35% the efficiency for $W_G = 0.2$mJ and 10% the efficiency for $W_G = 0.05$mJ. This corroborates the hypothesis that the surface potential is screened by the surface carriers.

2.4.6 Conclusions

To conclude, we have proposed a new technique for mapping the DC surface potential in semiconductors. The THz field is generated uniquely in the DC surface field-region by optical rectification and the efficiency of the process is directly dependent on the DC surface field. We tested our method by analysing the inhibiting effect in the THz generation of photo-induced free-carriers by an optical screening pump. We observed that the THz generation is strongly inhibited by the presence of the photo-carriers and that the reduction of the efficiency generation is linear with the optical screening pump energy at low injections.

In addition, when compared to the standard OPTP, our enhanced sensitivity to the surface carriers is due to the inherent physical difference between the two methods, the OPTP approach being based on a screening effect of the charges on the THz probe, that increases its reflectivity, while our OPRE is based on a modulation of the generation directly related to the screening of the DC surface field. This was also confirmed by verifying the linearity of the reduction in

generation efficiency with the optical energy.

Finally, as opposed to OPTP, which is not specifically related to carrier dynamics at the surface, nor directly related to the surface potential, the OPRE is directly related to the surface potential in semiconductors. This could lead to novel methods to qualify semiconductor surfaces with potential impact in electronics, photovoltaics and optical sensors.

Chapter 3

Published Paper: High-Energy Terahertz Surface Optical Rectification

Now armed with a proper technique for investigating surface-field carrier dynamics in the OPRE the next project was then to exploit it to study the THz conversion mechanisms at semiconductor surfaces [137], and, in particular, to understand how the SOR nonlinearity saturates at high fluence excitation, a common stumbling block in the production of bright THz sources. At low energies, the excitation of semiconductor surfaces represents an important benchmark in THz systems, where carrier drift-diffusion is responsible for the generation of photocurrent transients at THz frequencies [95, 104]. InAs in particular is often exploited due to its large mismatch between electron and hole mobilities resulting in a significant THz emission due to the Photo-Dember effect [138]. As the optical pulse energy increases however, the injection of higher densities of photocarriers results in a saturation of this effect due to excitation to other conduction band valleys [97], therefore SOR becomes the more relevant nonlinearity until it eventually saturates too. Previous work [109] had identified a saturation effect on the order of tens of μJ/cm^2, but the actual physical process by which this saturation occurs was never investigated. Following the establishment of the OPRE technique sensitive to surface field dynamics, I was then clearly able to begin to research how the injection of photocarriers in this surface field region modifies the emission, thus providing insight into how exactly this saturation occurs.

In this work my role was to study the free-carrier dynamics following photoexcitation. I discovered in the highly n-doped InAs substrates the recovery is much faster than the p-type

or undoped samples. I worked to understand these results in terms of the different thickness of the surface field region between dopings, which then lead to further insights into the saturation mechanism. I worked to create figures 3.3 and 3.5 as well as making significant contributions to the writing of the text. Furthermore, I conducted a thorough study on the implications of using focused beams at low energies to explore the same carrier dynamics, the result of which are the supplementary figures 3.12, 3.13 and the discussions surrounding them. The article was submitted to Nano Energy on the 24^{th} November 2017 and was accepted on the 13^{th} January 2018.

3.1 Characterisation of THz Emission

Prior to beginning the investigation into SOR dynamics at high energy, it was important to characterise the THz emission from InAs surfaces both at low and high energy to confirm that the behaviour I observed was in fact due to the SOR contribution.

The first of these relates to the confirmation of the polarisation dependence of the THz radiation emitted from ⟨100⟩ InAs under ultrashort pulse illumination. This was conducted at high energy using a setup similar to that shown in figure 2.3(b) excluding the screening pump SP with an optical pump pulse energy of $W_G = 1$mJ and its polarisation was controlled by introducing a zero-order half waveplate before the InAs substrate. The electro-optic sampling detection setup was also optimised for detection of p and s polarised THz fields by tuning the probe polarisation and ZnTe orientation following the approach outlined in [139]. With this I could observe the dependence on each THz component as a function of the pump polarisation, the results of which is shown in figure 3.1. As can be observed, both p and s polarised THz

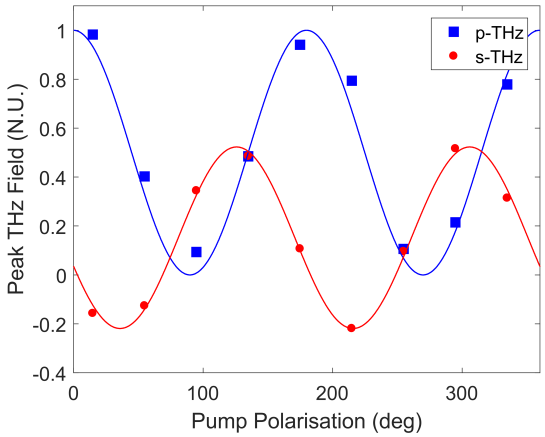

Figure 3.1: The peak THz field has been plotted against impinging pump polarisation for electro-optic sampling detection optimised individually for p and s polarised THz detection.

radiation are verified to exhibit the expected 2-fold symmetry as expected for SOR from ⟨100⟩ InAs as predicted by equations 2.5 and 2.6. With this information I can exclude parasitic THz contributions from photo-carrier driven mechanisms by detecting s-polarised THz fields and optimising the pump polarisation for maximum emission (Polarisation = 125° in figure 3.1), this was the condition used in the experiments presented in chapter 3.4. For completeness in the supplementary information the same investigation was repeated under the condition of maximum p-polarised THz emission (Polarisation = 0° in figure 3.1) and is shown in chapter 3.5.1.

The second experimental scenario that needed confirming was the choice of ultrafast laser source and its influence regarding the temporal smearing on the results presented in chapters 3.4 and 3.5. This necessitated that I expand the pump-probe methodology to a high repetition rate ultrafast oscillator (4W average power, 140fs pulse duration, 800nm central wavelength and 80MHz repetition rate) as in principle very similar intensity domains can be reached by tight focusing of the ultrashort pulses, as opposed to the large collimated beams used with the 1kHz regeneratively amplified source. I discovered however that there are some very significant limitations surrounding the use of high repetition rate sources. The first of which is

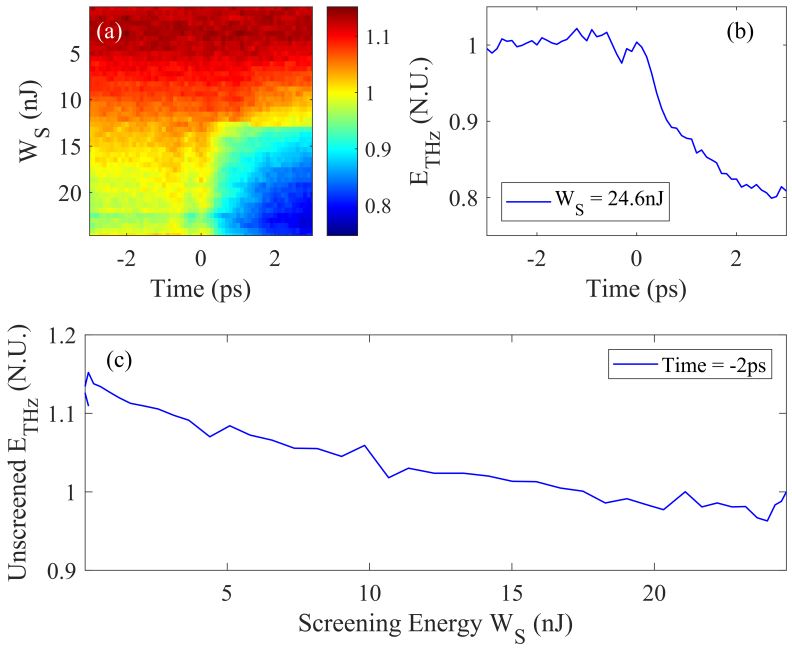

Figure 3.2: (a) The peak THz field as a function of the screening pump pulse energy W_S and time delay, where it can be seen that there is a clear influence of the screening pulse energy on the measured field even for negative delay times. (b) A representative OPRE trace for W_S = 24.6nJ. (c) The dependence of the unscreened (delay times < 0ps) peak THz field on W_S, demonstrating the significant accumulation of carriers by previous optical pulses.

that the tight focusing results in a highly localised THz source with significant divergence. A consequence of this is initially that a large numerical aperture collection and imaging optics is required to image the THz field onto the electro-optic sampling detection without major losses. A second and somewhat more important consequence is that the screening pump also has a large divergence and as such it is highly challenging to completely separate the cross-talk between screening and generation pumps. This scenario is discussed thoroughly in the supplementary information of the article and presented in chapter 3.5.2. In addition, the use of a high repetition rate source for pump-probe experimental campaigns has another drawback in the requirement that the semiconductor sample must decay fast enough such that all photocarriers are returned to the valence band before the next optical pulse arrives shortly after (12.5ns for an 80MHz source). This accumulation of photocarriers from previous pulses can be quantified by observing the OPRE trace for various screening pump energies W_S, as shown in figure 3.2. From which a macroscopic THz screening can be observed induced by the previous pulse in the ultrashort pulse train, where the truly unscreened case at $W_S = 0$nJ exhibits a peak field 15% greater (32% in THz energy) than that when the screening pump pulse is higher in energy. This effect is impossible to remove without complicated mitigation and so any pump-probe dynamics that are observed it should be considered that the free-carrier transition actually occurs from an intermediate excited state as opposed to the ideal case of the ground state. It is for these reasons that I chose in chapter 3.4 to perform the pump-probe based experiments using a low repetition rate, amplified ultrafast source.

3.2 Summary

It was previously known that the addition of dopants will drastically alter the surface states and hence the band bending establishment of the surface field [97, 140, 141]. In InAs in particular, the surface states are always positive regardless of the quantity of dopants added, hence the sign of the surface field always remains the same. A key difference however, is in the quantity of free carriers accumulating in a thin region at the surface as well as in the depth of the static field. The first noteworthy result in the investigation came in the saturation curves shown in figure 3.4, where we highlight two important factors. We show that the saturation never truly occurs, there is only a change in the steepness of the trend, after which the same expected quadratic energy relation is re-established. This is due to a fundamental limit as to how close carriers can approach the surface when they drift in this potential. Therefore, after a certain threshold in the carrier concentration, any additional photocarriers are generated outside of this surface field region and cannot move to screen it. The second interesting point is that the n-type

samples do not exhibit the same transition between quadratic trends, instead they display the second shallower trend only. This can be explained as the intrinsic carrier density provided by the dopants has already screened and shrunk the surface field close to this fundamental limit. To test this hypothesis, OPRE measurements were performed on the different doping types, remarkably showing a much faster recovery time for the n-type substrates with no evidence of spontaneous recombination. The timescale of this recovery was on the order of the time taken for carrier diffusion, and so we proposed that for all substrates, as the optical energy increases the surface field is screened and contracts up until a limit comparable to the free-carrier density of the n-InAs. After which any further increase in energy will result in carriers generated outside of this surface field region, hence they can no longer contribute to the screening and saturation. Lastly we confirmed this by taking the p-InAs and recreating the saturation trends of the other doping types by optically doping it with a quantity of hot carriers to match the surface field in the other samples.

3.3 Impact

This publication targeted the new Elsevier journal Nano Energy, which has a 5-year impact factor of 15.280. The journal targets the development of nanotechnologies for the manipulation of energy. The article was an investigation into the surface field dynamics, which is highly relevant in the behaviour of solar cells and other optoelectronic devices, so it fitted with the scope of the new journal.

Since publication has been cited 21 times according to Scopus and has been presented several times at international conferences and summer schools. Furthermore, the simultaneous press release conducted with the University triggered a widespread interest amongst popular science outlets resulting in an Altmetric score of 28.

3.4 Journal Article

3.4.1 Abstract

The interest in surface terahertz emitters lies in their extremely thin active region, typically hundreds of atomic layers, and the agile surface scalability. The ultimate limit in the achievable emission is determined by the saturation of the several different mechanisms concurring to the THz frequency conversion. Although there is a very prolific debate about the contribution of each process, surface optical rectification has been highlighted as the dominant process at high excitation, but the effective limits in the conversion are largely unknown.

The current state of the art suggests that in field-induced optical rectification a maximum limit of the emission may exist and it is ruled by the photocarrier induced neutralisation of the medium's surface field. This would represent the most important impediment to the application of surface optical rectification in high-energy THz emitters.

We experimentally unveil novel physical insights in the THz conversion at high excitation energies mediated by the ultrafast surface optical rectification process. The main finding is that the expected total saturation of the Terahertz emission vs pump energy does not actually occur. At high energy, the surface field region contracts towards the surface. We argue that this mechanism weakens the main saturation process, re-establishing a clearly observable quadratic dependence between the emitted THz energy and the excitation. This is relevant in enabling access to intense generation at high fluences.

3.4.2 Introduction

The improvement of the generation efficiency of Terahertz pulses (THz) from intense ultrafast optical sources is presently a very hot topic, with a wide spectrum of solutions ranging from the development of novel materials [24, 23, 142] with a higher nonlinear response to efficient non-trivial field-matter interaction geometries [143, 25, 26, 144]. Few options are left when ultrathin emitters are desired. Common quadratic nonlinear crystals have a low absolute conversion efficiency for effective thicknesses within the fraction of micrometres or less. In such scales the nonlinear field-matter interaction is only marginally governed by the bulk properties of the medium. Conversely, it is fundamentally ruled by a series of processes that belong to the domain of surface physics, responsible for THz conversion efficiencies per unit of thickness orders of magnitude larger. Although the literature on surface THz generation is quite vast, the generation at very high excitation and its physical limitations are quite untackled.

A significant fraction of the pioneering works on THz surface emission focuses on narrow band-gap III-V semiconductors, such as InAs and InSb, which exhibit surface terahertz (THz) emission when excited with ultrashort optical pulses. In most scenarios, the generation is driven by the kinetic carrier dynamics [107, 145, 104] and surface field induced Optical Rectification (OR) [110, 128, 146], upon excitation with photon energies well above the energy bandgap [124].

The interest is certainly driven by the surprisingly high conversion efficiencies. For materials possessing a direct band structure, the optical absorption depth for photons with energy exceeding the bandgap is typically very low (e.g. approximately 140nm at $\lambda = 800$nm in InAs [112]). A significant and macroscopic THz emission is then obtained in a very thin interaction region, with very high energy conversion per unit thickness [147, 148].

At low impinging fluences (below 100nJ/cm^2), InAs is perhaps one of the most important benchmarks for surface THz emission driven by the photo-Dember effect [149, 150]. However it has been argued that THz generation by carrier migration is quite saturated at high excitation energies such that the generation is dominated by surface OR [10]. This interpretation reconciles the observed dependence of the emission from the polarisation and crystal orientation in InAs and seeded through works about the microscopic mechanisms responsible for the nonlinearity [151, 152, 153].

A saturation fluence for surface OR has been identified within the order of tens of μJ/cm^2 by Reid et al. [109]. The specific mechanism has not been investigated. Yet, its understanding is clearly fundamental in boosting the THz conversion efficiency at semiconductor surfaces. The basic model of the surface Optical Rectification process suggests that the main saturation mechanism in OR is driven by the accumulation of photoinduced carriers that screens the static surface field of the semiconductor responsible for the surface nonlinearity [110].

In this paper we explore the emission limits, with a novel methodology. Our experimental approach involves the THz generation with an ultrafast generating pump and the simultaneous injection of photo-carriers in the surface field region (within 100nm→ 200nm of the surface) with a second optical screening pump. The underlying idea is to connect the change of the emitted field to the modulation of the surface field as it is neutralised by the photo-carrier drift. The photo-carriers frustrate the surface potential, changing its contribution to the third-order nonlinearity in surface OR, in a process that we can define as Optical Pump Rectification Emission (OPRE) [90] (by analogy with the popular Optical Pump Terahertz Probe (OPTP)). Krotkus et al. [154] argued that at moderate exciting peak powers the surface static field could be significantly augmented by the carrier diffusion but that this does not affect the OR frustration mechanism. With specific reference to our experimental campaign, the signature of this specific contribution is not present at high energy excitations (we present our complete characterisation set in the Supplementary materials). It is worth noting that the THz emission through surface OR is a third-order nonlinear phenomenon and is driven by the cubic relation [110]

$$\mathbf{E}_{\mathrm{THz}} \propto \chi^{(3)}(\omega_{\mathrm{THz}} : -\omega; \omega; 0) : \mathbf{E}_G(-\omega) : \mathbf{E}_G(\omega) : E^{(0)}_{\mathrm{surf}}(0)\hat{\mathbf{z}}. \tag{3.1}$$

As such it is not related to the bulk OR which is driven by the second-order medium nonlinear response ($\chi^{(2)}$) and is not relevant in the physics at semiconductor surfaces.

In this investigation, we argue that because of the very small penetration depth of the optical NIR excitation, the change of the THz generation is also significantly connected to the weakening and contraction of the surface field region upon carrier screening. Hence, at high

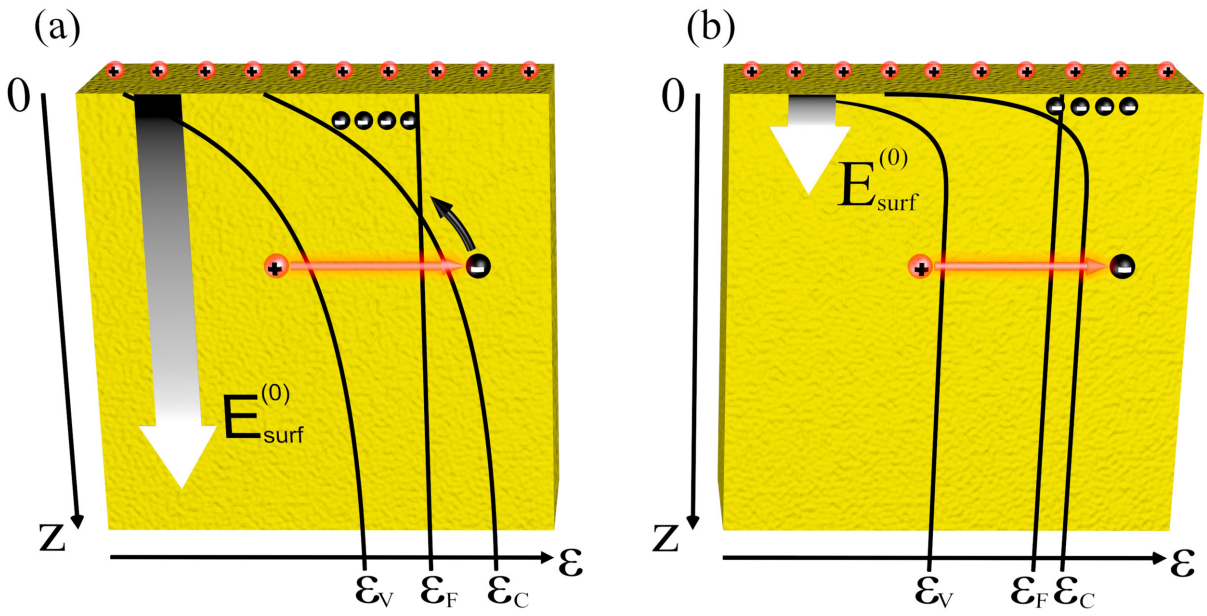

Figure 3.3: A representation of the bending of the boundary of the valence (ϵ_V) and conduction (ϵ_C) bands at the InAs surface for (a) Undoped InAs and (b) n-Type InAs, where the positive surface states pin the fermi level (ϵ_F) above the conduction band minimum at the surface. $E^{(0)}_{\text{surf}}$ is depicted by the gradated arrow where darker shades represent a higher field magnitude. In the latter case, photo-excited electron-hole pairs are mostly generated outside the surface field region, weakening their role in surface field screening.

pumping energies most of the photocarriers are generated outside of the surface field region and therefore they no longer contribute to the saturation. At this point the system converges again to a quadratic conversion efficiency because the progress of the screening of the surface field is no-longer significant. In different words, a real flattening of the pump vs emission trend is not observed.

3.4.3 The field-matter interaction mechanism

The field-matter interaction at the semiconductor band bending region is sketched in Fig. 3.3. In Indium Arsenide, our benchmark model, the surface states result in a positive charged surface density regardless of the doping type [96]. This pins the position of the Fermi-level above the conduction band minimum at the surface such that an electron accumulation layer is formed immediately below the surface. When photoexcited electron-hole pairs are generated, the electrons dominate the surface potential dynamics in light of their much higher mobility.

To infer the contraction, we start observing that in InAs the surface field region is known to weaken and contract as the concentration of free electrons increases [140, 141, 97]. Interestingly, because of the large difference in mobility, moderately doped p-type InAs exhibits lower

conduction and a thicker surface field region than intrinsic and n-doped InAs. At significant n-doping levels, at room temperature, the surface field region thickness (Fig. 3.3(b)) can be much smaller (tens of nm) than the optical penetration depth.

We show here that the typical generation vs excitation trend observed at any n-doping concentration can be reproduced by photo-exciting a p-type semiconductor, corroborating the hypothesis that even in this latter case the field region weakens and thins as the concentration of photocarriers increases. Hence, we argue that upon intense optical pumping the fraction of photocarriers neutralising the surface-field decays and that this is a relevant mechanism in re-establishing a quadratic dependence between emission and excitation.

3.4.4 The experimental setup

The experimental setup is described in Peters et al. [90]. It is supplied with a ultrashort 100fs optical pulse train with 1kHz repetition rate and centre wavelength $\lambda = 800$nm, generated by a mJ-class Ti:Sa regenerative amplifier (Coherent Libra-He). The beam diameter (intensity at $1/e^2$) is $d = 9$mm.

A Time-Domain Spectroscopy detection is implemented using a probe beam originating from a 3%-beam sampler. A motorised delay line controls the relative delay between the probe and the THz waves which are overlapped in a 1mm thick nonlinear ZnTe $\langle 110 \rangle$ crystal which functions as a THz electro-optical sampler [30]. The THz-emitting semiconductors are illuminated at an impinging angle of 45°.

For the implementation of the OPRE measurements a beamsplitter was placed to obtain two separate pump lines. A screening pump (SP) was directed towards a $\langle 100 \rangle$ InAs sample with an impinging angle of 11.9° relative to the THz-generating pump (TP). The SP is delayed by τ_s using a second independent motorised translation stage. $\tau_s = 0$ represents the synchronisation of the two optical pulses.

We verified that the screening does not induce an appreciable change in the emitted THz pulse field profile (which is expected for a DC surface field modulation). In addition, the actual THz-generating pump beam size is reduced with an iris in order to mitigate the temporal smearing (down to the ps scale) in the synchronisation with the screening pump because of their slightly different impinging angle. Nevertheless, by changing the iris size, we verified that our observations are marginally affected by the beam profile.

Central in this investigation, in order to isolate the contribution of the OR from any parasitic contribution of carrier-mediated generation mechanisms, we rotated the detection crystal to detect the s-polarised (perpendicular to the impinging plane) Terahertz emission and we

maximised it by changing the generating pump polarisation. We argue that for ⟨100⟩ InAs under the given illumination condition the potential out-of-plane (s) carrier dynamics induced by structural anisotropies for both the field-driven surge-current and photo-Dember mechanisms should be negligible. We also verified that no Terahertz contamination from the screening pump (p-polarised) is perceived in the detection. We stress here that a typical advantage in using large collimated pumps, made possible thanks to the availability of millijoule pulses, is the absence of cross-talk with the screening pump (for comparison, examples of OPRE with focused generation are presented in the Supplementary materials). Finally, no cross-frequency mixing between screening and generating optical fields can be present for τ_s larger than a few ps, as both pulses and the nonlinear response of the medium are shorter.

For pump photons with energy much larger than the energy bandgap, we can assume that the density of photocarriers is proportional to the impinging TP pulse energy W_G at any z.

$$n_{Ph} \propto W_G \tag{3.2}$$

The surface accumulation layer is essentially a 2-dimensional distribution of electrons centred up to tens of nanometres below the surface because of the quantisation of motion of the electrons in the z-direction [99]. We assume that a fraction of the photo-electrons drift to screen the surface field $E_{\text{surf}}^{(0)}$ and approximated that as equivalent to an effective 2-D layer of density n_{Ph}.

$$E_{\text{surf}}(z=0) = E_{\text{surf}}^{(0)} - n_{Ph}\frac{e}{\epsilon} \tag{3.3}$$

However, as the field weakens at high excitations, n_{Ph} becomes a progressively smaller fraction of the total population of photoexcited carriers, mitigating any further increment of n_{Ph}, i.e. weakening the main saturation mechanism. This is a potential source of the trend observed in Fig. 3.4, where a linear dependence between THz peak field and pump energy (i.e. a quadratic conversion) is re-established after a 'knee'. Quite interestingly, in the case of highly n-doped materials (blue and red plots), in which the surface field region is known to be very thin, this high-energy linear dependence between peak field and energy (i.e. a quadratic conversion) almost covers the entire generation pump energy range.

In Reid et al. [109], the saturation curve in the OR process is fitted with a typical saturation equation

$$E_{\text{THz}} = \frac{AW_G}{W_G + W_{\text{sat}}} \tag{3.4}$$

Where A represents the maximum THz peak field, E_{THz} is the THz field and W_{sat} is the

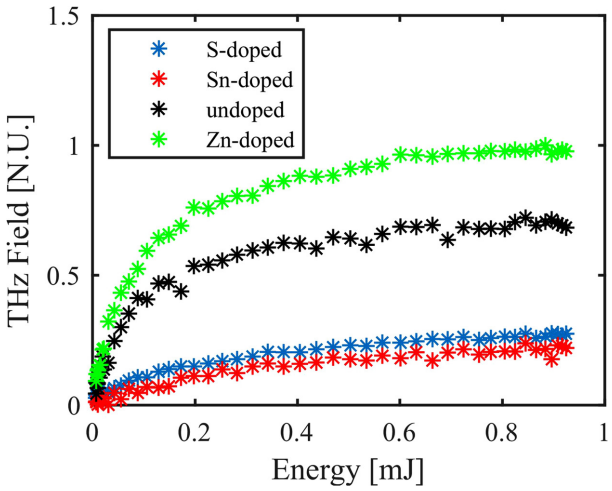

Figure 3.4: The peak THz field has been plotted for various excitation energies, for a number of different freestanding ⟨100⟩ InAs substrates, two n-type samples doped with Sn and S donors, one undoped sample and one p-type sample doped with Zn acceptors. The peak THz field has been normalised across all substrates with respect to the maximum field achieved with the Zn-doped InAs.

saturation energy. The best fit values for W_{sat} for each of the curves are displayed in Table 1. In light of the sufficient accuracy of our experimental measurement, we can observe in Fig. 3.4. that at high energy E_{THz} does not exhibit the plateau predicted by Eq. (3.4). This results in a very poor fit quality at high excitation energy [109]. The observed linear trend corroborates the hypothesis that the main saturation mechanism weakens at high energy.

Substrate	**Doping [cm^{-3}]**	W_{sat} **[μJ]**	τ_1 **[ps]**	τ_2 **[ns]**	R^2 **[N.U.]**	**Relative Dark Conductivity [N.U.]**
n-InAs S-doped ⟨100⟩	$n = 1 \times 10^{18}$	201	40	N/A	0.817	2.83 ± 0.01
n-InAs Sn-doped ⟨100⟩	$n = 3 - 10 \times 10^{17}$	371	31	N/A	0.846	3.40 ± 0.01
n-InAs undoped ⟨100⟩	$n < 3 \times 10^{16}$	88	54	> 1.0	0.947	1.00 ± 0.01
p-InAs Zn-doped ⟨100⟩	$p = 5.3 \times 10^{18}$	86	37	> 1.0	0.982	0.28 ± 0.01

Table 3.1: Shows the known carrier concentration, saturation power and THz recovery times for a number of different substrates. The R^2 (statistical coefficient of determination) values show the goodness of the fit used to retrieve recovery times. Considering the very different accuracies in the doping specified by the different sample suppliers, we also report the measured dark conductivity, relative to the undoped sample.

It is worth noting that because of the much higher mobility of electrons, the undoped substrate (that possesses a process-induced n-doping around 2×10^{16}cm^{-3}) exhibits a weaker surface field and a lower conversion efficiency when compared to the p-doped sample.

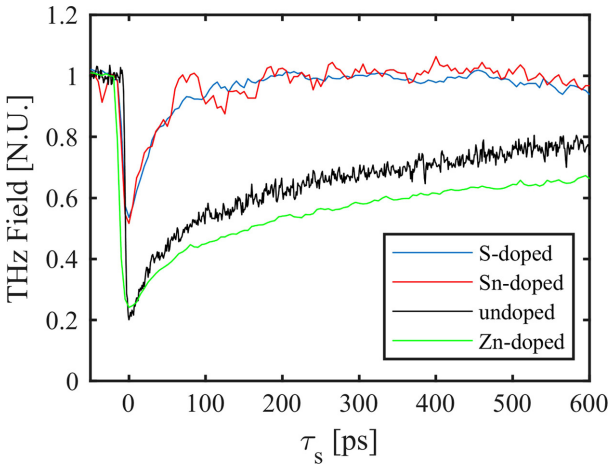

Figure 3.5: OPRE measurements of the peak THz field vs the screening pump delay for the four different freestanding ⟨100⟩ InAs substrates of Table 3.1. Each curve is normalised with respect to the unscreened peak THz field. Each measurement was performed with a generating pump energy W_G of 0.1mJ and a screening pump energy W_S of 0.1mJ.

In Fig. 3.5, the OPRE measurement in the different samples is presented: it is clear that the free electron concentration has an important impact on these dynamics. Following a similar approach in literature we fit the normalised recovery trend as [92]

$$E_{\mathrm{THz}} = 1 - k_1 \times e^{-\frac{\tau_s}{\tau_1}} - k_2 \times e^{-\frac{\tau_s}{\tau_2}} \tag{3.5}$$

where k_1, k_2, τ_1, τ_2 are the fitting parameters and τ_s is the time delay between the screening pump and the THz emission pump. τ_1 represents a fast recovery time. It is potentially consistent with the time scale of the migration of photocarriers away from the surface-field region as its thickness can be a very small fraction of the pump wavelength. Although we should expect the carrier diffusion to be a dominant process in the carrier dynamics (as recognized in a number of studies as the source of the photo-Dember mechanism) we cannot exclude a contribution from quasi-ballistic photo-electron dynamics [155] and from the electron scattering into other conduction band valleys. τ_2 is consistent with the slow recovery time typically associated with the bulk recombination of photoexcited carriers.

For the n-doped sample we consider $k_2 = 0$ as there is no appreciable slow decay in the traces: this appears consistent with the assumption that only the decay of the photocarrier density in a very thin region close to the surface dominates the dynamics. As soon as the concentration of carriers becomes comparable to the inherent free carrier concentration (from doping) the THz emission returns to its original level. Therefore, in n-doped substrates the bulk carrier recombination time does not appear to be relevant in the OPRE measurements.

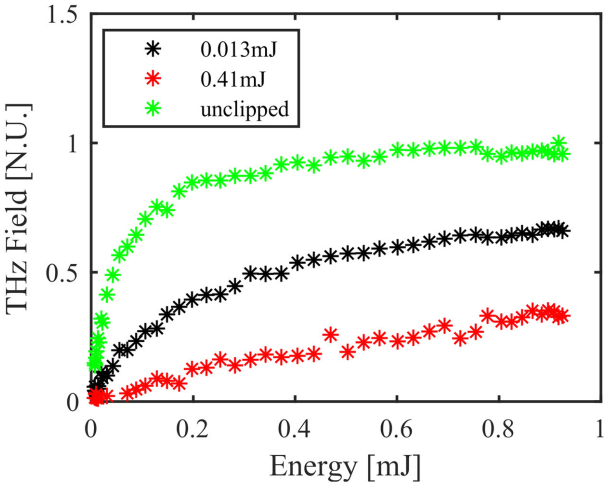

Figure 3.6: Peak THz field plotted against W_G, for a Zn-doped $\langle 100 \rangle$ p-InAs substrate, for various screening energies W_S fixed at $\tau_s = 0$. Each measurement was performed with a generating pump energy W_G of 0.1mJ. The peak THz field has been normalised across with respect to the maximum peak field generated by Zn-doped InAs.

The best-fitting parameters can be appreciated in Table 3.1.

We compared the doping of the substrates along with the calculated values for the saturation power (W_{sat}) and surface field recovery times in Table 3.1. For the sake of comparison, W_{sat} was extracted from the data fitted using Eq. (3.4). From this we observe that the apparent saturation of n-type samples occurs at significantly larger powers when we best fit the curve.

To test our hypotheses, we reproduced the conversion trend of Fig. 3.4 for the undoped and n-doped media by artificially pumping photocarriers within the surface field regions in the p-type InAs, using the SP with appropriate energy. We fixed the delay of the SP to obtain the maximum screening. The expected effect is an increase in the electron-mediated screening of the surface field. The acquired data are presented in Fig. 3.6.

We could adjust the average screening pulse energy W_S to reproduce fairly accurately all the observed conversion trends in the undoped and n-doped cases of Fig. 3.4. Hence, we argue that the photo-carriers produce the same contraction of the surface field region as occurs in n-doped materials.

In addition, it is worth observing that the photo-excited carrier distribution in the example of Fig. 3.6 is certainly very different from the almost homogenous free-carrier density of the n-type sample. Then, the close matching of the trends of Fig. 3.4 and Fig. 3.6 suggests that all the screening dynamics must occur within depths much smaller than the optical skin depth (so that the carrier profile plays a minor role), which also corroborates the main hypothesis. This also suggests that the carrier induced screening of the THz propagating field plays a minor role

(the typical THz skin-depth in the used n-doped materials lies in the range of hundreds of nm to micrometre scales).

In conclusion, a physical process for the saturation of surface optical rectification at high fluences has been proposed. We argue that as the injection of photo-carriers increases, the thickness of the surface field region contracts and a progressively larger fraction of the photocarriers are excited outside of the surface field region. As those carriers do not contribute to the surface field screening, a quadratic conversion trend (i.e. a linear dependence of the peak THz field from the generating pump energy) is eventually re-established at high excitation energies. As confirmation of our hypothesis, we verified that the depth of this surface field layer, and therefore the saturation trend of the substrates, can be controlled with either doping of the material or by injecting an equivalent quantity of photocarriers. We believe this to be an advancement in the understanding of the THz surface generation physics at very high excitation and a step forward in the realisation of high energy surface THz emitters.

3.5 Supplementary Material

3.5.1 OPRE detecting p-polarised THz waves

In our investigation, in order to isolate the contribution of the OR from any parasitic contribution of carrier-mediated generation mechanisms, we detect the s-polarised THz field (perpendicular to the impinging plane). Fig. 3.7 shows the detected THz waveforms for both s- and p-polarised electric fields emitted by ⟨100⟩ Zn doped p-InAs, where the input optical polarisation has been oriented to maximise the emitted THz field.

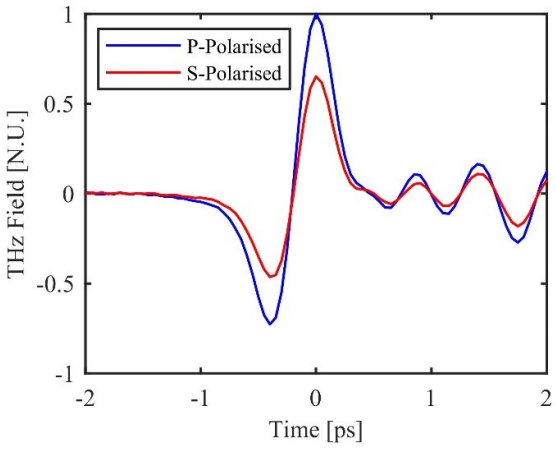

Figure 3.7: Detected THz waveform generated from ⟨100⟩ p-InAs. Both TDS measurements have been normalised with respect to the p-polarised peak field.

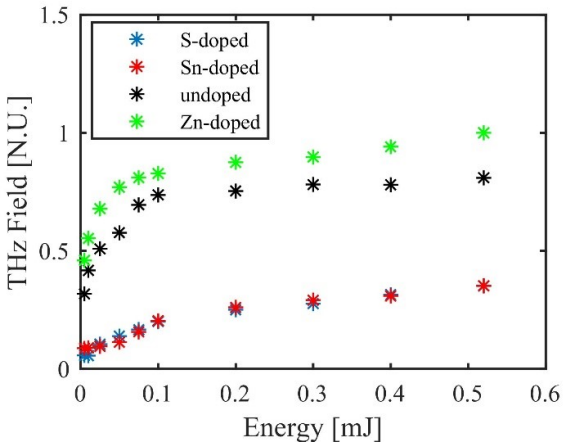

Figure 3.8: The peak THz field has been plotted for various excitation energies, for a number of different freestanding ⟨100⟩ InAs substrates, two n-type samples doped with Sn and S donors, one undoped sample and one p-type sample doped with Zn acceptors. The peak THz field has been normalised across all substrates with respect to the maximum field achieved with the Zn-doped InAs.

Although we cannot exclude contamination from carrier mediated generation, for the sake of completeness we recreated analogous cases of Figs. 3.4, 3.5, and 3.6 for the p-polarised emission (Figs. 3.8, 3.9, and 3.10 respectively) to highlight that the phenomenological trend is very similar. This is expected as the available literature concurs about the fact that at high energy OR is the dominant process.

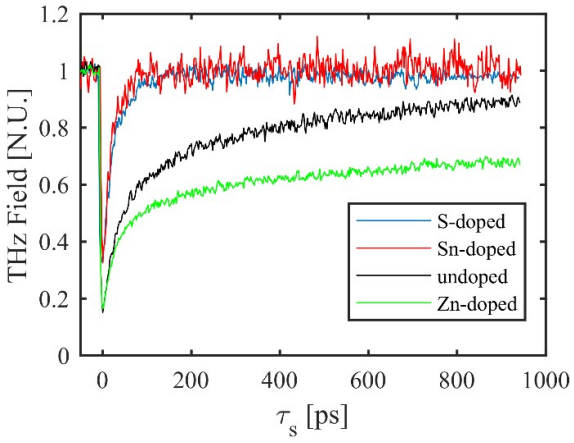

Figure 3.9: OPRE measurements of the peak THz field vs the screening pump delay for the four different freestanding ⟨100⟩ InAs substrates of table 3.1. Each curve is normalised with respect to the unscreened peak THz field. The energy and illumination conditions of both optical excitations are comparable to one of Fig. 3.5.

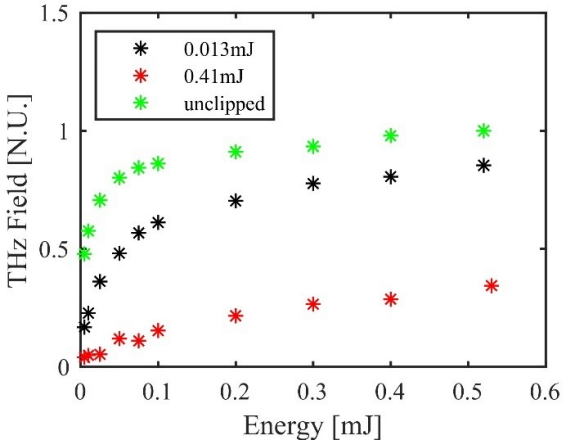

Figure 3.10: The peak THz field has been plotted against W_G, for a Zn-doped $\langle 100 \rangle$ p-InAs substrate, for various screening energies W_S fixed at $\tau_s = 0$. The peak THz field has been normalised across with respect to the maximum peak field generated by Zn-doped InAs.

3.5.2 Temporal smearing in the OPRE measurements

The angle between generating pump and screening pump induces a temporal smearing of the screening effect on the order of 3ps, because of the induced temporal mismatch of the wavefronts at the target surface.

To investigate possible artefacts induced by such a smearing, we performed an OPRE measurement detecting the s-polarisation for $\langle 111 \rangle$ undoped InAs while reducing the size of the THz generating pump to 1mm diameter and keeping the large screening pump. This corresponds to a maximum smearing estimated within the order of 600fs. As expected the screening transition appears steeper (the higher noise is induced by the lower THz field detected). However no other substantial differences are highlighted by the measurement.

To further reduce the temporal smearing to negligible scales we performed the OPRE measurement exploiting a highly focused THz generation. In order to keep a sufficiently high detected THz signal we performed the measurement using an ultrafast Ti:Sa oscillator (Coherent Chameleon Ultra II) that provides an ultrashort pulse train with 80MHz repetition rate, 140fs pulse duration and 4W average power at a centre wavelength of 800nm.

It is important to stress that to achieve sufficient screening fluences 2.2W were diverted to the screening pump and focused to a spot size of 0.7mm. This may result in two potential issues:

-(i) the first is common to all pump-and-probe measurements performed using a high-repetition rate source and it is due to the low temporal separation between two consecutive pulses. Because the observed relaxation time for InAs in our experimental condition is on the

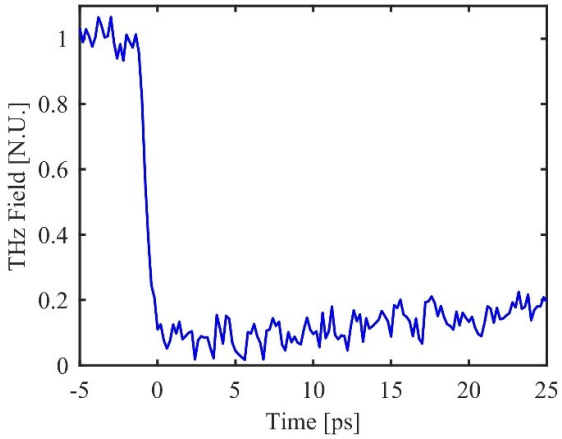

Figure 3.11: OPRE measurement of ⟨111⟩ InAs with a reduced impinging optical spot size of 1mm. The measurement was performed with a generating pump energy W_G of 0.1mJ and a screening pump energy W_S of 0.1mJ. The peak THz field has been normalised with respect to the average unscreened field.

scale of ns, the 12.5ns pulse period is not sufficiently large to ensure the complete decay of all the photo-excited carriers. This means the observed dynamics can in principle be affected by an accumulated screening observable even when the screening pulse impinges after the generation pulse.

-(ii) when the screening pump is focused the cross talk between generation and screening pump increases. Normally, in typical lock-in signal detection the generating pump is chopped to introduce an oscillating THz signal. Therefore, the photo carrier density injected by the generation also oscillates at the chopping frequency. Hence, the THz generated by the screening pump is chopped by the screening induced by the generating pump. If the screening pump is Gaussian with 0.7mm FWHM (our case), the resulting THz intensity profile has a FWHM on the order of 0.49mm because of the quadratic relation between pump and THz. The peak spectral efficiency for the InAs emission is usually at a frequency $f_{peak} = 0.7$THz ($\lambda_{peak} = 427\mu$m) or lower. At 0.7THz we can estimate a Gaussian beam divergence (half-angle) of about 18.6°. At this angle the field is still 36% of the maximum and a small fraction of the power is still contained on one side of the beam at larger angles (i.e. a relevant portion of the total field). This means that a good isolation requires very large angles between screening pump and generating pump and small numerical apertures of the THz collecting optics (which has the effect of reducing the detected signal). It is important also to consider that the emitted spectrum also contains much lower frequency components (typically down to 0.3THz).

There is also another factor that potentially increases the cross talk at any screening pump

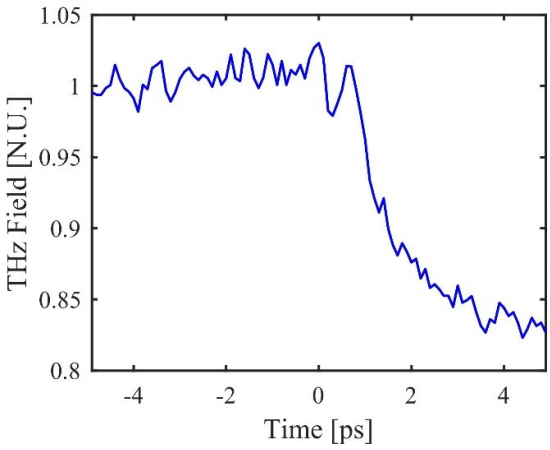

Figure 3.12: S-polarised OPRE traces of ⟨111⟩ InAs measured with a focused generation (20μm spot) the screening pump was focused to a spot size of 0.7mm. The measurements were performed with a generating pump energy W_G of 2nJ and a screening pump energy W_S of 27.5nJ. The screening pump impinged onto the sample at 10° to the normal.

size, which is due to the nature of the photocarrier induced modulation. The carrier modulation severely alters the THz emission profile of the screening pump, punching a hole in the THz profile of the typical dimension of the generating pump. Hence, the modulation potentially induces THz scattering at much larger angles, which becomes more visible as the generating pump becomes stronger.

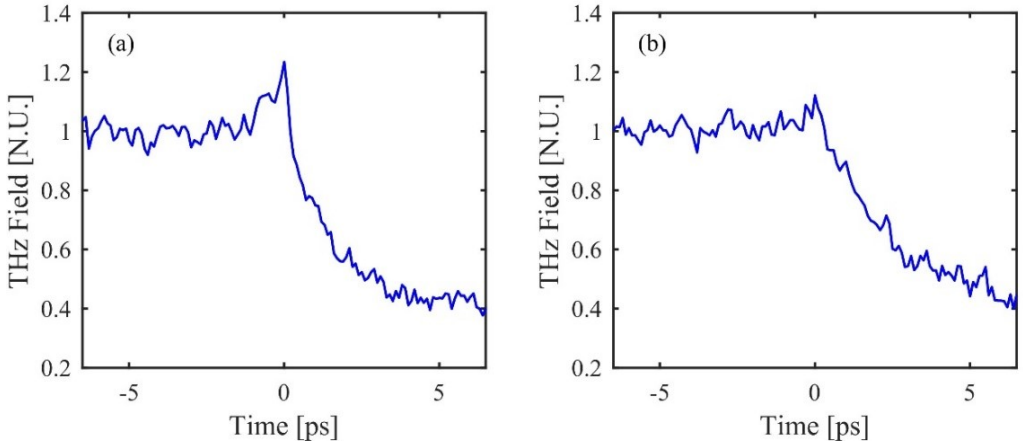

Figure 3.13: S-polarised OPRE traces of ⟨111⟩ InAs measured with a focused generation (20μm spot) the screening pump was focused to a spot size of 0.7mm. The measurements were performed with a generating pump energy W_G of 0.5nJ and a screening pump energy W_S of 27.5nJ. In (a) The screening pump impinged onto the sample at 10° to the normal. In (b) The screening pump impinged onto the sample $-70°$ from the normal.

For the data presented in Fig. 3.12, the screening pump impinges onto the sample at 10° to the normal (i.e. 35° between the two pump wavevectors) of the semiconductor surface, which results in a sub-100fs smearing. We can observe that there are no fundamental differences in the screening dynamics after excitation. However, a modulation in the detected s-polarised field is observed within the timescale of the THz generated by the screening pump at the overlap between the two pulses. For the sake of completeness, at lower generation pump energies the photocarrier modulation is less significant and manifests as an increase in the detected peak field before the main drop (shown in Fig. 3.13(a)), which could be consistent with the phenomenon investigated by Krotkus et al[154]. However, in our experimental conditions a contamination from the screening pump appears to have a major role as this feature significantly changes with the numerical aperture (NA) of the optics collecting the THz wave and with the screening pump angle. In fact, the oscillation at the edge of the slope in Fig. 3.12 resembles the field profile of the screening pump. It was also confirmed that this modulation remains present even when the generation pump precedes the screening pump by 3ps, by delaying the optical-sampling of the same amount, so it is synchronised with the screening pump and not with the generation pump (the THz-field related to the generation pump is very weak at that time section). Again, this appears to indicate that the feature arises from a contamination due to the focussed illumination geometry. In the plot in Fig. 3.13 the screening pump impinging angle was changed (to achieve better immunity from the screening pump) such that it counter propagates in the same quadrant of the THz wavevector, at $-70°$ from the InAs normal. The increased temporal smearing induced by the large angle is still well within the sub-ps scale. This configuration certainly reduces the average fluence, which appears to be the only determining factor in the observed decay dynamics, as verified at high energy with larger beams.

Chapter 4

Published Paper: All-Optical Two-Colour Terahertz Emission from Quasi-2D Nonlinear Surfaces

In the pursuit of creating highly efficient THz emitting surfaces, inspiration came from the generation of THz in air using the highly nonlinear ionised plasma [156]. In this extreme regime, a pulse is combined with its second harmonic within a very tightly confined and highly intense region in air. Initial descriptions of this process modelled it as a third order perturbative $\chi^{(3)}$ nonlinearity mixing the incident fields to produce a rectified THz field [157, 158] while the air provided a medium which is naturally phase matched. Further studies have revealed that a more accurate interpretation of the THz conversion is provided by the field ionisation and subsequent electron dynamics [159, 160]. At semiconductor surfaces however, under above bandgap excitation conditions, the $\chi^{(3)}$ is significantly high and relevant, as demonstrated by surface optical rectification. Therefore I considered the case where, instead of seeding the rectification with the surface field (which is now known to be heavily screened), we could seed the nonlinear product with the second harmonic of the pump field. In doing so, we would enhance the total emitted THz energy by surpassing the soft-saturation limits of SOR. Another important factor to note, is that the skin depth of 400nm light is significantly shorter than that of the fundamental (16nm as opposed to 140nm at a wavelength of 800nm). Therefore the interaction region is highly subwavelength and is in principle free from any phase matching limitations of bulk nonlinear processes.

In this work I initially designed and carried out the experimental campaign. I then worked to describe the subwavelength physical process and its interpretation in the data. Including the

analysis of the saturation results, separating the contributions of the standard SOR process from our two-colour scheme. Lastly I made significant contributions to the writing of the whole text prior to submission. The article was submitted to PRL on 2^{nd} September 2020 and published on 21^{st} December 2020.

4.1 Enhancing the THz Conversion Efficiency

Prior to introducing this novel application of two-colour THz generation, it is also important to note other means by which one might enhance the nonlinear optical-THz conversion, without arbitrarily increasing the optical pump power up until the damaging threshold of the semiconductor. With the third-order nonlinearity there is therefore two main approaches, the first would be to modify the surface states to increase the surface field and the second would be to bypass the surface field entirely. The latter becomes a focal point of this chapter but there are still interesting physics associated with the former that should be considered. There have, in fact, been investigations where such an idea has been exploited to enhance the surface field in Silicon by electrically biasing the surface, assessed via the induced THz emission of the Si surface [102]. A more passive increase to the surface field is preferred however, and can be achieved by scalable deposition processes involving novel 2D materials with remarkable electronic properties, graphene being a highly promising candidate [161, 162]. The extreme interest in graphene has resulted in many exfoliation and deposition techniques being developed with scalability in mind. Therefore, it was proposed that we exploit liquid phase exfoliated [163] (LPE) graphene deposited on InAs via a Langmuir-Schaefer approach [164] in order to fundamentally enhance the surface field and thus the emitted THz energy. Interestingly, 2D-materials have also been proposed as potential THz sources: where rectified THz pulses have been observed in graphene [165] and several layered transition-metal dichalcogenides [166, 167], mediated by plasmonic photocurrents and optical rectification.

Graphene-on-semiconductor based devices however, have already been extensively studied for their rectifying behavior, fuelling a large amount of experimental work on graphene Schottky junction diodes [168, 169]. A key factor in the passive increase of the surface field at any interface is related to the alignment of the Fermi levels across the interface, where inter-facial charge transfer must occur to accomplish this. For a Graphene-InAs interface therefore, due to the fact that the Fermi energy of graphene is higher than that of InAs, an electron charge transfer towards the InAs bulk is induced. The net effect is an enrichment of the surface charge density and an additional built-in potential difference between the graphene surface and the

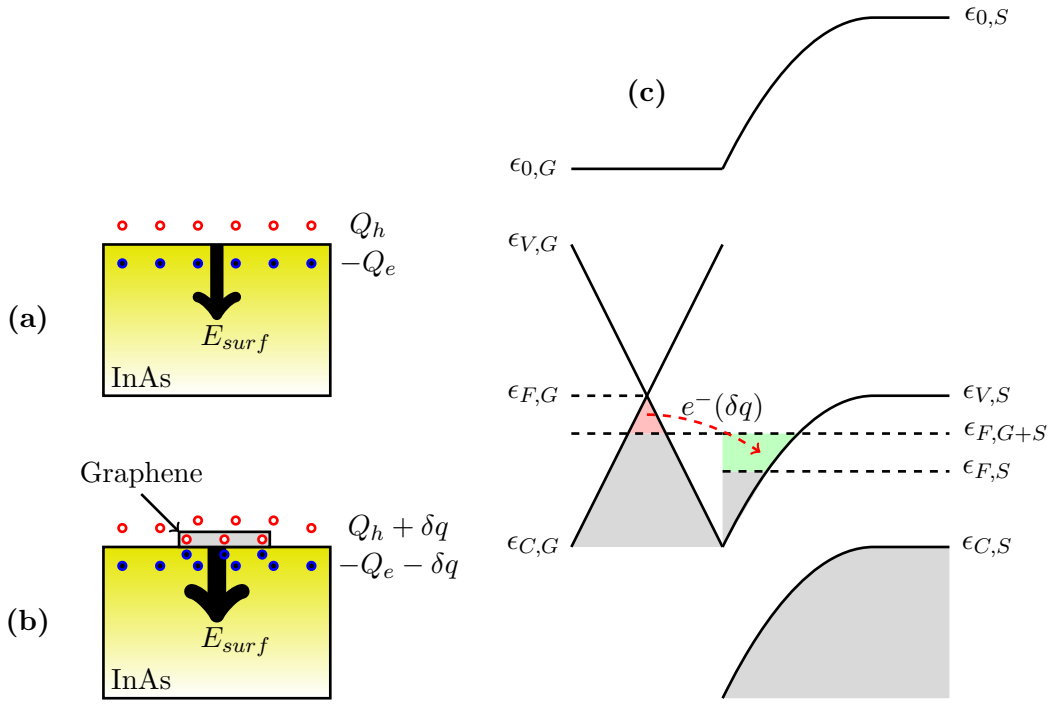

Figure 4.1: Sketch of the Graphene-InAs Schottky junction. (a) Shows the bare InAs surface, where a surface density of positive charges Q_h (white and red) forms a static DC field E_{surf} in proximity to the surface holding a 2D distribution of negative electrons Q_e (black and blue). (b) Shows the effect of graphene deposition on the surface, where electrons are transferred into the substrate, contributing to an additional positive charge δq on the surface, enhancing the localised potential at the flake position. (c) Shows the band structure of the junction after charge transfer due to the Fermi level alignment (from $\epsilon_{F,G}$ and $\epsilon_{F,S}$ individually to $\epsilon_{F,G+S}$).

InAs bulk given by

$$V_b = \frac{1}{e}(\epsilon_{F,G} - \epsilon_{F,S}) \tag{4.1}$$

where $\epsilon_{F,G}$ and $\epsilon_{F,S}$ represent the Fermi energy of the graphene and semiconductor prior to electronic contact respectively. This potential V_b is additive to the intrinsic surface potential and contributes its own electric field oriented from the positive surface towards the negative depletion region, thus enhancing the intrinsic surface field at the interface which would thus be given by

$$E^{\text{tot}}_{\text{surf}}\hat{\mathbf{z}} = E^{(0)}_{\text{surf}}\hat{\mathbf{z}} + \nabla V_b, \tag{4.2}$$

where $E^{(0)}_{\text{surf}}$ is the initial, vacuum-InAs surface field [169]. This then feeds into equation 3.1 to result in local increases to the radiated THz field wherever Graphene is deposited on the surface.

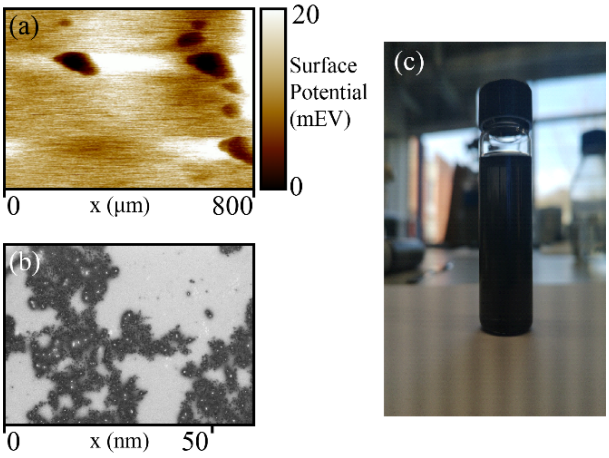

Figure 4.2: (a) Kelvin probe Force Micrograph of the individual graphene platelets. (b) Scanning electron micrograph of a graphene flake coated surface. (c) Image of prepared graphite powder in NMP solution.

The graphene platelets were prepared via liquid phase deposition of graphite powder in N Methyl-Pyrrolidone (NMP) solution [163, 170], as depicted in Fig. 4.2, and deposited onto the $\langle 100 \rangle$ InAs surface using a Langmuir-Schaefer approach [164].

By varying the surface density of graphene on the substrates, evaluated via SEM images. I took the bare InAs surface as a reference, and defined a relative coverage density parameter RD as normalized to the lowest coverage in our sample set (roughly corresponding to a visible 1.16% of area coverage). Fig. 4.3 shows the THz TDS of the samples. At $RD = 1.5$ the peak field enhancement is on the order of 26.6%, which corresponds to a 60.3% increase in emitted

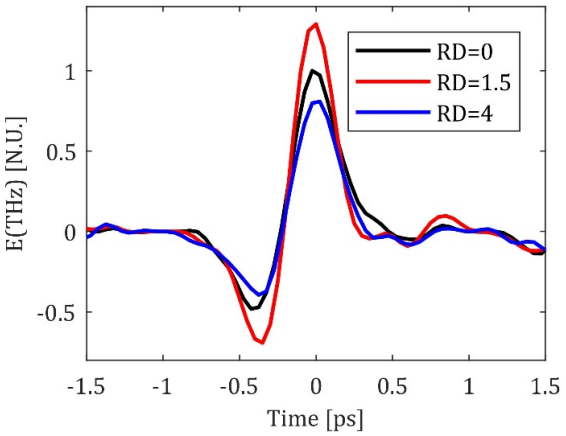

Figure 4.3: THz-TDS scans of an undoped $5 \times 5 \times 0.5$mm $\langle 100 \rangle$ InAs along with TDS scans of samples with relative coverage density of 1.5 and 4.0. All three TDS scans are normalized to the maximum peak of the bare InAs sample.

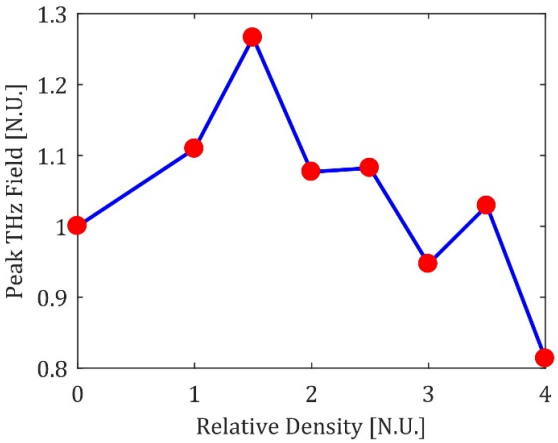

Figure 4.4: The emitted peak THz field as a function of the relative graphene coverage density. The figure is normalized to the maximum peak field of the bare InAs sample.

THz power, and demonstrates that graphene has indeed enhanced the emitted THz field as expected. Notably, the sample with $RD = 4$ actually exhibited a reduction in the radiated THz field, suggesting that as the graphene platelets percolate across the surface, the screening and absorption of the interacting fields becomes more relevant [171]. From another point of view therefore, SOR is actually assessing the ratio between area coverage and percolation, this holds a number of potential applications in process control of the deposition.

For completeness, an overall assessment of the peak THz field obtained for different RD is presented in Fig. 4.4, where a clear peak around $RD = 1.5$ can be observed. Therefore demonstrating that although these measurements are highly promising, there are limits to the enhancement and so I begun to consider other all-optical means to bypass the surface field instead, which is presented as a published article later in this chapter.

4.2 THz Emission from Laser-Induced Plasma

When approaching a scheme for all-optical THz generation at semiconductor surfaces, it is critical to consider how rectified near-DC frequency photons can be created from a combination of fundamental photons at frequency ω. For a $\chi^{(2)}$ process such as OR (as described in chapter 1.1.1), this is trivial as the difference frequency between two photons within the same ultrashort pulse achieves this as [27, 28, 9]

$$\omega_{\mathrm{THz}} \approx 0_{\mathrm{THz}} = \omega - \omega. \tag{4.3}$$

As has previously been discussed in chapters 2 and 3 however, the primary source of THz radiation at semiconductor surfaces is in fact due to the large resonant $\chi^{(3)}$ response, where the

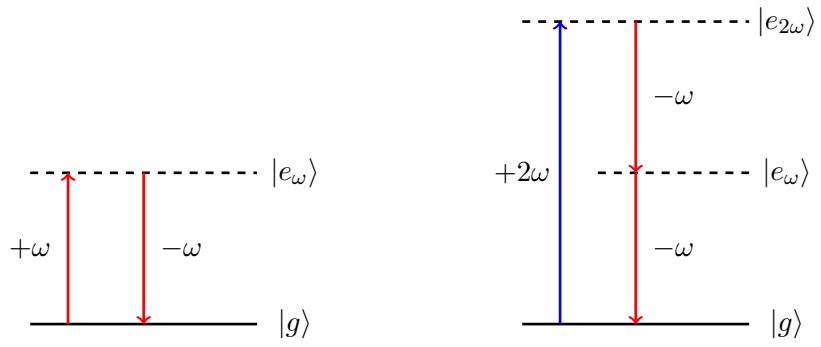

(a) $\chi^{(2)}$-driven energy levels.

(b) $\chi^{(3)}$-driven energy levels.

Figure 4.5: The electronic energy level diagrams displaying how the different combinations of photons can sum to 0_{THz} via transitions between virtual energy levels.

frequency difference is supplemented by the DC surface field, i.e. $\omega_{\mathrm{THz}} \approx 0_{THz} = 0_{DC} + \omega - \omega$ [110, 109]. When moving to the all-optical scheme however, the nonlinearity must be seeded by the second harmonic field at 2ω as

$$\omega_{\mathrm{THz}} \approx 0_{\mathrm{THz}} = 2\omega - \omega - \omega. \tag{4.4}$$

A schematic representation of these processes is shown in figure 4.5.

This scheme is entirely analogous to the generation of THz radiation from a laser-induced plasma in air [172, 173, 156]. In the seminal work on THz plasma generation, it was in fact described exactly this way in terms of a perturbative $\chi^{(3)}$ nonlinear mixing of photons represented in figure 4.5b and modelled by equation 4.5 [174]. Although this theoretical model was in fact later replaced by non-perturbative mechanisms involving the electron trajectories in the free-electron plasma [175], the scheme can still be applied to solid-state semiconducting materials and the plasma generation used to characterise the experimental setup is shown in figure 4.7. By tightly focusing the intense fundamental ultrashort optical pulse with its second harmonic in air, a highly nonlinear air-plasma is formed and the radiated THz photons are critically dependent on the temporal overlap between the two optical pulses. To characterise and determine the $\tau_{CP} = 0$ point (made non-trivial by the required subsequent optics), the birefringent calcite plate in the setup was rotated while observing the THz radiated from the laser-induced air-plasma. The peak THz pulse (shown in figure 4.6) detected in this way corresponds therefore to the orientation of the calcite plate for perfect temporal overlap which could then be applied to the two-colour generation at the InAs surface which will be explored in the following sections.

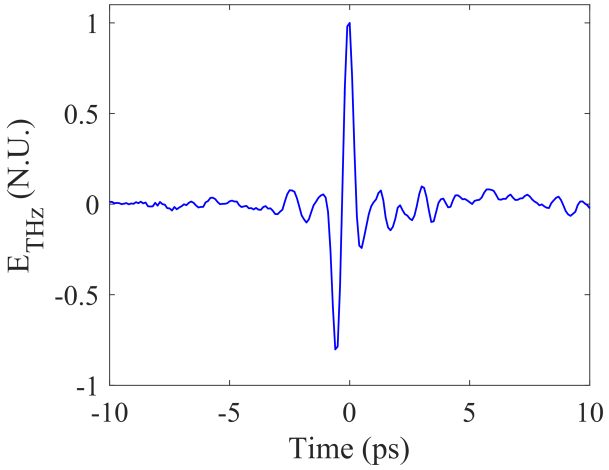

Figure 4.6: The THz field generated via laser-induced air plasma excited by two-colour fields.

4.3 Summary

The presented article therefore, is a thorough investigation of the coherent generation of THz radiation from narrow-bandgap semiconductor surfaces exploiting two-colour, deeply above-bandgap illumination. This process we denoted as All Optical Surface Optical Rectification (AO-SOR) described by:

$$\mathbf{P}_{\mathrm{THz}} = \chi^{(3)}(\omega_{\mathrm{THz}} : 2\omega; -\omega; -\omega) : \mathbf{E}_{2\omega}(t) : \mathbf{E}^{*}_{\omega}(t) : \mathbf{E}^{*}_{\omega}(t), \tag{4.5}$$

where $\mathbf{E}_{\omega}(t)$ is the fundamental electric field of the optical pulse and $\mathbf{E}_{2\omega}(t)$ is its second harmonic. To observe this emission the fundamental field was first converted into second harmonic via type I phase matching in a β-BBO crystal cut for SHG at 800nm. Furthermore, by introducing a birefringent calcite plate after this, the phase delay between the fundamental and second harmonic fields could be controlled and a beating between them was expected at the SH frequency. From this beating it is then possible to isolate the contributions from both SOR and AO-SOR, demonstrating the shorter THz pulse duration and thus enhanced bandwidth due to the thinner interaction region of AO-SOR. The article then demonstrates the high-energy behaviour of the emission, where again by separating the contributions it can be demonstrated that the SOR component displays the same expected soft-saturating trend while the AO-SOR component increases quadratically with the square of the pump energy, as expected by considering $\mathbf{E}_{2\omega} \propto \mathbf{E}^{2}_{\omega}$. Lastly, a quantitative estimate for the $\chi^{(3)}$ nonlinearity can be made by considering the dependence on the AO-SOR component from the crystal orientation, which has a strong 4-fold symmetry when detecting the s-polarised THz field and illuminating with

p-polarised optical fields

$$E_{s,\mathrm{THz}} \propto E_{p,2\omega} E_{p,\omega}^2 (\chi_{iiii}^{(3)} - 2\chi_{iijj}^{(3)} - \chi_{ijji}^{(3)}) sin(4\phi), \tag{4.6}$$

where ϕ is the crystal orientation angle measured from the 100 crystal axis. This resulted in an estimation of the nonlinear susceptibility of $\chi^{(3)} \approx 9 \times 10^{-21} \frac{m^2}{V^2}$.

4.4 Impact

This publication targeted the highly prestigious journal Physical Review Letters, which has a 5-year impact factor of 9.227 and a very broad scope covering all areas of science.

4.5 Journal Article

4.5.1 Abstract

Two-color terahertz (THz) generation is a field-matter process combining an optical pulse and its second-harmonic. Its application in condensed matter is challenged by the lack of phase-matching among multiple interacting fields. Here, we demonstrate phase-matching-free two-color THz conversion in condensed matter by introducing a highly-resonant absorptive system. The generation is driven by a third-order nonlinear interaction localized at the surface of a narrow-bandgap semiconductor, and depends directly on the relative phase between the two colors. We show how to isolate the third-order effect among other competitive THz-emitting surface mechanisms, exposing the general features of the two-color process.

4.5.2 Main Text

The nonlinear generation of broadband terahertz (THz) fields from ultrafast optical pulses is a subject of great interest for fundamental research and disruptive applications in imaging, spectroscopy and the design of materials and devices [176, 177, 178, 179, 180, 181, 182, 183, 184, 185, 186, 187]. Current research focuses on identifying new materials and generation mechanisms to boost the efficiency and versatility of nonlinear THz sources, as in the case of organic crystals [188, 189], spintronic substrates [190], and tunable gas lasers [191]. Second-order optical rectification (OR) in non-centrosymmetric $\chi^{(2)}$ bulk crystals, such as ZnTe or $LiNbO_3$ [130, 143] has been at the core of bright THz source development for many years. The stringent requirement to maintain the longitudinal phase-matching condition among the interacting fields across a wide optical bandwidth, strongly limits both the laser sources and nonlinear materials. This is achieved via sophisticated settings, and it is certainly a growing challenge when synchronous

propagation of multiple fields is required, as in the case of third-order phenomena. A promising alternative is provided by new types of emitters based on thermally-induced spin-current transients, capable of high-conversion efficiency over short propagation distances [188], as in the case of ultra-thin spintronic substrates [190, 192, 193]. In this context, specific classes of narrow-bandgap semiconductor surfaces have emerged as remarkably efficient surface THz sources, under ultrafast (typically 100fs-class pulses) illumination. Indium Arsenide (InAs), in particular, provides exceptionally high conversion efficiencies per unit length and stands as one of the standard benchmarks for surface nonlinear THz generation [137]. While at lower fluences ($< 100\text{nJ/cm}^2$), InAs sources are mostly driven by carrier diffusion dynamics [104], in the high-pump regime ($>10\mu\text{J/cm}^2$) their emission is dominated by DC-biased Surface Optical Rectification (DC-SOR) [128, 90, 194]. Similarly to second-harmonic generation from centrosymmetric surfaces [195], in DC-SOR the optical pump interacts with a symmetry-broken medium provided by the surface depletion field E_{surf} of the semiconductor, which leads to an effective quadratic

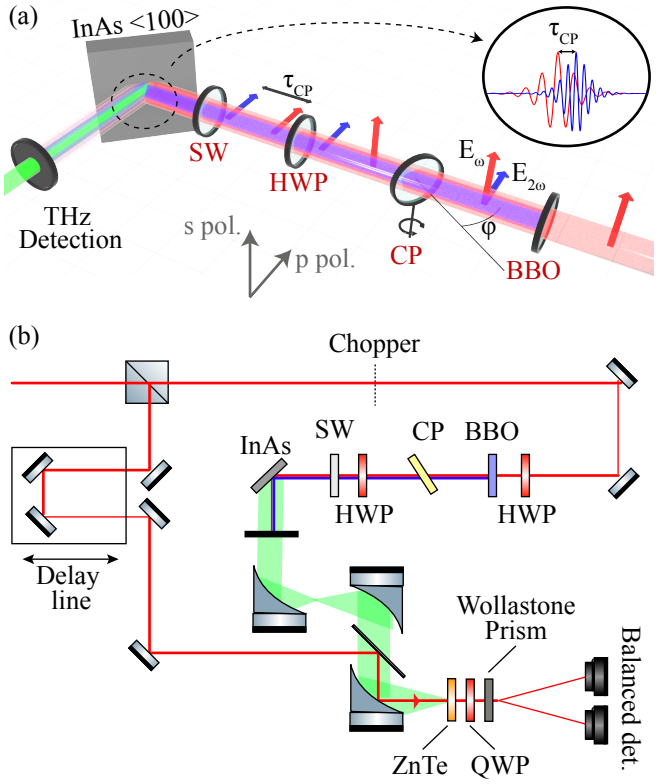

Figure 4.7: Experimental setup. (a) The red, blue and green beams denote the 800nm, 400nm and THz beam paths, respectively. The inset displays the role played by the phase delay. (b) A schematic of the whole setup. HWP: Half-wave plate, BBO: Barium Borate crystal, CP: Calcite plate, SW: UV fused silica window, QWP: Quarter-wave plate, ZnTe: Zinc Telluride.

response in the proximity of the surface [110]. Due to the neutralisation of the surface depletion field from excited photo-carriers, however, the emission from DC-SOR typically saturates at high pumping fluences [137, 109]. This saturation, however, does not directly affect the third-order $\chi^{(3)}$ nonlinearity, which can be exploited to generate THz radiation by mixing an optical pulse with its second-harmonic through a process known as two-colour OR:

$$E_{\mathrm{THz}}(t) \propto \chi^{(3)}(\Omega, 2\omega, -\omega, -\omega) E_{2\omega}(t) E^{*}_{\omega}(t) E^{*}_{\omega}(t), \tag{4.7}$$

where $E_{\omega}(t)$ and $E_{2\omega}(t)$ are the electric fields of the optical and second-harmonic pulses, and * denotes complex conjugate.

The key signature of this interaction is the dependence of the THz amplitude from the mutual phase and frequencies of the interacting fields [196, 197], a degree of control generally not attainable in $\chi^{(2)}$-based THz sources. Two-color generation has been extensively exploited in laser-induced gas plasmas, leading to the demonstration of THz sources with record-breaking bandwidths [173, 198, 199, 172, 200, 201, 202, 203]. In these systems, the role of the four-wave-mixing is negligible, as demonstrated by [175], whereas the THz emission is rather the result of highly non-perturbative mechanisms. Two-color excitation also plays a key role in the injection and coherent control of ultrafast ballistic currents in bulk semiconductors [204, 205, 206, 207]. In these experiments, the interference between two quantum pathways, single-photon absorption at 2ω and two-photon absorption at ω, leads to the ultrafast injection of directional currents, acting as a THz source [205, 208, 209]. Quantum interference is mediated by a below-bandgap optical illumination seeding the two-photon absorption process ($\hbar\omega < E_g < 2\hbar\omega$, where E_g is the semiconductor bandgap). However, in the presence of highly above-bandgap illumination in narrow-bandgap semiconductors, ($E_g < \hbar\omega$), the direct one-photon absorption is the dominant mechanism, effectively reducing the number of photons available for multi-photon nonlinear current injection processes. [209]. A central challenge in implementing Eq.(4.7) is in keeping synchronous interactions among all the interacting fields, a condition practically out-of-reach in bulk condensed matter.

In this Letter, we demonstrate, for the first time, two-color optical rectification at an air-InAs interface via a highly-resonant above-bandgap excitation, a process we denote as All-Optical Surface Optical Rectification (AO-SOR) to distinguish it from the DC-SOR. The strong absorbing regime is responsible for the very high effective $\chi^{(3)}$ nonlinearity and results in a deeply sub-wavelength penetration depth that localizes the interaction within a quasi-2D surface (in the scale of 25 atomic layers). The dimensionally-reduced interaction length allows the relaxation of typical phase-matching constraints found in bulks. It also affects the dynamics of competitive surface mechanisms, e.g. the photo-carriers-driven screening, on the emission.

Figure 4.7 illustrates our experimental setup comprising a fundamental (FH) excitation beam

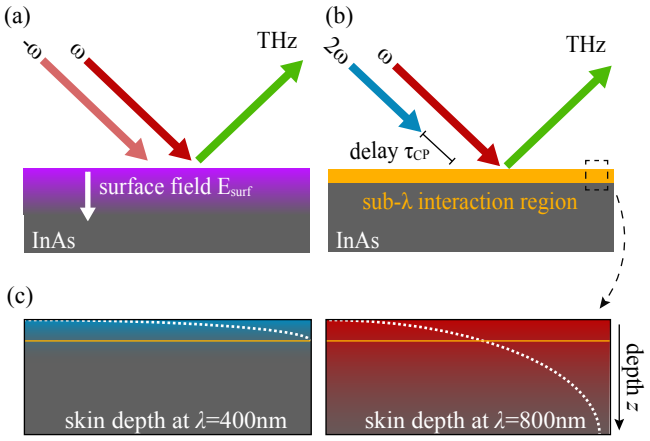

Figure 4.8: THz emission from (a) DC-SOR, and (b) AO-SOR. In (c), the interaction region (yellow line) is compared to the skin-depth of the interacting fields, λ =400nm and λ =800nm respectively.

(λ = 800nm, 100fs, 1kHz, $\sim$ 1.0mJ, red beam) co-propagating with its second-harmonic (SH) signal (λ = 400nm, $\sim$ 35.4μJ, blue beam). The cross-polarised SH pulse at 400nm was generated via type-I process (oo-e) in a 0.1mm thick β-Barium Borate (BBO) crystal. A birefringent calcite plate (CP)[1] introduced a tunable phase delay $\tau_{CP}(\phi)$ between the two cross-polarized fields. Specifically, the phase delay is due to the difference in optical path length between the ordinary wave at ω and the extraordinary wave at 2ω [210]. A second half-wave plate at 800nm rotated the polarisation of the fundamental field, resulting in the two pumps being co-polarised. As a nonlinear surface, we exploited an undoped $\langle 100 \rangle$ InAs substrate. The pumps illuminated the surface at 45° respect to its normal. The THz signal was collected along the specular reflection direction (green beam) through a standard Time-Domain Spectroscopy (TDS) setup, implemented via a nonlinear $\langle 110 \rangle$ ZnTe crystal [1]. In this configuration, the generated THz field consists of three major contributions:

$$\begin{aligned} E_{\mathrm{THz}}(t) \propto \chi^{(3)} E_\omega(t) E_\omega^*(t) E_{\mathrm{surf}} \\ + \chi^{(3)} E_{2\omega}(t-\tau_{CP}) E_{2\omega}^*(t-\tau_{CP}) E_{\mathrm{surf}} \\ + \chi^{(3)} E_{2\omega}(t-\tau_{CP}) E_\omega^*(t) E_\omega^*(t) \cos(2\omega\tau_{CP}). \end{aligned} \quad (4.8)$$

The first two terms account for separate DC-SOR contributions from the fundamental E_ω and second-harmonic $E_{2\omega}$ fields (Fig. 4.8a). The third term, conversely, represents the AO-SOR mechanism under investigation, where fundamental and SH fields interact through the third-order $\chi^{(3)}$ process from Eq. (4.7) (Fig. 4.8b), where τ_{CP} is the delay between E_ω and $E_{2\omega}$.

[1] EKSMA BBAR@800+400 nm-310-450 fsec

We neglected any term arising from carrier dynamics as they are highly saturated at the considered fluences [137, 109]. Both DC-SOR and AO-SOR are localised within the sub-wavelength

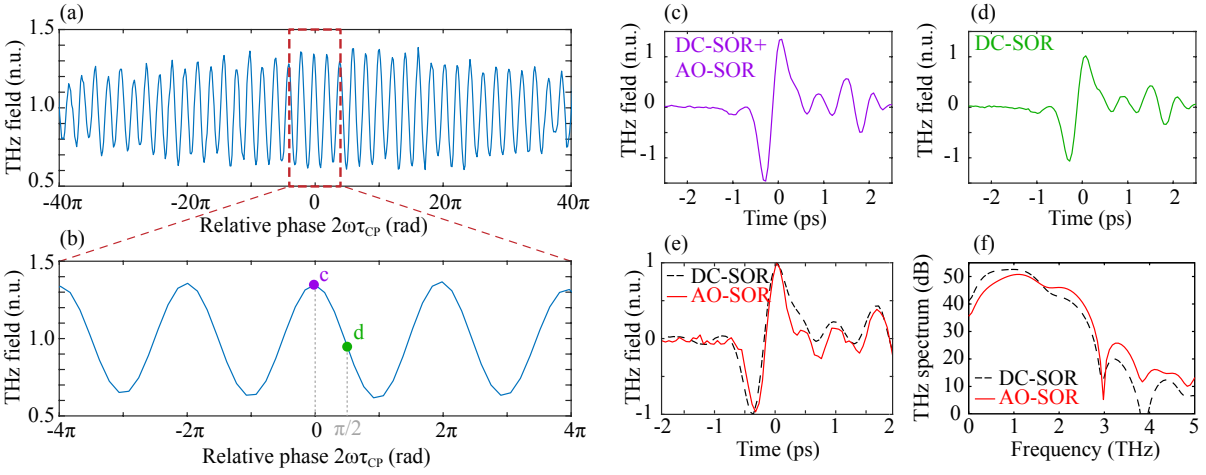

Figure 4.9: (a,b) Peak THz emitted field as a function of the phase delay τ_{CP}. In both plots, the THz field has been normalised with respect to the DC-SOR contribution. (c, d) Detected THz pulse for $\tau_{CP} = 0$ and $\tau_{CP} = \pi/4\omega$ respectively. In both cases, we considered p-polarised excitation and detection. (e, f) Comparison of the pulse temporal and spectral amplitudes obtained by AO-SOR (red line) and DC-SOR (black dashed line), respectively. In these experiments, the incident pump energy was 1.2mJ

region defined by the short skin depth of the incident optical fields (approximately 140nm at $\lambda_\omega = 800$nm and 16nm at $\lambda_{2\omega} = 400$nm) [112]. In this condition, longitudinal phase-matching does not play a significant role in the emission (Fig. 4.8c). The delay τ_{CP} is controlled by rotating the calcite plate [210], and it affects only the amplitude of the all-optical process. By holding the TDS delay in the position of maximum field detected, a change of τ_{CP} produces a beating pattern of period $1/(2f) = \pi/\omega$ (Fig. 4.9(a-b)), as predicted by Eq. (4.8). When $\tau_{CP} = 0$, all the sources components are in phase, resulting in a peak in the emission. Interestingly, in this case, the emitted THz field is enhanced by a factor of ≈40% (96% in power) (Fig. 4.9c) when considering an incident pump energy of 1.2mJ. When $\tau_{CP} = \pi/4\omega$, conversely, the AO-SOR component is suppressed, and we can isolate the DC-SOR contribution (Fig. 4.9d). By subtracting the two signals, we can thus determine the THz field generated solely by AO-SOR. As illustrated in Fig. 4.9(e,f), the THz pulse generated by AO-SOR is shorter in time and broader in spectrum than that from DC-SOR. In the range 2-2.5THz the AO-SOR power spectral density is 3.5-4dB above the corresponding spectrum for the DC-SOR. It is worth noting that our current ZnTe-based detection limits the appreciable bandwidth creating a slope in the spectrum as the frequency approaches 3THz. This limitation, however, could be removed

by employing different nonlinear detection crystals operating at different wavelengths, such as GaP [211], or an air-ABCD detection scheme [212]. We obtained further insights on the AO-

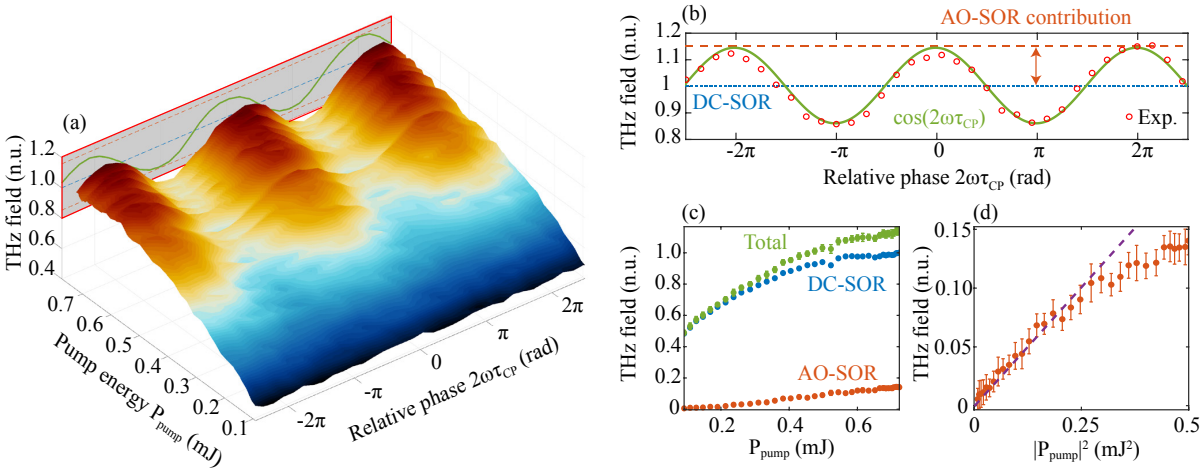

Figure 4.10: (a,b) THz peak emission as a function of the phase delay τ_{CP} and the pump energy P_ω. For each pump energy, we extracted the SOR contribution (panel b, blue line), corresponding to the centre value, and the AO-SOR contribution (orange line), corresponding to the beating amplitude. For each pump value, we extracted these values by fitting the experimental data (red circles) (c) Total emission and DC-SOR contribution as a function of the pump power, highlighting the soft saturation at high pump energies characteristic of the DC-SOR emission mechanism. (d) AO-SOR emission as a function of $|P_{pump}|^2$. The dashed line highlights the fitted ideal quartic dependence

SOR emission mechanism by measuring the emitted THz field as a function of the incident optical power, as summarised in Fig. 4.10. To this end, we measured the peak THz field as a function of τ_{CP} and the incident pump energy (Fig. 4.10(a)). As shown in fig. 4.10(b), for each value of the pumping power we can employ the interference signal (green line) to isolate the DC-SOR contribution (mean value of the oscillation, dashed blue line) from the cosine-like AO-SOR contribution (amplitude of the interference oscillations, dashed orange line). For each pump energy, we extracted the individual contributions by fitting the experimental data (red circles). The analysis of these contributions is particularly useful to discriminate the saturation dynamics of the two competing mechanisms, as illustrated in Fig. 4.9(c). The DC-SOR contribution (blue dots) shows an initial linear trend at lower energies, followed by a soft saturation profile characteristic of the field-induced DC-SOR [109, 137]. The AO-SOR, conversely, does not show any appreciable saturation effect at the high fluences of our experiment, as the mechanism is not affected by the screening of the semiconductor surface field. Note that direct THz photo-carriers screening tends to be also negligible due to the extremely short skin-depth of the

second harmonic that defines the interaction region. This result is illustrated in Fig. 4.10(d): by extracting the AO-SOR field contribution, we observe how it increases quadratically with the square of the input optical energy ($P^2_{\text{pump}} \propto |E_\omega|^4$, Fig. 4.10(d)) as dictated by Eq.(4.7) in the presence of a second-harmonic field of the form $E_{2\omega} \propto E^2_\omega$.

Quite interestingly, we were able to observe the onset of a sub-quartic trend for high pump energies. Main contributors to this effect are potentially the self-phase and cross-phase modulation in the BBO crystal, which can induce a change of the nonlinear product at the InAs surface by slightly detuning the fundamental and SH waves at high pump rates. Further insights on the AO-SOR process can be obtained by observing the THz emission dependence from crystal rotation. To this end, we analytically calculated such a dependence by generalising the full-vector approach described in [213, 214, 215]. We derived a set of nonlinear Fresnel reflection coefficients for the p and s polarisation components by matching the incident fields with the nonlinear polarisation field P_{NL} generating the THz field. Following the standard approach outlined in Ref. [8], we obtained the THz field generated in reflection by matching P_{NL} with a wave reflected at the air-InAs interface. Our calculations show that the crystal orientation affects each generation mechanism differently. A particularly relevant case involves the s-polarised THz field generated by a $\langle 100 \rangle$ InAs by p-polarised pumps. In this configuration, the standard DC-SOR is suppressed by the symmetry properties of the nonlinear tensor $\chi^{(3)}$ [109, 128]. The two-colour THz emission, on the contrary, reads as follows:

$$E_{p,s} = \frac{3}{4}\Omega L_{\text{eff}} A_s f_c^2 f_{2c} t_p^2 t_{2p} \times \sin(4\phi) \left[\chi_{iiii} - 2\chi_{iijj} - \chi_{ijji}\right] E_{2\omega)} E_\omega^2 \tag{4.9}$$

where ϕ is the crystal orientation angle measured from the 100 axis, and χ_{iiii},χ_{iijj} and χ_{ijji} are the three independent components of the tensor $\chi^{(3)}$. To ease a direct comparison with the DC-SOR case, all the other quantities in Eq. (4.9) are identical to those in [109]. Our experiments captured the four-fold symmetry predicted by Eq. (4.9), as illustrated in Fig. 4.11. These results confirm that the AO-SOR emission originates from the nonlinear susceptibility tensor of InAs. Interestingly, Eq. (4.9) allows us to also estimate the value of the nonlinear susceptibility $\chi^{(3)}$ for the AO-SOR process in InAs as $\chi^{(3)} \approx 9 \times 10^{-21} m^2/V^2$.

In conclusion, we provide here the first experimental demonstration of phase-matching free, two-colour THz generation in condensed matter. This process, which is not observed in bulk crystals, occurs in highly absorptive systems within a subwavelength interaction region dictated by the skin depth of the SH field ($\sim$ 16nm at λ = 400nm). The reduced interaction length acts as a quasi-2D structure and ensures that the optical-to-THz conversion is unaffected by longitudinal phase mismatch between the interacting waves. We predict that this approach could be ideal for the generation of THz waves with large frequency detuning between the

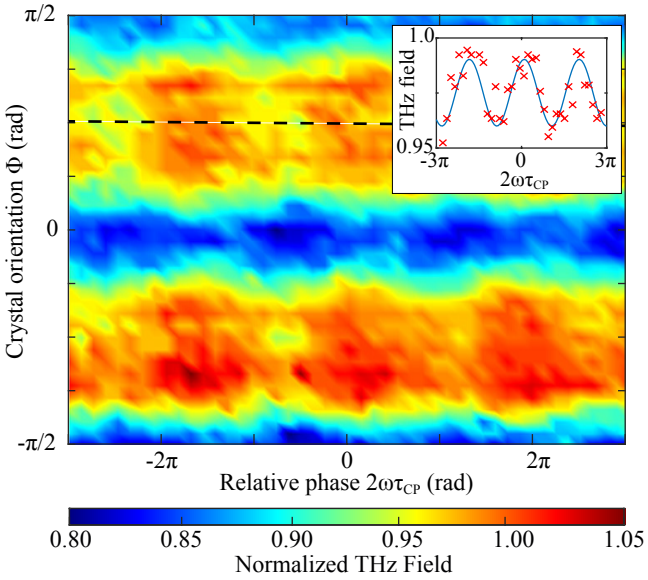

Figure 4.11: AO-SOR THz emission as a function of the crystal orientation angle (φ) and the mutual delay τ_{CP}. As predicted by analytical theory, the emission is characterised by a four-fold symmetry which descends from the symmetry properties of the nonlinear susceptibility $\chi^{(3)}$ of InAs. (inset) Peak-field trace as a function of $2\omega\tau_{CP}$ for $\phi = \pi/4$ (dashed line).

two-colour excitations, opening to the realisation of non-zero-frequency-carrier THz parametric amplification. Our results also suggest that AO-SOR can significantly outperform DC-SOR for the same total input pump power. Indeed, in our experiments, a minor amount of SH contribution (about 3.5% in Fig. 4.9) produces a macroscopic enhancement of the optical to THz conversion from InAs. If we denote as α the total fractional power of the second-harmonic generated from the 800nm pump, the THz fields increase as $E_{\mathrm{THz}} \propto (1-\alpha)\sqrt{\alpha}$. Such a function has a very steep gradient around $\alpha \approx 3.5\%$ and peaks at about $\alpha \approx 33\%$. Although this consideration does not account for the losses, it indicates that this process yields a much higher net efficiency when compared to standard benchmark surface emitters. We believe that our proof-of-concept results could seed new developments in the implementation of ultra-thin THz emitters for, e.g., near field imaging applications and integrated nanophotonic devices, in which traditional nonlinear crystals cannot be scaled to the same size without reducing to unpractical levels the optical-THz conversion efficiency [186, 187, 216]. In addition, the lack of any observable physical saturation mechanisms typically related to photo-carrier mediated screening of the surface field in DC-SOR, strongly suggests that the conversion limit of AO-SOR is set by mechanisms that become relevant only close to the damage threshold of the substrate.

Chapter 5

Accepted Paper: Terahertz Emission from Ultrafast Temporal Metamaterials

In my investigations of using pump-probe methodologies on THz emitting surfaces, I considered one fundamental idea which can exploit the low frequency of THz waves. That being that it is simple to achieve an transition in a material's dielectric function which is in fact much shorter than the THz period. The physics of sub-period excitations had previously been quite thoroughly explored theoretically and can give rise to exotic nonlinear responses such as time refraction and photon acceleration [74, 75, 76]. Experimentally however, when exploiting typical optical responses, achieving a sub-period excitation is quite unreasonable. Therefore many of these effects have been studied with regard to the instantaneous flash ionization of gases in optical cavities, giving rise to these complex nonlinear responses [77]. Little work therefore had been conducted to observe any time-dependent nonlinearities in the THz range where not only is it possible to excite a sub-period transition but a field-resolved detection enables the exact measurement of phase effects. In the work on OPTP, it would be expected to observe some of these effects, however in practice the material properties at optics and THz are very different, resulting in very little overlap between the time-varying medium and the THz fields. A recent study has shown that it is possible to observe THz shockwaves, a cutting of the field profile in time caused by an extremely sub-period (8fs) pulse [78]. It is thus interesting to exploit the OPRE scheme I previously developed to excite a sub-period transition directly on the THz source, in this case choosing Black Silicon (B-Si) as the source in question. B-Si is a random assortment of Si nanopillars which acts to trap $> 96\%$ of impinging light [217]. It was chosen

both because of this highly enhanced absorption (hence a greater dielectric transition), but also due to it's ability to emit THz radiation when excited by ultrashort pulses [218], making the random metasurface ideal for this investigation.

In this work my role was to conduct the experimental pump-probe study of the time-dependent nature of the B-Si surface. I then analysed the results and formulated the physical description of the process. After which I developed a time-dependent Drude model to be used in a homebuilt by me 1D-FDTD simulation designed to observe the phase-shifting dynamics. Lastly, I wrote the majority of the text prior to submission. The article was accepted by Physical Review Research on 16^{th} September 2021.

5.1 All-Optical THz Generation in Si

Briefly before continuing with the discussion on B-Si it is worth discussing one of the advantages to the all-optical THz generation scheme presented in chapter 4, that being the use of the $\chi^{(3)}$ nonlinearity present in many optical materials. This provides the flexibility and opens to the possibility of expanding the result to other material platforms with their own advantages compared to InAs. Silicon for example being one such platform which is cheaper and far more widely used with more mature material processing and manufacturing capabilities. Such all-optical schemes for THz generation therefore could be used to quantitatively assess the $\chi^{(3)}$-specific nonlinearity of semiconductor devices. By using the same optical setup as in 4.7, I then replaced the InAs by Si to see if I could observe the same THz signal as predicted by equation 4.7. Additionally, Si has another advantage as there isn't any significant background THz signal in

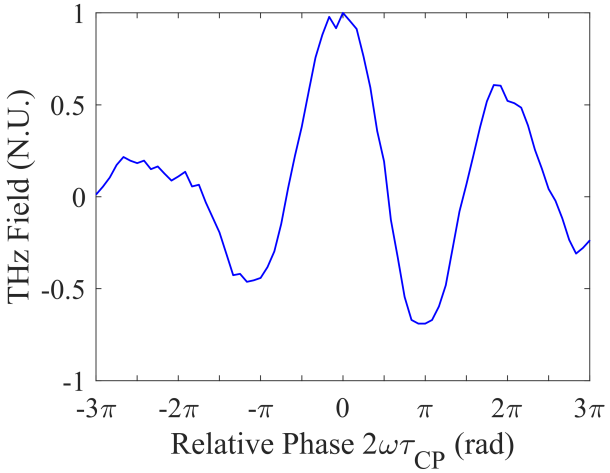

Figure 5.1: The All-Optical Surface Optical Rectification signal obtained from a Si surface as a function of the phase delay τ_{CP}.

the measurement, this is due to the $\chi^{(2)}$ nonlinearity being non-existent and the fact that the first two terms in equation 4.8 are negligible in the current scenario due to a much lower surface field strength, thus the all-optical THz signal is fully decoupled from any other component. The result of this measurement can be appreciated in figure 5.1, where the oscillations are clearly visible about zero due to this negligible background. This proof-of-concept demonstrates the flexibility of the AOSOR scheme to enable a much broader range of THz surface sources to be implemented in a wide variety of practical scenarios where advanced fabrication processes are possible, for instance via the use of metasurfaces to enhance such nonlinear effects. Black Silicon therefore represents an interesting concept where the increased surface area due to the nanopillars could result in novel physics being revealed.

5.2 Black Silicon THz Emission Dependencies

One of these novel physical processes is a remarkable phase-shifting dynamic due to the presence of a fast-varying refractive index and is a main focus of this chapter, discussed thoroughly in section 5.5. An additional result presented however is a large amplification of the THz signal at the overlap between pump and probe pulses, which can be observed in figure 5.6 at $\tau = 0$ps. Where such an effect can be explained as a higher order phenomenon involving the potential resonant and localized plasmonic coupling between pump and probe beams which are enabled by the B-Si surface morphology. Here I will briefly present some experimental evidence for such a plasmonic coupling that aren't presented in the article itself.

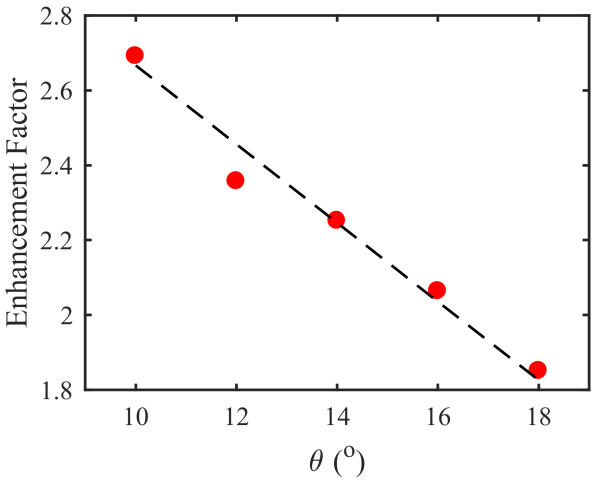

Figure 5.2: The B-Si enhancement factor as a function of the finite angle θ between pump and probe pulses.

The first of which is a dependence between the enhancement factor, defined as the ratio

between the peak THz field radiated at $\tau = 0$ps in figure 5.6 and the peak THz field radiated at $\tau = -10$ps, and the impinging angle between pump and probe pulses. In this scenario, the coupling of the pump electric field to surface-plasmon-polariton (SPP) waves requires that the pump impinging angle scatters at the surface such that the k-vectors between the optical and SPP fields match [238]. This impinging angle dependence can be observed in figure 5.2, where it can be seen that the smaller the angle the greater the enhancement. Worth noting however that smaller angles weren't possible due to the contamination of the detected dynamics by the metallisation-pump-radiated THz field which is less efficiently spatially decoupled at shallower angles.

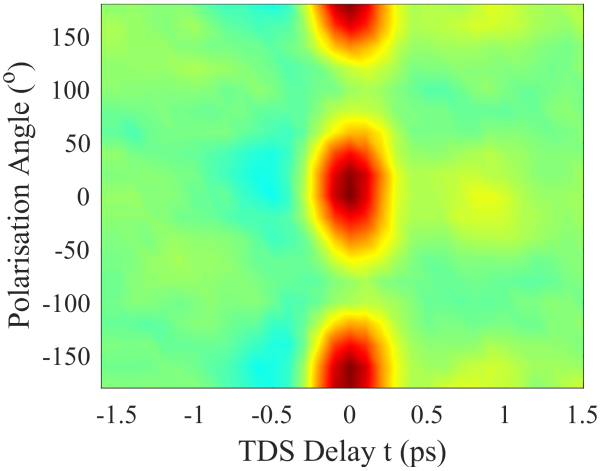

Figure 5.3: The enhanced THz field radiated from B-Si at the overlap between pump pulses as a function of the pump polarisation angle.

The second dependency which was verified was the pump polarisation dependence, which should show a clear preference for p-polarised electric fields which are aligned along the direction of the nanopillars (i.e. the normal to the surface itself). It can be seen in figure 5.3 that the enhancement only exists for polarisation angles of 0°, +180° and −180°, with a degree of control over the enhancement possible by tuning the polarisation.

The final dependency is on the impinging wavelength which should be specific to the morphology of the specific sample. This measurement was made by introducing a BBO crystal and 400nm bandpass filter in the metallisation pump beam path prior to photoexcitation. The result of which can be seen in the full transient THz dynamics shown in figure 5.4. In this case however there is no evidence of any enhancement at the temporal overlap, potentially due to the fact that the nanopillar geometry being too large to act as a metasurface at 400nm. In this case though it is important to mention that the migration from the near infrared to the ultraviolet represents a very large modification to the material response, where the vast differ-

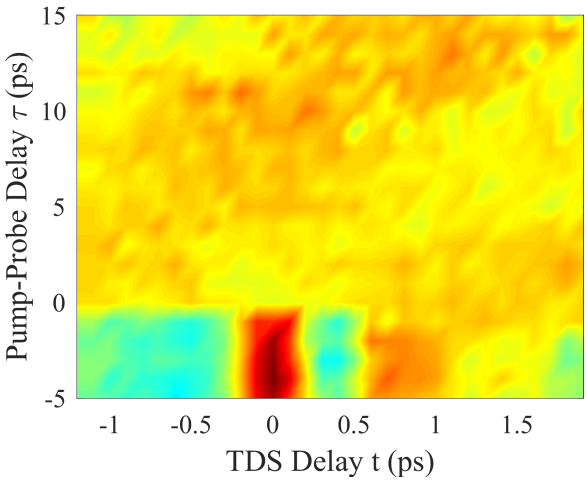

Figure 5.4: The pump-probe dynamics of B-Si when a pump central wavelength of 400nm is used.

ences in skin-depths and absorption profiles can significantly influence the observed dynamics. Furthermore, the lack of any AOSOR component is due to the coarse temporal resolution used as well as the spatial separation of the detected THz field.

These effects in combination demonstrate a potential plasmonic coupling which is also compatible with the results presented in section 5.5, with applications given in the coherent control enabled purely by acting on the external pumping parameters. These other dynamics represent an avenue by which this work can be taken further in the future by including more comprehensive experimental campaigns into these effects as well as a full 3D simulation including the interactions between the free-carrier dynamics and the optical field propagation.

5.3 Summary

The article is an experimental and numerical investigation into the photo-excitation dynamics at B-Si surfaces following THz emission. The experimental setup was similar to that of the OPRE in chapter 2, however instead of observing the free-carrier modulation to surface optical rectification, I am investigating how the ultrashort exciton injection affects a drift-diffusion THz source given by

$$\mathbf{E}_{\mathrm{THz}}(t) \propto \frac{\partial \mathbf{J}(t)}{\partial t}, \tag{5.1}$$

where $\mathbf{J}(t)$ is the photocurrent density. Similarly to previously, by exploiting two optical pulses for the pump and probe, I am able to confine the photocarrier density to precisely the same region as the THz source. Firstly B-Si samples were fabricated using a self-masking Inductively Coupled Plasma - Reactive Ion Etching (ICP-RIE) protocol based on an SF_6/O_2 plasma [219].

These samples were characterised using scanning electron microscopy, where it was observed that high aspect ratio (base $\sim$ 100nm, height $\sim 1\mu$m) nanopillars were etched into the surface. Such that the surface enables light trapping and a smooth index transition which minimises reflections and enhances the absorption, giving it its black appearance. In the pump-probe temporal dynamics several remarkable regimes were observed, the unscreened THz field typical of B-Si, a phase-shifted enhancement during excitation and the subsequent recovery of the sample as carriers diffuse and recombine. I then develop the time-dependent Drude model of the dielectric function given by

$$\epsilon(\omega, t, \tau) = \epsilon_\infty - \frac{\omega_p^2(\omega, t, \tau)}{\omega^2 - i\omega\gamma(\omega, t, \tau)}, \tag{5.2}$$

where ϵ_∞ is the high-frequency dielectric constant, $\gamma(t, \tau)$ is the rate of carrier scattering and

$$\omega_p^2(t, \tau) = \frac{e^2 N(t, \tau)}{m^* \epsilon_0 \epsilon_\infty}, \tag{5.3}$$

with e, m^*, ϵ_0 being the electron charge, effective mass and vacuum permittivity respectively. By propagating THz fields within the temporally-varying dielectric function via a 1D-FDTD, similar phase shifting dynamics were able to be recreated.

5.4 Impact

This publication targeted the new American Physical Society journal Physical Review Research. The journal scope covers the whole spectrum of physics research, focusing on important and novel publications which fits with this work due to its fundamental linking of THz science with the exciting field of time-dependent media.

The article has also been presented at several conferences. Including oral presentations given by myself at the 2018 Advanced Photonics Congress in Zurich and the 2021 virtual conference CLEO/EUROPE-EQEC.

5.5 Journal Article

5.5.1 Abstract

Systems with ultrafast time-varying dielectric properties represent an emerging novel physical framework. We demonstrate here the first observation of sub-cycle dynamics interacting directly with a photoexcited electromagnetic source. The photoelectron dynamics occurring on timescales faster than the carrier-envelope field, confined in nanostructured silicon surfaces induces a for nonlinear ultrafast phase shifts in the terahertz emission, exposing a completely novel physical setting.

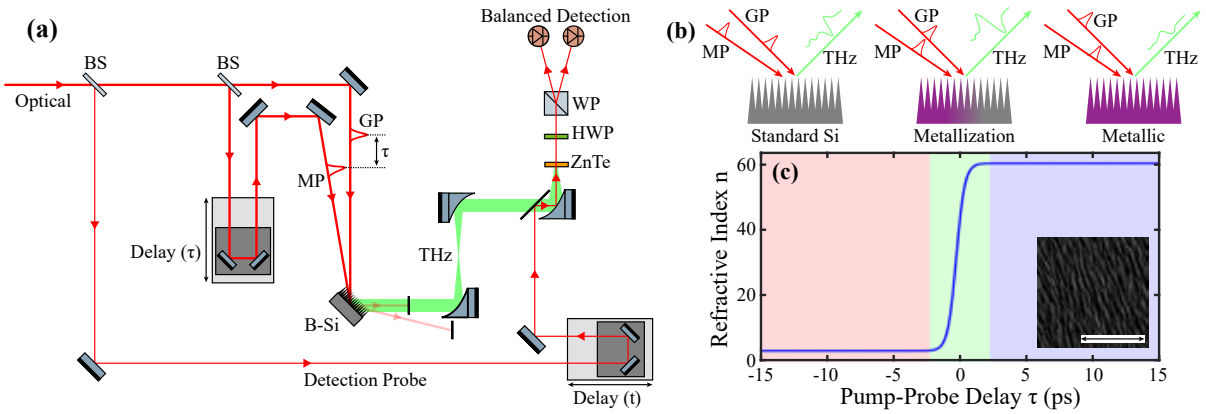

Figure 5.5: (a) The full experimental setup for THz generation and ultrafast metallization of black Silicon substrates. BS: Beam Splitter, GP: Generation Pump, MP: Metallization Pump, B-Si: Black Silicon, ZnTe: Zinc Telluride, HWP: Half-wave Plate, WP: Wollaston Prism. (b) A schematic displaying the three major regimes in the transient measurements as the B-Si transitions from a semiconducting to the metallic state. (c) The corresponding shift in the real part of the time-dependent refractive index induced by the MP, the inset shows a SEM image of the B-Si surface (scale bar 5μm).

5.5.2 Main Text

Materials with time-varying optical and physical properties provide an intriguing emerging physical framework to study new forms of nonlinear light-matter interactions [72, 71, 220]. In these systems, any electric field propagating in the medium perceives a temporal variation in the dielectric properties of the medium as a temporal boundary [70, 221]. In the presence of a temporal discontinuity of the refractive index between two values n_i and n_f, the conservation of the electromagnetic field components leads to the definition of "temporal" refraction and reflection laws affecting the energy and spectral properties of the waves and involving the evolution of the frequency from ω_i to ω_f via $n_i\omega_i = n_f\omega_f$ [69, 75, 222]. By taking advantage of these relationships, it is possible to directly modify the spatiotemporal properties of the electromagnetic wave and induce exotic nonlinear responses such as time refraction and photon acceleration [74, 75, 76]. These phenomena have also been applied to achieve adiabatic frequency conversion [223, 224, 225], anti-reflection couplers in waveguides [226], spontaneous photon emission [227] and to dynamically tune the direction of the Poynting vector [228]. In this context, the absorption of ultrashort optical pulses in semiconductor nanostructures and photonic crystals provides an ideal framework to study time-dependent optical responses in accessible experimental settings [89, 229]. Due to the optical injection of a large density of excited photo-carriers, the material undergoes an ultrafast metallization process corresponding

to a time-dependent complex susceptibility [55, 230]. Such an effect is analogous to the flash ionization of gases in optical cavities, where the ultrafast formation of plasma leads to the onset of complex interactions between the optical waves [77]. An interesting open question is whether an ultrafast temporal boundary can affect the spatiotemporal properties of nonlinear sources localized within the medium. When the dielectric transient occurs within timescales shorter than the optical period, in particular, the mismatch between the characteristic timescales of photonic responses and their coupling with the propagating fields poses a significant challenge. Interestingly, this condition is met in the framework of terahertz (THz) pulse generation by photo-excited carrier systems. The typical THz period ($\sim$ 1ps) can be significantly longer than the metallization transient induced by standard ultrafast optical sources ($\sim$ 100fs pulses). An additional advantage arising from exploiting THz pulses for physical investigation lies in the ability to perform fully coherent field-sensitive detection, as in the case of Time Domain Spectroscopy (TDS), where the time-resolved detection of the field oscillations allows the retrieval of the amplitude and phase information of the pulse [10]. TDS detection thus provides the ability to perceive fast-arising time-boundaries beyond the effect they produce on the power spectral density distribution of the electromagnetic wave [78, 70, 231]. In the past few years, this possibility has been explored in a series of Optical Pump Terahertz Probe (OPTP) spectroscopy experiments focused on the direct observation of the impact of rapid variations of the density of free carriers on the THz electric field [62, 65, 91]. Quite interestingly, for transitions much faster than the THz field, researchers have observed the formation of additional frequencies in the THz pulse due to the THz shockwaves reflected from an ultrashort step in the conductivity [78]. In these experiments, however, the ultrafast transient would simply cut the THz waveform in time, and the new frequencies would actually result from ultrafast damping of the dynamics. As in the case of standard temporal refraction in CW systems, no energy transfer takes place between the pump and probe pulses and the energy at these new frequencies has simply been distributed from the original spectral profile [223, 232]. In OPTP, moreover, the actual overlap between the dielectric transient and the THz field can be minimal due to the conspicuous mismatch between the optical and THz penetration depths [90]. More importantly, in these conditions the propagating wave interacts with a spatially static temporal conductivity transient, and the modulation is critically smeared in time by the large velocity mismatch between the modulating mechanism and the propagating wave.

In this work, we investigate an entirely different physical scenario where a nonlinear THz source lies within the time-varying medium. To this end, we employ a Black Silicon (B-Si) material platform consisting of a random distribution of Si nanopillars [233]. As B-Si is known to

emit THz radiation when excited by optical pulses [218], this platform allows us to observe the effects of the ultrafast metallization on a concurrent THz generation mechanism. Although the precise origin of THz emission from B-Si is still a matter of debate in the literature [218, 234], it is widely accepted that the morphological confinement of the carrier dynamics plays a primary role. In our experiments, we investigated the effect of the ultrafast metallization on the THz generation mechanism through a dual-pump optical setup inspired by the Optical Pump Rectification Emission (OPRE) scheme discussed thoroughly in [90, 137]. Our experimental setup is illustrated in figure 5.5(a). We employed a regenerative-amplified ultrafast source (Coherent Libra HE+) which provides a train of ultrashort pulses with 1kHz repetition rate, 800nm central wavelength, 100fs pulse duration and a beam diameter at e^{-2} of 9mm, as determined by a knife-edge technique. We split the beam into three lines. The two main lines are responsible for the generation of THz (generation pump, 0.6mJ) and to induce the ultrafast metallization in the sample (metallization pump, 0.3mJ). We controlled the delay between the two pumps by means of a mechanical translation stage. The third line ($\sim 1\mu$J) acted as an optical probe for the detection of the generated THz field via electro-optic sampling [30]. We fabricated our B-Si samples through a self-masking inductively coupled plasma-reactive ion etching (ICP-RIE) protocol in a $SF_6/0_2$ plasma [219]. In this procedure, the competition between surface passivation, ion bombardment and chemical etching leads to a highly anisotropic etching which results in the spontaneous formation of sharp Silicon needles on the surface [233]. In our configuration, the generation pump induces a photo-current $\mathbf{J}(t)$ which acts as a direct THz source:

$$\mathbf{E}_{\mathrm{THz}}(t) \propto \frac{\partial \mathbf{J}(t)}{\partial t}. \tag{5.4}$$

The metallization pump, conversely, drives an ultrafast metallization transient, i.e. a temporal variation in the free-carrier density N:

$$N(t-\tau) = [H(t-\tau) * A(t-\tau)]e^{-\frac{t-\tau}{\tau_{\mathrm{Si}}}}. \tag{5.5}$$

where τ is the intra-pump delay, $H(t)$ is the Heaviside step function, $A(t-\tau)$ is the pump pulse envelope, and τ_{Si} ($>$ 1ns) is the characteristic carrier recombination time (we assume the rising front of the metallization is instantaneous in the timescale of the THz wave period). By acting on the delay τ between the two optical pumps, we could observe the effects of the temporal discontinuity on the THz emission across all the different stages of the metallization process. As illustrated in the temporal trace shown in Fig. 5.6, we observed the onset of rather different and counter-intuitive regimes in the emitted far-field THz waveform. When $\tau < -5$ps, the generation pulse reaches the sample before the metallization pulse. In this condition, the generated THz field corresponds to the standard emission from B-Si substrates and it originates from

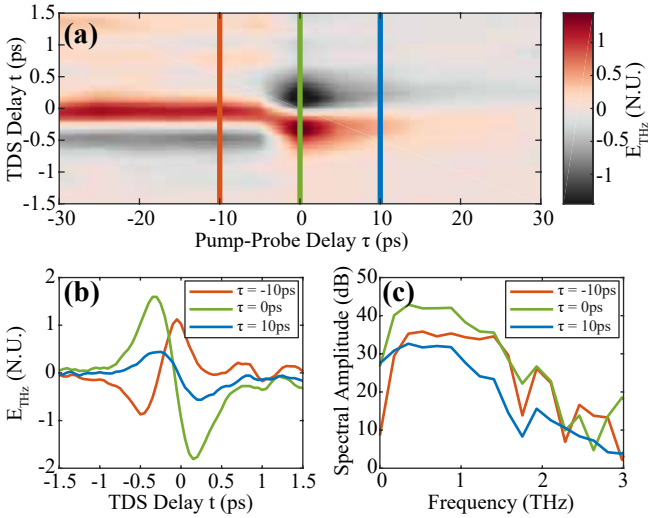

Figure 5.6: (a) The full transient THz dynamics spanning tens of picoseconds before and after photoexcitation. (b) The B-Si THz waveforms taken at the pump-probe delay times depicted by the lines marked in (a). With $\tau = -10$ps, $\tau = 0$ps and $\tau = 10$ps corresponding to the standard unexcited B-Si, the transient metallization region and the metallic state respectively. (c) The THz spectra obtained via the fast Fourier transform of the temporal waveforms shown in (b).

photocarrier drift-diffusion mechanisms (Fig. 5.6(b), red line) [218]. At $\tau \approx -5$ps, the generation and metallization pulses begin overlapping in the sample, where the ultrafast injection of photocarriers leads to a rapid change in the complex dielectric function in proximity to the THz source. Quite interestingly, the effect of the ultrafast metallisation on the THz emission manifests through a stark coherent phase shift and enhancement of the generated pulse. This effect peaks at $\tau = 0$ps (Fig. 5.6(b), green line). In this scenario, the conductivity transient acts as a temporal boundary which is perfectly overlapped in space and synchronized in time with the THz source, causing the shift in the position of the peak of the detected THz field. It should be noted that the delayed onset of the shift, which is maximized at $\tau = 0$ps, is a direct consequence of the finite angle between generation and metallization pumps, which results in unavoidable temporal smearing (on the scale of a few ps) between the two. After the transition is completed ($\tau > 5$ps), the system relaxes to a stationary condition following two notable timescales. At first, the field enhancement decays quite rapidly as the temporal overlap between the probe and the index step increases within the smearing. Secondly, the system follows a slow recovery dynamics due to the spontaneous recombination of photocarriers in the sample. Quite notably, the phase shift is preserved even after the temporal transition is complete, suggesting that it is fundamentally related to the onset of a metallic state in the BSi needles. In our experiments,

we further noticed that the magnitude of the phase shift varies across samples with different morphologies and it appears independent of the pumping rate, suggesting that it depends on the specific geometry of the B-Si nanopillars. Furthermore, we observed that the amplitude can be tuned by acting on several pumping parameters such as wavelength, polarization and pulse energy, which modify the photocarrier density, energy, and spatial overlap with the interacting fields.

To provide further insights on the fundamental process driving the phase-shift, we studied the ultrafast metallization process through fully-dispersive (implemented via a Auxillary Differential Equation method), 1D-FDTD simulations [235]. More specifically, we integrated a time-varying material configuration by generalising a standard Drude model to the time-dependent material configuration. Following standard approaches, we expressed the Drude dielectric function as follows:

$$\epsilon(\omega, t-\tau) = \epsilon_\infty - \frac{[2\pi\nu_p(t-\tau)]^2}{\omega^2 - i\omega\gamma(t-\tau)}, \tag{5.6}$$

where ϵ_∞ is the high-frequency dielectric constant [236]. In Eq. (5.6), we explicitly introduced the time-dependent properties of the medium through the scattering rate $\gamma(t-\tau)$ and the material's plasma frequency $\nu_p(t-\tau)$. The first is determined by a combination of electron-electron scattering as well as electron-phonon scattering contributions, while in a semiconductor the latter is expressed as:

$$\nu_p(t-\tau) = \frac{1}{2\pi}\sqrt{\frac{e^2 N(t-\tau)}{m^*\epsilon_0\epsilon_\infty}}, \tag{5.7}$$

with e, m^*, ϵ_0 denote the electron charge, effective mass and vacuum permittivity, respectively. We assumed a plasma frequency of $\nu_p = 0.75$ THz for the stationary case and $\nu_p = 70$ THz for the photo-excited case, corresponding to an excitation free-carrier density of $2.6 \times 10^{20}\mathrm{cm}^{-3}$ compatible with our experimental conditions. Following the approach described in Ref. [237], we also assumed scattering rate of $\frac{1}{0.8fs}$ before excitation and $\frac{1}{10.5fs}$ upon excitation due to reduced electron scattering in the higher conductivity regime [238]. These values correspond to a refractive index discontinuity of ~ 57, consistent with the magnitude normally achievable in plasmonic systems. This suggests that the temporal boundary is in fact mediated by surface plasmon polariton (SPP) electronic waves [238, 80, 81] enabled by the nanopillar geometry, where the jump in refractive index can be much larger than that of the planar case. We also considered a slightly longer excitation pulse duration of 640fs to minimise the onset of spurious reflections in the FDTD propagator [235]. Our FDTD simulations consisted of a THz pulse source launched from within a Si substrate whose dielectric function is varying as given by Eqs. 5.5-5.7 for different values of the intra-pump delay τ. The model accounts for the experimental

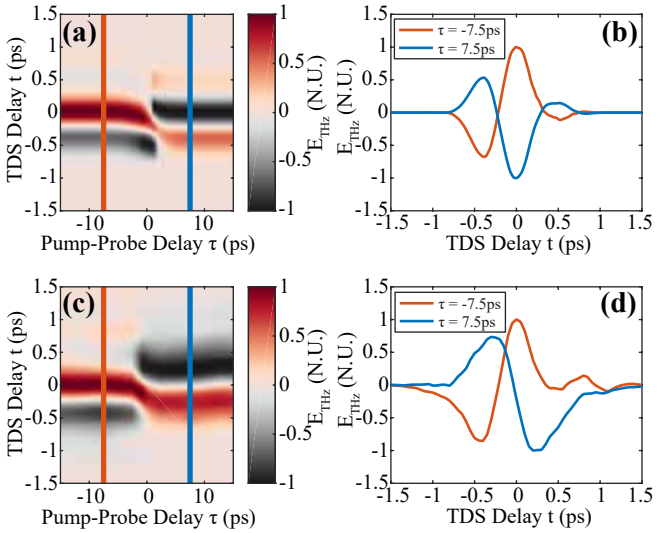

Figure 5.7: (a) The fully simulated THz time-dependent dynamics, where all waveforms have been normalized with respect to themselves to highlight the phase shift induced by the material metallization. (b) The temporal THz fields corresponding to the pump-probe delay times marked in (a). With $\tau = -7.5$ps and $\tau = 7.5$ps being the semiconducting and metallic states respectively. (c) The experimental dynamics shown in figure 5.6 with the same normalization to demonstrate the behaviour similar to that shown in (a). (d) The experimental waveforms taken at the same delay τ as in (b).

temporal smearing with a low-pass filter (with a time constant of 3ps) along the pump-probe delay axis τ, but does not include any corrective effect for reproducing the morphology of the surface. As a result, any potential resonant and localized plasmonic effects induced by the metallic cones or nonlinear mixing cannot be appreciated here. Such effects possibly contribute to higher order effects, such as the field enhancement observed in Fig. 5.6, but are remarkably not necessary to reproduce the fundamental phase dynamics of the phenomenon. This is evident in Fig. 5.7, where we compare the simulations with the experimental results. Remarkably, our simple model reproduces accurately the experimental phase shift and this is a core evidence that our photo-excited metasurface mainly behaves as a temporally varying material.

In conclusion, we have provided the first experimental characterisation of the effects of an optically-induced, ultrafast temporal discontinuity on the field generated by a nonlinear THz-source. This physical scenario is significantly different from previous investigations as the nonlinear source is embedded in the time-varying medium. This novel physical framework enables the observation of a coherent time-dependent phase-shifting dynamic in the emission and in a net gain of the optical-to-terahertz conversion efficiency. Quite significantly, the phase-inversion dynamics can be fully retraced to the time-dependent transition in the medium, as demonstrated

by introducing a time-dependent Drude susceptibility model in FDTD simulations. Finally, our results suggest that inducing a time-dependent refractive index within nonlinear optical sources can enable novel intriguing features. For example, while photocarriers are traditionally only exploited to screen a THz field in a standard pump-probe embodiment [234], we demonstrated that a *time-varying* photoexcitation can control the far-field THz phase by acting solely on the pump-probe delay. By allowing direct access to the amplitude and phase properties of the emitted THz pulse, we expect that this new physical framework could trigger new perspectives and methodologies to gain full-field control on the THz emission, while simultaneously providing a benchmark for further investigations on time-dependent phenomena exploiting the optical excitation of THz field sources. Furthermore, we predict that such schemes can also create impact in complex nonlinear imaging [187, 186] and in the optical control of electron-electron interactions [182, 183].

Chapter 6

Conclusion

To conclude, a large quantity of physical advances have been made and presented within this thesis. Starting with chapter 2, my work on the specific measurement of surface potentials and their modification due to the injection of photocarriers. Which provides novel insights into the emission of THz radiation from semiconductor surfaces with application in the quantitative characterisation of semiconductor devices with impact in electronics, photovoltaics and in optical sensors. Directly relating to this work, chapter 3 presented novel insights into the saturation of surface optical rectification was presented, demonstrating for the first time the actual lack of any hard saturation process, instead showing the return of the quadratic dependence on the THz emission. Such a result was discussed in context to the general THz community with impact in the understanding of semiconductor surface emitters and their applicability to imaging systems. I have also presented a method by which the SOR process can be circumvented. This method, discussed in chapter 4, showed that it was possible to circumvent the SOR process by illuminating the surface with both the fundamental and second harmonic ultrashort pulses, and as such separate the contribution from the surface field which can in fact be detrimental to the emission at extreme excitations. Such a result furthermore removes the requirement that the surface emitter has any significant surface field, as such it is in principle able to be extended to other material platforms exhibiting a high $\chi^{(3)}$ nonlinearity at a lower cost, such as in Silicon.

I then applied in chapter 5 all the knowledge that I had gained so far on THz photonics and free carrier dynamics to provide the first measurement on the THz dynamics in black Silicon surfaces, with novel results being revealed whose roots can be attributed to the rapidly expanding and exciting field of time-dependent media. This result has the potential to generate a large amount of excitement in the metamaterials and THz fields where the combination of the sub-period excitation timescales with the field detection enabled by TDS can provide a platform for the experimental study of these novel dynamics. Lastly, I presented in the

appendices how some of my work has been applied. Firstly, in appendix A, I explain how my gained expertise in the pump-probe measurement techniques was then exploited in the optical domain. Demonstrating yet again the strengths of such techniques in the direct measurement of photocarrier motional dynamics in the time domain. Then, in appendix B, the development of a novel nonlinear ghost imaging system is presented, where the THz image is built up by a correlation between the spatial patterning of an optical pulse with the detected THz waveform.

6.1 Future Work

There are several potential avenues that shall be taken in the future due to this work. Firstly, the all optical surface optical rectification scheme presented in chapter 4 is currently being expanded to enable the systematic investigation of the $\chi^{(3)}$ based nonlinearity in a range of semiconductors including ZnTe. Furthermore, by the addition of a significantly sensitive phase measurement, it is expected to be used to reveal the dynamics of the quantum interference mechanism and its contribution to the nonlinearity. Secondly, my work on the black Silicon shall be continued to the realisation of a fully complete model fitting to all aspects of the experimental results. Furthermore, the time-dependent nature enables my approach to be targeted towards the broader metasurfaces and plasmonic communities, where a doubly resonant structure can be designed with a tunability afforded by the pump induced temporal variation in the refractive index. An additional area where my work can be continued outside of the field of terahertz is in the optical observation of charge carrier dynamics enabled by the Trans-Carrier spectroscopy presented in appendix A. Through which the experimental scheme may be used to investigate other samples where charge-transfer dynamics are relevant in their operation, such as in certain forms of nanostructured catalysts. Lastly, the continued development of THz ghost imaging systems (like those presented in appendix B) which can integrate THz emitting surfaces to enable a highly subwavelength propagation in order to minimize the spatio-temporal coupling experienced by the THz field in its current configuration.

Bibliography

[1] Q. Wu, M. Litz, and X. C. Zhang. Broadband detection capability of ZnTe electro-optic field detectors. *Applied Physics Letters*, 68(21):2924–2924, 1995. xi, 30, 31, 66

[2] A.J. DeMaria, W.H. Glenn, M.J. Brienza, and M.E. Mack. Picosecond laser pulses. *Proceedings of the IEEE*, 57(1):2–25, 1969. 2

[3] G. Steinmeyer. Frontiers in Ultrashort Pulse Generation: Pushing the Limits in Linear and Nonlinear Optics. *Science*, 286(5444):1507–1512, November 1999. 2

[4] L. E. Hargrove, R. L. Fork, and M. A. Pollack. Locking of He-Ne Laser Modes Induced by Synchronous Intracavity Modulation. *Applied Physics Letters*, 5(1):4–5, July 1964. 2

[5] The Horse in motion. "Abe Edgington," owned by Leland Stanford; driven by C. Marvin, trotting at a 2:24 gait over the Palo Alto track, 15th June 1878 / Muybridge. Library Catalog: www.loc.gov. 2

[6] Andrew Marc Weiner. *Ultrafast optics*. Wiley series in pure and applied optics. Wiley, Hoboken, N.J, 2009. OCLC: ocn262882128. 3

[7] P. A. Franken, A. E. Hill, C. W. Peters, and G. Weinreich. Generation of optical harmonics. *Physical Review Letters*, 7(4):118–119, 1961. 3

[8] Robert W Boyd. *Nonlinear Optics*. Academic Press, 3rd edition, 2007. 3, 69

[9] Xi-Cheng Zhang and Jingzhou Xu. *Introduction to THz Wave Photonics*. Springer US, Boston, MA, 2010. 4, 7, 8, 60

[10] Susan L. Dexheimer. *Terahertz spectroscopy: principles and applications*. CRC press, 2007. 4, 78

[11] Alain Maestrini, John Ward, Goutam Chattopadhyay, Erich Schlecht, and Imran Mehdi. Terahertz Sources Based on Frequency Multiplication and Their Applications. *Frequenz*, 62(5-6):118–122, June 2008. 4

[12] Rüdeger Köhler, Alessandro Tredicucci, Fabio Beltram, Harvey E. Beere, Edmund H. Linfield, A. Giles Davies, David A. Ritchie, Rita C. Iotti, and Fausto Rossi. Terahertz semiconductor-heterostructure laser. *Nature*, 417(6885):156–159, May 2002. 4

[13] F. Sizov and A. Rogalski. THz detectors. *Progress in Quantum Electronics*, 34(5):278–347, September 2010. 4

[14] P. U. Jepsen, D. G. Cooke, and M. Koch. Terahertz spectroscopy and imaging - Modern techniques and applications. *Laser and Photonics Reviews*, 5(1):124–166, January 2011. 4

[15] D. Grischkowsky, Søren Keiding, Martin Van Exter, and Ch Fattinger. Far-infrared time-domain spectroscopy with terahertz beams of dielectrics and semiconductors. *JOSA B*, 7(10):2006–2015, 1990. 01931. 4, 26

[16] Masayoshi Tonouchi. Cutting-edge terahertz technology. *Nature Photonics*, 1(2):97–105, February 2007. 4

[17] D Zimdars, J S White, G Stuk, A Chernovsky, G Fichter, and S Williamson. Large area terahertz imaging and non-destructive evaluation applications. *Insight - Non-Destructive Testing and Condition Monitoring*, 48(9):537–539, September 2006. 4

[18] E Pickwell and V P Wallace. Biomedical applications of terahertz technology. *Journal of Physics D: Applied Physics*, 39(17):301–310, September 2006. 4

[19] T K Gustafson, J-P E Taran, P L Kelley, and R Y Chiao. Self-modulation of picosecond pulses in electro-optic crystals. *Optics Communications*, 2(1):17–21, 1970. 4

[20] R. Eckardt and J. Reintjes. Phase matching limitations of high efficiency second harmonic generation. *Journal of Quantum Electronics*, 20(10):1178–1187, 1984. 5

[21] G. Gallot, Jiangquan Zhang, R. W. McGowan, Tae-In Jeon, and D. Grischkowsky. Measurements of the THz absorption and dispersion of ZnTe and their relevance to the electro-optic detection of THz radiation. *Applied Physics Letters*, 74(23):3450–3450, 1999. 5

[22] P. Y. Han and X.-C. Zhang. Coherent, broadband midinfrared terahertz beam sensors. *Applied Physics Letters*, 73(21):3049–3051, November 1998. 5

[23] X.-C. Zhang, X. F. Ma, Y. Jin, T.-M. Lu, E. P. Boden, P. D. Phelps, K. R. Stewart, and C. P. Yakymyshyn. Terahertz optical rectification from a nonlinear organic crystal. *Applied Physics Letters*, 61(26):3080–3082, December 1992. 5, 42

[24] Arno Schneider, Max Neis, Marcel Stillhart, Blanca Ruiz, Rizwan U. A. Khan, and Peter Günter. Generation of terahertz pulses through optical rectification in organic DAST crystals: theory and experiment. *Journal of the Optical Society of America B*, 23(9):1822–1822, 2006. 5, 42

[25] David H. Auston, K. P. Cheung, J. A. Valdmanis, and D. A. Kleinman. Cherenkov radiation from femtosecond optical pulses in electro-optic media. *Physical Review Letters*, 53(16):1555, 1984. 5, 42

[26] Janos Hebling, Gabor Almasi, Ida Kozma, and Jurgen Kuhl. Velocity matching by pulse front tilting for large area THz-pulse generation. *Optics Express*, 10(21):1161–1166, 2002. 5, 42

[27] J. A. Giordmaine. Mixing of light beams in crystals. *Physical Review Letters*, 8(1):19–20, 1962. 6, 60

[28] T Löffler, T Hahn, M Thomson, F Jacob, and H Roskos. Large-area electro-optic ZnTe terahertz emitters. *Optics Express*, 13(14):5353–5362, July 2005. 6, 60

[29] C. Winnewisser, P. Uhd Jepsen, M. Schall, V. Schyja, and H. Helm. Electro-optic detection of THz radiation in $LiTaO_3$, $LiNbO_3$ and ZnTe. *Applied Physics Letters*, 70(23):3069–3069, 1997. 6

[30] Q. Wu and X. C. Zhang. Ultrafast electro-optic field sensors. *Applied Physics Letters*, 68(12):1604–1606, 1996. 6, 45, 79

[31] Amnon Yariv. *Quantum electronics*. Wiley, New York, 3rd ed edition, 1989. 6

[32] P. Uhd Jepsen, R. H. Jacobsen, and S. R. Keiding. Generation and detection of terahertz pulses from biased semiconductor antennas. *Journal of the Optical Society of America B*, 13(11):2424, November 1996. 7

[33] D. H. Auston, K. P. Cheung, and P. R. Smith. Picosecond photoconducting Hertzian dipoles. *Applied Physics Letters*, 45(3):284–286, August 1984. 7

[34] D. Dragoman and M. Dragoman. Terahertz fields and applications. *Progress in Quantum Electronics*, 28(1):1–66, January 2004. 8

[35] Masahiko Tani, Kwang-Su Lee, and X.-C. Zhang. Detection of terahertz radiation with low-temperature-grown GaAs-based photoconductive antenna using 1.55 μm probe. *Applied Physics Letters*, 77(9):1396–1398, August 2000. 8

[36] Martin Van Exter, Ch Fattinger, and D. Grischkowsky. Terahertz time-domain spectroscopy of water vapor. *Optics letters*, 14(20):1128–1130, 1989. 11

[37] Edward P. J. Parrott, J. Axel Zeitler, Tomislav Friščić, Michael Pepper, William Jones, Graeme M. Day, and Lynn F. Gladden. Testing the Sensitivity of Terahertz Spectroscopy to Changes in Molecular and Supramolecular Structure: A Study of Structurally Similar Cocrystals. *Crystal Growth & Design*, 9(3):1452–1460, March 2009. 11

[38] Stephanie M. Teo, Benjamin K. Ofori-Okai, Christopher A. Werley, and Keith A. Nelson. Invited Article: Single-shot THz detection techniques optimized for multidimensional THz spectroscopy. *Review of Scientific Instruments*, 86(5):051301, May 2015. 11

[39] Shayne M. Harrel, Rebecca L. Milot, James M. Schleicher, and Charles A. Schmuttenmaer. Influence of free-carrier absorption on terahertz generation from ZnTe(110). *Journal of Applied Physics*, 107(3):033526–033526, 2010. 11

[40] Shane Ardo and Gerald J. Meyer. Photodriven heterogeneous charge transfer with transition-metal compounds anchored to TiO $_2$ semiconductor surfaces. *Chem. Soc. Rev.*, 38(1):115–164, 2009. 11

[41] Fausto Rossi and Tilmann Kuhn. Theory of ultrafast phenomena in photoexcited semiconductors. *Reviews of Modern Physics*, 74(3):895, 2002. 11, 13

[42] Ahmed H. Zewail. Femtochemistry: Atomic-Scale Dynamics of the Chemical Bond†. *The Journal of Physical Chemistry A*, 104(24):5660–5694, June 2000. 11, 14

[43] G Porter. Flash photolysis and spectroscopy. A new method for the study of free radical reactions. *Proceedings of the Royal Society of London. Series A. Mathematical and Physical Sciences*, 200(1061):284–300, January 1950. 11

[44] G. L. Eesley. Observation of Nonequilibrium Electron Heating in Copper. *Physical Review Letters*, 51(23):2140–2143, December 1983. 11, 12

[45] Chunlei Guo, George Rodriguez, and Antoinette J. Taylor. Ultrafast Dynamics of Electron Thermalization in Gold. *Physical Review Letters*, 86(8):1638–1641, February 2001. 11

[46] Rudi Berera, Rienk van Grondelle, and John T. M. Kennis. Ultrafast transient absorption spectroscopy: principles and application to photosynthetic systems. *Photosynthesis Research*, 101(2-3):105–118, September 2009. 12

[47] Majed Chergui and Eric Collet. Photoinduced Structural Dynamics of Molecular Systems Mapped by Time-Resolved X-ray Methods. *Chemical Reviews*, 117(16):11025–11065, August 2017. 12, 14

[48] Guichuan Xing, Nripan Mathews, Shuangyong Sun, Swee Sien Lim, Yeng Ming Lam, Michael Gratzel, Subodh Mhaisalkar, and Tze Chien Sum. Long-Range Balanced Electron- and Hole-Transport Lengths in Organic-Inorganic $CH_3NH_3Pbl_3$. *Science*, 342(6156):344–347, October 2013. 12

[49] Taiha Joo, Yiwei Jia, Jae-Young Yu, Matthew J. Lang, and Graham R. Fleming. Third-order nonlinear time domain probes of solvation dynamics. *The Journal of Chemical Physics*, 104(16):6089–6108, April 1996. 12

[50] Chunlei Guo, George Rodriguez, Ahmed Lobad, and A. J. Taylor. Structural phase transition of aluminum induced by electronic excitation. *Physical Review Letters*, 84(19):4493, 2000. 12

[51] Daniel V Schroeder. *An Introduction to Thermal Physics*. Addison Wesley, 2000. 12

[52] V. V. Kruglyak, R. J. Hicken, P. Matousek, and M. Towrie. Spectroscopic study of optically induced ultrafast electron dynamics in gold. *Physical Review B*, 75(3), January 2007. 12

[53] Xiaoping Hong, Jonghwan Kim, Su-Fei Shi, Yu Zhang, Chenhao Jin, Yinghui Sun, Sefaattin Tongay, Junqiao Wu, Yanfeng Zhang, and Feng Wang. Ultrafast charge transfer in atomically thin MoS_2/WS_2 heterostructures. *Nature Nanotechnology*, 9(9):682–686, September 2014. 14

[54] Sreejith Kaniyankandy, S. N. Achary, Sachin Rawalekar, and Hirendra N. Ghosh. Ultrafast Relaxation Dynamics in Graphene Oxide: Evidence of Electron Trapping. *The Journal of Physical Chemistry C*, 115(39):19110–19116, October 2011. 14

[55] A. J. Sabbah and D. M. Riffe. Femtosecond pump-probe reflectivity study of silicon carrier dynamics. *Physical Review B*, 66(16), October 2002. 14, 78

[56] Gautham Nair and Moungi G. Bawendi. Carrier multiplication yields in CdSe and CdTe nanocrystals by transient photoluminescence. *Physical Review B*, 76(8):081304, August 2007. arXiv: 0708.3866. 14

[57] Matthew E. Sykes, Jon W. Stewart, Gleb M. Akselrod, Xiang-Tian Kong, Zhiming Wang, David J. Gosztola, Alex B. F. Martinson, Daniel Rosenmann, Maiken H. Mikkelsen, Alexander O. Govorov, and Gary P. Wiederrecht. Enhanced generation and anisotropic Coulomb scattering of hot electrons in an ultra-broadband plasmonic nanopatch metasurface. *Nature Communications*, 8(1), December 2017. 14

[58] Zhi Guo, Yan Wan, Mengjin Yang, Jordan Snaider, Kai Zhu, and Libai Huang. Long-range hot-carrier transport in hybrid perovskites visualized by ultrafast microscopy. *Science*, 356(6333):59–62, April 2017. 14

[59] Geok-Kieng Lim, Zhi-Li Chen, Jenny Clark, Roland G. S. Goh, Wee-Hao Ng, Hong-Wee Tan, Richard H. Friend, Peter K. H. Ho, and Lay-Lay Chua. Giant broadband nonlinear optical absorption response in dispersed graphene single sheets. *Nature Photonics*, 5(9):554–560, September 2011. 14

[60] N. Liaros, S. Couris, E. Koudoumas, and P. A. Loukakos. Ultrafast Processes in Graphene Oxide during Femtosecond Laser Excitation. *The Journal of Physical Chemistry C*, 120(7):4104–4111, February 2016. 14

[61] Anatoly A. Ischenko, Peter M. Weber, and R. J. Dwayne Miller. Capturing Chemistry in Action with Electrons: Realization of Atomically Resolved Reaction Dynamics. *Chemical Reviews*, 117(16):11066–11124, August 2017. 14

[62] M. C. Nuss, D. H. Auston, and F. Capasso. Direct subpicosecond measurement of carrier mobility of photoexcited electrons in gallium arsenide. *Physical review letters*, 58(22):2355, 1987. 14, 17, 23, 78

[63] R. H. M. Groeneveld and D. Grischkowsky. Picosecond time-resolved far-infrared experiments on carriers and excitons in GaAs-AlGaAs multiple quantum wells. *JOSA B*, 11(12):2502–2507, 1994. 14

[64] Tae-In Jeon and D. Grischkowsky. Nature of conduction in doped silicon. *Physical Review Letters*, 78(6):1106, 1997. 15

[65] Charles A. Schmuttenmaer. Exploring Dynamics in the Far-Infrared with Terahertz Spectroscopy. *Chemical Reviews*, 104(4):1759–1780, April 2004. 15, 17, 78

[66] Han-Kwang Nienhuys and Villy Sundström. Intrinsic complications in the analysis of optical-pump, terahertz probe experiments. *Physical Review B*, 71(23):235110, 2005. 15

[67] F. H. Su, F. Blanchard, G. Sharma, L. Razzari, A. Ayesheshim, T. L. Cocker, L. V. Titova, T. Ozaki, J.-C. Kieffer, R. Morandotti, M. Reid, and F. A. Hegmann. Terahertz pulse induced intervalley scattering in photoexcited GaAs. *Optics Express*, 17(12):9620, June 2009. 15

[68] Matthias C. Hoffmann, Janos Hebling, Harold Y. Hwang, Ka-Lo Yeh, and Keith A. Nelson. Impact ionization in InSb probed by THz-pump THz-probe spectroscopy. *Physical Review B*, 79(16):161201, April 2009. arXiv: 0812.4754. 15

[69] R. Fante. Transmission of electromagnetic waves into time-varying media. *IEEE Transactions on Antennas and Propagation*, 19(3):417–424, May 1971. 15, 77

[70] Andrei Rogov and Evgenii Narimanov. Space–Time Metamaterials. *ACS Photonics*, June 2018. 15, 77, 78

[71] Juan Sabino Martínez-Romero, O. M. Becerra-Fuentes, and P. Halevi. Temporal photonic crystals with modulations of both permittivity and permeability. *Physical Review A*, 93(6), June 2016. 15, 77

[72] Yuzhe Xiao, Drew N. Maywar, and Govind P. Agrawal. Reflection and transmission of electromagnetic waves at a temporal boundary. *Optics Letters*, 39(3):574, February 2014. 15, 77

[73] J. T. Mendonça, A. Guerreiro, and Ana M. Martins. Quantum theory of time refraction. *Physical Review A*, 62(3), August 2000. 15

[74] Markus Cirone, Kazimierz Rząz-dotewski, and Jan Mostowski. Photon generation by time-dependent dielectric: A soluble model. *Physical Review A*, 55(1):62–66, January 1997. 15, 71, 77

[75] J. T. Mendonça. *Theory of photon acceleration*. Series in plasma physics. Institute of Physics Pub, Bristol, UK ; Philadelphia, PA, 2001. OCLC: ocm47163838. 15, 71, 77

[76] Stefano Vezzoli, Vincenzo Bruno, Clayton DeVault, Thomas Roger, Vladimir M. Shalaev, Alexandra Boltasseva, Marcello Ferrera, Matteo Clerici, Audrius Dubietis, and Daniele Faccio. Optical Time Reversal from Time-Dependent Epsilon-Near-Zero Media. *Physical Review Letters*, 120(4):043902, January 2018. 15, 71, 77

[77] Aleksandr B. Shvartsburg. Optics of nonstationary media. *Physics-Uspekhi*, 48(8):797, 2005. 16, 71, 78

[78] Johannes Bühler, Jonas Allerbeck, Gabriel Fitzky, Daniele Brida, and Alfred Leitenstorfer. Terahertz shockwaves generated by a precise subcycle cut of the electric field. *Optica*, 5(7):821, July 2018. 16, 71, 78

[79] M. I. Stockman. *Plasmonics: theory and applications*. Springer, New York, 2013. 16

[80] Dmitri K. Gramotnev and Sergey I. Bozhevolnyi. Plasmonics beyond the diffraction limit. *Nature Photonics*, 4(2):83–91, February 2010. 16, 81

[81] Anatoly V. Zayats, Igor I. Smolyaninov, and Alexei A. Maradudin. Nano-optics of surface plasmon polaritons. *Physics Reports*, 408(3-4):131–314, March 2005. 16, 81

[82] Nanfang Yu, Patrice Genevet, Mikhail A. Kats, Francesco Aieta, Jean-Philippe Tetienne, Federico Capasso, and Zeno Gaburro. Light Propagation with Phase Discontinuities: Generalized Laws of Reflection and Refraction. *Science*, 334(6054):333–337, October 2011. 16

[83] G.A. Wurtz and A.V. Zayats. Nonlinear surface plasmon polaritonic crystals. *Laser & Photonics Review*, 2(3):125–135, July 2008. 16

[84] Renjie Hou, Vasyl Shynkar, Clément Lafargue, Radoslaw Kolkowski, Joseph Zyss, and François Lagugné-Labarthet. Second harmonic generation from gold meta-molecules with three-fold symmetry. *Physical Chemistry Chemical Physics*, 18(11):7956–7965, 2016. 16

[85] Shay Keren-Zur, Ori Avayu, Lior Michaeli, and Tal Ellenbogen. Nonlinear Beam Shaping with Plasmonic Metasurfaces. *ACS Photonics*, 3(1):117–123, January 2016. 16

[86] Jongwon Lee, Mykhailo Tymchenko, Christos Argyropoulos, Pai-Yen Chen, Feng Lu, Frederic Demmerle, Gerhard Boehm, Markus-Christian Amann, Andrea Alù, and Mikhail A. Belkin. Giant nonlinear response from plasmonic metasurfaces coupled to intersubband transitions. *Nature*, 511(7507):65–69, July 2014. 16

[87] Jürgen Sautter, Isabelle Staude, Manuel Decker, Evgenia Rusak, Dragomir N. Neshev, Igal Brener, and Yuri S. Kivshar. Active Tuning of All-Dielectric Metasurfaces. *ACS Nano*, 9(4):4308–4315, April 2015. 16

[88] Raktim Sarma, Salvatore Campione, Michael Goldflam, Joshua Shank, Jinhyun Noh, Sean Smith, Peide D. Ye, Michael Sinclair, John Klem, Joel Wendt, Isaac Ruiz, Stephen W. Howell, and Igal Brener. Low dissipation spectral filtering using a field-effect tunable III–V hybrid metasurface. *Applied Physics Letters*, 113(6):061108, August 2018. 16

[89] Song Han, Longqing Cong, Yogesh Kumar Srivastava, Bo Qiang, Mikhail V. Rybin, Abhishek Kumar, Ravikumar Jain, Wen Xiang Lim, Venu Gopal Achanta, Shriganesh S. Prabhu, Qi Jie Wang, Yuri S. Kivshar, and Ranjan Singh. All-Dielectric Active Terahertz Photonics Driven by Bound States in the Continuum. *Advanced Materials*, page 1901921, July 2019. 16, 77

[90] L. Peters, J. Tunesi, A. Pasquazi, and M. Peccianti. Optical Pump Rectification Emission: Route to Terahertz Free-Standing Surface Potential Diagnostics. *Scientific Reports*, 7(1), December 2017. 17, 43, 45, 64, 78, 79, 162

[91] P. Uhd Jepsen, W. Schairer, I. H. Libon, U. Lemmer, N. E. Hecker, M. Birkholz, K. Lips, and M. Schall. Ultrafast carrier trapping in microcrystalline silicon observed in optical pump–terahertz probe measurements. *Applied Physics Letters*, 79(9):1291, 2001. 17, 23, 78

[92] Valynn Katrine Mag-usara, Stefan Funkner, Gudrun Niehues, Elizabeth Ann Prieto, Maria Herminia Balgos, Armando Somintac, Elmer Estacio, Arnel Salvador, Kohji Yamamoto, Muneaki Hase, and Masahiko Tani. Low temperature-grown GaAs carrier lifetime evaluation by double optical pump terahertz time-domain emission spectroscopy. *Optics Express*, 24(23):26175, November 2016. 17, 24, 33, 48

[93] Masayoshi Tonouchi. Dynamic terahertz emission microscope. In *ICECom, 2010 Conference Proceedings*, pages 1–2. IEEE, 2010. 17, 24

[94] Hidetoshi Nakanishi, Akira Ito, Kazuhisa Takayama, Iwao Kawayama, Hironaru Murakami, and Masayoshi Tonouchi. Visualization of Photoexcited Carrier Responses in a Solar Cell Using Optical Pump—Terahertz Emission Probe Technique. *Journal of Infrared, Millimeter, and Terahertz Waves*, 37(5):498–506, 2016. 17, 19, 24

[95] M. B. Johnston, D. M. Whittaker, A. Corchia, A. G. Davies, and E. H. Linfield. Simulation of terahertz generation at semiconductor surfaces. *Physical Review B*, 65(16), March 2002. 18, 37

[96] James N. Heyman, H. Wrage, C. Lind, D. Hebert, P. Neocleous, P. A. Crowell, T. Mueller, and Karl Unterrainer. Terahertz emission from magnetoplasma oscillations in semiconductors. In *Symposium on Integrated Optoelectronic Devices*, pages 12–18. International Society for Optics and Photonics, 2002. 00001. 18, 29, 44

[97] Antanas Reklaitis. Terahertz emission from InAs induced by photo-Dember effect: Hydrodynamic analysis and Monte Carlo simulations. *Journal of Applied Physics*, 108(5), 2010. 18, 20, 33, 37, 40, 44

[98] C. A. Mead and W. G. Spitzer. Fermi level position at semiconductor surfaces. *Physical Review Letters*, 10(11):471, 1963. 18, 24

[99] Shoinji Kawaji and Harry C. Gatos. Electric field effect on the magnetoresistance of indium arsenide surfaces in high magnetic fields. *Surface Science*, 7(2):215–228, June 1967. 18, 28, 46

[100] Hans Lüth. *Solid Surfaces, Interfaces and Thin Films*. Graduate Texts in Physics. Springer International Publishing, Cham, 2015. 18, 28

[101] Yuji Sakai, Iwao Kawayama, Hidetoshi Nakanishi, and Masayoshi Tonouchi. Visualization of GaN surface potential using terahertz emission enhanced by local defects. *Scientific Reports*, 5:13860, September 2015. 19, 24

[102] Toshimitsu Mochizuki, Akira Ito, Jonathon Mitchell, Hidetoshi Nakanishi, Katsuto Tanahashi, Iwao Kawayama, Masayoshi Tonouchi, Katsuhiko Shirasawa, and Hidetaka Takato. Probing the surface potential of oxidized silicon by assessing terahertz emission. *Applied Physics Letters*, 110(16):163502, April 2017. 19, 24, 57

[103] Harry Dember. Uber eine photoelektronische Kraft in Kupferoxydul-Kristallen. *Physikalische Zeitschrift*, 32:554, 1931. 19

[104] V Apostolopoulos and M E Barnes. THz emitters based on the photo-Dember effect. *Journal of Physics D: Applied Physics*, 47(37):374002–374002, September 2014. 00031. 19, 20, 37, 42, 64, 160

[105] C. Weiss, R. Wallenstein, and R. Beigang. Magnetic-field-enhanced generation of terahertz radiation in semiconductor surfaces. *Applied Physics Letters*, 77(25):4160–4160, 2000. 20

[106] M E Barnes, S a Berry, P Gow, D McBryde, G J Daniell, H E Beere, D a Ritchie, and V Apostolopoulos. Investigation of the role of the lateral photo-Dember effect in the generation of terahertz radiation using a metallic mask on a semiconductor. *Optics express*, 21(14):16263–72, July 2013. 00022. 20

[107] Ping Gu, Masahiko Tani, Shunsuke Kono, Kiyomi Sakai, and X. C. Zhang. Study of terahertz radiation from InAs and InSb. *Journal of Applied Physics*, 91(9):5533–5537, 2002. 00277. 20, 42

[108] W. Y. Ching and Ming-Zhu Huang. Calculation of optical excitations in cubic semiconductors. III. Third-harmonic generation. *Physical Review B*, 47(15):9479, 1993. 20

[109] M. Reid and R. Fedosejevs. Terahertz emission from (100) InAs surfaces at high excitation fluences. *Applied Physics Letters*, 86(1):011906, December 2004. 20, 21, 37, 43, 46, 47, 61, 65, 67, 68, 69, 160

[110] Shun Lien Chuang, Stefan Schmitt-Rink, Benjamin I. Greene, Peter N. Saeta, and Anthony FJ Levi. Optical rectification at semiconductor surfaces. *Physical review letters*, 68(1):102, 1992. 20, 21, 24, 42, 43, 61, 65

[111] J. E. Sipe, D. J. Moss, and H. M. Van Driel. Phenomenological theory of optical second- and third-harmonic generation from cubic centrosymmetric crystals. *Physical Review B*, 35(3):1129, 1987. 21

[112] D. E. Aspnes and A. A. Studna. Dielectric functions and optical parameters of si, ge, gap, gaas, gasb, inp, inas, and insb from 1.5 to 6.0 ev. *Physical review B*, 27(2):985, 1983. 21, 23, 25, 27, 30, 42, 67

[113] Winfried Mönch. *Semiconductor Surfaces and Interfaces*, volume 26 of *Springer Series in Surface Sciences*. Springer Berlin Heidelberg, Berlin, Heidelberg, 2001. 22

[114] François Léonard and J. Tersoff. Role of Fermi-level pinning in nanotube Schottky diodes. *Physical Review Letters*, 84(20):4693, 2000. 00000. 23

[115] Marc Burgelman, Peter Nollet, and Stefaan Degrave. Modelling polycrystalline semiconductor solar cells. *Thin Solid Films*, 361:527–532, 2000. 00521. 23

[116] John F. O'Hara, Ranjan Singh, Igal Brener, Evgenya Smirnova, Jiaguang Han, Antoinette J. Taylor, and Weili Zhang. Thin-film sensing with planar terahertz metamaterials: sensitivity and limitations. *Optics Express*, 16(3):1786–1795, 2008. 23

[117] A. Brodde, St. Tosch, and H. Neddermeyer. Scanning tunnelling microscopy and spectroscopy on Cu(111) and Au(111). *Journal of Microscopy*, 152:441–448, March 1988. 00018. 23

[118] G. Hörmandinger. Imaging of the Cu (111) surface state in scanning tunneling microscopy. *Physical Review B*, 49(19):13897, 1994. 00000. 23

[119] Noriaki Horiuchi. Terahertz technology: Endless applications. *Nature Photonics*, 4(3):140, March 2010. 23, 138

[120] Benjamin I. Greene, John F. Federici, D. R. Dykaar, A. F. J. Levi, and L. Pfeiffer. Picosecond pump and probe spectroscopy utilizing freely propagating terahertz radiation. *Optics letters*, 16(1):48–49, 1991. 00087. 23

[121] Matthew C. Beard, Gordon M. Turner, and Charles A. Schmuttenmaer. Terahertz Spectroscopy. *The Journal of Physical Chemistry B*, 106(29):7146–7159, July 2002. 00493. 23

[122] Ronald Ulbricht, Euan Hendry, Jie Shan, Tony F. Heinz, and Mischa Bonn. Carrier dynamics in semiconductors studied with time-resolved terahertz spectroscopy. *Reviews of Modern Physics*, 83(2):543–586, June 2011. 23

[123] Hannah J Joyce, Callum J Docherty, Qiang Gao, H Hoe Tan, Chennupati Jagadish, James Lloyd-Hughes, Laura M Herz, and Michael B Johnston. Electronic properties of GaAs, InAs and InP nanowires studied by terahertz spectroscopy. *Nanotechnology*, 24(21):214006, May 2013. 00000. 23

[124] J. B. Héroux and M. Kuwata-Gonokami. Photoexcited Carrier Dynamics in InAs, GaAs, and InSb Probed by Terahertz Excitation Spectroscopy. *Physical Review Applied*, 7(5), May 2017. 24, 30, 42

[125] R. Valdés Aguilar, A. V. Stier, W. Liu, L. S. Bilbro, D. K. George, N. Bansal, L. Wu, J. Cerne, A. G. Markelz, S. Oh, and N. P. Armitage. Terahertz Response and Colossal Kerr Rotation from the Surface States of the Topological Insulator Bi 2 Se 3. *Physical Review Letters*, 108(8), February 2012. 24

[126] Gurpreet Kaur, Pengyu Han, and Xi-Cheng Zhang. Transmission coefficient enhancement in undoped Indium Arsenide by high THz field. In *Quantum Electronics and Laser Science Conference*, page QMB1. Optical Society of America, 2011. 00000. 26

[127] H.-E. Ponath and G. I. Stegeman, editors. *Nonlinear surface electromagnetic phenomena*. Number v. 29 in Modern problems in condensed matter sciences. North-Holland ; Sole distributors for the USA and Canada, Elsevier Science Pub. Co, Amsterdam ; New York : New York, NY, USA, 1991. 27

[128] Matthew Reid, Igor V. Cravetchi, and Robert Fedosejevs. Terahertz radiation and second-harmonic generation from InAs: Bulk versus surface electric-field-induced contributions. *Physical Review B - Condensed Matter and Materials Physics*, 72(3):1–9, 2005. 27, 30, 42, 64, 69, 160

[129] Y. R. Shen. Surface properties probed by second-harmonic and sum-frequency generation.pdf. *Nature*, 337:519–525, February 1989. 27

[130] A. Rice, Y. Jin, X. F. Ma, X. C. Zhang, D. Bliss, J. Larkin, and M. Alexander. Terahertz optical rectification from <110> zinc-blende crystals. *Applied Physics Letters*, 64(1994):1324–1326, 1994. 00416. 27, 63

[131] L. Ö. Olsson, C. B. M. Andersson, M. C. Håkansson, J. Kanski, L. Ilver, and U. O. Karlsson. Charge accumulation at InAs surfaces. *Physical review letters*, 76(19):3626, 1996. 28

[132] H. S. Karlsson, G. Ghiaia, and U. O. Karlsson. Electron dynamics and accumulation on the InAs (110) surface. *Surface science*, 407(1-3):L687–L692, 1998. 28

[133] S. A. Kovalenko. Descartes-Snell law of refraction with absorption. *Semiconductor Physics, Quantum Electronics & Optoelectronics*, 4(3):214–218, 2001. 00000. 30

[134] Thomas B. A. Senior and J. L. Volakis. *Approximate boundary conditions in electromagnetics*. Institution of Electrical Engineers, London, 1995. OCLC: ocm32509096. 32

[135] T. Dekorsy, X. Q. Zhou, K. Ploog, and H. Kurz. Subpicosecond electric field dynamics in low-temperature-grown GaAs observed by reflective electro-optic sampling. *Materials Science and Engineering: B*, 22(1):68–71, 1993. 33

[136] Gaofang Li, Xin Xue, Xian Lin, Sannan Yuan, Naiyun Tang, Fenghong Chu, Haoyang Cui, and Guohong Ma. Evolution of terahertz conductivity in ZnSe nanocrystal investigated with optical-pump terahertz-probe spectroscopy. *Applied Physics A*, 116(1):45–50, July 2014. 33

[137] L. Peters, J. Tunesi, A. Pasquazi, and M. Peccianti. High-energy terahertz surface optical rectification. *Nano Energy*, 46:128–132, April 2018. 37, 64, 65, 67, 68, 79, 147, 160, 161

[138] S. Robert Goldman, Kalman Kalikstein, and Bernard Kramer. Dember-effect theory. *Journal of Applied Physics*, 49(5):2849–2854, May 1978. 37

[139] Paul C. M. Planken, Han-Kwang Nienhuys, Huib J. Bakker, and Tom Wenckebach. Measurement and calculation of the orientation dependence of terahertz pulse detection in ZnTe. *Journal of the Optical Society of America B*, 18(3):313–313, 2001. 38

[140] K. Smit, L. Koenders, and W. Monch. Adsorption of chlorine and oxygen on cleaved InAs(110) surfaces: Raman spectroscopy, photoemission spectroscopy, and Kelvin probe

measurements. *Journal of Vacuum Science & Technology B: Microelectronics and Nanometer Structures*, 7(4):888, July 1989. 40, 44

[141] L. F. J. Piper, T. D. Veal, M. J. Lowe, and C. F. McConville. Electron depletion at InAs free surfaces: Doping-induced acceptorlike gap states. *Physical Review B*, 73(19), May 2006. 40, 44

[142] Seung-Heon Lee, Jian Lu, Seung-Jun Lee, Jae-Hyun Han, Chan-Uk Jeong, Seung-Chul Lee, Xian Li, Mojca Jazbinšek, Woojin Yoon, Hoseop Yun, Bong Joo Kang, Fabian Rotermund, Keith A. Nelson, and O-Pil Kwon. Benzothiazolium Single Crystals: A New Class of Nonlinear Optical Crystals with Efficient THz Wave Generation. *Advanced Materials*, 29(30):1701748, August 2017. 42

[143] H. Hirori, A. Doi, F. Blanchard, and K. Tanaka. Single-cycle terahertz pulses with amplitudes exceeding 1 MV/cm generated by optical rectification in $LiNbO_3$. *Applied Physics Letters*, 98(9):091106, 2011. 42, 63, 136

[144] Sen-Cheng Zhong, Jun Li, Zhao-Hui Zhai, Li-Guo Zhu, Jiang Li, Ping-Wei Zhou, Jian-Heng Zhao, and Ze-Ren Li. Generation of 0.19-mJ THz pulses in $LiNbO_3$ driven by 800-nm femtosecond laser. *Optics Express*, 24(13):14828, June 2016. 42

[145] Kai Liu, Jingzhou Xu, Tao Yuan, and X.-C. Zhang. Terahertz radiation from InAs induced by carrier diffusion and drift. *Physical Review B*, 73(15):155330–155330, April 2006. 42

[146] R. Adomavičius, A. Urbanowicz, G. Molis, A. Krotkus, and E. Šatkovskis. Terahertz emission from p-lnAs due to the instantaneous polarization. *Applied Physics Letters*, 85(13):2463, 2004. 00105. 42

[147] H. Jeong, S. H. Shin, S. Y. Kim, J. D. Song, S. B. Choi, D. S. Lee, J. Lee, and Y. D. Jho. Relationship between phase and generation mechanisms of THz waves in InAs. *Current Applied Physics*, 12(3):668–672, 2012. 00000. 42

[148] Yutarou Ishibasi, Shigehiko Sasa, Toshihiko Maemoto, Masataka Inoue, Kei Takeya, and Masayoshi Tononuchi. Thickness dependence of intense terahertz emission from InAs thin films. In *Infrared Millimeter and Terahertz Waves (IRMMW-THz), 2010 35th International Conference on*, pages 1–2. IEEE, 2010. 42

[149] R. Mendis, M. L. Smith, L. J. Bignell, R. E. M. Vickers, and R. A. Lewis. Strong terahertz emission from (100) p-type InAs. *Journal of Applied Physics*, 98(12):126104–126104, 2005. 43

[150] Hiroshi Takahashi, Alex Quema, Ryoichiro Yoshioka, Shingo Ono, and Nobuhiko Sarukura. Excitation fluence dependence of terahertz radiation mechanism from femtosecond-laser-irradiated InAs under magnetic field. *Applied Physics Letters*, 83(6):1068–1070, 2003. 43

[151] I. Nevinskas, K. Vizbaras, A. Trinkūnas, R. Butkutė, and A. Krotkus. Terahertz pulse generation from (111)-cut InSb and InAs crystals when illuminated by 1.55-μm femtosecond laser pulses. *Optics Letters*, 42(13):2615, July 2017. 43

[152] P. Cicėnas, A. Geižutis, V. L. Malevich, and A. Krotkus. Terahertz radiation from an InAs surface due to lateral photocurrent transients. *Optics Letters*, 40(22):5164, November 2015. 43

[153] Y. V. Malevich, R. Adomavičius, A. Krotkus, and V. L. Malevich. Anisotropic picosecond photoconductivity caused by optical alignment of electron momenta in cubic semiconductors. *Journal of Applied Physics*, 115(7):073103, February 2014. 43

[154] A. Krotkus, R. Adomavičius, G. Molis, and V. L. Malevich. TeraHertz Emission from InAs Surfaces Excited by Femtosecond Laser Pulses. *Journal of Nanoelectronics and Optoelectronics*, 2(1):108–114, April 2007. 43, 55

[155] B.-Y. Hsieh, Ning Wang, and Mona Jarrahi. Toward ultrafast pump-probe measurements at the nanoscale. *Optics and Photonics News*, 22(12):48–48, 2011. 48

[156] Jianming Dai, Nicholas Karpowicz, and X.-C. Zhang. Coherent Polarization Control of Terahertz Waves Generated from Two-Color Laser-Induced Gas Plasma. *Physical Review Letters*, 103(2), July 2009. 00237. 56, 61

[157] D. J. Cook and R. M. Hochstrasser. Intense terahertz pulses by four-wave rectification in air. *Optics letters*, 25(16):1210–1212, 2000. 00755. 56

[158] Mark D. Thomson, Markus Kreß, Torsten Löffler, and Hartmut G. Roskos. Broadband THz emission from gas plasmas induced by femtosecond optical pulses: From fundamentals to applications. *Laser and Photonics Reviews*, 1(4):349–368, December 2007. 56

[159] K. Y. Kim, A. J. Taylor, J. H. Glownia, and G. Rodriguez. Coherent control of terahertz supercontinuum generation in ultrafast laser–gas interactions. *Nature Photonics*, 2(10):605–609, July 2008. 56

[160] Alexey V. Balakin, Alexander V. Borodin, Igor A. Kotelnikov, and Alexander P. Shkurinov. Terahertz emission from a femtosecond laser focus in a two-color scheme. *Journal of the Optical Society of America B*, 27(1):16–16, December 2010. 56

[161] K. S. Novoselv, A. K. Geim, S. V. Morozov, D. Jiang, Y. Zhang, S. V. Dubonos, I. V. Grigorieva, and A. A. Firsov. Electric Field Effect in Atomically Thin Carbon Films. *Science*, 306(5696):666 – 669, October 2004. 57

[162] A. K. Geim and K. S. Novoselov. The rise of graphene. *Nature Materials*, 6:183, March 2007. 57

[163] J. N. Coleman, M. Lotya, A. O'Neill, S. D. Bergin, P. J. King, U. Khan, K. Young, A. Gaucher, S. De, R. J. Smith, I. V. Shvets, S. K. Arora, G. Stanton, H.-Y. Kim, K. Lee, G. T. Kim, G. S. Duesberg, T. Hallam, J. J. Boland, J. J. Wang, J. F. Donegan, J. C. Grunlan, G. Moriarty, A. Shmeliov, R. J. Nicholls, J. M. Perkins, E. M. Grieveson, K. Theuwissen, D. W. McComb, P. D. Nellist, and V. Nicolosi. Two-Dimensional Nanosheets Produced by Liquid Exfoliation of Layered Materials. *Science*, 331(6017):568–571, February 2011. 02810. 57, 59

[164] Irving Langmuir and Vincent J. Schaefer. Activities of urease and pepsin monolayers. *Journal of the American Chemical Society*, 60(6):1351–1360, 1938. 57, 59

[165] Young-Mi Bahk, Gopakumar Ramakrishnan, Jongho Choi, Hyelynn Song, Geunchang Choi, Yong Hyup Kim, Kwang Jun Ahn, Dai-Sik Kim, and Paul C. M. Planken. Plasmon Enhanced Terahertz Emission from Single Layer Graphene. *ACS Nano*, 8(9):9089–9096, September 2014. 57

[166] Yuanyuan Huang, Lipeng Zhu, Qiyi Zhao, Yaohui Guo, Zhaoyu Ren, Jintao Bai, and Xinlong Xu. Surface Optical Rectification from Layered MoS_2 Crystal by THz Time-Domain Surface Emission Spectroscopy. *ACS Applied Materials & Interfaces*, 9(5):4956–4965, February 2017. 57

[167] Longhui Zhang, Yuanyuan Huang, Qiyi Zhao, Lipeng Zhu, Zehan Yao, Yixuan Zhou, Wanyi Du, and Xinlong Xu. Terahertz surface emission of d-band electrons from a layered tungsten disulfide crystal by the surface field. *Physical Review B*, 96(15), October 2017. 57

[168] Dhiraj Sinha and Ji Ung Lee. Ideal Graphene/Silicon Schottky Junction Diodes. *Nano Letters*, 14(8):4660–4664, August 2014. 57

[169] Antonio Di Bartolomeo. Graphene Schottky diodes: An experimental review of the rectifying graphene/semiconductor heterojunction. *Physics Reports*, 606:1–58, January 2016. 57, 58

[170] Mustafa Lotya, Yenny Hernandez, Paul J. King, Ronan J. Smith, Valeria Nicolosi, Lisa S. Karlsson, Fiona M. Blighe, Sukanta De, Zhiming Wang, I. T. McGovern, Georg S. Duesberg, and Jonathan N. Coleman. Liquid Phase Production of Graphene by Exfoliation of Graphite in Surfactant/Water Solutions. *Journal of the American Chemical Society*, 131(10):3611–3620, March 2009. 59

[171] A. V. Melezhyk, V. A. Kotov, and A. G. Tkachev. Optical Properties and Aggregation of Graphene Nanoplatelets. *Journal of Nanoscience and Nanotechnology*, 16(1):1067–1075, January 2016. 60

[172] V. A. Andreeva, O. G. Kosareva, N. A. Panov, D. E. Shipilo, P. M. Solyankin, M. N. Esaulkov, P. González de Alaiza Martínez, A. P. Shkurinov, V. A. Makarov, L. Bergé, and S. L. Chin. Ultrabroad Terahertz Spectrum Generation from an Air-Based Filament Plasma. *Physical Review Letters*, 116(6):063902, February 2016. 61, 65

[173] Matteo Clerici, Marco Peccianti, Bruno E. Schmidt, Lucia Caspani, Mostafa Shalaby, Mathieu Giguère, Antonio Lotti, Arnaud Couairon, François Légaré, Tsuneyuki Ozaki, Daniele Faccio, and Roberto Morandotti. Wavelength Scaling of Terahertz Generation by Gas Ionization. *Physical Review Letters*, 110(25):253901, June 2013. 61, 65

[174] Xu Xie, Jianming Dai, and X.-C. Zhang. Coherent Control of THz Wave Generation in Ambient Air. *Physical Review Letters*, 96(7), February 2006. 61

[175] Ki-Yong Kim, James H. Glownia, Antoinette J. Taylor, and George Rodriguez. Terahertz emission from ultrafast ionizing air in symmetry-broken laser fields. *Optics Express*, 15(8):4577, 2007. 61, 65

[176] C. G. Wade, N. Šibalić, N. R. de Melo, J. M. Kondo, C. S. Adams, and K. J. Weatherill. Real-time near-field terahertz imaging with atomic optical fluorescence. *Nature Photonics*, 11(1):40–43, January 2017. 63

[177] Ulrike Frühling, Marek Wieland, Michael Gensch, Thomas Gebert, Bernd Schütte, Maria Krikunova, Roland Kalms, Filip Budzyn, Oliver Grimm, Jörg Rossbach, Elke Plönjes, and Markus Drescher. Single-shot terahertz-field-driven X-ray streak camera. *Nature Photonics*, 3(9):523–528, August 2009. 63, 148

[178] Tobias Kampfrath, Koichiro Tanaka, and Keith A. Nelson. Resonant and nonresonant control over matter and light by intense terahertz transients. *Nature Photonics*, 7(9):680–690, September 2013. 63, 148

[179] C. Kealhofer, W. Schneider, D. Ehberger, A. Ryabov, F. Krausz, and P. Baum. All-optical control and metrology of electron pulses. *Science*, 352(6284):429–433, April 2016. 63

[180] S. Baierl, M. Hohenleutner, T. Kampfrath, A. K. Zvezdin, A. V. Kimel, R. Huber, and R. V. Mikhaylovskiy. Nonlinear spin control by terahertz-driven anisotropy fields. *Nature Photonics*, 10(11):715–718, November 2016. 63

[181] Vedran Jelic, Krzysztof Iwaszczuk, Peter H. Nguyen, Christopher Rathje, Graham J. Hornig, Haille M. Sharum, James R. Hoffman, Mark R. Freeman, and Frank A. Hegmann. Ultrafast terahertz control of extreme tunnel currents through single atoms on a silicon surface. *Nature Physics*, 13(6):591, June 2017. 63

[182] Emilio A. Nanni, Wenqian R. Huang, Kyung-Han Hong, Koustuban Ravi, Arya Fallahi, Gustavo Moriena, R. J. Dwayne Miller, and Franz X. Kärtner. Terahertz-driven linear electron acceleration. *Nature Communications*, 6(1):1–8, October 2015. 63, 83

[183] D. A. Walsh, D. S. Lake, E. W. Snedden, M. J. Cliffe, D. M. Graham, and S. P. Jamison. Demonstration of sub-luminal propagation of single-cycle terahertz pulses for particle acceleration. *Nature Communications*, 8(1):1–9, September 2017. 63, 83

[184] Kaushik Sengupta, Tadao Nagatsuma, and Daniel M. Mittleman. Terahertz integrated electronic and hybrid electronic–photonic systems. *Nature Electronics*, 1(12):622–635, December 2018. 63, 148

[185] Jiawei Zhang, Xinzhong Chen, Scott Mills, Thomas Ciavatti, Ziheng Yao, Ryan Mescall, Hai Hu, Vyacheslav Semenenko, Zhe Fei, Hua Li, Vasili Perebeinos, Hu Tao, Qing Dai, Xu Du, and Mengkun Liu. Terahertz Nanoimaging of Graphene. *ACS Photonics*, 5(7):2645–2651, July 2018. 63

[186] Luana Olivieri, Juan S. Totero Gongora, Luke Peters, Vittorio Cecconi, Antonio Cutrona, Jacob Tunesi, Robyn Tucker, Alessia Pasquazi, and Marco Peccianti. Hyperspectral terahertz microscopy via nonlinear ghost imaging. *Optica*, 7(2):186, February 2020. 63, 70, 83, 149, 153, 159

[187] Luana Olivieri, Juan S. Totero Gongora, Alessia Pasquazi, and Marco Peccianti. Time-Resolved Nonlinear Ghost Imaging. *ACS Photonics*, 5(8):3379–3388, August 2018. 63, 70, 83, 136, 139, 140, 142, 146, 149, 152

[188] C. Vicario, A. V. Ovchinnikov, S. I. Ashitkov, M. B. Agranat, V. E. Fortov, and C. P. Hauri. Generation of 0.9-mJ THz pulses in DSTMS pumped by a Cr:Mg_2SiO_4 laser. *Optics Letters*, 39(23):6632–6635, December 2014. 63, 64, 147

[189] Carlo Vicario, Balazs Monoszlai, and Christoph P. Hauri. GV/m Single-Cycle Terahertz Fields from a Laser-Driven Large-Size Partitioned Organic Crystal. *Physical Review Letters*, 112(21):213901, May 2014. 63, 147

[190] T. Seifert, S. Jaiswal, U. Martens, J. Hannegan, L. Braun, P. Maldonado, F. Freimuth, A. Kronenberg, J. Henrizi, I. Radu, E. Beaurepaire, Y. Mokrousov, P. M. Oppeneer, M. Jourdan, G. Jakob, D. Turchinovich, L. M. Hayden, M. Wolf, M. Münzenberg, M. Kläui, and T. Kampfrath. Efficient metallic spintronic emitters of ultrabroadband terahertz radiation. *Nature Photonics*, 10(7):483–488, July 2016. 63, 64, 147, 160

[191] Paul Chevalier, Arman Amirzhan, Fan Wang, Marco Piccardo, Steven G. Johnson, Federico Capasso, and Henry O. Everitt. Widely tunable compact terahertz gas lasers. *Science*, 366(6467):856–860, November 2019. 63

[192] Yang Wu, Mehrdad Elyasi, Xuepeng Qiu, Mengji Chen, Yang Liu, Lin Ke, and Hyunsoo Yang. High-Performance THz Emitters Based on Ferromagnetic/Nonmagnetic Heterostructures. *Advanced Materials*, 29(4):1603031, January 2017. 64

[193] Mengji Chen, Rahul Mishra, Yang Wu, Kyusup Lee, and Hyunsoo Yang. Terahertz Emission from Compensated Magnetic Heterostructures. *Advanced Optical Materials*, 6(17), September 2018. 64

[194] Alessandro Tomasino, Anna Mazhorova, Matteo Clerici, Marco Peccianti, Sze-Phing Ho, Yoann Jestin, Alessia Pasquazi, Andrey Markov, Xin Jin, Riccardo Piccoli, Sebastien Delprat, Mohamed Chaker, Alessandro Busacca, Jalil Ali, Luca Razzari, and Roberto Morandotti. Solid-state-biased coherent detection of ultra-broadband terahertz pulses. *Optica*, 4(11):1358–1362, November 2017. 64

[195] Massimo Cazzanelli and Joerg Schilling. Second order optical nonlinearity in silicon by symmetry breaking. *Applied Physics Reviews*, 3(1):011104, March 2016. 64, 161

[196] Zhelin Zhang, Yanping Chen, Sen Cui, Feng He, Min Chen, Zhen Zhang, Jin Yu, Liming Chen, Zhengming Sheng, and Jie Zhang. Manipulation of polarizations for broadband terahertz waves emitted from laser plasma filaments. *Nature Photonics*, 12(9):554–559, September 2018. 65

[197] Spencer W. Jolly, Nicholas H. Matlis, Frederike Ahr, Vincent Leroux, Timo Eichner, Anne-Laure Calendron, Hideki Ishizuki, Takunori Taira, Franz X. Kärtner, and Andreas R. Maier. Spectral phase control of interfering chirped pulses for high-energy narrowband terahertz generation. *Nature Communications*, 10(1):1–8, June 2019. 65

[198] N. V. Vvedenskii, A. I. Korytin, V. A. Kostin, A. A. Murzanev, A. A. Silaev, and A. N. Stepanov. Two-Color Laser-Plasma Generation of Terahertz Radiation Using a Frequency-Tunable Half Harmonic of a Femtosecond Pulse. *Physical Review Letters*, 112(5):055004, February 2014. 65

[199] P. González de Alaiza Martínez, I. Babushkin, L. Bergé, S. Skupin, E. Cabrera-Granado, C. Köhler, U. Morgner, A. Husakou, and J. Herrmann. Boosting Terahertz Generation in Laser-Field Ionized Gases Using a Sawtooth Wave Shape. *Physical Review Letters*, 114(18):183901, May 2015. 65

[200] V. A. Kostin, I. D. Laryushin, A. A. Silaev, and N. V. Vvedenskii. Ionization-Induced Multiwave Mixing: Terahertz Generation with Two-Color Laser Pulses of Various Frequency Ratios. *Physical Review Letters*, 117(3):035003, July 2016. 65

[201] Zhelin Zhang, Yanping Chen, Min Chen, Zhen Zhang, Jin Yu, Zhengming Sheng, and Jie Zhang. Controllable Terahertz Radiation from a Linear-Dipole Array Formed by a Two-Color Laser Filament in Air. *Physical Review Letters*, 117(24):243901, December 2016. 65

[202] Liang-Liang Zhang, Wei-Min Wang, Tong Wu, Rui Zhang, Shi-Jing Zhang, Cun-Lin Zhang, Yan Zhang, Zheng-Ming Sheng, and Xi-Cheng Zhang. Observation of Terahertz Radiation via the Two-Color Laser Scheme with Uncommon Frequency Ratios. *Physical Review Letters*, 119(23):235001, December 2017. 65

[203] Anastasios D. Koulouklidis, Claudia Gollner, Valentina Shumakova, Vladimir Yu. Fedorov, Audrius Pugžlys, Andrius Baltuška, and Stelios Tzortzakis. Observation of extremely efficient terahertz generation from mid-infrared two-color laser filaments. *Nature Communications*, 11(1), December 2020. 65

[204] E. Dupont, P. B. Corkum, H. C. Liu, M. Buchanan, and Z. R. Wasilewski. Phase-Controlled Currents in Semiconductors. *Physical Review Letters*, 74(18):3596–3599, May 1995. 65

[205] D. Côté, J. M. Fraser, M. DeCamp, P. H. Bucksbaum, and H. M. van Driel. THz emission from coherently controlled photocurrents in GaAs. *Applied Physics Letters*, 75(25):3959–3961, December 1999. 65

[206] J. Gudde, M. Rohleder, T. Meier, S. W. Koch, and U. Hofer. Time-Resolved Investigation of Coherently Controlled Electric Currents at a Metal Surface. *Science*, 318(5854):1287–1291, November 2007. 65

[207] Shawn Sederberg, Fanqi Kong, Felix Hufnagel, Chunmei Zhang, Ebrahim Karimi, and Paul B. Corkum. Vectorized optoelectronic control and metrology in a semiconductor. *Nature Photonics*, 14(11):680–685, November 2020. 65

[208] J. B. Khurgin. Generation of the Terahertz radiation using in $\chi^{(3)}$ semiconductor. *Journal of Nonlinear Optical Physics & Materials*, 04(01):163–189, January 1995. 65

[209] Marko Spasenović, Markus Betz, Louis Costa, and Henry M. van Driel. All-optical coherent control of electrical currents in centrosymmetric semiconductors. *Physical Review B*, 77(8):085201, February 2008. 65

[210] K. A. Stankov, V. P. Tzolov, and M. G. Mirkov. Compensation of group-velocity mismatch in the frequency-doubling modelocker. *Applied Physics B Photophysics and Laser Chemistry*, 54(4):303–306, April 1992. 66, 67

[211] Q. Wu and X.-C. Zhang. 7 terahertz broadband GaP electro-optic sensor. *Applied Physics Letters*, 70(14):1784–1786, April 1997. 68

[212] Jianming Dai, Xu Xie, and X.-C. Zhang. Detection of Broadband Terahertz Waves with a Laser-Induced Plasma in Gases. *Physical Review Letters*, 97(10), September 2006. 68

[213] N. Bloembergen and P. S. Pershan. Light Waves at the Boundary of Nonlinear Media. *Physical Review*, 128(2):606–622, October 1962. 69

[214] P. N. Saeta and N. A. Miller. Distinguishing surface and bulk contributions to third-harmonic generation in silicon. *Applied Physics Letters*, 79(17):2704–2706, October 2001. 69

[215] W. Hübner, K. H. Bennemann, and K. Böhmer. Theory for the nonlinear optical response of transition metals: Polarization dependence as a fingerprint of the electronic structure at surfaces and interfaces. *Physical Review B*, 50(23):17597–17605, December 1994. 69

[216] Jiapeng Zhao, Yiwen E, Kaia Williams, Xi-Cheng Zhang, and Robert W. Boyd. Spatial sampling of terahertz fields with sub-wavelength accuracy via probe-beam encoding. *Light: Science & Applications*, 8(1):55, June 2019. 70, 139, 140, 144, 149, 151

[217] C. Wu, C. H. Crouch, L. Zhao, J. E. Carey, R. Younkin, J. A. Levinson, E. Mazur, R. M. Farrell, P. Gothoskar, and A. Karger. Near-unity below-band-gap absorption by microstructured silicon. *Applied Physics Letters*, 78(13):1850–1852, March 2001. 71

[218] P. Hoyer, M. Theuer, R. Beigang, and E.-B. Kley. Terahertz emission from black silicon. *Applied Physics Letters*, 93(9):091106, 2008. 72, 79, 80

[219] Henri Jansen, Meint de Boer, Rob Legtenberg, and Miko Elwenspoek. The black silicon method: a universal method for determining the parameter setting of a fluorine-based reactive ion etcher in deep silicon trench etching with profile control. *Journal of Micromechanics and Microengineering*, 5:115–120, 1995. 75, 79

[220] Vincent Bacot, Matthieu Labousse, Antonin Eddi, Mathias Fink, and Emmanuel Fort. Time reversal and holography with spacetime transformations. *Nature Physics*, 12(10):972–977, October 2016. 77

[221] Iñigo Liberal, Yue Li, and Nader Engheta. Reconfigurable epsilon-near-zero metasurfaces via photonic doping. *Nanophotonics*, 7(6):1117–1127, 2018. 77

[222] Christophe Caloz and Zoe-Lise Deck-Leger. Spacetime Metamaterials—Part II: Theory and Applications. *IEEE Transactions on Antennas and Propagation*, 68(3):1583–1598, March 2020. 77

[223] Masaya Notomi and Satoshi Mitsugi. Wavelength conversion via dynamic refractive index tuning of a cavity. *Physical Review A*, 73(5), May 2006. 77, 78

[224] Evan J. Reed, Marin Soljačić, and John D. Joannopoulos. Color of Shock Waves in Photonic Crystals. *Physical Review Letters*, 90(20), May 2003. 77

[225] Xingping Zhou, Samit Kumar Gupta, Xueyi Zhu, Guangxu Su, Peng Zhan, Yongmin Liu, Zhuo Chen, Minghui Lu, and Zhenlin Wang. Nonreciprocal Isolation and Wavelength Conversion via a Spatiotemporally Engineered Cascaded Cavity. *Physical Review Applied*, 13(4), April 2020. 77

[226] Victor Pacheco-Peña and Nader Engheta. Antireflection temporal coatings. *Optica*, 7(4):323, April 2020. 77

[227] F. Belgiorno, S. L. Cacciatori, M. Clerici, V. Gorini, G. Ortenzi, L. Rizzi, E. Rubino, V. G. Sala, and D. Faccio. Hawking Radiation from Ultrashort Laser Pulse Filaments. *Physical Review Letters*, 105(20), November 2010. 77

[228] Victor Pacheco-Peña and Nader Engheta. Temporal aiming. *Light: Science & Applications*, 9(1), December 2020. 77

[229] K. Kondo and T. Baba. Adiabatic wavelength redshift by dynamic carrier depletion using p - i - n -diode–loaded photonic crystal waveguides. *Physical Review A*, 97(3), March 2018. 77

[230] Matthew C. Beard, Gordon M. Turner, and Charles A. Schmuttenmaer. Transient photoconductivity in GaAs as measured by time-resolved terahertz spectroscopy. *Physical Review B*, 62(23):15764, 2000. 78

[231] Kanghee Lee, Jaehyeon Son, Jagang Park, Byungsoo Kang, Wonju Jeon, Fabian Rotermund, and Bumki Min. Linear frequency conversion via sudden merging of meta-atoms in time-variant metasurfaces. *Nature Photonics*, 12(12):765–773, December 2018. 78

[232] Xingping Zhou, Samit Kumar Gupta, Guangxu Su, Peng Zhan, Minghui Lu, and Zhenlin Wang. Multiple-wavelength conversion based on the anomalous Doppler effect induced by dynamic tuning in a self-collimation photonic crystal. *Physical Review A*, 100(1), July 2019. 78

[233] Xiaogang Liu, Paul R. Coxon, Marius Peters, Bram Hoex, Jacqueline M. Cole, and Derek J. Fray. Black silicon: fabrication methods, properties and solar energy applications. *Energy & Environmental Science*, 7(10):3223–3263, 2014. 78, 79

[234] Ulrike Blumröder, Matthias Zilk, Hannes Hempel, Patrick Hoyer, Thomas Pertsch, Rainer Eichberger, Thomas Unold, and Stefan Nolte. Influence of structure geometry on THz emission from Black Silicon surfaces fabricated by reactive ion etching. *Optics Express*, 25(6):6604, March 2017. 79, 83

[235] Allen Taflove and Susan C. Hagness. *Computational electrodynamics: the finite-difference time-domain method*. Artech House antennas and propagation library. Artech House, Boston, 3rd ed edition, 2005. 81

[236] Stefan A. Maier. *Plasmonics: fundamentals and applications*. Springer, New York, 2007. 81

[237] Giuseppe Della Valle, Ben Hopkins, Lucia Ganzer, Tatjana Stoll, Mohsen Rahmani, Stefano Longhi, Yuri S. Kivshar, Costantino De Angelis, Dragomir N. Neshev, and Giulio Cerullo. Nonlinear Anisotropic Dielectric Metasurfaces for Ultrafast Nanophotonics. *ACS Photonics*, 4(9):2129–2136, September 2017. 81

[238] M. I. Stockman. *Plasmonics: theory and applications*. Springer, New York, 2013. 74, 81

[239] Bipin Kumar Gupta, Garima Kedawat, Pawan Kumar, Mohammad A. Rafiee, Priyanka Tyagi, Ritu Srivastava, and Pulickel M. Ajayan. An n-type, new emerging luminescent polybenzodioxane polymer for application in solution-processed green emitting OLEDs. *Journal of Materials Chemistry C*, 3(11):2568–2574, 2015. 121, 123, 127, 134

[240] Naiying Du, Jingshe Song, Gilles P. Robertson, Ingo Pinnau, and Michael D. Guiver. Linear High Molecular Weight Ladder Polymer via Fast Polycondensation of 5,5',6,6'-Tetrahydroxy-3,3,3',3'-tetramethylspirobisindane with 1,4-Dicyanotetrafluorobenzene. *Macromolecular Rapid Communications*, 29(10):783–788, May 2008. 121

[241] Koen Vandewal, Steve Albrecht, Eric T. Hoke, Kenneth R. Graham, Johannes Widmer, Jessica D. Douglas, Marcel Schubert, William R. Mateker, Jason T. Bloking, George F. Burkhard, Alan Sellinger, Jean M. J. Fréchet, Aram Amassian, Moritz K. Riede, Michael D. McGehee, Dieter Neher, and Alberto Salleo. Efficient charge generation by relaxed charge-transfer states at organic interfaces. *Nature Materials*, 13(1):63–68, January 2014. 123

[242] Veaceslav Coropceanu, Jérôme Cornil, Demetrio A. da Silva Filho, Yoann Olivier, Robert Silbey, and Jean-Luc Brédas. Charge Transport in Organic Semiconductors. *Chemical Reviews*, 107(4):926–952, April 2007. 123

[243] H. Sirringhaus. Device Physics of Solution-Processed Organic Field-Effect Transistors. *Advanced Materials*, 17(20):2411–2425, October 2005. 123

[244] S. Gelinas, A. Rao, A. Kumar, S. L. Smith, A. W. Chin, J. Clark, T. S. van der Poll, G. C. Bazan, and R. H. Friend. Ultrafast Long-Range Charge Separation in Organic Semiconductor Photovoltaic Diodes. *Science*, 343:512–516, 2014. 123

[245] Michael K. Bates, Qingying Jia, Huong Doan, Wentao Liang, and Sanjeev Mukerjee.

Charge-Transfer Effects in Ni–Fe and Ni–Fe–Co Mixed-Metal Oxides for the Alkaline Oxygen Evolution Reaction. *ACS Catalysis*, 6(1):155–161, January 2016. 123

[246] Fenglin Liao, T. W. Benedict Lo, Jin Qu, Anna Kroner, Andrew Dent, and S. C. Edman Tsang. Tunability of catalytic properties of Pd-based catalysts by rational control of strong metal and support interaction (SMSI) for selective hydrogenolyic C–C and C–O bond cleavage of ethylene glycol units in biomass molecules. *Catalysis Science & Technology*, 5(7):3491–3495, 2015. 123

[247] Weiran Zheng, Simon Jones, Xinlin Hong, and Shik Chi Edman Tsang. Photo and electronic excitation for low temperature catalysis over metal nanoparticles using an organic semiconductor. *RSC Adv.*, 4(88):47488–47496, 2014. 123

[248] Peter M. Budd, Bader S. Ghanem, Saad Makhseed, Neil B. McKeown, Kadhum J. Msayib, and Carin E. Tattershall. Polymers of intrinsic microporosity (PIMs): robust, solution-processable, organic nanoporous materials. *Chemical Communications*, 2:230, 2004. 123

[249] Bader S. Ghanem, Neil B. McKeown, Peter M. Budd, and Detlev Fritsch. Polymers of Intrinsic Microporosity Derived from Bis(phenazyl) Monomers. *Macromolecules*, 41(5):1640–1646, March 2008. 123, 126

[250] Nhamo Chaukura. Interaction of a Polymer of Intrinsic Microporosity (PIM-1) with Penetrants. *American Journal of Applied Chemistry*, 3(3):139, 2015. 123

[251] Jingshe Song, Naiying Du, Ying Dai, Gilles P. Robertson, Michael D. Guiver, Sylvie Thomas, and Ingo Pinnau. Linear High Molecular Weight Ladder Polymers by Optimized Polycondensation of Tetrahydroxytetramethylspirobisindane and 1,4-Dicyanotetrafluorobenzene†. *Macromolecules*, 41(20):7411–7417, October 2008. 123

[252] Songfeng Pei and Hui-Ming Cheng. The reduction of graphene oxide. *Carbon*, 50(9):3210–3228, August 2012. 124

[253] Goki Eda and Manish Chhowalla. Chemically Derived Graphene Oxide: Towards Large-Area Thin-Film Electronics and Optoelectronics. *Advanced Materials*, 22(22):2392–2415, June 2010. 124

[254] Kian Ping Loh, Qiaoliang Bao, Goki Eda, and Manish Chhowalla. Graphene oxide as a chemically tunable platform for optical applications. *Nature Chemistry*, 2(12):1015–1024, December 2010. 125

[255] Kian Ping Loh, Qiaoliang Bao, Priscilla Kailian Ang, and Jiaxiang Yang. The chemistry of graphene. *Journal of Materials Chemistry*, 20(12):2277, 2010. 125

[256] Cristina Vallés, Pablo Jiménez, Edgar Muñoz, Ana M. Benito, and Wolfgang K. Maser. Simultaneous Reduction of Graphene Oxide and Polyaniline: Doping-Assisted Formation of a Solid-State Charge-Transfer Complex. *The Journal of Physical Chemistry C*, 115(21):10468–10474, June 2011. 125

[257] Minas M. Stylianakis, Emmanuel Stratakis, Emmanuel Koudoumas, Emmanuel Kymakis, and Spiros H. Anastasiadis. Organic Bulk Heterojunction Photovoltaic Devices Based on Polythiophene–Graphene Composites. *ACS Applied Materials & Interfaces*, 4(9):4864–4870, September 2012. 125

[258] Qian Liu, Zunfeng Liu, Xiaoyan Zhang, Liying Yang, Nan Zhang, Guiling Pan, Shougen Yin, Yongsheng Chen, and Jun Wei. Polymer Photovoltaic Cells Based on Solution-Processable Graphene and P3HT. *Advanced Functional Materials*, 19(6):894–904, March 2009. 125

[259] Emin Istif, Javier Hernández-Ferrer, Esteban P. Urriolabeitia, Anastasios Stergiou, Nikos Tagmatarchis, Giuseppe Fratta, Matthew J. Large, Alan B. Dalton, Ana M. Benito, and Wolfgang K. Maser. Conjugated Polymer Nanoparticle-Graphene Oxide Charge-Transfer Complexes. *Advanced Functional Materials*, 28(23):1707548, June 2018. 125, 127, 130, 134

[260] Mengmeng Chen, Faizal Soyekwo, Qiugen Zhang, Chuan Hu, Aimei Zhu, and Qinglin Liu. Graphene oxide nanosheets to improve permeability and selectivity of PIM-1 membrane for carbon dioxide separation. *Journal of Industrial and Engineering Chemistry*, 63:296–302, July 2018. 125

[261] Elvin M. Aliyev, Muntazim Munir Khan, Afig M. Nabiyev, Rasim M. Alosmanov, Irada A. Bunyad-zadeh, Sergey Shishatskiy, and Volkan Filiz. Covalently Modified Graphene Oxide and Polymer of Intrinsic Microporosity (PIM-1) in Mixed Matrix Thin-Film Composite Membranes. *Nanoscale Research Letters*, 13(1), December 2018. 125

[262] Jens Weber, Naiying Du, and Michael D. Guiver. Influence of Intermolecular Interactions on the Observable Porosity in Intrinsically Microporous Polymers. *Macromolecules*, 44(7):1763–1767, April 2011. 127

[263] J. Kim and T. M. Swager. Control of conformational and interpolymer effects in conjugated polymers. *Nature*, 411(6841):1030–1034, June 2001. 127, 128

[264] Jangwon Seo, Sehoon Kim, and Soo Young Park. Strong Solvatochromic Fluorescence from the Intramolecular Charge-Transfer State Created by Excited-State Intramolecular Proton Transfer. *Journal of the American Chemical Society*, 126(36):11154–11155, September 2004. 128

[265] Kevin M. Noone, Selvam Subramaniyan, Qifeng Zhang, Guozhong Cao, Samson A. Jenekhe, and David S. Ginger. Photoinduced Charge Transfer and Polaron Dynamics in Polymer and Hybrid Photovoltaic Thin Films: Organic vs Inorganic Acceptors. *The Journal of Physical Chemistry C*, 115(49):24403–24410, December 2011. 128, 130

[266] T. L. Jennings, M. P. Singh, and G. F. Strouse. Fluorescent Lifetime Quenching near $d = 1.5$ nm Gold Nanoparticles: Probing NSET Validity. *Journal of the American Chemical Society*, 128(16):5462–5467, April 2006. 130

[267] Syamantak Khan, Abhishek Gupta, Navneet C. Verma, and Chayan K. Nandi. Time-Resolved Emission Reveals Ensemble of Emissive States as the Origin of Multicolor Fluorescence in Carbon Dots. *Nano Letters*, 15(12):8300–8305, December 2015. 130

[268] L. S. Panchakarla, K. S. Subrahmanyam, S. K. Saha, Achutharao Govindaraj, H. R. Krishnamurthy, U. V. Waghmare, and C. N. R. Rao. Synthesis, Structure, and Properties of Boron- and Nitrogen-Doped Graphene. *Advanced Materials*, pages NA–NA, August 2009. 130

[269] A. M. Rao, P. C. Eklund, Shunji Bandow, A. Thess, and R. E. Smalley. Evidence for charge transfer in doped carbon nanotube bundles from Raman scattering. *Nature*, 388(6639):257–259, July 1997. 130, 131

[270] Yuyoung Shin, Eric Prestat, Kai-Ge Zhou, Patricia Gorgojo, Khalid Althumayri, Wayne Harrison, Peter M. Budd, Sarah J. Haigh, and Cinzia Casiraghi. Synthesis and characterization of composite membranes made of graphene and polymers of intrinsic microporosity. *Carbon*, 102:357–366, June 2016. 130

[271] Yuanqin Yu, Ke Lin, Xiaoguo Zhou, Hua Wang, Shilin Liu, and Xingxiao Ma. New C-H Stretching Vibrational Spectral Features in the Raman Spectra of Gaseous and Liquid Ethanol†. *The Journal of Physical Chemistry C*, 111(25):8971–8978, June 2007. 131

[272] K. Saravanan, G. Jayalakshmi, K. Suresh, B. Sundaravel, B. K. Panigrahi, and D. M. Phase. Structural evaluation of reduced graphene oxide in graphene oxide during ion irradiation: X-ray absorption spectroscopy and *in-situ* sheet resistance studies. *Applied Physics Letters*, 112(11):111907, March 2018. 131

[273] M. B. Avinash, K. S. Subrahmanyam, Y. Sundarayya, and T. Govindaraju. Covalent modification and exfoliation of graphene oxide using ferrocene. *Nanoscale*, 2(9):1762, 2010. 131

[274] Matteo Bruna, Anna K. Ott, Mari Ijäs, Duhee Yoon, Ugo Sassi, and Andrea C. Ferrari. Doping Dependence of the Raman Spectrum of Defected Graphene. *ACS Nano*, 8(7):7432–7441, July 2014. 131

[275] S. J. Kim, S. J. Park, H. Y. Kim, G. S. Jang, D. J. Park, Ji-Yong Park, Soonil Lee, and Y. H. Ahn. Characterization of chemical doping of graphene by *in-situ* Raman spectroscopy. *Applied Physics Letters*, 108(20):203111, May 2016. 132

[276] A. Das, S. Pisana, B. Chakraborty, S. Piscanec, S. K. Saha, U. V. Waghmare, K. S. Novoselov, H. R. Krishnamurthy, A. K. Geim, A. C. Ferrari, and A. K. Sood. Monitoring dopants by Raman scattering in an electrochemically top-gated graphene transistor. *Nature Nanotechnology*, 3(4):210–215, April 2008. 132, 134

[277] Sayanti Samaddar, Johann Coraux, Sylvain C. Martin, Benjamin Grévin, Hervé Courtois, and Clemens B. Winkelmann. Equal variations of the Fermi level and work function in graphene at the nanoscale. *Nanoscale*, 8(33):15162–15166, 2016. 132

[278] A J Marsden, D G Papageorgiou, C Vallés, A Liscio, V Palermo, M A Bissett, R J Young, and I A Kinloch. Electrical percolation in graphene–polymer composites. *2D Materials*, 5(3):032003, June 2018. 132

[279] Veerappan Mani, Balamurugan Devadas, and Shen-Ming Chen. Direct electrochemistry of glucose oxidase at electrochemically reduced graphene oxide-multiwalled carbon nanotubes hybrid material modified electrode for glucose biosensor. *Biosensors and Bioelectronics*, 41:309–315, March 2013. 134

[280] Lucia Leonat, Gabriela Sbârcea, and Ioan Viorel Brânzoi. Cyclic Voltammetry for Energy Levels Estimation of Organic Materials. *U.P.B Sci. Bull.*, 75:111–118, 2013. 134

[281] Fei Zheng, Wei-Long Xu, Han-Dong Jin, Xiao-Tao Hao, and Kenneth P. Ghiggino. Charge transfer from poly(3-hexylthiophene) to graphene oxide and reduced graphene oxide. *RSC Advances*, 5(109):89515–89520, 2015. 134

[282] Rayko Ivanov Stantchev, Baoqing Sun, Sam M. Hornett, Peter A. Hobson, Graham M. Gibson, Miles J. Padgett, and Euan Hendry. Noninvasive, near-field terahertz imaging of

hidden objects using a single-pixel detector. *Science Advances*, 2(6):e1600190, June 2016. 136, 139, 149, 151

[283] Rayko I. Stantchev, Jessica C. Mansfield, Ryan S. Edginton, Peter Hobson, Francesca Palombo, and Euan Hendry. Subwavelength hyperspectral THz studies of articular cartilage. *Scientific Reports*, 8(1):6924, May 2018. 136, 139, 140, 144

[284] J. A. Fülöp, L. Pálfalvi, S. Klingebiel, G. Almási, F. Krausz, S. Karsch, and J. Hebling. Generation of sub-mJ terahertz pulses by optical rectification. *Optics letters*, 37(4):557–559, 2012. 136

[285] Juan S. Totero Gongora, Luana Olivieri, Luke Peters, Jacob Tunesi, Vittorio Cecconi, Antonio Cutrona, Robyn Tucker, Vivek Kumar, Alessia Pasquazi, and Marco Peccianti. Route to Intelligent Imaging Reconstruction via Terahertz Nonlinear Ghost Imaging. *Micromachines*, 11(5):521, May 2020. 137

[286] D Huang, E. Swanson, C. Lin, J. Schuman, W. Stinson, W Chang, M. Hee, T Flotte, K Gregory, C. Puliafito, and al. et. Optical coherence tomography. *Science*, 254(5035):1178–1181, November 1991. 138

[287] Liliana Borcea, George Papanicolaou, Chrysoula Tsogka, and James Berryman. Imaging and time reversal in random media. *Inverse Problems*, 18:1247–1279, 2002. 138

[288] Geoffroy Lerosey, Julien de Rosny, Arnaud Tourin, and Mathias Fink. Focusing Beyond the Diffraction Limit with Far-Field Time Reversal. *Science*, 315(5815):1120–1122, February 2007. 138

[289] Jacopo Bertolotti, Elbert G. van Putten, Christian Blum, Ad Lagendijk, Willem L. Vos, and Allard P. Mosk. Non-invasive imaging through opaque scattering layers. *Nature*, 491(7423):232–234, November 2012. 138

[290] Claudia Errico, Juliette Pierre, Sophie Pezet, Yann Desailly, Zsolt Lenkei, Olivier Couture, and Mickael Tanter. Ultrafast ultrasound localization microscopy for deep super-resolution vascular imaging. *Nature*, 527(7579):499–502, November 2015. 138

[291] Ioannis N. Papadopoulos, Jean-Sébastien Jouhanneau, James F. A. Poulet, and Benjamin Judkewitz. Scattering compensation by focus scanning holographic aberration probing (F-SHARP). *Nature Photonics*, 11(2):116–123, February 2017. 138

[292] Aaron V. Diebold, Mohammadreza F. Imani, Timothy Sleasman, and David R. Smith. Phaseless coherent and incoherent microwave ghost imaging with dynamic metasurface apertures. *Optica*, 5(12):1529, December 2018. 138

[293] Yair Rivenson, Yibo Zhang, Harun Günaydın, Da Teng, and Aydogan Ozcan. Phase recovery and holographic image reconstruction using deep learning in neural networks. *Light: Science & Applications*, 7(2):17141, February 2018. 138, 148

[294] Lianlin Li, Hengxin Ruan, Che Liu, Ying Li, Ya Shuang, Andrea Alù, Cheng-Wei Qiu, and Tie Jun Cui. Machine-learning reprogrammable metasurface imager. *Nature Communications*, 10(1):1082, March 2019. 138

[295] A.A. Gowen. Hyperspectral imaging - an emerging process analytical tool for food quality and safety control. *Trends in Food Science & Technology*, 2007. 138

[296] David Bannon. Cubes and slices. *Nature Photonics*, 3(11):627–629, November 2009. 138

[297] Guolan Lu and Baowei Fei. Medical hyperspectral imaging: a review. *Journal of Biomedical Optics*, 19(1):010901, January 2014. 138

[298] Wiebke Jahr, Benjamin Schmid, Christopher Schmied, Florian O. Fahrbach, and Jan Huisken. Hyperspectral light sheet microscopy. *Nature Communications*, 6(1):7990, November 2015. 138

[299] Iban Amenabar, Simon Poly, Monika Goikoetxea, Wiwat Nuansing, Peter Lasch, and Rainer Hillenbrand. Hyperspectral infrared nanoimaging of organic samples based on Fourier transform infrared nanospectroscopy. *Nature Communications*, 8(1):14402, April 2017. 138

[300] Xavier Hadoux, Flora Hui, Jeremiah K. H. Lim, Colin L. Masters, Alice Pébay, Sophie Chevalier, Jason Ha, Samantha Loi, Christopher J. Fowler, Christopher Rowe, Victor L. Villemagne, Edward N. Taylor, Christopher Fluke, Jean-Paul Soucy, Frédéric Lesage, Jean-Philippe Sylvestre, Pedro Rosa-Neto, Sulantha Mathotaarachchi, Serge Gauthier, Ziad S. Nasreddine, Jean Daniel Arbour, Marc-André Rhéaume, Sylvain Beaulieu, Mohamed Dirani, Christine T. O. Nguyen, Bang V. Bui, Robert Williamson, Jonathan G. Crowston, and Peter van Wijngaarden. Non-invasive in vivo hyperspectral imaging of the retina for potential biomarker use in Alzheimer's disease. *Nature Communications*, 10(1):4227, December 2019. 138

[301] Filiz Yesilkoy, Eduardo R. Arvelo, Yasaman Jahani, Mingkai Liu, Andreas Tittl, Volkan Cevher, Yuri Kivshar, and Hatice Altug. Ultrasensitive hyperspectral imaging and biodetection enabled by dielectric metasurfaces. *Nature Photonics*, 13(6):390–396, June 2019. 138

[302] Xiaoxia Yin, Brian W.-H. Ng, and Derek Abbott. *Terahertz Imaging for Biomedical Applications: Pattern Recognition and Tomographic Reconstruction*. Springer Science & Business Media, March 2012. 138

[303] D.H. Auston and M.C. Nuss. Electrooptical generation and detection of femtosecond electrical transients. *IEEE Journal of Quantum Electronics*, 24(2):184–197, February 1988. 138

[304] Ch. Fattinger and D. Grischkowsky. Terahertz beams. *Applied Physics Letters*, 54(6):490–492, February 1989. 138

[305] B. B. Hu and M. C. Nuss. Imaging with terahertz waves. *Optics Letters*, 20(16):1716–1716, August 1995. 138, 144

[306] Jeffrey H. Shapiro. Computational ghost imaging. *Physical Review A - Atomic, Molecular, and Optical Physics*, 78(6):061802–061802, December 2008. 139, 148, 151

[307] Yaron Bromberg, Ori Katz, and Yaron Silberberg. Ghost imaging with a single detector. *Physical Review A - Atomic, Molecular, and Optical Physics*, 79(5):053840–053840, May 2009. 139

[308] Wai Lam Chan, Kriti Charan, Dharmpal Takhar, Kevin F. Kelly, Richard G. Baraniuk, and Daniel M. Mittleman. A single-pixel terahertz imaging system based on compressed sensing. *Applied Physics Letters*, 93(12):121105, September 2008. 139, 149

[309] Claire M. Watts, David Shrekenhamer, John Montoya, Guy Lipworth, John Hunt, Timothy Sleasman, Sanjay Krishna, David R. Smith, and Willie J. Padilla. Terahertz compressive imaging with metamaterial spatial light modulators. *Nature Photonics*, 8(8):605–609, August 2014. 139, 149

[310] T Yuan, J.Z Xu, and X.-C Zhang. Development of terahertz wave microscopes. *Infrared Physics & Technology*, 45(5-6):417–425, October 2004. 139

[311] Manuel Unternährer, Bänz Bessire, Leonardo Gasparini, Matteo Perenzoni, and André Stefanov. Super-resolution quantum imaging at the Heisenberg limit. *Optica*, 5(9):1150–1154, September 2018. 139

[312] Austin P. Spencer, Boris Spokoyny, Supratim Ray, Fahad Sarvari, and Elad Harel. Mapping multidimensional electronic structure and ultrafast dynamics with single-element detection and compressive sensing. *Nature Communications*, 7(1), December 2016. 139

[313] David B. Phillips, Ming-Jie Sun, Jonathan M. Taylor, Matthew P. Edgar, Stephen M. Barnett, Graham M. Gibson, and Miles J. Padgett. Adaptive foveated single-pixel imaging with dynamic supersampling. *Science Advances*, 3(4):e1601782, April 2017. 139

[314] B. Sun, M. P. Edgar, R. Bowman, L. E. Vittert, S. Welsh, A. Bowman, and M. J. Padgett. 3D Computational Imaging with Single-Pixel Detectors. *Science*, 340(6134):844–847, May 2013. 139

[315] Caroline Amiot, Piotr Ryczkowski, Ari T. Friberg, John M. Dudley, and Goëry Genty. Supercontinuum spectral-domain ghost imaging. *Optics Letters*, 43(20):5025–5028, October 2018. 139

[316] Han Wu, Piotr Ryczkowski, Ari T. Friberg, John M. Dudley, and Goëry Genty. Temporal ghost imaging using wavelength conversion and two-color detection. *Optica*, 6(7):902, July 2019. 139

[317] Ryan S Bennink, Sean J Bentley, and Robert W Boyd. "Two-Photon" coincidence imaging with a classical source. *Physical review letters*, 89(11):113601–113601, August 2002. 139

[318] Yoann Altmann, Stephen McLaughlin, Miles J. Padgett, Vivek K. Goyal, Alfred O. Hero, and Daniele Faccio. Quantum-inspired computational imaging. *Science*, 361(6403):eaat2298, August 2018. 139

[319] Hugo Defienne, Matthew Reichert, Jason W. Fleischer, and Daniele Faccio. Quantum image distillation. *Science Advances*, 5(10):eaax0307, October 2019. 139

[320] Piergiorgio Caramazza, Oisín Moran, Roderick Murray-Smith, and Daniele Faccio. Transmission of natural scene images through a multimode fibre. *Nature Communications*, 10(1):1–6, May 2019. 139

[321] Ashley Lyons, Francesco Tonolini, Alessandro Boccolini, Audrey Repetti, Robert Henderson, Yves Wiaux, and Daniele Faccio. Computational time-of-flight diffuse optical tomography. *Nature Photonics*, 13(8):575–579, August 2019. 139

[322] Rayko I. Stantchev, David B. Phillips, Peter Hobson, Samuel M. Hornett, Miles J. Padgett, and Euan Hendry. Compressed sensing with near-field THz radiation. *Optica*, 4(8):989–992, August 2017. 139, 140, 141, 142, 144, 149, 151

[323] Si-Chao Chen, Liang-Hui Du, Kun Meng, Jiang Li, Zhao-Hui Zhai, Qi-Wu Shi, Ze-Ren Li, and Li-Guo Zhu. Terahertz wave near-field compressive imaging with a spatial resolution of over $\lambda/100$. *Optics Letters*, 44(1):21, January 2019. 139, 140, 144, 149

[324] Hichem Guerboukha, Kathirvel Nallappan, and Maksim Skorobogatiy. Exploiting k-space/frequency duality toward real-time terahertz imaging. *Optica*, 5(2):109–116, February 2018. 141

[325] Ming-Jie Sun, Ling-Tong Meng, Matthew P. Edgar, Miles J. Padgett, and Neal Radwell. A Russian Dolls ordering of the Hadamard basis for compressive single-pixel imaging. *Scientific Reports*, 7(1), December 2017. 141, 154, 156

[326] M. Peccianti, M. Clerici, A. Pasquazi, L. Caspani, S. P. Ho, F. Buccheri, J. Ali, A. Busacca, T. Ozaki, and R. Morandotti. Exact Reconstruction of THz Sub-λSource Features in Knife-Edge Measurements. *IEEE Journal of Selected Topics in Quantum Electronics*, 19(1):8401211–8401211, January 2013. 142, 151

[327] Alexey Tikan, Serge Bielawski, Christophe Szwaj, Stéphane Randoux, and Pierre Suret. Single-shot measurement of phase and amplitude by using a heterodyne time-lens system and ultrafast digital time-holography. *Nature Photonics*, 12(4):228, April 2018. 148

[328] Yoav Shechtman, Yonina C. Eldar, Oren Cohen, Henry Nicholas Chapman, Jianwei Miao, and Mordechai Segev. Phase Retrieval with Application to Optical Imaging: A contemporary overview. *IEEE Signal Processing Magazine*, 32(3):87–109, May 2015. 148

[329] Erwin Hack and Peter Zolliker. Terahertz holography for imaging amplitude and phase objects. *Optics Express*, 22(13):16079, June 2014. 148

[330] Ho-Jin Song and Tadao Nagatsuma. *Handbook of Terahertz Technologies: Devices and Applications*. CRC Press, 2015. 148, 159

[331] Liu Yu, Liu Hao, Tang Meiqiong, Huang Jiaoqi, Liu Wei, Dong Jinying, Chen Xueping, Fu Weiling, and Zhang Yang. The medical application of terahertz technology in non-invasive detection of cells and tissues: opportunities and challenges. *RSC Advances*, 9(17):9354–9363, 2019. 148

[332] Xiang Yang, Xiang Zhao, Ke Yang, Yueping Liu, Yu Liu, Weiling Fu, and Yang Luo. Biomedical Applications of Terahertz Spectroscopy and Imaging. *Trends in Biotechnology*, 34(10):810–824, October 2016. 148

[333] Daniel M. Mittleman. Twenty years of terahertz imaging [Invited]. *Optics Express*, 26(8):9417–9431, April 2018. 148, 153

[334] Alan WeiMin Lee and Qing Hu. Real-time, continuous-wave terahertz imaging by use of a microbolometer focal-plane array. *Optics letters*, 30(19):2563–2565, 2005. 148

[335] Emmanuel Abraham, Harsono Cahyadi, Mathilde Brossard, Jérôme Degert, Eric Freysz, and Takeshi Yasui. Development of a wavefront sensor for terahertz pulses. *Optics Express*, 24(5):5203, March 2016. 148

[336] Paul-Antoine Moreau, Ermes Toninelli, Thomas Gregory, and Miles J. Padgett. Ghost Imaging Using Optical Correlations. *Laser & Photonics Reviews*, 12(1):1700143, January 2018. 148

[337] Miles J. Padgett and Robert W. Boyd. An introduction to ghost imaging: quantum and classical. *Philosophical Transactions of the Royal Society A: Mathematical, Physical and Engineering Sciences*, 375(2099):20160233, August 2017. 148, 157

[338] Baris I. Erkmen and Jeffrey H. Shapiro. Ghost imaging: from quantum to classical to computational. *Advances in Optics and Photonics*, 2(4):405, December 2010. 148

[339] L. Olivieri, J.S. Totero Gongora, A. Pasquazi, and M. Peccianti. Time-resolved nonlinear ghost imaging: Route to hyperspectral single-pixel reconstruction of complex samples at THz frequencies. In *Nonlinear Frequency Generation and Conversion: Materials and Devices XVIII*, San Francisco, CA, USA, 2019. SPIE. 149

[340] Kedar Khare. *Fourier optics and computational imaging*. Wiley, John Wiley & Sons Ltd, Chichester, West Sussex, 2016. OCLC: 935538133. 152, 153

[341] Martin Harwit and N. J. A. Sloane. *Hadamard transform optics*. Academic Press, New York, 1979. 153

[342] D. Scott Davis. Multiplexed imaging by means of optically generated Kronecker products: 1. The basic concept. *Applied optics*, 34(7):1170–1176, 1995. 153

[343] Lee Streeter, G. R. Burling-Claridge, M. J. Cree, and Rainer Künnemeyer. Optical full Hadamard matrix multiplexing and noise effects. *Applied optics*, 48(11):2078–2085, 2009. 153

[344] Yonina C. Eldar and Gitta Kutyniok, editors. *Compressed sensing: theory and applications*. Cambridge University Press, Cambridge ; New York, 2012. 153

[345] Shi Dongfeng, Huang Jian, Meng Wenwen, Yin Kaixin, Sun Baoqing, Wang Yingjian, Yuan Kee, Xie Chenbo, Liu Dong, and Zhu Wenyue. Radon single-pixel imaging with projective sampling. *Optics Express*, 27(10):14594–14609, May 2019. 153

[346] Meng Wenwen, Meng Wenwen, Shi Dongfeng, Shi Dongfeng, Huang Jian, Huang Jian, Yuan Kee, Yuan Kee, Yuan Kee, Wang Yingjian, Wang Yingjian, Fan Chengyu, and Fan Chengyu. Sparse Fourier single-pixel imaging. *Optics Express*, 27(22):31490–31503, October 2019. 153

[347] A. Hedayat and W. D. Wallis. Hadamard Matrices and Their Applications. *The Annals of Statistics*, 6(6):1184–1238, November 1978. 154

[348] Le Wang and Shengmei Zhao. Fast reconstructed and high-quality ghost imaging with fast Walsh–Hadamard transform. *Photonics Research*, 4(6):240, December 2016. 154

[349] F. Rousset, N. Ducros, A. Farina, G. Valentini, C. D'Andrea, and F. Peyrin. Adaptive Basis Scan by Wavelet Prediction for Single-Pixel Imaging. *IEEE Transactions on Computational Imaging*, 3(1):36–46, March 2017. 154

[350] Vladislav Kravets, Paul Kondrashov, and Adrian Stern. Compressive ultraspectral imaging using multiscale structured illumination. *Applied Optics*, 58(22):F32–F39, August 2019. 154, 162

[351] Max Born and Emil Wolf. *Principles of optics: electromagnetic theory of propagation, interference and diffraction of light*. Cambridge University Press, Cambridge ; New York, 7th expanded ed edition, 1999. 157

[352] Huidong Dai, Guohua Gu, Weiji He, Fajian Liao, Jiayan Zhuang, Xingjiong Liu, and Qian Chen. Adaptive compressed sampling based on extended wavelet trees. *Applied Optics*, 53(29):6619, October 2014. 162

[353] Huidong Dai, Guohua Gu, Weiji He, Ling Ye, Tianyi Mao, and Qian Chen. Adaptive compressed photon counting 3D imaging based on wavelet trees and depth map sparse representation. *Optics Express*, 24(23):26080, November 2016. 162

[354] George Barbastathis, Aydogan Ozcan, and Guohai Situ. On the use of deep learning for computational imaging. *Optica*, 6(8):921, August 2019. 162

Appendix A

Published Paper: Charge Transfer Hybrids of Graphene Oxide and the Intrinsically Microporous Polymer PIM-1

As I had rapidly gained advanced competences in nonlinear surfaces, free-carrier dynamics and pump-probe methodologies, I joined a collaboration with the Material's Physics Group at the University of Sussex. They had developed hybrids of nanoparticles of a novel polymer of intrinsic microporosity (PIM) with graphene oxide (GO) nanosheets. PIM-1 in particular has been suggested as a new material with efficient charge transport and semiconducting properties suitable for low cost, flexible polymer light-emitting diodes [239]. Furthermore, the microporous nature of the polymer structures make it an exciting material for heterogeneous catalysis [240]. Introducing other materials such as GO into hybrids can both further the understanding of the optoelectronic properties of the PIM-1 nanoparticles, the signature of which was still unexamined in literature.

My role in this work was to investigate the ultrafast charge transport properties of the PIM-1/GO nanohybrids by performing transient absorption measurements of three samples, pure PIM-1, pure GO, and a 50% hybrid. I designed and performed the experiment, including the data analysis, fitting and retrieval of the decay time constants, the result of which can be seen in figure 2F. I also contributed significantly to the writing of the section of the text referencing the figure and the description of the experimental setup. The article was submitted to Applied Materials and Interfaces on the 5^{th} June 2019 and was published on the 2^{nd} August 2019.

A.1 Summary

The article presents a thorough characterisation of the optical properties and the electronic charge transfer dynamics of nanohybrids of PIM-1/GO. This is initially done via time-resolved photo-luminescence spectroscopy, where the sample is photoexcited with a pump pulse at an above band-gap excitation wavelength of 358nm. The spontaneous recombination is then observed by the emission of photons with an energy equal to the band-gap, corresponding to a wavelength of 510nm, which is then mapped over nanoseconds by observing the decay in the brightness of the photo-emission. While the photo-carrier lifetime can be extracted from these measurements, with the hybrids demonstrating a faster recovery, charge transfer typically occurs on much shorter timescales. The second characterisation therefore was the transient absorption spectroscopy, to observe the carrier dynamics on sub-picosecond timescales. In this measurement, a strong ultrashort ($<$ 100fs) pump pulse at 400nm was exploited to excite carriers into the conduction band of the samples. The enhanced conductivity is then mapped by observing the modulation in the transmission of a weak 800nm probe pulse, which otherwise doesn't interfere with the sample. By delaying the pump pulse with respect to the probe pulse, the decay of the differential transmission provides insight into the carrier drift, diffusion and recombination dynamics. Noteworthy, was that the hybrids displayed a shorter recovery when compared to the GO samples, evidence that the PIM-1 polymer has provided additional trap states and charge transfer pathways for the photocarriers. As these measurements provided evidence for excited state charge transfer between the two materials, Raman mapping and Kelvin probe force microscopy was used to observe modifications to the doping density and work function of the nanohybrid. From this thorough characterisation, a simple model of the charge transfer interaction was then presented as an alignment of their Fermi levels and the movement of excitons from the GO across the PIM-1 before recombination and photon emission.

A.2 Impact

This publication targeted the American Chemical Society journal Applied Materials and Interfaces, which has a 5-year impact factor of 8.456. The journal scope covers the development of novel polymers and composite materials such as PIM-1/GO, surface and interface physics, as well as in the application of electronic devices / catalysis. Clearly therefore, the journal provided a perfect fit for this article.

Since publication, the article is yet to be cited or presented at any conferences.

A.3 Journal Article

A.3.1 Abstract

Nanohybrid materials based on nanoparticles of the intrinsically microporous polymer PIM-1 and graphene oxide (GO) are prepared from aqueous dispersions with a reprecipitation method, resulting in the surface of the GO sheets being decorated with nanoparticles of PIM-1. The significant blueshift in fluorescence signals for the GO/PIM-1 nanohybrids indicates modification of the optoelectronic properties of the PIM-1 in the presence of the GO due to their strong interactions. The stiffening in the Raman G peak of GO (by nearly 6cm^{-1}) further indicates p-doping of the GO in the presence of PIM. Kelvin probe force microscopy (KPFM) and electrochemical reduction measurements of the nanohybrids provide direct evidence for charge transfer between the PIM-1 nanoparticles and the GO nanosheets. These observations will be of importance for future applications of GO-PIM-1 nanohybrids as substrates and promoters in catalysis and sensing.

A.3.2 Introduction

Charge transfer processes on the nanoscale play a key role in a range of organic electronic devices such as solar cells [241], light emitting diodes [242], and field-effect transistors [243, 244]. The efficiency of charge transfer at the interfaces between the electron-donating and electron-accepting materials is critical to the performance of such devices. The effect of charge transfer is also observed in the fields of sensing and catalysis [245]. In particular, the charging effect between the individual component [245] and the substrates [246] could facilitate the formation of conductive phases thus further promoting the catalytic efficiency [247].

Polymers of intrinsic microporosity (PIMs) have emerged as a novel class of materials in a range of applications including gas permeation [248, 249, 250], gas separation [249, 250], and hydrogen storage [248]. In particular, a polybenzodioxane polymer, PIM-1, the first synthesized soluble and processable PIM (see structure in Figure A.1A), due to its conjugated nature, exhibits strong fluorescence and is solution processable allowing it to be cast as a transparent, yellow-tinted freestanding film. Recently, it has been suggested that PIM-1 possesses n-type semiconductor characteristics and efficient electron charge transport for low cost and flexible polymer light-emitting diodes (PLEDs) [239]. Moreover, PIM-1 exhibits molecularly rigid and constrained structures leading to microporosity, which make it a useful material for heterogeneous catalysis [251]. Introduction of other materials to form the hybrids seems to be a feasible route to further understand and improve the properties of PIM-1. However, to the best of our

knowledge, the nanoscale electronic properties and the associated optical signature of the PIM-1 nanohybrids have never been reported.

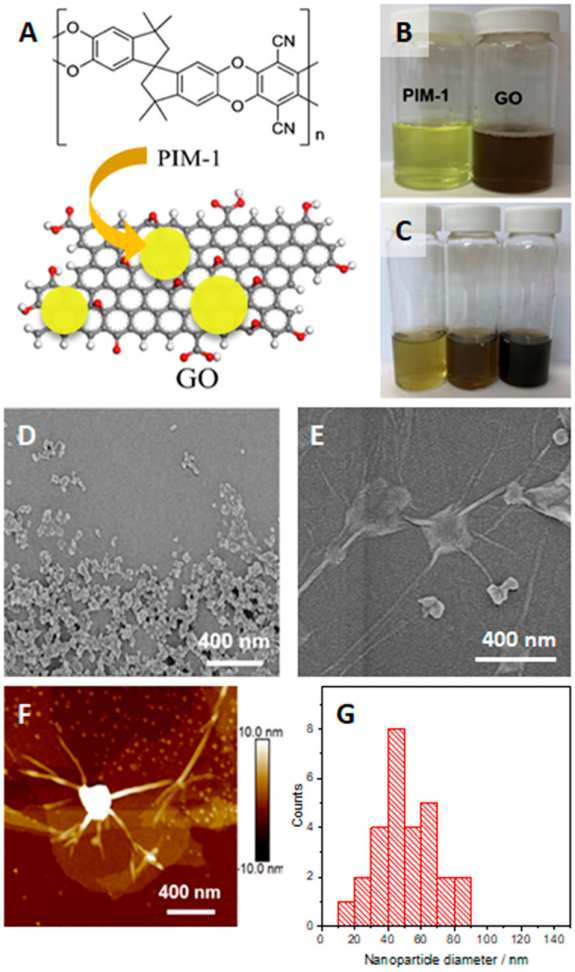

Figure A.1: (A) Molecular structure of PIM-1 and schematic illustrating the formation of GO/PIM-1 charge transfer nanohybrid materials. (B) Photographs of aqueous dispersions of PIM-1 nanoparticles and GO. (C) Photographs of the GO/PIM-1 nanohybrids with 33, 50, and 67 wt % GO from left to right. (D) Scanning electron micrograph of PIM-1 nanoparticles on a silicon wafer and (E) GO/PIM-1 (50wt%) nanohybrid. (F) Atomic force micrograph of the nanohybrid in E. (G) Particle size histogram from AFM for the GO/PIM-1 nanohybrid.

Graphene oxide (GO) is usually employed as a precursor for the large-scale production of graphene [252] because of two important characteristics, solution processability from aqueous colloidal dispersions and synthetic accessibility from inexpensive raw graphite. Recently, GO has been highlighted not only for its relevance to graphene production but also for its own unique chemical structure and characteristics, which enable new applications in fields like catalysis, electronics, and optolelectronics [253]. One of the most interesting properties of GO is related to its heterogeneous electronic structure, which results from the existence of both sp^2

and sp^3 hybridized carbon atoms [254] in an atomically thin 2D nanosheet. The presence of functional groups on the basal plane and at the edges of GO allow interaction with a range of chemicals through either covalent or noncovalent bonds to produce nanohybrid materials with novel properties [255]. The charge-transfer phenomena between graphene and conjugated polymers have been extensively reported, and the resulting nanohybrids exhibit enhanced conductivity and better efficiency, for example, in photovoltaic devices [256, 257, 258]. However, the interesting properties of graphene oxide nanohybrids with polymer systems are only beginning to emerge. In previous work [259], we employed the reprecipitation approach to prepare conjugated polymer/GO nanohybrids to facilitate the intimate contact between both materials. These nanohybrids were found to exhibit interesting charge transfer behavior. Hence, it is of great interest to apply this same approach to develop novel GO-functionalized or nanohybrid materials and to understand and tailor nanohybrid properties. Previous work on hybridization of graphene oxide and polymers of intrinsic microporosity has been sparse. Graphene oxide has been incorporated into PIM-1 membranes with enhanced gas transport and gas separation performance [260, 261], but the nanoscale interactions between these two materials have not previously been investigated. Here, a novel type of nanohybrid is studied based on these two interesting materials, graphene oxide and the fluorescent polymer of intrinsic microporosity (PIM-1), in order to reveal the inherent electronic properties.

In this paper, we demonstrate the presence of localized charge transfer effects based on extensive characterization of GO/PIM-1 nanohybrids (illustrated in Figure A.1). The nanohybrid materials were fabricated in water dispersions with varying GO concentration. The structural morphology was characterized by scanning electron microscopy (SEM) and atomic force microscopy (AFM). UV–visible photoluminescence (both steady-state and time-resolved) and Raman spectroscopies were employed to understand the interaction and resultant optoelectronic properties. Electrochemical measurements were performed to characterize the ease of reduction of GO to graphene as a function of PIM-1 polymer content. It is illustrated that charge transfer in the nanohybrid materials is likely to cause tuning of some spectroscopic and surface properties for both GO and PIM-1. This opens up opportunities for further exploration, in particular for microporous nanocomposites as substrates/promoters for catalysis and for sensing.

A.3.3 Experimental Section

Chemical Reagents

Polymer PIM-1 was prepared following a literature recipe; the dibenzodioxane formation reaction was performed using the commercially available bis-catechol $5,5',6,6'$-tetrahydroxy-

3, 3, 3′, 3′-tetramethyl-1, 1′-spirobisindane and 2, 3, 5, 6-tetrafluororo-terephthalonitrile [249]. Graphene oxide in an aqueous dispersion (25mg/mL) was obtained from Graphenea (San Sebastián, Spain) (flake size $\sim 10\mu$m, monolayers, C/O ratio ~ 2.1). Tetrahydrofuran, phosphoric acid (85%), and sodium hydroxide were purchased from Fisher Scientific and used without further purification. Solutions were prepared with deionized water of resistivity of 18.2MΩ·cm freshly prepared using a Thermo Scientific Barnstead Smart2Pure purifier.

Synthesis of GO-PIM-1 Nanohybrid Materials in Dispersion

PIM-1 nanoparticles and GO/PIM-1 nanohybrids were synthesized using the reprecipitation method. A volume of 1mL of PIM-1 in THF solution (1mg/mL) was added into 20mL of GO water dispersion (GO weight, 0mg, 0.5mg, 1mg, or 2mg) drop-by-drop under vigorous stirring (6000rpm for 10min) in a Silverson LM5-A high shear mixer. The GO/PIM weight ratios in the resulting nanohybrid dispersions in water were 33, 50, and 67 wt %, respectively.

Characterization

Scanning electron microscopy (SEM) measurements were performed using the Zeiss SIGMA field emission gun (FEG-SEM). The working conditions were an accelerating voltage of 1.00kV and working distance of 2mm. AFM was performed on thin films coated on a silicon wafer with a Bruker Dimension Icon in QNM mode and KPFM mode. Silicon probes doped with nitrogen (PFQNE-Al) were used for the investigation, $Kn \gg 0.6 \pm 0.1$N/m. Freshly cleaved HOPG was used as a reference to measure the work function of the tip (4.31 ± 0.04eV) in ambient air conditions at 33% humidity. The VCPD (contact potential difference) data was recorded at a lift height of 10nm. UV–vis absorption spectra were recorded with Shimadzu UV3600Plus UV–vis–NIR from 250 to 600nm. Photoluminescence emission spectroscopy was performed on a Shimadzu RF 6000, and time-resolved photoluminescence was performed using a Horiba Deltaflex with a 10mm path-length quartz cuvette with an excitation wavelength of 358nm. All the PL measurements were carried out with the samples exhibiting the same optical density to be consistent. Raman spectroscopy was carried out with a Renishaw inVia Raman-AFM with an excitation wavelength of 660nm.

Electrochemical measurements were recorded with a Gamry Reference 600+ potentiostat with glassy carbon as the working electrode (3mm diameter, BASi), platinum wire as the counter electrode, and Ag/AgCl (3M KCl) as the reference electrode in phosphate buffer solution. A volume of 4mL of GO and GO/PIM-1 nanohybrid dispersions was deposited onto the glassy carbon electrode. Cyclic voltammetry experiments were performed (scan rate 10mVs^{-1}) to

investigate the electrochemical reduction of GO in aqueous 0.1M PBS, $pH = 5$. Size distribution measurements were performed with an Anton Paar Litesizer 500 particle analyzer.

A.3.4 Results and Discussion

Figure 1A schematically illustrates the chemical structures of the component materials. PIM-1 nanoparticles and GO/PIM-1 nanohybrids dispersed in water were synthesized using a reprecipitation method. The polymer is dissolved in a good solvent (THF) which is miscible with an antisolvent. Mixing of these two dispersions causes the solvated polymer chains to contract and precipitate as solid nanoparticles. Stable dispersions were obtained by this method (see Figure A.1B,C) with 1mg of PIM-1 and 0.0, 0.5, 1.0, or 2.0mg of GO in 20mL of water. The morphology of PIM-1 nanoparticles and GO/PIM-1 nanohybrids were studied by scanning electron microscopy (SEM) and atomic force microscopy (AFM). Figure 1D shows that uniform PIM-1 nanoparticles are successfully prepared, and they are smaller than 100nm in diameter. For the nanohybrids, Figure A.1E,F suggests that PIM-1 nanoparticles formed in the GO dispersion tended to graft uniformly to the surface of the GO sheets. The particle size histogram (Figure A.1G) produced from AFM images of the hybrids is consistent with observations of the pristine PIM-1 nanoparticles.

PIM-1 is a nonconductive molecule with interesting nanoscale structural and optical properties. As such investigation of the optical properties can yield information on the interactions of the PIM-1 chains with one another and their environment. It has been suggested that intermolecular interactions, such as hydrogen bonding, could lead to rearrangement of PIM-1 chains in different molecular environments (as may be produced through the reprecitpitation process), but it is hard to completely confirm [262]. To the best of our knowledge, the effect of chain arrangement of PIM-1 on optical and electronic properties has never been reported. As for other conjugated polymers, there is extensive prior work in the literature [263]. Indeed, our previous work on nanohybrids of poly(3-hexylthiophene) (P3HT) showed evidence for polymer conformational effects in the form of vibronic features in the optical spectroscopy measurements [259]. UV–visible extinction spectra are shown in Figure A.2A for PIM-1 nanoparticles and for GO/PIM-1 nanohybrids in an aqueous dispersion over a wavelength range of 250 to 600nm. In agreement with previously reported data [239], two intense peaks are observed for PIM-1. The peak centered around 291nm corresponds to the $\sigma - \pi^*$ transition, and the peak centered at 429nm arises from a $\pi - \pi^*$ transition, which is commonly observed for conjugated aromatic compounds. In the hybrid materials, both absorption peaks for PIM-1 are observed to be diminished and slightly red-shifted with increasing GO content (see also Figure S1 for a

second derivative plot of the data in Figure A.2A). The inset in Figure A.2A shows the optical bandgaps of the component materials derived from Tauc plots (see Figure S2) of the UV–vis spectra. We observe a negligible trend in the optical gap with increasing GO content in the hybrids, suggesting that there is no strong structural or chemical interactions of the component materials. This suggests the observed peak shift of the PIM-1 UV–vis features is likely due to increased scattering caused by the addition of GO [263].

PIM-1 exhibits strong fluorescence due to the presence of conjugated ring groups within the polymer backbone [264] (see Figure A.1A). The spectra in Figure A.2B show that the fluorescence intensity is quenched by the presence of GO (see also Figure S3). The inset in Figure A.2B shows that the peak intensity scales approximately linearly with the GO/PIM-1 ratio. Additionally, the emission peak is significantly blue-shifted (see also a Gaussian deconvolution in Figure S4), which indicates a strong interaction between these two materials [265]. Since there is no significant change to the PIM-1 optical gap we can reason that the decrease in the Stokes shift (see also emission and excitation spectra in Figure S5) in the hybrid indicates a decrease in the exciton binding energy [264]. The Stokes shift is approximately 200meV in the pristine PIM and is reduced by $\sim$ 75meV in the hybrid. In many conjugated systems the Stokes shift, determined from the difference in energy of the absorption edge and emission energy, is found to decrease as the rigidity of the polymer backbone is increased. Similar effects may be responsible for the observed decrease in Stokes shift in the nanohybrids. Moreover, the energy gap for an electronic transition of a chromophore is influenced by the fluctuations in the environment. In our hybrid systems, as the GO content increases, it may be that the associated reduction in Stokes shift can be explained by a steric interaction of the PIM-1 adsorbed onto the GO.

Figure A.2C,D shows the time-resolved emission spectra under 358nm excitation. Although it is not the optimum excitation for this measurement, the energy is above the optical gap and as such can still produce excited carriers, which relax nonradiatively before PL emission. In addition, the lower emission intensity does not influence the PL lifetime measurement for the same emission energy between the excited state and the ground state. Both plots have a contour at 50% intensity (relative to peak emission) which show that the hybrid lifetime is reduced over the whole emission range. Since the maximum position of the fluorescence peak is at 510nm for excitation at 358nm, Figure A.2E shows the temporal decay curves at this wavelength ($\lambda_{em} = 510$nm) for both the PIM-1 nanoparticles and the GO/PIM-1 nanohybrid. The decay data for the pristine nanoparticles is best fitted to a double-exponential function with component lifetimes of $\tau_1 = 0.66$ns and $\tau_2 = 2.66$ns. Delocalization of the electron–hole pair across two chains gives longer-lived PL while the exciton confined to a single chain gives

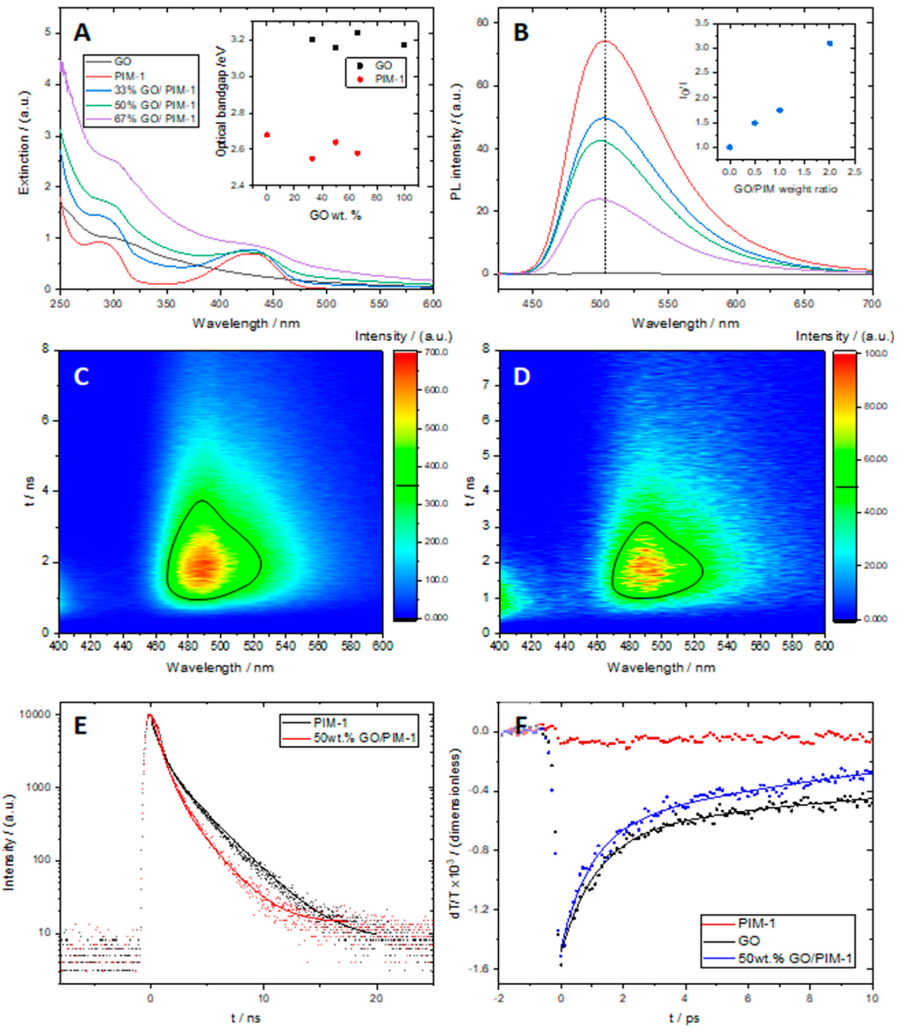

Figure A.2: (A) UV–vis extinction spectra for GO, PIM-1 nanoparticles, and GO/PIM-1 nanohybrids in aqueous dispersion. (Inset) Optical bandgap energies for the component materials in all dispersions, measured from Tauc plots. (B) Steady-state fluorescence data ($\lambda_{ex} = 358$nm) for PIM-1 nanoparticles and GO/PIM-1 nanohybrids. (Inset) Relative fluorescence intensity versus the GO/PIM-1 weight ratio. Time-resolved emission spectral data for PIM-1 nanoparticles (C) and GO-PIM-1 nanohybrids (D). The black contour denotes 50% of the peak intensity in both cases. (E) Single-wavelength time-resolved fluorescence decay curve ($\lambda_{ex} = 358$nm, $\lambda_{em} = 510$nm) for PIM-1 nanoparticles and GO/PIM-1 nanohybrids. (F) Transient differential transmission curves for GO, PIM-1 nanoparticles, and GO/PIM-1 hybrids as a function of pump–probe delay with a 400nm pump (5.4GW/cm^2) and a 800nm probe (0.6GW/cm^2).

short-lived PL. This is due to an increase in electron–hole wave function overlap (and hence recombination probability) for decreasing binding radius. Therefore, we attribute the two component lifetimes to intra- and interchain emission, respectively. In the hybrids, the short-lived

intrachain component is unmodified while the long-lived interchain component reduces in intensity and lifetime [259, 266, 267]. As such we observe a consistent reduction of the total PL lifetime of GO/PIM-1 nanohybrids with increasing mass ratios (33, 50, 67wt% GO) (see Figure S6).

The photophysical properties of the nanohybrids were further investigated by pump–probe transient absorption measurements (Figure A.2F). In this technique a pump pulse (at 400nm) is employed to generate a population of electrons in an excited state which are then probed with delayed pulses (at 800nm) to investigate the effect of the modified electron population on the transient absorption. This method facilitates investigation of the short-time carrier dynamics in the GO and how the addition of the PIM-1 modifies this behavior. Since PIM-1 does not contain extended conjugated segments, charges elevated to excited states by the pump pulse do not contribute to the optical behavior below the HOMO–LUMO transition energy; this results in the negligible change in sample transmittance observed in Figure A.2. In GO, charges elevated by the pump pulse are free to move due to extended (though not globally connected) conjugated regions. This carrier mobility means that the generated population of carriers acts as a free electron gas, increasing the sample reflectance (and lowering the transmittance) at the probe photon energy, which is below the bandgap of the material. Depopulation of this excited state, and therefore recovery of the sample transmittance, can occur by recombination of the electron–hole pairs or by charge trapping. The data for both pristine GO and the nanohybrid were fitted with double exponential functions (shown in Figure A.2F). For the pristine GO the time constants τ_1 and τ_2 were 1.15 and 23.6ps, respectively. For the GO/PIM-1 nanohybrid the corresponding values were $\tau_1 = 0.94$ps and $\tau_2 = 11.4$ps. A significant decrease in the transient state lifetime of GO with the presence of adsorbed PIM-1 nanoparticles is noted, suggesting an increase in recombination rate as carriers become trapped by PIM states through nonradiative energy loss (and are subsequently able to undergo radiative relaxation) [265].

Given the spectroscopic evidence of excited state charge transfer between the two materials in the nanohybrid, we applied other characterization techniques to elucidate the presence of any ground state interactions. Raman spectroscopy is convenient for this purpose, as it has been demonstrated that electronic doping of the extended conjugated regions of graphene materials causes reproducible shifts to their characteristic Raman features [268, 269]. The Raman spectrum (660nm excitation) for PIM-1 nanoparticles is shown in Figure A.3A. There are several modes in the range between 1300 and 1700cm^{-1}, which are consistent with the reported Raman spectrum for PIM-1 [270] and arise from the conjugated ring species present in the polymer backbone (see Figure A.1A). An intense mode at 2236cm^{-1} is attributed to $C \equiv N$

bond stretching, and the broad feature centered at 2900cm^{-1} can be attributed to the various C–H stretches [271].

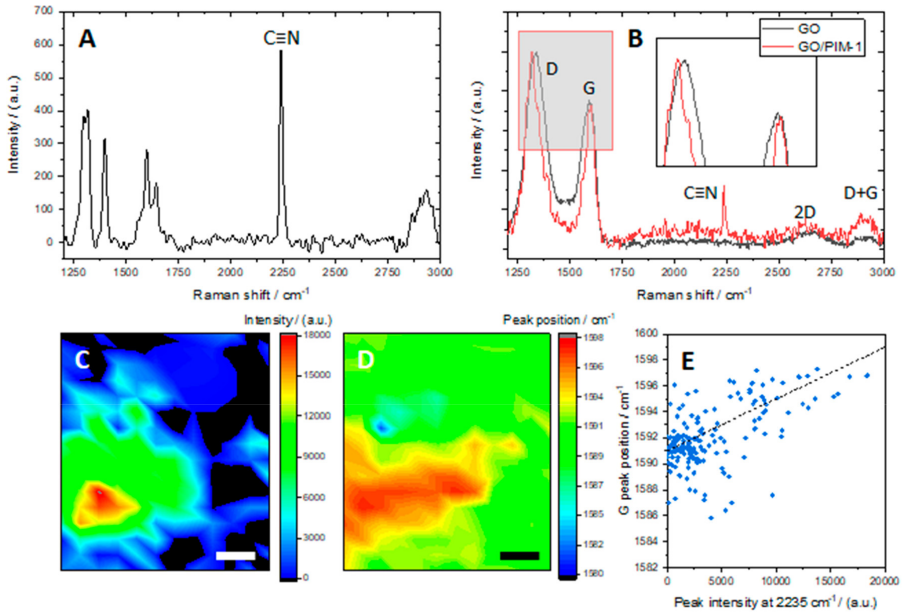

Figure A.3: (A) Raman spectrum for PIM-1 nanoparticles ($\lambda_{ex} = 660$nm). (B) Comparison of normalized Raman data for GO and GO/PIM-1. The highlighted area is enlarged in the inset, for clarity. (C, D) Raman mapping for GO/PIM-1 nanohybrids, showing the peak intensity at 2236cm^{-1} and G peak position, respectively. Scale bars are 5μm. (E) Pixelwise correlation analysis of the G peak position and the peak intensity at 2236cm^{-1} for GO/PIM-1 nanohybrids. The line shown is a guide to the eye based on the observed G peak shifts in the low-magnification point spectra.

Figure A.3B compares normalized Raman spectra of GO and the GO/PIM-1 nanohybrids. For GO the typical D-peak at 1335cm^{-1} and G-peak at 1590cm^{-1} are observed in addition to the 2D peak at 2680cm^{-1} and the D+G peak at 2880cm^{-1} [272]. An increase of intensity observed in the D+G peak in the nanohybrids is due to overlap with the C–H band in the polymer [269]. The stiffening of the G peak (by nearly 6cm^{-1}) indicates a charge transfer process [273]. The significant softening of both D- (15cm^{-1}) and 2D-peaks (30cm^{-1}) indicates effective p-doping of the GO, as observed in other work on defective graphene [274]. In the literature, softening of the 2D peak with decrease in carrier concentration (lowering of the Fermi energy, corresponding to p-doping of the GO), which is observed in our data, is noted. However, for pristine, defect-free graphene systems, the opposite effect is indicated (softening of the D and 2D modes indicates n-doping) [272]. The difference in behavior of the D and 2D modes appears to be related to the nature of the defects within the carbon lattice that are prevalent in graphene oxide but not

observed in pristine graphene.

Figure A.3C,D shows Raman mapping of the hybrids (over a $25 \times 25\mu$m area) for the peak intensity at 2236cm^{-1} and G-peak position, respectively. Clearly visible is a correlation between the intensity of the PIM feature and the G-peak shift in the GO. Figure 3E plots the G-peak position against the peak intensity at 2236cm^{-1} using pixel-wise data from Figure A.3C,D. This data is binned and averaged to clarify the overall trend. Additionally, a line is shown as a "guide to the eye", based on G-peak positions in point spectra of the pristine GO and hybrid. According to the equation [275] $\hbar\omega_G = \alpha'|\epsilon_F| = \alpha'\sqrt{n_d\pi}\hbar\nu_F$ (where ϵ_F is the Fermi energy, n_d is the doping density, $\hbar\nu_F = 5.52$eV, and $\alpha' = 4.39 \times 10^{-3}$ at 0K), the shift in the G-peak can be used to estimate the doping density, resulting in a value of 2.25×10^{12}cm^{-2}. From this value it is possible to estimate the resultant shift of the work function of the nanohybrid [276] as 75meV. This prediction of the modification to the work function can be experimentally investigated through the use of Kelvin probe force microscopy (KPFM).

KPFM is a scanning probe technique that measures the local contact potential difference (V_{CPD}, in mV) between the probe and the sample. The CPD relates to the surface charges formed as a result of Fermi level alignment between the tip and the sample materials (through external circuit connections). The value of V_{CPD} can be directly related to the work functions ϕ of the two materials in question by $V_{\mathrm{CPD}} = (\phi_{\mathrm{sample}} - \phi_{\mathrm{tip}})/e$, where e is the electronic charge [277]. Either by use of a tip with calibrated work function or by examining measurements relative to a common material in multiple samples (such as the silicon substrate), it is possible to infer relative changes to the work functions in the nanohybrids by comparison to the pristine materials.

Figure A.4A,B shows the AFM topography and KPFM contact potential difference (CPD) maps of the nanohybrids where the PIM-1 nanoparticles appear on top of the GO sheet. Figure A.4C,D shows equivalent data for a region of the sample where the GO sheet lays on top of the nanoparticles. The line sections marked in Figure A.4A,D are plotted in Figure A.4E–H. We observe from the height profiles in both cases (Figure A.4E,G) that the nanoparticles have diameters consistent with the histogram presented in Figure A.1G. For the PIM-on-GO samples in Figure A.4A,B, the GO is measured as having V_{CPD} around 100mV, while the PIM-1 nanoparticles are measured to have V_{CPD} values between 200 and 350mV. This is taken to be representative of the pristine materials due to their separation when probing the surface of the PIM-1. By contrast, GO is atomically thin and has non-negligible conductivity [278], meaning that the influence of the PIM-1 on the V_{CPD} can be determined by measuring GO-on-PIM samples. The isolated area of GO in Figure 4C,D has broadly similar V_{CPD} as in the PIM-on-

GO samples, while V_{CPD} of GO in the presence of wrapped PIM-1 nanoparticles is found to increase to around 200mV (Figure A.4H). This can be interpreted as a modification to the work function of the GO sheet due to doping by the underlying PIM-1 nanoparticle. This work function modification is in agreement with the shift calculated from the doping density determined by Raman spectroscopy, suggesting the GO is indeed p-doped by a charge transfer interaction with the PIM-1.

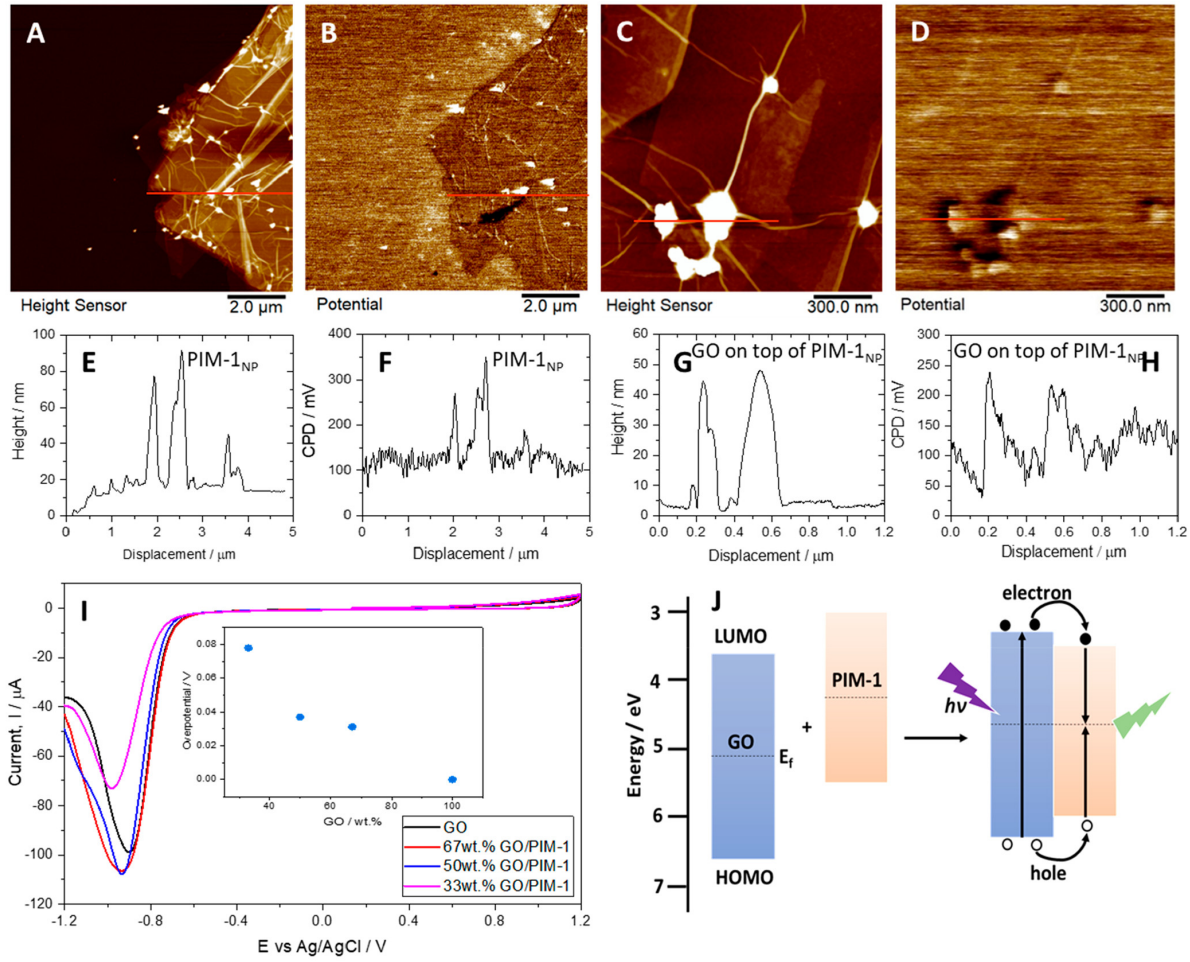

Figure A.4: (A, B) AFM topography and KPFM (respectively) of the GO/PIM-1 nanohybrid. (C, D) AFM topography and KPFM of GO sheets on top of "wrapped" PIM-1 nanoparticles. (E, G) Height and CPD line profiles of PIM-1 nanoparticles on top of the GO sheet, from the data in A and B, respectively. (G, H) Height and CPD line profiles of GO sheets on top of the "wrapped" PIM-1 nanoparticles, from the data in C and D, respectively. (I) Electrochemical reduction for GO and GO/PIM-1 nanohybrids deposited onto a glassy carbon electrode in phosphate buffer solution (pH 5, first cycle, scan rate 10mVs^{-1}). (Inset) Overpotential of GO reduction against GO/PIM-1 weight ratio. (J) Schematic energy level diagram of the isolated materials and nanohybrid.

For electrochemical measurements (see Figure A.4I), a volume of 4mL of GO and GO/PIM-1 nanohybrid was deposited onto a glassy carbon electrode. Cyclic voltammetry was performed to study the electrochemical reduction of GO in aqueous 0.1M phosphate buffer solution (PBS) at pH 5. The reduction of GO is observed as a chemically irreversible process, which is in agreement with ref [279]. Therefore, the first linear potential sweeps were recorded for comparison. Clear and sharp peaks are observed in all cases. For the GO/PIM-1 nanohybrids, the shape of the peak shows some broadening consistent with a kinetic barrier to the GO-to-graphene transition due to surface coverage of the GO by PIM-1. The underlying mechanism for the electron transfer is due to the relative energies of states in the electrode and the species. If the Fermi level in the electrode is higher than the lowest unoccupied molecular orbital (LUMO) of the species, electrons will be transferred from the electrode to the species, resulting in reduction of the species. Therefore, since the overpotential for the GO/PIM-1 nanohybrids (plotted in the inset to Figure A.4I) increases with increasing PIM-1 content, we can infer a lowering of the Fermi energy and corroborate the observation of p-doping of the GO [259] through the other measurement techniques above. Finally, The LUMO energy can be calculated from the onset reduction potential as $E(LUMO) = -e[E_{\text{red}}^{\text{onset}} + 4.4]$ [280], so the LUMO energy of the GO is estimated as 3.6eV.

Based on the measurements presented, a simple model of the charge transfer interaction in the hybrid system can be illustrated as in Figure A.4J. From the literature [239, 276], the HOMO (5.5eV) and LUMO (3.0eV) levels in PIM-1 are higher than in GO (6.6eV, 3.6eV) in good agreement with the values presented here, where measured. In addition, the alignment of their Fermi levels in the hybrid presents the possibility of intermolecular exciton diffusion due to the narrower bandgap in the polymer. The photoexcited electrons and holes generated in the GO ($\sim$ 350nm) can be injected into PIM-1 in an exciton transfer process. Subsequently, the exciton can recombine in the PIM-1 to emit in the green ($\sim$ 500nm). While this does not account for the extrinsic nature of these semiconductors (n-type PIM-1 and p-type GO) [281], it is even possible that bound excitons are delocalized across the interface of the materials with electrons preferentially transferred to the PIM-1 and holes remaining in (and resulting in doping of) the GO until recombination. The ability to design such charge transfer complexes on the nanoscale is important, and application of effects at this length scale are most likely in sensing and catalysis where charging can translate into chemical effects, for example, in promotion effects in catalysis.

A.3.5 Conclusion

In this report, we prepare GO/PIM-1 nanohybrid charge transfer materials through a facile reprecipitation approach. By this method, PIM-1 nanoparticles form and associate with GO sheets in dispersion, resulting in the nanohybrid materials. Microscopy analysis by both SEM and AFM reveal uniformly dispersed nanoparticles attached to the GO surface. The optical properties of the GO/PIM-1 nanohybrids are investigated using UV–visible extinction, steady-state and time-resolved photoluminescence spectroscopies, Raman spectroscopy, and pump–probe transient absorption spectroscopy. We conclude from these techniques that there are both excited state and ground state charge transfer effects present. Kelvin probe force microscopy and electrochemical measurements provide direct evidence for ground state charge transfer causing a shift in the Fermi level of the GO component in the nanohybrids. In summary, graphene oxide is p-doped while PIM-1 is n-doped in the GO/PIM-1 nanohybrids. The resulting charging effects are chemically significant and could be important in other fields such as in gas adsorption and separation, in membrane development, and in sensing and catalysis.

Appendix B

Published Paper: Hyperspectral Terahertz Microscopy via Nonlinear Ghost Imaging

The vast work pursued previously on nonlinear surfaces has been in the pursuit of developing efficient THz emission from quasi-2D media. This is due to the development of nonlinear THz imaging systems, where the diffraction of THz fields represents a significant limiting factor in the resolution of any images recovered. One such solution to this problem therefore is to place the object as close to the THz source as possible such that the distance propagated by the THz field is minimal, a condition easily fulfilled by the generation from surfaces. Parallel to my investigations therefore includes the development of novel THz imaging systems where such limits can be overcome, primarily via ghost imaging techniques [187, 282, 283]. These ghost imaging systems use a single pixel bucket detector (which are much more convenient in the THz region thanks to TDS) and spatially pattern the beam with a series of orthogonal matrices in order to retrieve the image. The idea being that the bucket detector signal varies with each pattern depending on the spatial frequencies of the pattern, by correlating the patterns with the detected field and summing over them the image is formed. The motivation for using such a scheme in the THz range is because in principle, by patterning the optical beam prior to THz generation, the actual observed resolution is limited by the spatial light modulator pixel size instead of the much longer THz wavelength.

My role in this work was supervisory and in the design of the experimental setup. I had gained some previous expertise in the tilted pulse front THz generation method [143, 284] when developing a THz near-field microscope, therefore I provided the geometrical specification of the

ultrafast pulse tilt induced by the digital micromirror device (DMD) used for the spatial light modulation. The DMD induces a pulse tilt which is detrimental to the ghost imaging process and so needs to be compensated for by pre-tilting the pulse prior to the DMD. In addition, I designed and realized the ultrafast diagnostics of the experiments, required to specify the high-energy ultrashort input pulse. The article was submitted to Optica on the 25^{th} October 2019 and was published on the 19^{th} February 2020.

B.1 Summary

The article is an experimental demonstration of hyperspectral THz nonlinear ghost imaging, where the diffraction in the THz fields is overcome by detecting the full time-resolved waveform and backpropagating the image. The imaging system was first characterised using a metallic structure on kapton with fixed-time sampling, where the temporal evolution of the THz field can be observed clearly in the subwavelength imaging without backpropagation. The second demonstration of an organic leaf demonstrates the hyperspectral nature of the ghost imaging setup, where the spectral properties of the imaged object can be retrieved. Lastly, the overcoming of the space-time coupling via inverse propagation was demonstrated to significantly improve the hyperspectral image.

B.2 Impact

The article targeted the Optical Society of America journal Optica, which has an impact factor of 9.263. The journal scope spans all of optics and photonics, obviously fitting with the claims of the article. The article currently has 14 citations, and the potential impact is highly significant within the THz imaging community. Furthermore, as in chapter 3.3, a simultaneous press release garnered a large following among the media resulting in an Altmetric score of 134 and a large social media presence.

On the same topic, this research also resulted in the invitation to submit a follow up review to Micromachines (with 2 citations), in which methods to speed up the acquisition of the nonlinear image and how surface THz emission could be exploit to further improve this novel imaging scheme [285].

B.3 Journal Article

B.3.1 Abstract

Ghost imaging, based on single-pixel detection and multiple pattern illumination, is a crucial investigative tool in difficult-to-access wavelength regions. In the terahertz domain, where high-resolution imagers are mostly unavailable, ghost imaging is an optimal approach to embed the temporal dimension, creating a "hyperspectral" imager. In this framework, high resolution is mostly out of reach. Hence, it is particularly critical to developing practical approaches for microscopy. Here we experimentally demonstrate time-resolved nonlinear ghost imaging, a technique based on near-field, optical-to-terahertz nonlinear conversion and detection of illumination patterns. We show how space–time coupling affects near-field time-domain imaging, and we develop a complete methodology that overcomes fundamental systematic reconstruction issues. Our theoretical-experimental platform enables high-fidelity subwavelength imaging and carries relaxed constraints on the nonlinear generation crystal thickness. Our work establishes a rigorous framework to reconstruct hyperspectral images of complex samples inaccessible through standard fixed-time methods.

B.3.2 Introduction

The reconstruction of complex field distributions in space and time is a challenge in many domains, with a significant transversal impact in fields beyond optics, such as microwave beam steering, ultrasound imaging, and biology [286, 287, 288, 289, 290, 291, 292, 293, 294]. On another front, hyperspectral imaging has a pivotal assessment role in many disciplines, as it allows one to determine the 2D morphology of an absorption spectrum [295, 296, 297]. Hyperspectral imaging assumes a broader probing significance in time-resolved systems; in particular, the delay of each frequency component can be profitably used to access the 3D morphology of the spectral phase response of a target, i.e., its spatially resolved complex dielectric function. Modern photonic approaches have produced essential breakthroughs in medicine, biology, and material science imaging [297, 298, 299, 300, 301]. In this context, the ability to reconstruct the time-domain waveforms provides direct access to the field [302]; although these approaches are well established in microwave and ultrasound imaging [287, 290, 291, 292], they are sensibly less diffused in photonics. Terahertz (THz), in this regard, has emerged as one of the most relevant photonics frameworks in which the time evolution of a field amplitude is experimentally accessible. Indeed, THz time-domain spectroscopy (TDS) has played a pivotal role in establishing THz as an independent research field [303, 304, 305, 119].

Single-pixel imaging approaches find their origin in domains where single-point detectors outperform detector-arrays in terms of specifications or availability [306, 307]; for this reason, they have attracted interest also in the THz community [308, 309, 310]. In photonics, these methods have unlocked the powerful ability to add multiple dimensions and novel functionalities to simple spatial probing, enabling several breakthroughs in classical and quantum imaging [309, 311, 312, 313, 314, 315, 316]. In its most modern connotation, ghost imaging (GI) is a form of computational imaging that employs the sequential illumination of an object with a set of predetermined patterns [307, 317, 318, 319, 320, 321].

In terms of accessing newly emerging wave domains, such as THz, GI offers the option of closing relevant technological gaps while raising new challenges, such as the limited availability of THz spatial light modulators (SLMs) and the coarse diffraction limit [309].

The combination of single-pixel imaging and TDS provides the exciting possibility of exploiting novel space–time computational imaging approaches [315, 316], and the TDS-GI has been recently proposed as viable for THz imaging [322, 282, 283, 323, 216]. The THz field can be densely sampled in space, giving access to subwavelength microscopy when an object is exposed to the near field of a THz source, detector, or mask. Besides its potential practical impact in THz microscopy, GI microscopy provides an accessible fundamental framework for investigating time-resolved imaging in the presence of strong spatiotemporal coupling, a dominant condition in the near-field domain.

In this paper, we experimentally implement an imaging protocol based on the time-resolved nonlinear ghost imaging (TNGI), which we have recently theoretically proposed as a single-pixel imaging method where a set of nonlinear wavelength transformations are inserted in both the illumination and detection chains [187]. We generate the THz patterns used for the GI reconstruction by nonlinear conversion of spatially modulated optical pulses in a quadratic medium. Leveraging the time-dependent field detection, as opposed to the intensity detection usually implemented in the optics GI-equivalent, we implement the detection in the Fourier plane, effectively acquiring the average value of the scattered field. With this approach, the system resolution is effectively independent of the numerical aperture of the detection system, in sharp contrast with standard single-pixel approaches working in optics. We test our time-dependent THz microscope on benchmark images, showing the capability of our system to extract the spectrally resolved morphology, such as the water content in a leaf.

Most importantly, we demonstrate near-field, coherent hyperspectral imaging in a regime where spatiotemporal coupling is strongly evident. We experimentally show that, in this regime, the image information is inherently inaccessible when the reconstruction is performed at

fixed-time slices of the transmitted field, as the traditional isotime imaging approaches become affected by errors and artifacts. We show experimentally that in the near field, the full spatiotemporal signal is required to preserve space–time imaging, and we provide a methodology, which we refer to as "space–time refocusing" for high-fidelity reconstruction. Interestingly, we also show experimentally that the thickness of the generation crystal does not preclude significantly higher resolutions (as in some of the proposed THz-GI approaches).

B.3.3 Methods: The TNGI

We formulated the TNGI as a single-pixel imaging approach based on the time-resolved detection of the electromagnetic field scattered by a sample, as opposed to the standard formulation of GI that relies on the time-averaged field intensity [187]. Without loss of generality, the TNGI describes the optical and morphological features of a sample through a spatiotemporal transfer function $T_{\text{sample}}(x, y, t)$ that is reconstructed through a sequence of measurements as follows:

$$T_{\text{sample}}(x, y, t) = \langle C_n(t) I_n(x, y) \rangle_n - \langle C_n(t) \rangle_n \langle I_n(x, y) \rangle_n , \tag{B.1}$$

where $I_n(x, y)$ is the intensity distribution of the n^{th} incident optical pattern, and $\langle \cdots \rangle_n$ is the average over the distribution of patterns. In Eq. (B.1), the expansion coefficients $C_n(t)$ are defined as

$$C_n(t) = \int E_n^+(x, y, t) dx dy, \tag{B.2}$$

and correspond to the spatial average of the complex electric field $E_n^+(x, y, t)$ transmitted by the sample and acquired by TDS detection (see Supplement 1 Section S3). Note that Eq. (B.1) is closely related to the linear formulation of standard GI, where the incident and scattered intensities are linearly related. Such a similarity is a direct consequence of the optical-to-THz conversion taking place in quadratic media, where the generated THz field is expressed as

$$E_{\text{THz}}(x, y) \propto \chi^{(2)} I_n(x, y), \tag{B.3}$$

where $\chi^{(2)}$ is the second-order nonlinear susceptibility of the nonlinear medium. The capability of directly controlling the THz field by acting on the incident optical intensity is an essential feature of our approach, as in casting Eq. (B.1) we do not require any assumption stemming from the binary nature of the illumination (as required, e.g., in mask-based GI [322, 283, 323, 216]). It is also worth noting that, differently from the standard GI formulation, the coefficients in

Eqs. (B.1) and (B.2) are built up by coherent measurements of the electric field, and they do not represent the scattered intensity.

The principal elements of our experimental implementation of the TNGI are shown in Fig. B.1. We impressed a series of intensity patterns on an ultrafast optical beam ($\lambda = 800$nm, repetition rate 1kHz, pulse duration 75fs) using a commercial wavefront-shaping device. In our experiments, we employed both a binary amplitude digital micromirror device (DMD) and a phase-only liquid crystal on silicon (LCoS) SLM. We converted the optical pattern to a THz field distribution $E_{\mathrm{THz}}(x, y, t)$ through nonlinear optical rectification in a quadratic crystal (ZnTe) of thickness z_0. The generated THz pattern sampled different targets (in our experiments different metallic masks and dielectrics) placed in proximity to the crystal surface, and the average transmitted field was measured through electro-optic (EO) detection. In our THz implementation, the $C_n(t)$ coincide with the electric field detected via TDS at the center of the Fourier plane (i.e., at $k_x = k_y = 0$) [324]. As an image-reconstruction protocol, we exploited a Walsh–Hadamard encoding scheme (with "Russian doll" ordering [325]) based on binary amplitude patterns, which is known to maximize the SNR of single-pixel imaging schemes [322]. A detailed schematic and further details on the optical setups are included in the supplementary information (SI).

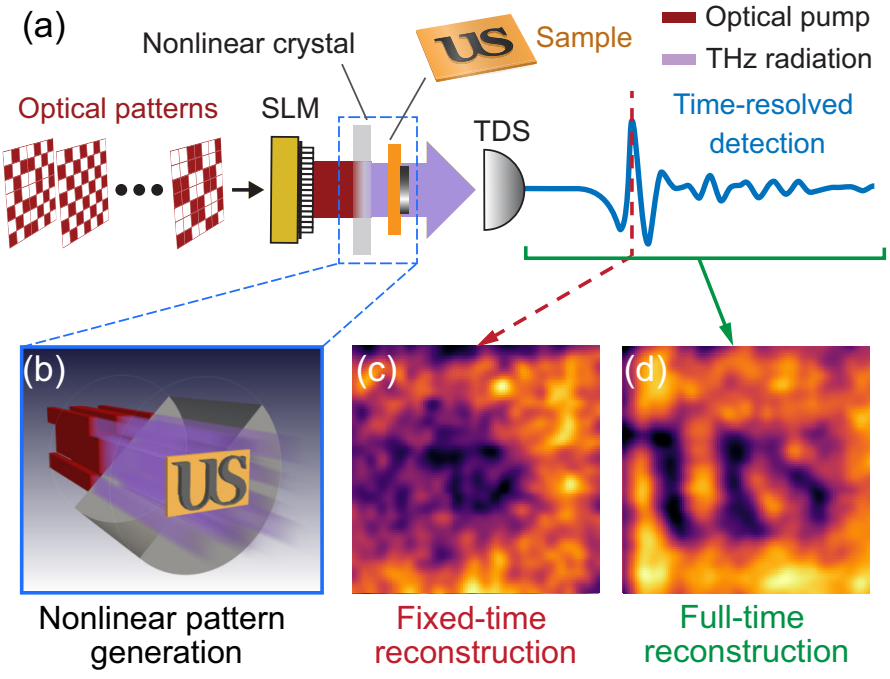

Figure B.1: Conceptual description of the TNGI approach. (a) Key experimental components and methodology; (b) volumetric representation of the nonlinear generation of THz patterns; (c) fixed-time reconstruction with a field of view 2mm×2mm and 32×32 spatial sampling; (d) backpropagated hyperspectral image, averaged between 1 and 2THz.

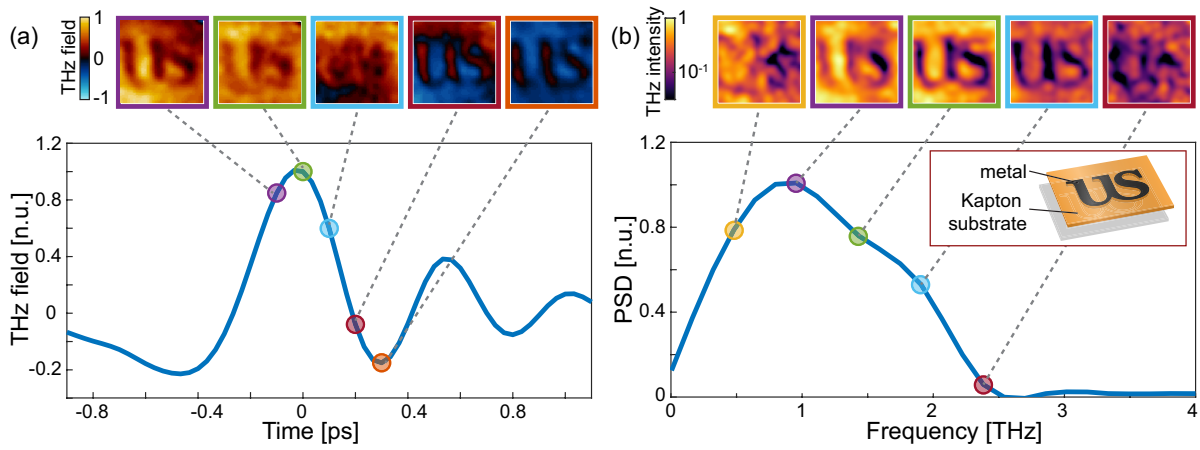

Figure B.2: Spatiotemporal image of a metallic sample. (a) Temporal response of the metallic sample with fixed-time image reconstructions. It is worth noting that field evolution (color change) can be appreciated underneath the metallic mask as the structure resonance produces a secondary emission. (b) Spectral response with hyperspectral images. The field of view was 2mm×2mm with a 16×16 spatial sampling.

The use of nonlinear conversion to generate THz patterns provides a series of features when developing a single-pixel TDS imaging scheme. First, the ability to control the THz field distribution by shaping the optical field, as expressed by Eq. (B.3), allows us to generate patterns with subwavelength resolution when compared to the THz wavelength (300μm, at 1THz). The resolution of the optical pattern $I_n(x, y)$ is ultimately bound by the optical diffraction limit and the numerical aperture of the optical setup. Second, the SNR of the detected THz signal increases linearly with the incident optical intensity. Finally, there is perfect temporal coherence and spatial correspondence between the pump pulse and the distribution of THz sources. Temporal and spatial coherence is a direct consequence of the nonlinear conversion process and has significant consequences for our abililty to image samples in challenging experimental conditions. An open issue in THz-GI concerns the impact of the distance between the THz pattern source and the sample, as required when assessing the transmission from a sample placed on a holding substrate. As discussed in Refs. [322, 187], the near-field propagation of subwavelength patterns exhibits spatiotemporal coupling, altering the spatial and temporal features of the pattern [326]. Under these conditions, the sampling function impinging on the object is not the original, predetermined pattern, but its space–time "propagated" version. Such discrepancy introduces a systematic and uneliminable error in determining the scattered waveform from the object using a time-sliced (or isotime) imaging. While the effect of spatiotemporal coupling could be reduced when the sample distance from the sources is much smaller than the resolu-

tion targeted (i.e., by employing a thin patterning substrate), the error introduced by diffraction (and by the interaction with samples with complex transmission properties) is always present. Such an error is not quantifiable in the case of single time-slice acquisition, and it cannot be represented by standard definitions of SNR employed in image analysis. The combination of optical coherence and direct field detection allows us to reverse the effects of spatiotemporal coupling, to obtain the correct time-domain reconstruction of a sample within one wavelength of distance, and to perform coherent hyperspectral imaging through TNGI.

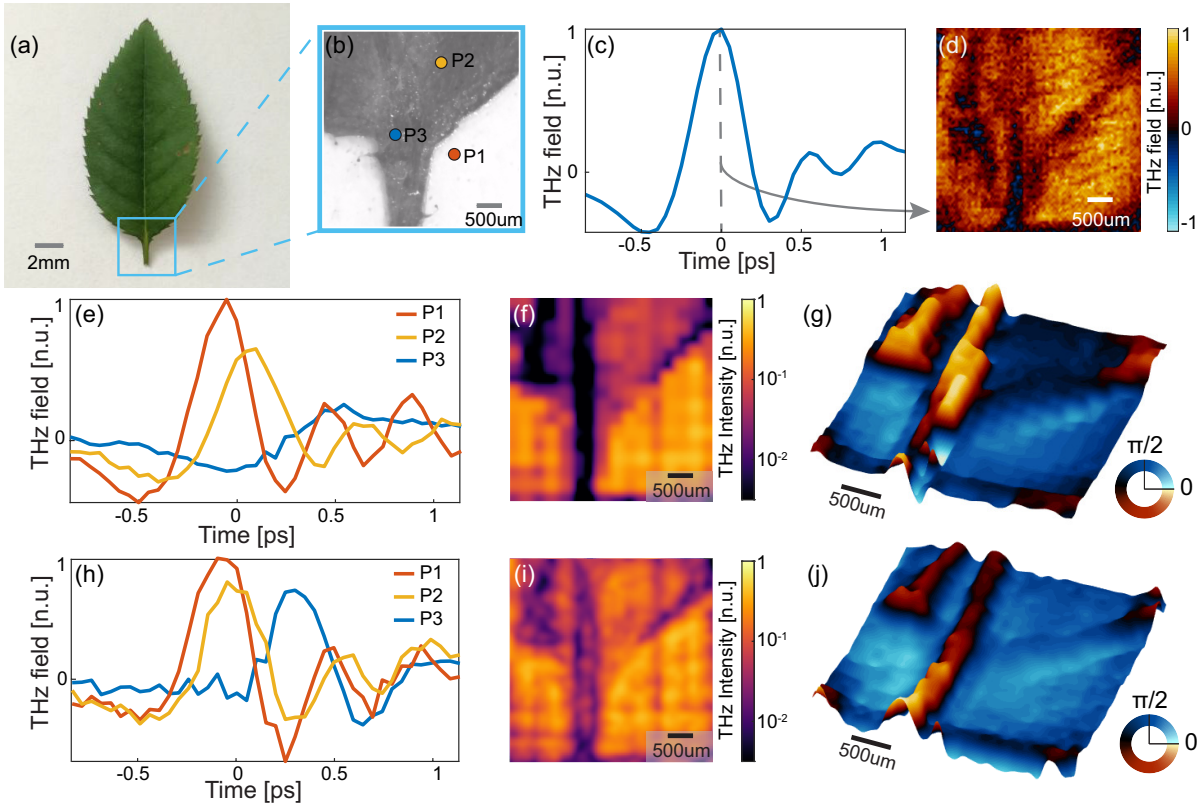

Figure B.3: Hyperspectral image of a leaf. (a) Optical image of the leaf; (b) microscope image; (c) temporal response of the field transmitted by the leaf; (d) fixed-time reconstruction (128pixels×128pixels); (e) local temporal response of the fresh leaf in the points indicated in (b); (f) hyperspectral image of a fresh leaf at 1.5THz (16pixels×16pixels); (g) phase image of the fresh leaf, obtained without phase unwrapping of the experimental data; (h)–(j) same as the previous panel for a dried leaf (32pixel×32pixel images). All the images correspond to a field of view of 4mm×4mm.

B.3.4 Experimental Results: Hyperspectral Imaging

As a first case study, in Fig. B.2 we present the 2mm×2mm spatiotemporal image of a metallic structure deposited on a 50μm Kapton substrate. The image was retrieved by shaping the

optical illumination with a binary DMD and by placing the metallic structure in the proximity of a $z_0 = 1$mm thick ZnTe generation crystal. We achieved analogous results using an LCoS modulator, as shown in Supplement 1 Fig. 2. By retrieving the spatiotemporal image of the sample [Fig. B.2(a)], we can capture the full effects of the interaction between the THz field and its subwavelength metallic features. As can be observed at $t = 0.2$ps, in fact, the object does not appear just as a blocking mask, but it features complex resonances from the edges of the object. The time-resolved measurement of the scattered field also allows us to reconstruct the hyperspectral image of the sample [Fig. B.2(b)]. Interestingly, in our experiments, we were able to resolve features within the 50–100μm scale even in the presence of a relatively thick generation crystal (as opposed to the typical thickness requirements in other approaches [322, 283, 323, 216]). This is a direct consequence of the nonlinear conversion of optical patterns taking place across the entire volume of the generating crystal and not only at its surface. In this condition, the field-spatial spectra of each generating layer in the ZnTe do not mix incoherently and, differently from the linear case, allow single-pixel reconstruction of subwavelength features (see Supplement 1 Section S2 for a detailed discussion).

The access to the coherent temporal field response allowed us to reconstruct full spatiotemporal images of semitransparent samples. As a relevant example (and to credit a similar image in Ref. [305], widely considered one of the first milestones in THz imaging), we show in Fig. B.3 an image of a leaf at different stages of desiccation. As can be evinced from Figs. B.3(c) and B.3(d), the isotime image of a semitransparent sample is significantly harder to interpret than a standard metallic mask, as the different parts of the sample induce different temporal delays and phase shifts. Nevertheless, we were able to retrieve the TDS time trace in different points of the sample [Figs. B.3(e) and B.3(h)] and retrieve its hyperspectral image both in terms of amplitude [Figs. B.3(f) and B.3(i)] and spectral phase [Figs. B.3(g) and B.3(j)], allowing us to reconstruct its morphology and spectral fingerprint. As relevant examples, we present data for a fresh leaf [Figs. B.3(e)– B.3(g)] and a dried leaf [Figs. B.3(h)– B.3(j)]. By comparing the transmission from the two samples, it is possible to assess the changes in water content, as in Ref. [305].

B.3.5 Imaging Through Inverse Propagation

The experimental results presented in Fig. B.4 explore a relevant consequence of the space–time coupling in near-field TNGI. In this case, we collected the image of a metallic sample, analogous to the one in Fig. B.2, but introducing a nonnegligible distance between the sample and the emitter, which includes the Kapton substrate, in a typical time-of-flight imaging case.

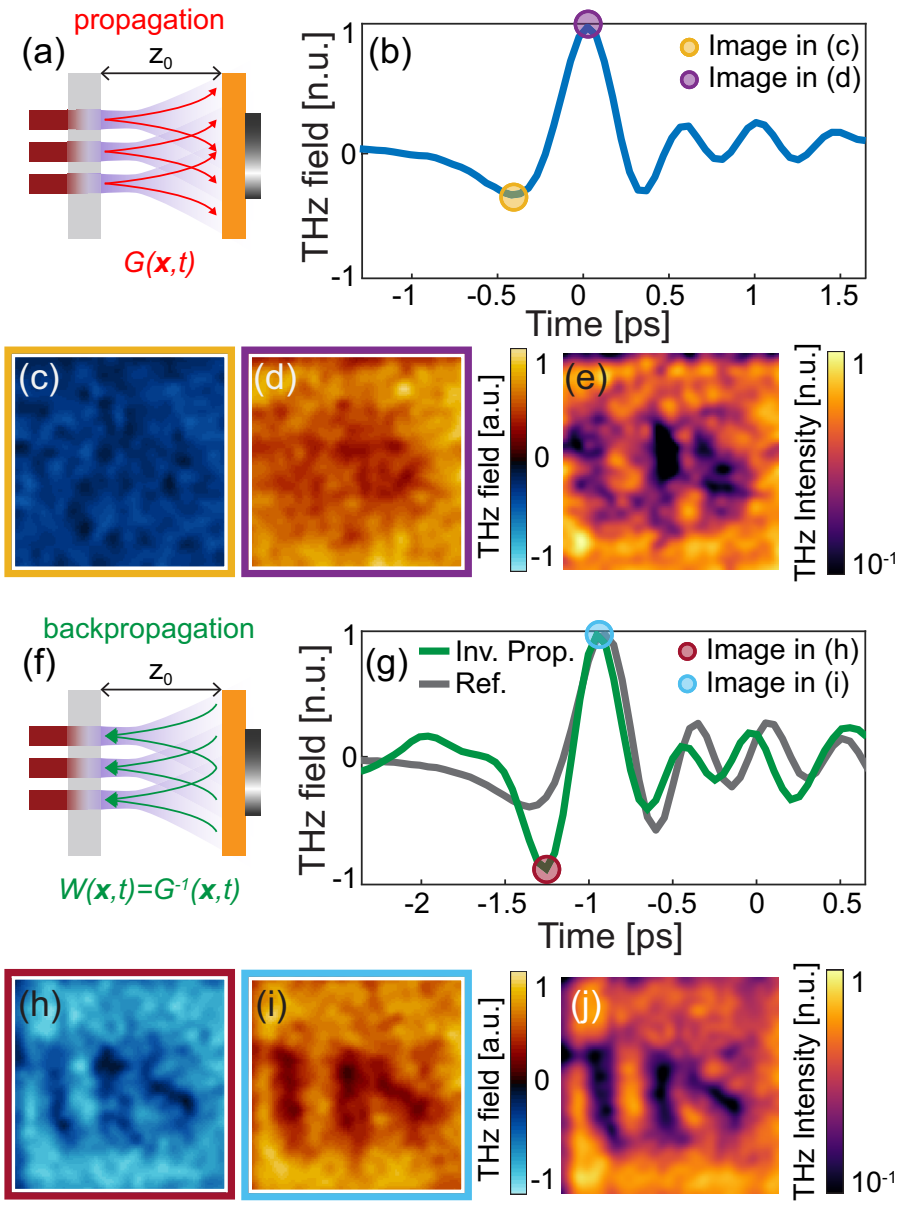

Figure B.4: Time-resolved image reconstruction: inverse propagation approach. (a) Conceptual illustration of the propagating imaging scheme: the sample is placed at $z_0 = 300\mu$m from the crystal. (b) Temporal response of the sample; (c)–(d) fixed-time reconstructed images at the points indicated in (b); (e) hyperspectral image averaged between 1 and 2THz; (f) conceptual illustration of the backpropagation scheme; (g) temporal response of the backpropagated image (green) and the temporal response without the sample (gray); (h)–(i) fixed-time reconstruction of the backpropagated image at the points indicated in (g); (j) backpropagated hyperspectral image, averaged between 1 and 2THz. In all panels, the field of view was 2mm×2mm with a 32×32 spatial sampling.

In these conditions, the sample morphology cannot be appreciated in any of the isotime images regardless of their temporal position [Figs. B.4(c), B.4(d) show some examples], or in the hyperspectral image [Fig. B.4(e)], which shows a quite distorted image even if in some pixels a high contrast is reached. As theoretically demonstrated in Ref. [187], such a limitation is a direct consequence of spatiotemporal coupling, which leads to a substantial modification of the incident sampling patterns as they propagate [Fig. B.4(a)]. At this stage, it should be observed that our TNGI protocol relies on the collection of the average field as performed by sampling the origin of an optical Fourier plane (i.e., $k_x = k_y = 0$). As a result, it only requires an optical system capable of collecting a very narrow spatial spectrum, and the numerical aperture of the imaging system plays a minimal role in defining the image resolution. On the contrary, the SNR of the THz detection plays a fundamental role in resolving the vanishing near-field scattered contributions (at high spatial frequencies) for increasing values of the distance between the sample and the emitter.

With the sensitivity available, we could then backpropagate the pattern sampling function in order to "space–time refocus" the image [Fig. B.4(f)] and reverse the effect of spatiotemporal coupling (see Supplement 1 Section S3 for a theoretical discussion on the inverse propagation reconstruction) [187]. This procedure allows us to retrieve the correct time-resolved image of the scattered field in the proximity of the sample, restoring the morphological and spectral features of its hyperspectral image [Figs. B.4(i)– B.4(j)]. We argue that the inverse propagation reconstruction is a strict requirement to reconstruct the sample properties at different depths, i.e., in near-field time-of-flight imaging.

B.3.6 Conclusions

In conclusion, we performed the first experimental example of the TNGI approach exploiting a nonlinear quadratic conversion. We devised a general reconstruction method based on the linear dependence between impinging optical patterns and the detected THz time-domain field average. The approach enables hyperspectral imaging as performed in the state-of-the-art by TDS imagers. It features near-field imaging and shows relaxed constraints in terms of thickness of the nonlinear converter (our proof-of-concept exploits off-the-shelf nonlinear substrates). As predicted in Ref. [187], we demonstrated that popular isotime approaches are not suitable for near-field spatiotemporal microscopy, and this is a central issue when an object comprises elements at different optical depths. We proved experimentally that, thanks to the spatial and temporal coherence, it is possible to devise an inverse propagation operator capable of "refocusing" the image in space–time and, therefore, correctly reconstructing the hyperspectral

image of the sample. We believe this work can have a substantial impact in the field of near-field imaging, especially in light of the emergence of thinner and more efficient THz emitters (e.g., spintronic substrates, surface emitters, or novel materials with exceptionally high nonlinear coefficients such as DSTMS crystals) [137, 190, 189, 188].

B.4 Published Paper: Route to Intelligent Imaging Reconstruction via Terahertz Nonlinear Ghost Imaging

B.4.1 Abstract

Terahertz (THz) imaging is a rapidly emerging field, thanks to many potential applications in diagnostics, manufacturing, medicine and material characterisation. However, the relatively coarse resolution stemming from the large wavelength limits the deployment of THz imaging in micro- and nano-technologies, keeping its potential benefits out-of-reach in many practical scenarios and devices. In this context, single-pixel techniques are a promising alternative to imaging arrays, in particular when targeting subwavelength resolutions. In this work, we discuss the key advantages and practical challenges in the implementation of time-resolved nonlinear ghost imaging (TIMING), an imaging technique combining nonlinear THz generation with time-resolved time-domain spectroscopy detection. We numerically demonstrate the high-resolution reconstruction of semi-transparent samples, and we show how the Walsh–Hadamard reconstruction scheme can be optimised to significantly reduce the reconstruction time. We also discuss how, in sharp contrast with traditional intensity-based ghost imaging, the field detection at the heart of TIMING enables high-fidelity image reconstruction via low numerical-aperture detection. Even more striking—and to the best of our knowledge, an issue never tackled before—the general concept of "resolution" of the imaging system as the "smallest feature discernible" appears to be not well suited to describing the fidelity limits of nonlinear ghost-imaging systems. Our results suggest that the drop in reconstruction accuracy stemming from non-ideal detection conditions is complex and not driven by the attenuation of high-frequency spatial components (i.e., blurring) as in standard imaging. On the technological side, we further show how achieving efficient optical-to-terahertz conversion in extremely short propagation lengths is crucial regarding imaging performance, and we propose low-bandgap semiconductors as a practical framework to obtain THz emission from quasi-2D structures, i.e., structure in which the interaction occurs on a deeply subwavelength scale. Our results establish a comprehensive theoretical and experimental framework for the development of a new generation of terahertz hyperspectral imaging devices.

B.4.2 Introduction

In recent years, there has been increasing interest in the development of imaging techniques that are capable of reconstructing the full-wave properties (amplitude and phase) of arbitrary electromagnetic field distributions [327, 328, 293]. While standard optical technologies, such as cameras and photodiodes, are usually sensitive to the field intensity, a large part of the sample information is encoded in the optical phase of the scattered field [329]. Interestingly, the direct detection of the field evolution is achievable at terahertz (THz) frequencies thanks to the availability of the time-domain spectroscopy (TDS) technique. TDS detection provides a time-resolved measurement of the electric field (e.g., via electro-optical sampling [330]), allowing researchers to retrieve the complex-valued dielectric function of a sample. Such a capability, coupled with the existence of specific and distinctive spectral fingerprints in the terahertz frequency range, are critical enabling tools for advanced applications, such as explosive detection, biological imaging, artwork conservation and medical diagnosis [178, 177, 331, 332, 333]. However, despite the vast body of potential applications, the development of TDS devices that are capable of high-resolution imaging is still regarded as an open challenge. A typical TDS implementation relies on complex and expensive optical components that cannot be easily integrated into high-density sensor arrays [184].

To date, THz imaging mostly relies on thermal cameras, essentially the equivalent of optical cameras, which employ arrays of micro-bolometers to measure the time-averaged intensity of the THz signal. As such, they cannot be employed for time-resolved THz detection and they are insensitive to the optical phase and temporal delay of the transmitted THz field. In an attempt to develop arrays of TDS detectors, researchers have proposed two-dimensional full-wave imaging devices that are composed of arrays of photoconductive antennas or Shack–Hartmann sensors [334, 335]. However, these devices require complex and expensive technological platforms and their practicality is still a matter of debate. Furthermore, they fundamentally sample the image information in an array of single and well-separated small points. Hence, obtaining a high resolution can still require mechanical action on the sample.

A promising alternative to TDS imaging arrays is single-pixel imaging, or ghost imaging (GI). In these approaches, the sensor array is replaced by a single bucket detector, which collects the field scattered by the sample in response to a specific sequence of incident patterns. By correlating each acquired signal with its corresponding incident field distribution, it is possible to reconstruct the sample image [336, 337, 306, 338]. However, despite its simplicity, the implementation of GI at terahertz frequencies is affected by the limited availability of wavefront-shaping devices (e.g., spatial light modulators) that are capable of impressing arbitrary pat-

terns on an incident THz pulse. Following the initial experimental demonstrations with metallic masks and metamaterial devices [308, 309], several research groups' researchers have proposed indirect patterning techniques for the generation of high-resolution THz patterns. One of the most successful approaches relies on the generation of transient photocarrier masks on semiconductor substrates [282, 322, 216, 323]. In these experiments, a standard optical Spatial Light Modulator (SLM) impresses a spatial pattern on an ultrafast optical beam. Upon impinging on a semiconductor substrate, the latter generates a distribution of carriers matching the desired pattern profile, which acts as a transient metallic mask and can be used to pattern an external THz beam. While this technique has been successfully employed to achieve THz imaging with a deeply subwavelength resolution, it is also affected by a few limitations. In particular, recent works have shown that the maximum resolution achievable with these techniques is strongly dependent on the semiconductor substrate thickness: in Stantchev and coworkers [282, 322], for example, researchers have demonstrated that deeply subwavelength resolutions are achievable only when considering patterning substrates with a thickness below 10μm.

In a series of recent works, we have proposed a new imaging technique, time-resolved nonlinear ghost imaging (TIMING), which overcomes several of these limitations [187, 339, 186]. TIMING relies on the integration of nonlinear THz pattern generation with TDS single-pixel field detection. In this work, we discuss the main features of our approach and present our latest results on the theoretical framework underlying our image reconstruction process. Via analysis of the compression properties of the incident pattern distribution, we show how a TIMING implementation based on an optimised Walsh–Hadamard encoding scheme can significantly reduce the number of incident patterns required to obtain a high-fidelity image of the sample. Finally, we discuss how the development of ultra-thin THz emitters can provide a significant improvement to the imaging performance of TIMING.

B.4.3 Time-Resolved Nonlinear Ghost Imaging: A Conceptual Overview

A conceptual schematic of our imaging setup is shown in Figure B.5a. A spatial pattern is impressed on the optical beam through a binary spatial light simulator, e.g., a digital micromirror device (DMD), obtaining the optical intensity distribution $I_n^{\mathrm{opt}}(x, y, \omega)$. The THz patterns $E_n^0(x, y, t)$ are generated using a nonlinear conversion of $I_n^{\mathrm{opt}}(x, y, \omega)$ in a nonlinear quadratic crystal (ZnTe) of thickness z_0. The THz pattern propagates across the crystal and interacts with the object, yielding a transmitted field, which is collected by a TDS detection setup. Different from the standard formulations in optics, which relies on the optical intensity, our object reconstruction scheme relies on the time-resolved detection of the electric field scattered by the

object. More specifically, the electric field distribution is defined immediately before and after the object as $E^-(x,y,t) = E(x,y,z_0-\epsilon,t)$ and $E^+(x,y,t) = E(x,y,z_0+\epsilon,t)$, respectively, where z_0 is the object plane and $\epsilon > 0$ is an arbitrarily small distance (Figure B.5a, inset). Without loss of generality, the transmission properties of the object are represented by defining the transmission function $T(x,y,t)$, which is defined on both the spatial and temporal components to account for the spectral response of the sample. To simplify our analysis, in the following, we considered two-dimensional objects, i.e., we restricted ourselves to transmission functions of the form $T(x,y,t)$. Under this position, the transmitted field is straightforwardly defined as:

$$E^+(x,y,t) = \int dt' T(x,y,t-t')E^-(x,y,t). \tag{B.4}$$

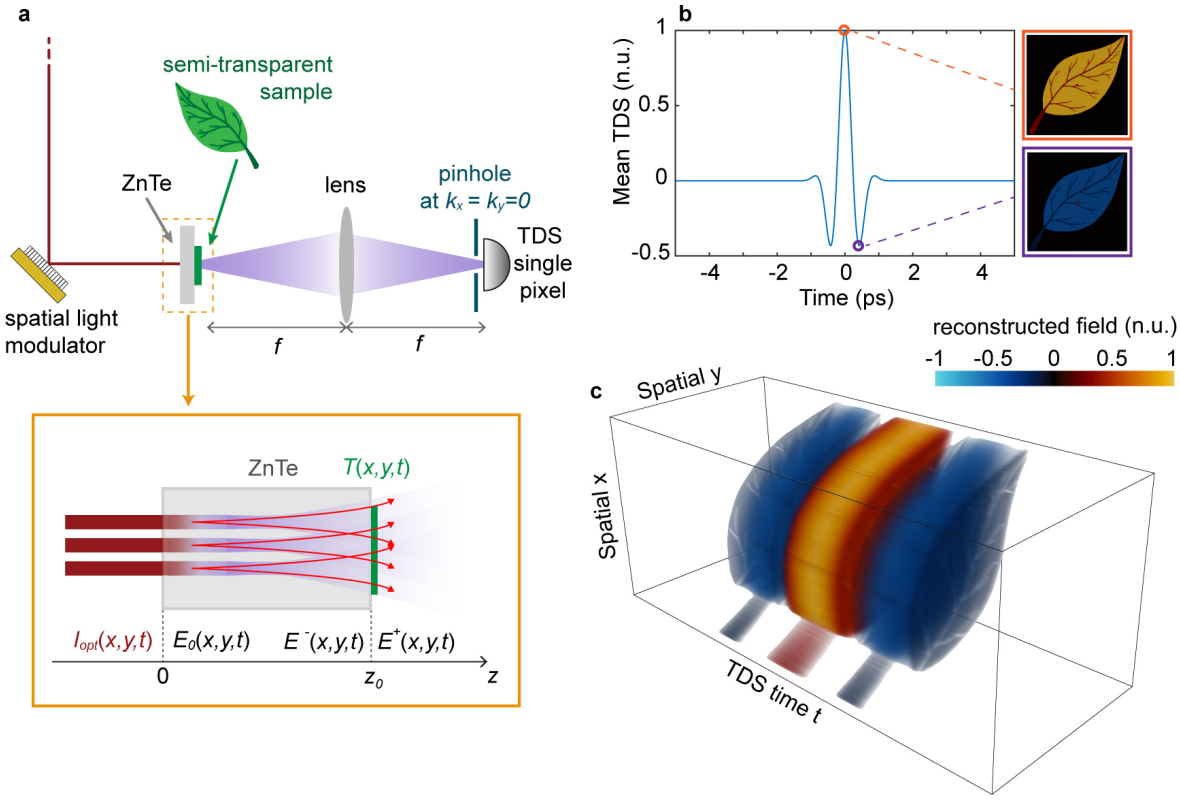

Figure B.5: Conceptual description of time-resolved nonlinear ghost imaging (TIMING). (a) Schematic of the experimental setup. (b,c) Simulation of the TIMING reconstruction of a semi-transparent sample, including the average field transmission (panel b) and the full spatiotemporal image of the sample (panel c). The simulated object size was 10.24cm×10.24cm, sampled with a spatial resolution of 512 × 512pixels ($\Delta x = 200\mu$m) and a temporal resolution of $\Delta t = 19.5$fs. The nonlinear crystal thickness was $z_0 = 10\mu$m. n.u.: normalised units, TDS: Time-domain spectroscopy.

The objective of a single-pixel imaging methodology is to reconstruct the transmitted field distribution $E^+(x,y,t)$ through a sequence of measurements to retrieve the transmission function of the object. In our approach, this corresponds to measuring the TDS trace of the spatially-averaged transmitted field from the object in response to a sequence of predefined patterns (a procedure known as computational ghost imaging) [306]. The nth pattern is denoted by $E_n^-(x,y,t) = P_n(x,y)f(t)$, where $P_n(x,y)$ is the deterministic spatial distribution of the pattern and $f(t)$ is the temporal profile of the THz pulse. The reconstruction process is defined as follows:

$$T(x,y,t) = \langle C_n(t)P_n(x,y)\rangle_n - \langle C_n(t)\rangle_n \langle P_n(x,y)\rangle_n , \tag{B.5}$$

where $\langle\cdots\rangle_n$ represents an average over the distribution patterns and the expansion coefficients $C_n(t)$ are defined as follows:

$$C_n(t) = \int dxdyE_n^+(x,y,t) = \int dxdydt'T(x,y,t-t')E_n^-(x,y,t). \tag{B.6}$$

A numerical implementation of the image reconstruction process is shown in Figure B.5b,c, where we employed TIMING to reconstruct the transmitted field from a semi-transparent sample (a leaf). In Figure B.5b, we report the spatial average of the reconstructed field, exhibiting the characteristic temporal profile of the incident THz pulse. Since our image reconstruction operates simultaneously in time and space, it allows for not only retrieving the spatial distribution of the object but also its temporal/spectral features. The specific result of a TIMING scan is a spatiotemporal image of the transmitted field, as shown in Figure B.5c.

An interesting question is whether the distance between the distribution of THz sources and the sample has any effect on the image reconstruction capability of our setup. This point is pivotal when time-resolved imaging is desired, as propagation always induces space–time coupling. This condition represents a typical challenge in mask-based ghost imaging when time-domain detection is sought. The propagation within the patterning crystal is known to lead to significant reconstruction issues when considering deeply subwavelength patterns [282, 322, 216]. These issues are related to the intrinsic space–time coupling that takes place within the crystal [326]. In essence, once the patterns are impressed on the THz wave at the surface of the crystal (at $z = 0$), they undergo diffraction. As a result, the electric field distribution $E_n^-(x,y,t)$ probing the sample is not the initial distribution $E_n^0(x,y,t)$, but rather a space-time propagated version of it. The latter is mathematically expressed as:

$$E_n^-(x,y,t) = E_n(x,y,z_0-\epsilon,t) = \int dxdydt'G(x-x',y-y',z_0-\epsilon,t-t')E_n^0(x,y,t), \tag{B.7}$$

where $G(x, y, z_0 - \epsilon, t)$ is the dyadic Green's function propagating the field from $z = 0$ to $z = z_0 - \epsilon$. Since space–time coupling is essentially a linear process, it can be inverted by applying a Weiner filter to the reconstructed image to mitigate the effects of diffraction. In the angular spectrum coordinates (k_x, k_y, z, ω), the Weiner filter is defined as:

$$W(k_x, k_y, z, \omega) = \frac{G^{\dagger}(k_x, k_y, z, \omega)}{|G(k_x, k_y, z, \omega)| + \alpha NSR(k_x, k_y, \omega)}, \tag{B.8}$$

where $NSR(k_x, k_y, \omega)$ is the spectral noise-to-signal distribution, α is a noise-filtering fitting parameter and † stands for Hermitian conjugation [187]. As expressed by Equation (B.8), the Weiner filter is the equivalent of an inverse Green's function operator that is modified to take into account the presence of noise in the experimental measurements. The effect of the NSR term in the denominator, which is controlled by the parameter α, is to suppress the regions of the spectrum that are dominated by noise and could render the inversion operation an intrinsically ill-posed problem [340].

From a physical point of view, Equations (B.7) and (B.8) can be read as follows: when performing a time-domain reconstruction of the image, the spatial distribution of $E_n^+(x, y, t)$ is acquired at a given time. However, this is not the scattered field from the object in response to the incident pattern E_n^0 at that time; there is no time in which the scattered field $E_n^0(x, y, t)$ is univocally represented in the sampling pattern E_n^-. The reason is simply that the method is slicing a fixed-time contribution of a piece of information that is warped in the space-time. This warping is introduced by the distance between sources and the object plane; therefore, it is different for any plane of the object being imaged.

Said differently, using fixed-time images to reconstruct planar features produces a fundamentally incorrect picture of the evolving scattered field, with different degrees of "distortion" introduced by the amount of propagation. It is worth noting that, although related, this is not the same concept as that of resolution degradation of incoherent near-field systems. In fact, Equation (B.7) shows that any space-time information retained by the field can be accessed only by accounting for near-field propagation. TIMING reconstructs the image of a scattered field from an object with fidelity by applying the backpropagation kernel from Equation (B.8). Another interesting aspect is whether the thickness of the nonlinear crystal accounts for an overall separation between terahertz sources and the object, affecting the achievable resolution. The difference here is that the propagation is inherently nonlinear and although the generated terahertz signal diffracts linearly, for any desired resolution, there is always a given generating crystal section that is sufficiently close to the object to illuminate it within the required

near-field condition. We have recently theoretically and experimentally demonstrated that the diffraction limit does not directly apply in the nonlinear GI via the generation crystal thickness since the nonlinear conversion from optical to THz patterns is a process distributed across the crystal [186]. We argue that this general approach is particularly useful when considering samples stored in cuvettes or sample holders.

B.4.4 Compressed and Adaptive Sensing Applications

In this section, we discuss the image reconstruction performance of TIMING as a result of our particular choice of input pattern distribution. To reconstruct the sample, TIMING relies on the Walsh–Hadamard (WH) image decomposition, which constitutes the binary counterpart of standard Fourier-based image analysis [341]. In our approach, the choice of the incident pattern distribution was driven by three considerations: (i) the compatibility with the available wavefront-shaping technology impressing patterns on the optical beam, (ii) the average signal-to-noise ratio (SNR) of the signal associated with each incident pattern and (iii) the energy compaction (compressibility) properties of the image expansion base. The WH patterns can be implemented straightforwardly through a digital micromirror device (DMD) and they are known to maximise the SNR of the acquired signals in experiments [342, 343]. The latter is a significant advantage when compared to standard TDS imagers, which rely on a raster-scan reconstruction approach, where either the source or receiver (or both) are sequentially moved across the sample, leading to a combination of single-pixel detection and illumination [333]. While this approach is intuitive and straightforward to implement, a single-pixel illumination usually implies a degradation of the SNR of the expansion coefficients for a fixed intensity per pixel. Furthermore, raster-scan imaging is a local reconstruction algorithm that is not suitable for compressed sensing; in mathematical terms, the raster scan corresponds to expanding the sample image in the canonical Cartesian base $E_{n,m}(x, y) = \delta(x - x_n, y - y_n)$. Trivially speaking, to reconstruct the entire image with this approach, each pixel composing it needs to be scanned.

In contrast, the WH encoding scheme is a very popular example of energy compacting (compressive) decomposition, as in the case of Fourier-based or wavelet-based image analysis [344, 345]. In these approaches, the image is represented as an orthogonal basis of extended spatial functions. For example, in the case of Fourier image analysis, the sampling patterns are the basis of the two-dimensional Fourier Transform [340, 346]. The choice of an expansion basis composed of extended patterns has two main advantages. First, extended patterns are generally characterised by transmitted fields with higher SNRs because distributed sources generally carry

more power. In fact, for a given power limit per pixel, the Walsh–Hadamard decomposition allows for a total energy per pattern that is about $N/2$ higher than single-pixel illumination. Second, and more importantly, there is no one-to-one correspondence between individual image pixels and distinct measurements (as in the case of the raster scan). In fact, the incident patterns not only probe different parts of the sample in parallel but can also provide useful insights into its spatial structure, even before completing the entire set of illuminating patterns.

In practical terms, a WH pattern of size $N \times N$ is obtained by considering the tensor product between the columns (or, invariantly, rows) of the corresponding $N \times N$ Walsh–Hadamard matrix (see Figure B.6a). The columns (or rows) are mutually orthogonal and form a complete tensor basis for any two-dimensional matrix. Interestingly, the columns of the Hadamard matrix can be re-arranged in different configurations, leading to matrices with different orderings [347, 348, 325]. In Figure B.6, we compare two configurations: the Walsh (or sequency) order and the Hadamard (or natural) order. The Walsh ordering is particularly useful in image reconstruction as it mirrors the standard order of the discrete Fourier basis, i.e., the columns are sorted in terms of increasing spatial frequencies. This means that by using the Walsh matrix, it is possible to acquire complete lower-resolution images before completing the illumination set, which can be useful for applying decisional approaches and reducing the set dimension [349, 350].

To illustrate how the image information is distributed across the basis of incident patterns, it is useful to analyse the peak-field Walsh spectrum of the reconstructed image, which is shown in Figure B.6b. The WH spectrum is obtained by plotting the $C_n(t = t_{\text{peak}})$ coefficients as a function of their generating pattern indexes. As can be evinced from Figure B.6b, the WH decomposition re-organises the image information into a hierarchical structure, which mirrors the spectral content of the image. Interestingly, this property is at the core of the compression properties of the WH encoding scheme, as can be exploited to significantly reduce the number of measurements required to reconstruct the image. We illustrate this result in Figure B.6c, where we identify the coefficients with an amplitude exceeding a -60dB threshold with a red marker. As shown in Figure B.6c, these significant coefficients were mostly localised in correspondence with the smaller spatial frequencies of the image, and for this image, they represented 8.1% of the total number of patterns. Remarkably, this limited number of patterns was sufficient to accurately reconstruct the image (as shown in Figure B.6c, inset).

For a given Walsh–Hadamard matrix, it is also critical to consider the specific order employed when selecting the sequence of columns forming the distribution of incident patterns. In our approach, we implemented an optimised ordering of the WH patterns (denoted as “smart-Walsh”),

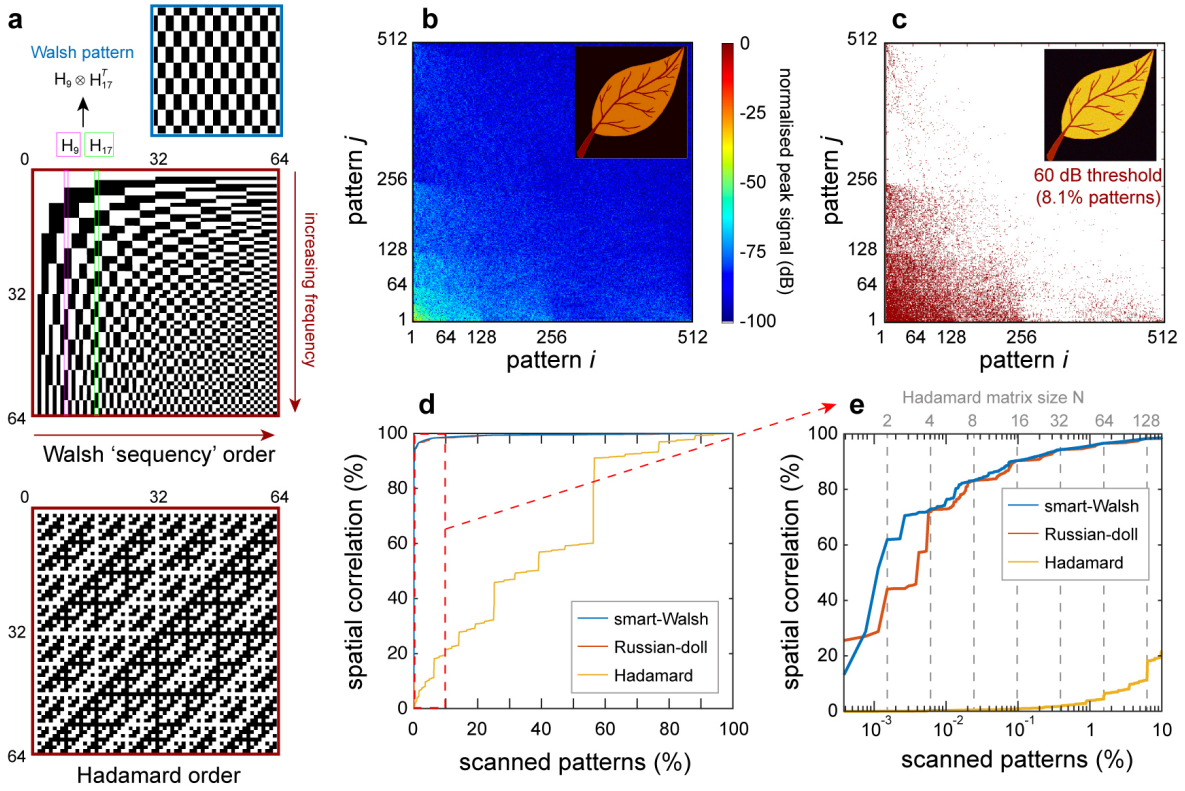

Figure B.6: Walsh–Hadamard image reconstruction. (a) Generation of incident patterns from the Walsh–Hadamard matrix. Each pattern is defined as the tensor product between two columns of the generating matrix. The patterns can be generated from different configurations of a Hadamard matrix: we show the Walsh, or "sequency", order (top, used in TIMING) and the standard Hadamard, or "natural", order (bottom). (b,c) Reconstructed Walsh spectrum of the peak-field object transmission. Interestingly, only a fraction of the patterns (8.1%) were associated with a spectral amplitude exceeding the −60dB threshold (with 0dB being the energy correlation of the fittest pattern—panel c). Nevertheless, these patterns were sufficient to provide a high-fidelity reconstruction of the image (insets). (d,e) Pearson correlation coefficients between reconstructed and original images as a function of the number of patterns employed in the reconstruction. The results refer to the entire scan (panel d) and the initial 10% of patterns (panel e).

which sorts the incident patterns in terms of increasing spatial frequency (see Supplementary Video 1). In Figure B.6d,e, we illustrate the fidelity of the TIMING reconstruction across the ensemble of incident patterns for different sorting schemes. The fidelity between reconstructed and original images is estimated through the Pearson correlation coefficient, which measures

the spatial correlation between the two datasets and is defined as:

$$\rho(A,B) = \frac{\Sigma_{m,n}(A_{m,n} - \bar{A})(B_{m,n} - \bar{B})}{\sqrt{\Sigma_{m,n}(A_{m,n} - \bar{A})^2 \cdot \Sigma_{m,n}(B_{m,n} - \bar{B})^2}}, \tag{B.9}$$

where $\bar{A}$ and $\bar{B}$ are the spatial averages of A and B, respectively. In our analysis, we considered the performance of our "smart-Walsh" sorting (blue line) with the natural Hadamard sorting (yellow line) and the recently proposed "Russian-doll" sorting (orange line) [325]. As shown in Figure B.6d, both the smart-Walsh and the Russian-doll sorting were capable of high-fidelity reconstructions of the sample image, even just by using a fraction of patterns, especially when compared to the standard Hadamard case. Further insights on the image reconstruction performance can be obtained by analysing the image reconstruction across the first 10% of patterns (Figure B.6e). Remarkably, both our approach and the Russian-doll sorting outperformed the standard Hadamard sorting, yielding a high-fidelity image (spatial correlation exceeding 90%) by considering only 0.1% of the total number of patterns. Interestingly, while the performance of our "smart-Walsh" approach matched the Russian-doll sorting as soon as each Hadamard order was completed (dashed grey lines), we observed that it outperformed it across incomplete scans.

B.4.5 Performance of Field-Based Ghost-Imaging Detection in the Fourier Plane

The possibility of performing field-sensitive detection provides TIMING with a significant advantage when compared with traditional GI. However, the typical GI correlation between detection parameters and image fidelity is broken by the nonlinear ghost imaging transformation, i.e., the need for establishing a correlation between coherent-field detection and the optical intensity patterns. More precisely, the implementation of a field average in the image extraction radically changes the way the image quality depends on the experimental parameters. Standard GI reconstruction relies on detecting the integrated scattered field to estimate the spatial correlation between the incident patterns and the sample, where:

$$C_n = \int dxdy I_n^+(x,y) = \int dxdydt' |T(x,y,t-t')E_n^-(x,y,t)|^2. \tag{B.10}$$

This corresponds to the direct acquisition of the total scattered field with a standard bucket detector, which integrates the transmitted intensity distribution. Fundamentally, it is an estimator of the total scattered power, and as such, it is directly affected by the numerical aperture of the detector and by the distance between the detector and the sample. As discussed in the

literature on optical GI, both these factors directly fix the amount of information that is available when reconstructing the image and directly affect its fidelity [337].

TIMING inherits the direct detection of the scattered THz field distribution from time-domain spectroscopy systems. By operating directly on the electric field, it allows for measuring the average THz scattered field (in a fully coherent sense) by performing a point-like detection in the Fourier plane. As defined by Equation (B.6), the coefficients C_n can be obtained by measuring the $(k_x, k_y) = 0$ spectral components of the THz transmitted field:

$$C_n = \int dxdy E_n^+(x, y, t) = \mathcal{F}[E_n^+(x, y, t)]|_{k_x=0, k_y=0}. \tag{B.11}$$

This implementation implies that the experimental measurement of the correlations C_n is not limited at all by the numerical aperture of the bucket detector. This type of measurement can be obtained by placing the object in the focal point of an arbitrary lens and by acquiring the signal in the central point of the opposite focal plane (Figure B.5a). The electric field in the focal plane reads as follows:

$$E_{focal}(x', y') \propto \mathcal{F}[E_n^+(x, y, t)](k_x = \frac{x'}{\lambda f}, k_y = \frac{y'}{\lambda f}), \tag{B.12}$$

where x' and y' are the physical coordinates in the Fourier plane [351].

However, in terms of implementation, the detector samples a finite small area of the Fourier plane with an area-sampling function $PH(k_x, k_y)$, obtaining the estimation $C'_n(t)$:

$$C_n^{\prime(t)} = \int PH(k_x, k_y) * \mathcal{F}[E_n^+(x, y, t)] dk_x dk_y, \tag{B.13}$$

where $PH(k_x, k_y)$ is physically represented by the profile of the probe beam in the electro-optical sampling (e.g., a Gaussian function), or by the shape of any aperture implemented in front of the nonlinear detection to fix its interaction area with the THz field.

The accuracy of the measurements is then directly related to how "point-like" our detection can be made. Although one could be tempted to foresee a general benefit of the high signal-to-noise ratio (SNR) resulting from large detection apertures as in the standard GI, this is also a source of artefacts, fundamentally establishing a trade-off between SNR and fidelity.

Figure B.7 illustrates the effects of the size d of the sampling function $PH(x' = k_x \lambda f, y' = k_y \lambda f)$ on the image reconstruction fidelity (Figure B.7e). Interestingly, the reduction of fidelity observed for increasing the sampling diameter is different from the typical limitations in standard imaging. In our case, a too-large area sampling function in the Fourier plane did not lead

to a reduction in the discernible details but rather in the disappearance of entire parts of the image (see Figure B.7e, insets).

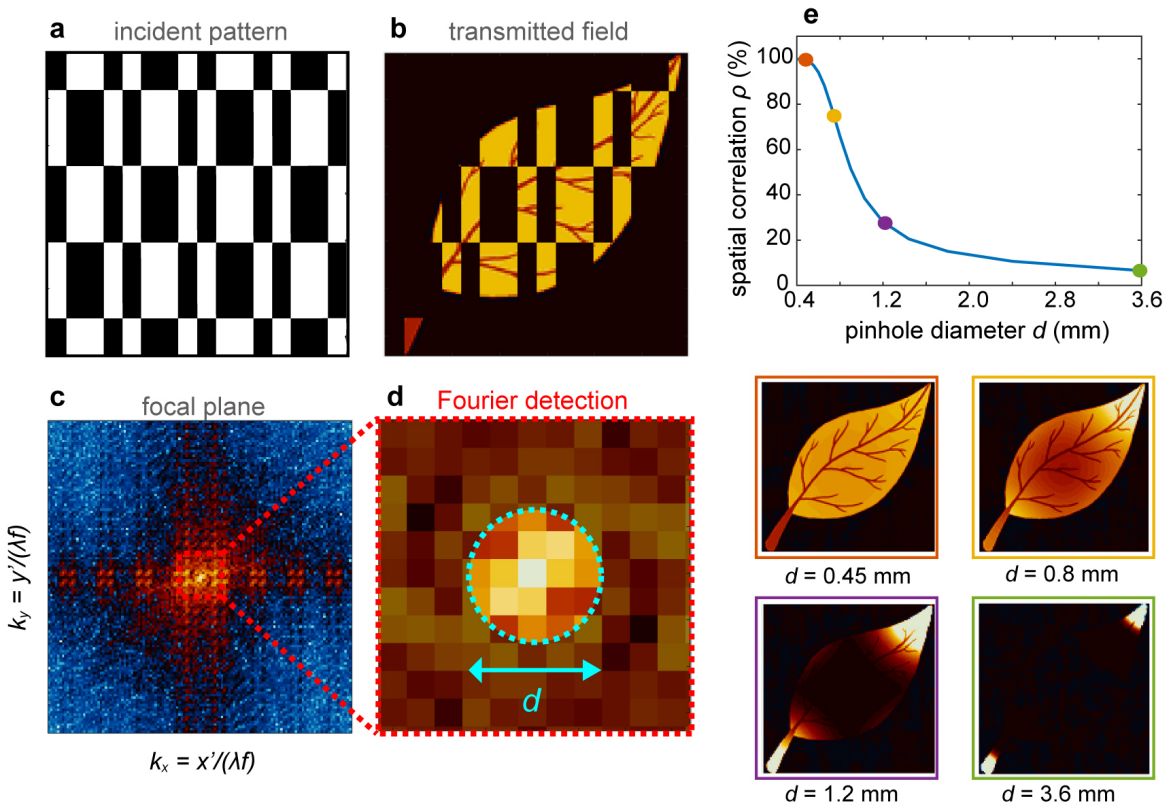

Figure B.7: Influence of the pinhole size on the Fourier detection of TIMING reconstruction coefficients. (a–d) The spatial average of the transmitted field (b) associated with each incident pattern (a) could be measured by performing a point-like detection in the centre of the Fourier plane (c,d). In realistic implementations, the centre of the Fourier plane is sampled using a sampling function PH of finite diameter d. (e) Spatial correlation between the reconstructed and original image as a function of the sampling function diameter. A departure from the point-like approximation led to a significant corruption of the reconstructed image (insets). Interestingly, the typical image degradation did not necessarily involve the total disappearance of highly resolved details.

Similarly, in Figure B.8, we illustrate the effect of a misalignment of the sampling function PH centre with respect to the centre of the Fourier plane. Trivially, the spatial correlation between the reconstructed and original images peaks at the centre of the Fourier plane and swiftly decayed in the case of off-axis detection (Figure B.8a). In these conditions, the reconstructed image showed the appearance of spurious spatial frequencies, corresponding to the (k_x, k_y) sampling position (Figure B.8b,d). Interestingly, however, the overall morphology and details of the image were still present in the images, and no noticeable blurring occurred.

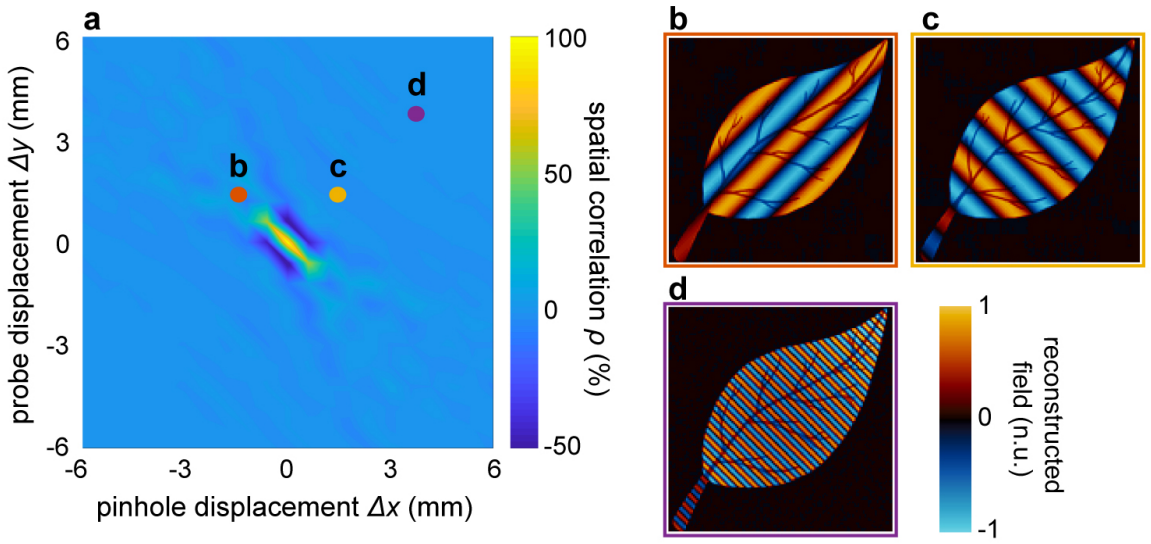

Figure B.8: Influence of the pinhole displacement on the Fourier detection of TIMING reconstruction coefficients. (a) Spatial correlation between the reconstructed and original image as a function of the sampling function position in the focal plane. The displacement $(\Delta x, \Delta y)$ was measured with respect to the lens axis and the sampling function diameter was set to $d = 0.36$mm, corresponding to a spatial correlation of 100% at the centre of the Fourier plane (cf. Figure B.7e). (b–d) Examples of image reconstruction with off-axis detection, illustrating the appearance of spurious spatial frequencies. Interestingly, the object morphology was still noticeable, even at a relatively large distance from the optical axis.

B.4.6 A Route towards Thinner THz Emitters: Surface Emission from Quasi-2D Semiconductor Structures

Deep near-field regimes are in general a requirement to obtain deep-subwavelength image resolutions. Here, we review this current technological solution that is under development in TIMING towards this goal.

In terms of nonlinear ghost imaging, the high resolution fundamentally results from the ability to achieve significant optical-to-terahertz conversions, keeping the sample in the proximity of the distribution of terahertz sources. This translates into the need for generating terahertz from quite thin devices (although we argued how TIMING exhibits significantly more relaxed constraints compared to previous literature [186]).

Although the technology is continuously evolving, the best-performing and most practical off-the-shelf sources are within the class of electro-optical switches. The terahertz emission is generated by a transient current that is sustained by an external electric source and is triggered by a change of conductivity induced by an ultrafast optical absorption [330]. This specific ap-

proach benefits from a virtually high optical-to-terahertz conversion efficiency since the actual source of radiation is a current sustained by the electric source. However, this technology is difficult to translate to TIMING since the integration into a single device of a dense distribution of independent electrical switches emitting terahertz signals is extremely challenging.

In terms of direct optical-to-terahertz conversion, improving the efficiency of nonlinear converters is undoubtedly a central research area with a vast spectrum of proposed solutions ranging from novel materials to the design of sophisticated propagation geometries, which allows for very long interaction lengths. However, very few alternatives are currently available for emitters with a thickness below the micrometre scale. One general issue is that the efficiency of bulk nonlinear interactions tend to be vanishingly low at this scale, whereas the ruling mechanisms of the nonlinear interactions are dominated by peculiar physical mechanisms that exist only in quasi-2D frameworks. Some very promising, recently explored solutions comprise exploiting spin-mediated current transients (spintronic emitters) in nano-hetero-metallic structures [190]. On the other hand, a significant fraction of the work in this research area focuses on achieving a very large interfacial nonlinear response or inducing carrier-mediated nonlinear dynamics at a surface.

In general, these effects are fundamentally driven by breaking the lattice symmetry, which is produced by the material discontinuity at the interface. The requirement of tightly reduced interaction lengths makes low-bandgap semiconductors, such as Indium Arsenide (InAs) and Indium Antimonide (InSb), very popular experimental frameworks. What motivated the interest in these systems is the surprisingly high conversion efficiency per interaction length [109, 128, 137]. In a traditional NIR ultrafast excitation setting, the mean absorption length for photons is very small, typically within the scale of $l_d = 140$nm at a wavelength $\lambda = 800$nm. At low fluences (below 100nJ/cm^2), InAs is probably considered the benchmark surface emitter. In this case, the generation is driven by the very large difference in mobility between holes and electrons via the photo-Dember effect (Figure B.9c,d): when a high density of photogenerated pairs is induced in the proximity of the surface, electrons quickly diffuse away from the surface, leaving uncompensated carriers of the opposite sign. Such a charge unbalance creates a fast stretching dipole, or equivalently, a local current transient that is the source of the terahertz emission [104].

At very high pumping energies (above 10μJ/cm^2), this phenomenon becomes critically saturated due to the electromagnetic screening role of dense carrier densities. Conversely, the optical surface rectification (SOR) dominates the emission [109]. The optical surface rectification is a quadratic phenomenon induced by the contribution of a local static field at the surface,

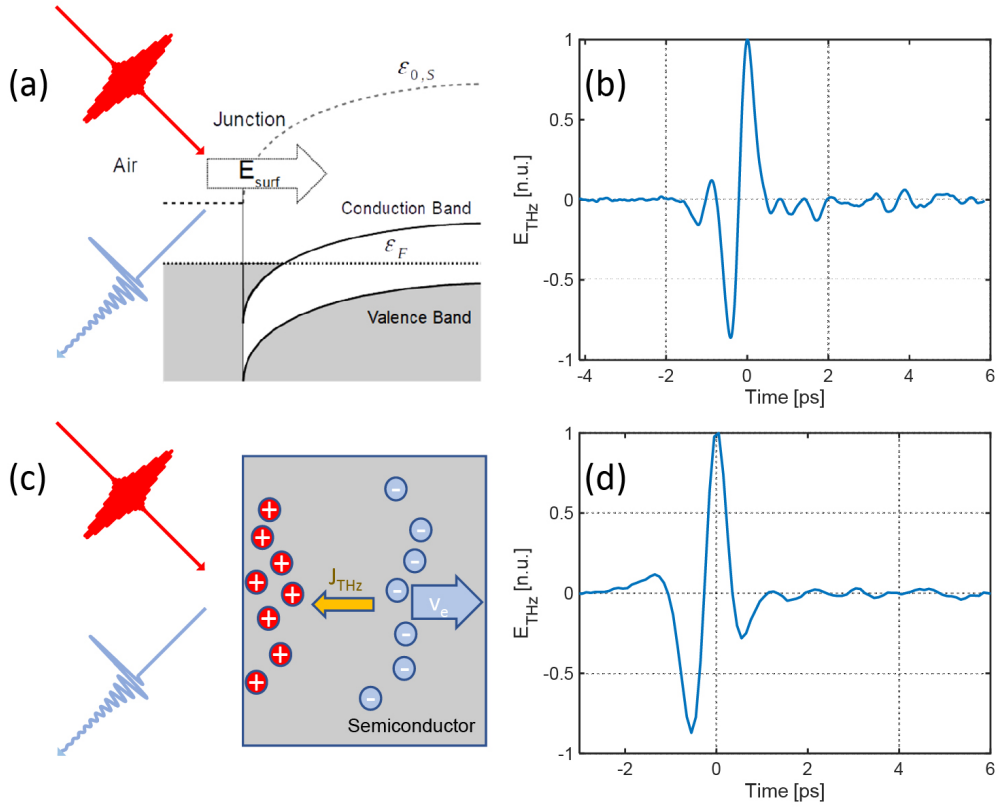

Figure B.9: Surface emission driving mechanisms. (a) Surface optical rectification—a surface field at the air–semiconductor barrier combines with the optical field in a four-wave mixing process (cubic), generating a terahertz mixing product (see Equation (B.10)). (b) Measurement of the terahertz emission using surface optical rectification with an optical pulsed excitation fluence of 7mJ/cm^2 (1kHz repetition rate) and a pulse with a wavelength of 800nm and a duration of 90fs. (c) Simplified sketch of the photo-Dember process in InAs. The absorption of an ultrashort pulse generates a high density of photogenerated hole–electron pairs within the optical penetration depth (140nm). The fast diffusion of the electrons induces a transient current J_{THz}, which is the source of the terahertz emission. (d) Measurement of the terahertz emission by photo-Dember mechanism with an optical pulsed excitation fluence of 0.28μJ/cm^2 (80MHz repetition rate) and pulse with a wavelength of 800nm and a duration of 140fs.

which is induced by surface states within the bulk cubic nonlinear response (Figure B.9a,b). The DC field effectively plays the role of a field contribution in a four-wave mixing process in a mechanism commonly referred to as a field-induced quadratic response [137, 195] and is described using:

$$E_{\mathrm{THz}} \propto \chi^{(3)} E_{\mathrm{surf}} E_{\omega}^{*} E_{\omega}, \tag{B.14}$$

where $\chi^{(3)}$ is the third-order susceptibility of InAs, E_{surf} is the intrinsic surface potential field, E_ω is the incident optical field and $*$ stands for the complex conjugate. Quite interestingly, because the phenomenon is driven by a surface potential, it is also a measurable way to probe the dynamics of the carrier at the surface, and it has been proposed as the optical analogy of a Kelvin probe [90].

B.4.7 Discussions and Conclusions

In this work, we have provided an overview of the advantages and implementation challenges of a time-resolved nonlinear ghost-imaging approach to THz single-pixel imaging. By combining nonlinear THz generation and single-pixel TDS detection, we demonstrated the high-resolution reconstruction of a semi-transparent sample with a subwavelength resolution (512×512pixels). By providing a detailed analysis of the Walsh–Hadamard reconstruction scheme, we have shown how a specific choice of patterns and the order of acquisition can play a beneficial role in speeding-up the reconstruction of the peak-field transmission from the sample. Remarkably, we have shown that less than 10% of the incident samples were required to achieve a high-fidelity reconstruction of the sample image in a general sequential reconstruction. Our approach, which is based on a lexicographical sorting of the incident patterns in terms of their spatial frequency (an approach we denoted as a "smart-Walsh" reconstruction), is general and image-independent and can be applied to reduce the overall reconstruction time for unknown samples. Interestingly, such a result could be further improved by considering that even a smaller percentage of incident patterns are required to reconstruct the sample: in our case, only 8% of the patterns were associated with an expansion coefficient exceeding 60dB. In practical terms, this would correspond to a 92% shorter acquisition time, corresponding to a 12.5× speed up of the image reconstruction process when compared to a full scan based on the Hadamard encoding scheme. These numbers suggest that the reconstruction process could be significantly sped up through the application of adaptive-basis-scan algorithms and deep-learning-enhanced imaging, which identify and predict the best set of scanning patterns in real time [350, 352, 353, 354].

Interestingly, our results suggest that the nonlinear GI methodology is not limited by the numerical aperture of the optical system in a "conventional" sense. Said differently, it operates under the assumption of a very low numerical aperture to obtain a faithful spectral representation of the image. However, our results highlight that the image reconstruction is quite sensitive to the size and alignment of the pinhole function selecting the $(k_x, k_y) = 0$ components of the scattered field. Most importantly, in sharp contrast with previous literature on the topic,

the reconstruction accuracy cannot simply be represented as a matter of effective "resolution". The drop in reconstruction fidelity, in fact, is not driven by the attenuation of high-frequency spatial components (i.e., blurring) as in standard imaging, but it can lead to the appearance of artefacts and spurious spatial frequencies. To the best of our knowledge, the reconstruction limits of single-pixel time-domain imaging have never been formalised elsewhere.

Finally, although thin emitters are a general requirement for this approach, TIMING exhibits relaxed constraints between the nonlinear interaction length and the image resolution. Yet, solutions for sub-micron-thick large-area terahertz generation are practically possible, enabling resolutions within the same scale or better. A promising platform to achieve this goal is narrow-bandgap semiconductor devices based on InAs or InSb platforms. These materials not only provide extremely high optical-to-terahertz conversion efficiency per unit length but they are also suitable for large-scale fabrication and deployment in real-world devices thanks to their established deployment in the electronic domain.

We believe that TIMING is a significant step forward in the development of terahertz microdiagnostics based on hyperspectral imaging devices. Our approach also addresses fundamental criticalities in the imaging reconstruction process, which generally affect any high-resolution imaging domain where high temporal resolution is sought. As such, TIMING establishes a comprehensive theoretical and technological platform that paves the way for new generations of terahertz imaging devices satisfying the requirements for high-resolution and spectral sensitivity in real-world applications.